Towards an Improvement of the Prediction of Geothermal Production Temperatures:

Uncertainty Assessment and Integrated Flow Zone Monitoring

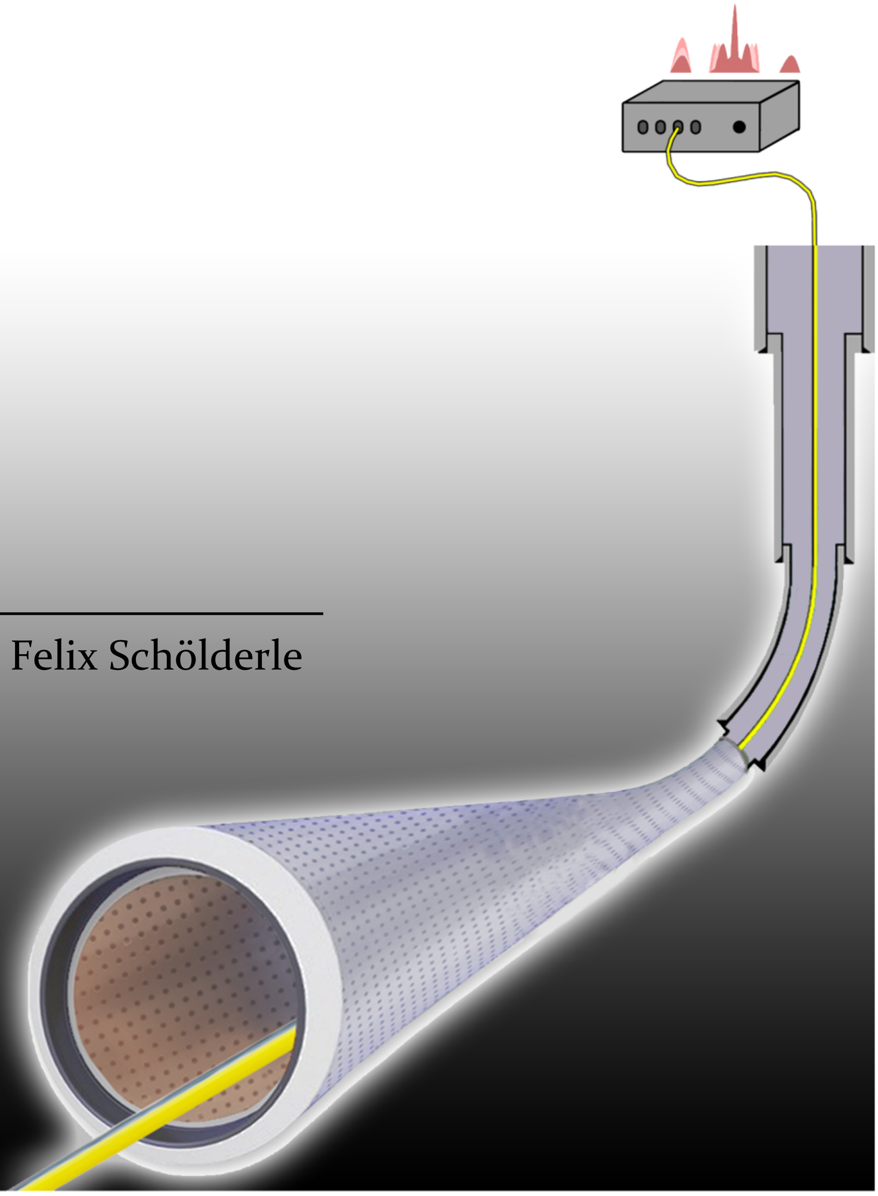

Felix Schölderle

Technische Universität München
TUM School of Engineering and Design

TOWARDS AN IMPROVEMENT OF THE PREDICTION OF GEOTHERMAL PRODUCTION TEMPERATURES: UNCERTAINTY ASSESSMENT AND INTEGRATED FLOW ZONE MONITORING

Felix Hermann Michael Schölderle

Vollständiger Abdruck der von der TUM School of Engineering and Design der Technischen Universität München zur Erlangung eines

Doktors der Ingenieurwissenschaften (Dr.-Ing.)

genehmigten Dissertation.

Vorsitz: Prof. Dr. Florian Einsiedl

Prüfende der Dissertation:

1. apl. Prof. Dr. Thomas Baumann
2. Prof. Dr. Michael Drews
3. Prof. Dr. Magdalena Scheck-Wenderoth

Die Dissertation wurde am 04.07.2024 bei der Technischen Universität München eingereicht und durch die TUM School of Engineering and Design am 01.11.2024 angenommen.

“Without data, you’re just another person with an opinion”

Edwards Deming

ABSTRACT

In areas with hydrothermal potential, the utilization of geothermal heat from deep reservoirs has become a climate mitigation strategy. The temperature of the produced fluid is a key parameter, as it directly controls the thermal and electrical power generated. High temperatures (~120 °C) enable electricity generation, while temperatures that are lower than expected can lead to the economic failure of a project. Forecasting the production temperature for a planned location is thus important and usually based on the available field-wide static temperature models. These specify the predicted value for planning at a certain depth in undisturbed conditions. The undisturbed temperatures and the subsequent production temperatures are only vaguely known before a borehole is drilled, with no or just an undetermined uncertainty.

Many of the static models are based on low-quality input data, usually bottom hole temperatures (BHTs). Measured shortly after drilling during geophysical logging, they are thermally disturbed by the prevailing drilling processes, are therefore subject to unknown errors, and must be corrected using error-prone methods. Since the uncertainty of the input parameters for the correction methods is rarely considered, it can be assumed that the actual error is higher than specified by the existing temperature models. To close this knowledge gap, uncertainties for the relevant parameters of BHT corrections are proposed in this thesis. In addition, a workflow based on Monte Carlo techniques was developed, which is based on standard correction methods but, contrary to common practice, generates correction results dependent on probabilistic principles. The workflow was developed for the geothermal and hydrocarbon well data set of the hydrothermal hotspot of the North Alpine Foreland Basin in Bavaria, southern Germany, and tested using high-quality temperature measurements. The method enables existing models to be improved or new models for the static depth temperature to be presented with a profound uncertainty that depends on the quality of the input data. For the study area, the results show indeed that the uncertainty of parameters used for common BHT correction exceeds the errors of the different methods themselves, which is not yet represented by the existing models. Using the p10 and p90 percentiles of the corrected values as the uncertainty range of the prediction, a value of 30 K or more is estimated for 5 % of the boreholes. However, in 20 % of the boreholes, there are also high-quality BHT data sets, resulting in a low uncertainty range of less than 5 K.

Dynamic temperature models, which represent a forecast of the production temperature, do not exist to the same extent as for the undisturbed depth temperature, because the production temperature in conductive systems depends strongly on the location of the hydraulically active zones and the quantity of the inflowing thermal water. These are unknown in advance and up to now hard to predict. Hydraulic and thermal investigations in the reservoir are rare and are not included in the standard design of geothermal wells after the production pump has been installed. To analyze how the dynamic state of a geothermal well differs from the static, undisturbed state, an approx. 3700 m MD deep production well in the study area was examined in detail for its hydraulically active zones. For this purpose, a conventional flowmeter interpretation was carried out, and a novel fiber optic monitoring system was developed and permanently installed along a pump string below the pump and into the reservoir. The system enables distributed temperature measurements (DTS), distributed acoustic/dynamic strain measurements (DAS), e.g., for future microseismicity studies, and point pressure and temperature measurements at a fiber optic sensor at the top of the reservoir. Based on uncertainty assumptions for the calibration parameters in positioning the system in the borehole, the DTS system provides temperature values accurate within a standard deviation of ± 1.6 K. The system measured the warm-back to the temperature equilibrium during and after a 16-month shutdown period. The inflow zones were characterized by evaluating DTS profiles during and after injection tests, and the conventional flowmeter interpretation was verified. After the well was put into operation, DTS profiles were evaluated again to quantitatively characterize the inflow zones under production conditions using an inverse model. The results show that the monitored well is primarily characterized by a 25 m thick karstified zone at the top of the reservoir, which accounts for approximately 80 % of the inflow. This flow zone also controls the mixing temperature in the reservoir, which is about 97 °C at the inlet to the casing. The water inflow in this upper zone is significantly cooler than in the deeper, less hydraulically active zones, where temperatures of over 107 °C are measured. During the injection tests, the design of the monitoring system was also tested for dynamic movement of the cable/pump rodding due to thermal stress by combining DTS and DAS. There were clear indications that the future use of the system for seismic monitoring with DAS is limited or only possible in good quality if the movement of the pump rodding can be better understood and filtered out of the DAS data.

This work shows that permanent fiber optic measurement systems are particularly suitable for characterizing hydraulically active zones during tests and also during the operation of a well. The location of hydraulically active zones plays a key role in the mixing temperature profile, which is why the prediction of wellhead temperatures based on static temperature models is often misleading. This is especially true if the uncertainties of the static temperature models remain unclear. A BHT correction workflow based on uncertainties can help to improve existing models. In a conductive-dominated system, the production temperature is usually higher than the static temperature at the top of the reservoir, so the static temperature can be considered a worst-case estimate.

ZUSAMMENFASSUNG

In Gebieten mit hydrothermalem Potenzial ist die Nutzung der Tiefengeothermie eine wichtige Klimaschutzstrategie geworden. Ein Schlüsselparameter ist dabei die Fördertemperatur, da sie die thermische und elektrische Leistung direkt beeinflusst. Hohe Temperaturen (~120 °C) ermöglichen die Stromerzeugung, während geringere Temperaturen als erwartet zum wirtschaftlichen Misserfolg führen können. Daher ist die Vorhersage der Produktionstemperatur von großer Bedeutung und basiert in der Regel auf den verfügbaren feldweiten statischen Temperaturmodellen, die den Planungswert in einer bestimmten Tiefe im ungestörten Zustand angeben. Die ungestörten Temperaturen und die späteren Fördertemperaturen sind vor einer Bohrung nur vage mit unspezifischer Unsicherheit oder gar nicht bekannt.

Viele der statischen Modelle beruhen auf Eingangsdaten von geringer Qualität, den Bottom Hole Temperaturen (BHTs). Diese werden kurz nach dem Bohrprozess während geophysikalischer Messungen erfasst, sind durch die Bohrprozesse thermisch gestört, unterliegen daher unbekannten Fehlern und müssen mit fehleranfälligen Methoden korrigiert werden. Da die Unsicherheit der Eingangsparameter für die Korrekturverfahren in der Regel nicht berücksichtigt wird, ist davon auszugehen, dass der tatsächliche Fehler höher ist, als durch die bestehenden Temperaturmodelle angegeben. Um diese Wissenslücke zu schließen, werden in dieser Arbeit Unsicherheiten für die relevanten Parameter gängiger BHT-Korrekturen vorgeschlagen. Darüber hinaus wird ein auf Monte-Carlo-Techniken basierender Arbeitsablauf vorgestellt, der zwar auf Standardverfahren aufbaut, die Korrekturergebnisse aber entgegen der üblichen Praxis von probabilistischen Prinzipien abhängig macht. Dieser Workflow wurde für Geothermie- und Kohlenwasserstoff-Bohrungen im hydrothermalen Hotspots des Nordalpinen Vorlandbeckens in Bayern, Süddeutschland, entwickelt und anhand hochwertiger Temperaturmessungen getestet. Das Verfahren ermöglicht es, bestehende Modelle zu verbessern oder neue Modelle für die statische Tiefentemperatur mit einer validen Unsicherheit darzustellen, die von der Qualität der Eingabedaten abhängt. Die Ergebnisse für das Untersuchungsgebiet zeigen, dass die Unsicherheit der für die allgemeine BHT-Korrektur verwendeten Parameter die Fehler der verschiedenen Methoden selbst übersteigt, was von den bestehenden Modellen bisher nicht dargestellt wird. Unter Verwendung der p10- und p90-Perzentile der korrigierten Werte als Unsicherheitsbereich der Vorhersage wird ein Wert von 30 K oder mehr für 5 % der Bohrlöcher geschätzt. In 20 % der Bohrlöcher gibt es jedoch auch hochwertigere BHT-Datensätze, was zu einem geringen Unsicherheitsbereich von weniger als 5 K führt.

Dynamische Temperaturmodelle, die eine Prognose der Produktionstemperatur darstellen, existieren nicht im selben Maße wie für die ungestörte Tiefentemperatur, denn die Produktionstemperatur hängt bei konduktiven Systemen stark von der Lage der hydraulisch aktiven Zonen und deren Anteil am zuströmenden Thermalwasser ab. Diese sind im Vorhinein unbekannt. Hydraulische und thermische Untersuchungen im Reservoir sind rar und im

Standarddesign von Geothermiebohrungen nach Einbau der Pumpe nicht vorgesehen. Um zu analysieren, wie sich der dynamische Zustand einer geothermischen Bohrung vom statischen, ungestörten Zustand unterscheidet, wurde eine ca. 3700 m MD tiefe Förderbohrung im Untersuchungsgebiet detailliert auf ihre hydraulisch aktiven Zonen untersucht. Zu diesem Zweck wurde eine konventionelle Flowmeter Interpretation durchgeführt und ein neuartiges faseroptisches Überwachungssystem entwickelt und permanent entlang eines Pumpengestänges unterhalb der Pumpe und bis ins Reservoir installiert. Das System ermöglicht verteilte Temperaturmessungen (DTS), verteilte akustische/dynamische Dehnungsmessungen (DAS), z.B. für zukünftige Studien der Mikroseismizität, und punktuelle Druck- und Temperaturmessungen an einem faseroptischen Sensor am Top des Reservoirs. Basierend auf Unsicherheitsannahmen für die Kalibrierparameter in der Positionierung des Systems im Bohrloch liefert das DTS System Temperaturwerte mit einer Unsicherheit von ± 1.6 K. Mithilfe des Systems wurde die statische Temperatur während und am Ende einer 16-monatigen Stillstandszeit gemessen. Durch die Auswertung von DTS-Profilen während und im Nachgang von Injektionstests wurden die Zuflusszonen charakterisiert und die konventionelle Flowmeter-Interpretation verifiziert. Nach dem Betriebsstart der Bohrung wurden erneut DTS-Profile ausgewertet, um die Zuflusszonen unter Produktionsbedingungen mit einem inversen Modell quantitativ zu charakterisieren. Die Ergebnisse zeigen, dass sich die überwachte Bohrung vor allem durch eine 25 m mächtige verkarstete Zone am Top des Reservoirs auszeichnet, die für etwa 80 % des Zuflusses sorgt. Diese Zuflusszone kontrolliert auch die Mischtemperatur im Reservoir, die am Eintritt in die Verrohrung etwa 97 °C beträgt. Der Wasserzufluss in dieser oberen Zone ist deutlich kühler als in den tieferen, hydraulisch weniger aktiven Zonen, wo Temperaturen von über 107 °C gemessen werden. Während der Injektionsversuche wurde zudem das Design des Überwachungssystems durch die Kombination von DTS und DAS auf die dynamische Bewegung des Kabels/des Pumpengestänges aufgrund der thermischen Belastung getestet. Es ergaben sich deutliche Hinweise darauf, dass die künftige Nutzung des Systems für eine z.B. seismische Überwachung mit DAS nur begrenzt oder nur in guter Qualität möglich ist, wenn die Bewegung des Pumpengestänges besser verstanden und aus den DAS-Daten herausgefiltert werden kann.

Diese Arbeit zeigt, dass fest installierte faseroptische Messsysteme besonders für die Charakterisierung hydraulisch aktiver Zonen geeignet sind. Die Lage der Fließzonen spielt eine Schlüsselrolle für das Mischtemperaturprofil, weshalb die Vorhersage von Bohrlochkopftemperaturen auf der Grundlage von statischen Temperaturmodellen oft irreführend ist. Dies gilt insbesondere dann, wenn die Unsicherheiten der statischen Temperaturmodelle weiterhin unklar bleiben. Ein auf Unsicherheiten basierender Workflow der BHT-Korrektur kann zur Verbesserung bestehender Modelle beitragen. In einem konduktiv dominierten System liegt die Produktionstemperatur im Allgemeinen über der statischen Temperatur am Top des Reservoirs, sodass die statische Temperatur als Worst-Case-Schätzung betrachtet werden kann.

STRUCTURE OF THE THESIS AND PUBLICATIONS

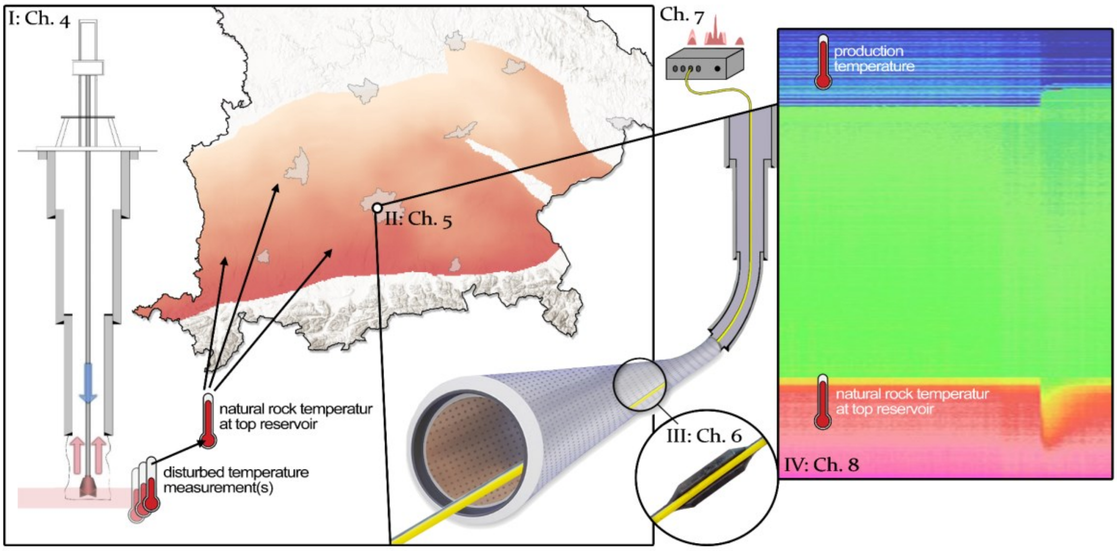

Graphical Abstract. Structure of the Thesis and accepted Publications (I – IV) in the respective Chapters.

The following work has been produced within the framework of the two research projects KompakT, financed by the Bavarian Environmental Agency, and Geothermal-Alliance Bavaria (GAB), financed by the Bavarian State Ministry of Science and Arts. The work carried out in these projects and combined in this thesis relates to the prediction of the temperatures in the subsurface of the deep hydrothermal aquifer in Bavaria and the extraction temperatures when the thermal fluid is being used. Four ISI-listed research articles were published during the work, which are marked with the numbers I, II, II, and IV in the Graphical Abstract.

The thesis is structured into 9 chapters, with Ch. 1 giving an introduction to geothermal energy and specifically to hydrothermal projects in a general context and relation to the study area, and explaining the significance of the static and dynamic temperature. Ch. 2 is intended to provide the reader with the necessary state of the art and theoretical background to this work and for the publications presented. Ch. 3 identifies research gaps from Ch. 2 and formulates the research questions for this thesis. The following Ch. 4, 5, 6, and 8 contain the accepted publications. In an additional Ch. 7, a technical note over the fiber optic monitoring system is presented that is intended as stand-alone lessons learned in which the technical experiences with the newly developed and implemented system are presented. The concept as such, the technical obstacles, the conclusions drawn, and the experience gained during the four years of operation are discussed. A concluding Ch. 9 summarizes the main findings and further considerations in a synoptic discussion.

To improve the readability of this work, all publications have been brought into a uniform format and the numbering of equations, figures, and tables has been standardized for the entire document. Some of the terms used differently in the publications (e.g. single-mode, single mode, singlemode or pT, P/T, p/T) have also been standardized throughout the document, as has the use of double and single quotation marks for literal quotes and the definition of terms. The references and appendices are separated into the joint list of references and supplements at the end of this thesis. No changes have been made to the content of the publications. The four publications are thematically linked as shown in the Graphical Abstract and build on each other as follows.

Publication 1 (Schölderle et al. 2022) (Ch. 4), quantifies the uncertainty of the standard temperature corrections that must be applied to estimate the temperature of deep formations under natural, undisturbed conditions. A new probabilistic workflow was developed to enable more reliable assessments and temperature models for the hydrothermal field in the future. Publications 2, 3, and 4 focus on a study site in the center of the research area, where the actual thermal conditions are monitored over an entire borehole, and the thermal influence of hydraulically active zones is highlighted. Therefore, the installation of a new fiber optic monitoring system in a geothermal production well is presented in publication 2 (Schölderle et al. 2021) (Ch. 5), and distributed temperature sensing is used to measure the undisturbed formation temperature. In addition, cold water injection tests are performed and analyzed with the fiber optic temperature and acoustic data to locate and characterize the flow zones in the wellbore. In publication 3 (Lipus et al. 2022) (Ch. 6), the overall performance of the system under thermal stress is tested by combining the distributed acoustic and temperature data. The results are helpful for future evaluations, as they provide an understanding of the behavior of the fiber optic system about external influences that do not necessarily indicate hydraulic processes in the reservoir. In publication 4 (Schölderle et al. 2023) (Ch. 8), the conversion of the monitoring system after pump installation is presented and distributed temperature data measured during the start of operation is presented and used to quantify the inflow zones with an inverse model under real production conditions.

List of Accepted Publications and Related Research Projects

Publication 1 (Research Article): Ch. 4

Schölderle F., Götzl, G., Einsiedl, F., Zosseder, K. (2022). Uncertainty Assessment of Corrected Bottom-Hole Temperatures Based on Monte Carlo Techniques. Energies, 15(17). https://doi.org/10.3390/en15176367

Personal contribution to the paper:

The author of this thesis conceptualized this work with an own share of 90 %, was involved 100 % in the acquisition of data, to 90 % in the analysis and data interpretation, and wrote the first draft with an own share of 90 % and revised the manuscript during the review process to 90 %.

Publication 2 (Research Article): Ch. 5

Schölderle, F., Lipus, M., Pfrang, D., Reinsch, T., Haberer, S., Einsiedl, F., Zosseder, K. (2021). Monitoring cold water injections for reservoir characterization using a permanent fiber optic installation in a geothermal production well in the Southern German Molasse Basin. Geotherm. Energy, 9(21). https://doi.org/10.1186/s40517-021-00204-0

Personal contribution to the paper:

The author of this thesis conceptualized this work with an own share of 60 %, was involved 75 % in the acquisition of data, 80 % in the analysis and data interpretation, and wrote the first draft with an own share of 90 % and revised the manuscript during the review process to 85 %.

Publication 3 (Research Article): Ch. 6

Lipus, MP., Schölderle, F., Reinsch, T., Wollin, C., Krawczyk, C., Pfrang, D., Zosseder, K. (2022). Dynamic motion monitoring of a 3.6 km long steel rod in a borehole during cold-water injection with distributed fiber-optic sensing. Solid Earth, 13(1), 161-176. https://doi.org/10.5194/se-13-161-2022

Personal contribution to the paper:

The author of this thesis conceptualized this work with an own share of 30 %, was involved 20 % in the acquisition of data, to 30 % in the analysis and data interpretation, and wrote the first draft with an own share of 30 % and revised the manuscript during the review process to 20 %.

Publication 4 (Research Article): Ch. 8

Schölderle, F., Pfrang, D., Zosseder, K. (2023). Inverse flow zone characterization using distributed temperature sensing in a deep geothermal production well located in the Southern German Molasse Basin. Adv. Geosci., 58, 101-108. https://doi.org/10.5194/adgeo-58-101-2023

Personal contribution to the paper:

The author of this thesis conceptualized this work with an own share of 90 %, was involved 90 % in the acquisition of data, to 95 % in the analysis and data interpretation, and wrote the first draft with an own share of 100 % and revised the manuscript during the review process to 90 %.

Research Project I: KompakT

KompakT (2020 – 2023) was a joint project funded by the Bavarian Environmental Agency between the assistant professorship for geothermal technology and the chair of hydrogeology of the Technical University of Munich. One part of this project, related to the content of this work, was to interpret deep surface temperature data in the hydrothermal hotspot of the North Alpine Foreland Basin in Bavaria and to estimate heat storage potentials. Publication 1 was realized in the course of this project and was financed by it.

Research Project II: Geothermal-Alliance Bavaria (GAB) Funding Phase 1 and 2

The GAB consortium consists of several Bavarian universities and is funded by the Bavarian State Ministry of Science and Arts to study the deep geothermal potential in Bavaria. During this project, a new fiber optic monitoring system was developed and installed into the reservoir of a production well as described in this thesis. The analyses of the collected fiber optic data presented in this thesis and the conclusions that contributed to an increased reservoir understanding were also part of the project.

ACKNOWLEDGMENTS

This thesis would not have been possible without the support, ideas, and effort of several people, whom I would like to thank at this point. First and foremost, I want to thank Dr. Kai Zosseder, who was the initiator and source of ideas for this work and who made it possible for me to immerse myself in geothermal energy and work in an incredibly exciting field of research and practice. Above all, his vision and enthusiasm for a successful heat transition for climate protection were always inspiring and highly motivating.

I also want to thank my supervisors, Prof. Dr. Florian Einsiedl and Prof. Dr. Thomas Baumann for their support and contribution to this work. In particular, Prof. Baumann was always available with helpful advice during the final stages of this thesis. I also thank my mentor Dr. Thomas Reinsch whose high competence in the techniques and physical details of fiber optic sensing helped a lot in writing this work.

I would also like to thank my dear family, partner, and friends for their support, as well as my former and current fellow doctoral students Fabian, Florian, Daniel, Florian, Alejandra, Manuel, Anne, Alberto, Theis, Tamara, Lea, Annette, Lilly, Aurelio, Valerie, Marlis, who made the professional and non-professional exchanges a pleasure with various beach volleyball games and weekend trips for skiing, hiking and biking.

Many people were crucial to the successful planning and installation of the fiber optic monitoring system, to whom I would like to express my gratitude. Thanks to Sven Haberer for his commitment to the project and his role as a problem solver, both in the planning process and the implementation at the borehole site. Many thanks also to Michael Meinecke, Franz Barenth, Sebastian Dirner, Daniel Lackner, Andreas Appel, Alexandros Savvatis, and Katja Thiemann from Stadtwerke München and the engineering office Erdwerk for believing in the project and having the courage to implement it despite the hurdles and risks in their boreholes.

A special thank you finally goes to Daniela Pfrang for putting her heart and soul into the planning of the fiber optic monitoring system and overcoming the technical and administrative challenges involved in its implementation.

CONTENTS

1 Introduction 1

1.1 Overall Context – Mitigation of Climate Change 1
1.2 Deep Geothermal Energy systems and their potential 2
1.3 Hydrothermal Utilization in Germany and Bavaria 4

2 State of the Art 6

2.1 Thermal Processes in Geothermal Foreland Basins 6
2.1.1 Temperature Terminology 6
2.1.2 Temperature Properties and Heat Transport 7
2.2 Specification and Characterization of the Hydraulically Active Zones 9
2.3 Measuring the Temperature in the Development Phases of a Borehole 11
2.3.1 Drilling Phase: Geophysical Logging and Bottom Hole Temperatures 11
2.3.2 Hydraulic Testing Phase: Temperature at Top of the Reservoir 13
2.3.3 Shut-in Phase: Additional Geophysical Logging 14
2.3.4 Commissioning Phase: Development of the Outflow Temperature 14
2.3.5 Wrapping up Conventional Downhole Tools 15
2.4 Downhole Fiber Optic Sensing as an Opportunity for Long-Term Monitoring 17
2.4.1 Brief Outline and Fundamental Principle 17
2.4.2 Design of Optical Fibers and Fiber Optic Cables 17
2.4.3 Optical Fiber as a Transmission Medium 18
2.4.4 Optical Fiber as Sensor Device – Distributed Sensing 18
2.4.5 Measurement Setups and Downhole Deployments 19
2.4.6 Potential to Use Fiber Optics for an Improved Temperature Prediction 20
2.5 The Hydrothermal Field of the North Alpine Foreland Basin 20
2.5.1 Geology and Classification 20
2.5.2 Temperature Models of the North Alpine Foreland Basin 21

3 Aims and Scope 25

4 Uncertainty Assessment of Corrected Bottom-Hole Temperatures Based on Monte Carlo Techniques 27

4.1 Introduction 28
4.2 Materials and Methods 31
4.2.1 Study Area and Data Set 31
4.2.2 Applied Correction Schemes 33
4.2.3 Global Sensitivity Analysis (GSA) 37
4.2.4 Uncertainty Study 42
4.2.5 BHT Correction at Flow Zones 44

4.3 Results ... 45
4.3.1 Uncertainty of 1BHTM ... 47
4.3.2 Uncertainty of Corrections for at Least Two BHT at One Depth ... 47
4.4 Discussion ... 49
4.4.1 Sensitivities of Parameters and Correction Schemes ... 50
4.4.2 Uncertainty ... 52
4.4.3 Implications for Temperature Predictions in the Bavarian Molasse Basin ... 53
4.5 Conclusions ... 55
5 Monitoring Cold Water Injections for Reservoir Characterization Using a Permanent Fiber Optic Installation in a Geothermal Production Well in the Southern German Molasse Basin ... 57
5.1 Introduction ... 58
5.1.1 Application of Fiber Optic Sensing in Geothermal Wells ... 60
5.1.2 DAS ... 60
5.1.3 DTS ... 60
5.2 Methods ... 62
5.2.1 Description of the Study Site Conditions and Wells ... 62
5.2.2 Implementation of the Fiber Optic Monitoring System ... 64
5.2.3 Performance of the FO-System and Calibration ... 67
5.2.4 Flowmeter Logging ... 70
5.2.5 Cold Water Injection Tests ... 71
5.2.6 Thermal Dynamics of the FO-Construction ... 72
5.2.7 Temperature Interpretation and Warm-Back Analysis ... 73
5.3 Results ... 74
5.3.1 Flow Zone Detection by Flowmeter Logging ... 75
5.3.2 Initial Temperature Log from DTS ... 76
5.3.3 FO-Sensing during Injection Tests ... 77
5.3.4 DTS during Warm-Back ... 79
5.3.5 Thermal Contraction ... 80
5.4 Discussion ... 80
5.4.1 Dynamic Temperature Development in the Monitored Well ... 81
5.4.2 Construction and Design Issues ... 82
5.4.3 Reservoir Characterization ... 86
5.5 Conclusion and Outlook ... 91
6 Dynamic Motion Monitoring of a 3.6 km Long Steel Rod in a Borehole During Cold-water Injection with Distributed Fiber-optic Sensing ... 93
6.1 Introduction ... 94
6.1.1 Well Description and Cable Installation ... 96

6.1.2 Monitoring Campaign 97
6.2 Data Analysis 97
6.2.1 Derivation of Strain from DTS 98
6.2.2 Direct Measurement of Strain via DAS 99
6.2.3 Stick–Slip Approach 99
6.2.4 Stick–Slip Event Detection and Picking 101
6.3 Results 101
6.3.1 Sucker Rod Contraction 102
6.3.2 Sudden Contraction Events 104
6.3.3 Friction Force Model 107
6.4 Discussion 110
6.4.1 Assessment of Measuring Errors 110
6.4.2 DAS Data Integration 110
6.4.3 Stick-Slip Rod Behavior 111
6.5 Conclusion 113
7 Technical Note - Integrated Fiber Optic Monitoring in a Geothermal Production Well: Lessons Learnt 115
7.1 Brief Summary and History of the FO System 115
7.2 Technical Design 116
7.2.1 Overall Fiber System and Downhole Cable 116
7.2.2 Sucker Rod 117
7.2.3 Pressure Loss due to the Reduced Flow Area 118
7.3 Technical Challenges and Recommendations 118
7.3.1 Monitoring the Installation and the Integrity of the Cable 118
7.3.2 Splicing 119
7.3.3 Well Interventions 120
7.4 Learnings about Measuring, Calibration and Accuracy 121
7.4.1 Depth Calibration 121
7.4.2 Temperature Calibration 122
7.4.3 Accuracy of the DTS 122
7.5 Long-Term Stability and Scientific Benefit 125
8 Inverse Flow Zone Characterization Using Distributed Temperature Sensing in a Deep Geothermal Production Well Located in the Southern German Molasse Basin 127
8.1 Introduction 128
8.2 Geological Setting and Studied Well 129
8.3 Methods 130
8.3.1 Fiber-Optic Data at the Well SLS TH4 130
8.3.2 Inverse Flow Profiling from DTS Data 131

8.4 Results 134
8.5 Discussion 134
8.6 Conclusion 137

9 Synoptic Discussion and Conclusion 138

9.1 Summarizing Overview 138
9.2 On the Prediction of the NAFB Natural Thermal Field 138
  9.2.1 Uncertainty Assessment of the Developed BHT-Correction Workflow 138
  9.2.2 Comparison with Real World Data and Other BHT Based Models 142
  9.2.3 Further Use of the Developed Workflow: Prospects and Potential 146
9.3 On the Integrated Fiber Optic Characterization of Reservoirs 147
  9.3.1 Suitability of the Fiber Optic System for Measuring in the Reservoir 147
  9.3.2 Insights into the Monitored Borehole and the Reservoir 148
  9.3.3 On the Influence of Hydraulically Active Zones 149
  9.3.4 Further Use of Integrated Geothermal Fiber Optic Monitoring: Prospects and Potential 151
9.4 Conclusions 152

LIST OF FIGURES

Figure 1-1. Shallow and deep geothermal systems for extraction of heat and cold/heat storage (modified after Fraunhofer-Gesellschaft and Helmholtz-Gemeinschaft, 2022). 3

Figure 2-1. Flow meter analysis with (a) cross plot of spinner data to find calibration thresholds and (b) illustration of a conventional full-bore spinner tool (modified after Schlumberger, 1997) and (c) three exemplary spinner velocity profiles with interpreted spinner profile and resulting flow zones (modified after Zarrouk and McLean, 2019). 10

Figure 2-2. Schematic of thermal influences on the rock formation during drilling and during borehole measurements on the left with exemplary illustration of a conductive system where the geothermal gradient is changing its slope at layers with different thermal conductivity. 13

Figure 2-3. The back-scattered light spectrum with fiber optic technologies DTS, DSTS, DAS and DSS. T and ε are Temperature and strain, respectively. Modified from Ekechukwu and Sharma (2021). 18

Figure 2-4. Comparison of three deep temperature models for the North Alpine Foreland Basin in Bavaria. The map was created with ArcGIS Pro 3.2.1. The visualized data were taken from (a): GeotIS temperatures at top of the reservoir, either Purbeck (Purb.) or Upper (Up.) Jurassic (Jura.) (Agemar et al., 2012; Agemar, 2022a). (b): GeoMol temperatures at top of Upper Jurassic (Team, 2015a). (c): Temperatures at top Upper Jurassic of the 3D basin model of GFZ (Przybycin et al., 2015). As the refined coupled model (Przybycin et al., 2017) was not available for this thesis at the top Jurassic layer, the purely conductive model is shown here. The legend shown in the upper left corner is related to the maps in (a), (b) and (c). 23

Figure 4-1. Schematic of exemplary bottom hole temperature (BHT) measurements in a borehole. The BHTs (black dots) can be present single or, if several were measured at one depth, as a series of measurements. Due to the thermal influence of the previous drilling, BHTs deviate from the static formation temperature (SFT), which can be derived by the geothermal gradient (red line) 29

Figure 4-2. BHT values and temperature profiles available for the Bavarian Molasse Basin temperature data set versus depth. The black profile is from a fiber optic DTS measurement in well SLS TH4 at the Schäftlarnstraße geothermal site. 32

Figure 4-3. BHT correction methods applied for quantifying uncertainty. 34

Figure 4-4. Shut-in times versus depth for the different borehole sections with varying radius a of the Bavarian Molasse Basin data set. The black dashed line marks the calculated limit over which the BHT correction stability criterion $a2 < 4 \cdot \kappa \cdot ts$ is still met for the respective borehole diameter when κ is $1.5 \cdot 10^{-7}$ m^2/s. Below each subplot, the representation of the data set for the stability criterion is indicated by a percentage. 39

Figure 4-5. Outflow temperatures from mud logs in the Bavarian Molasse Basin. The different colors represent 13 different wells. 41

Figure 4-6. Proof of convergence of a Sobol model run using Brennand's method for three BHT values. The abbreviations in the legend refer to the total order index of the first measured BHT and respective shut-in time (1st_BHT_ST, t1_ST), the increase in temperature from first to second BHT and the respective shut-in time gone by (delta_1stBHT_ST, delta_t1_ST), the increase in temperature from second to third BHT and the respective shut-in time gone by (delta_2ndBHT_ST, delta_t2_ST) and the circulation time (tc_ST). . 42

Figure 4-7. Fiber optic temperature log in SLS TH4 with BHT data at 2950 m with shut-in time of 86 400 s. The bold red line is a DTS profile measured after the well has been shut for 16 months with a spatial sampling of 1 m. The thin red line is the same DTS profile averaged over 30 m. The dashed line is the assumed reservoir gradient, derived from DTS. 43

Figure 4-8. DTS profiles measured before (red line) and after (blue lines) a cold-water injection test at the well SLS TH4. The grey box shows the profiles at the top interval of the reservoir section. Point data are Horner corrected (diamonds) and Brennand corrected (circles) temperatures from temperatures read from the blue DTS profiles. 44

Figure 4-9. Results of the GSA structured by borehole sections. Shown are Sobol total indices for each relevant input parameter. The margin of the total order index corresponds to the importance of the respective parameter to the model output. The diagrams on the left show the methods that are solved graphically, those on the right the analytical methods. The abbreviations refer to the first measured BHT and respective shut-in time (1st_BHT, t1), the increase in temperature from first to second BHT and the respective shut-in time gone by (delta_1stBHT, delta_t1), the increase in temperature from second to third BHT and the respective shut-in time gone by (delta_2nd^{d}BHT, delta_t2), the circulation time (tc), the mud temperature (Tm) and the bulk thermal diffusivity of the system mud/borehole (kappa). 46

Figure 4-10. Corrected BHTs after running the 1BHTM with Saltelli sampling displayed as box plots. For well no. 1, the results are also shown in a density plot. SFT is shown as red dashed line. p10, and p90 value are shown as first and second black dashed line. p50 (median) is displayed as grey line in each box plot and the result at base value is displayed as blue dashed line. 48

Figure 4-11. Distribution of corrected SFT at well no. 8 for five conventional methods (a): Lachenbruch and Brewer method LBM, (b): Forward modeling FM, (c): Horner plot method HM, (d): Brennand method BM. The SFT has been read from an undisturbed TLog with a shut-in time of approximately 2 years. A boxplot is included above every subplot with the SFT as the red dashed line. 49

Figure 4-12. Distribution of corrected SFT at well no. 9 for six conventional methods (a): Horner method HM, (b): Forward modeling FM, (c): Lachenbruch and Brewer method LBM, (d): Brennand method BM. The SFT has been estimated from a nearby (2300 m distance) undisturbed TLog with a shut-in time of 2 months. A boxplot is included above every subplot with the SFT as the red dashed line. 50

Figure 4-13. Distribution of corrected SFT at well no. 8 for the three corrections: linearization method LM (left), Brennand's method BM (middle), and forward modeling FM (right). A boxplot is included above every subplot. Due to an incomplete wireline TLog, there is no SFT information available at the depth of the BHT measurements and therefore it is not shown in the plots. The uncertainty of the LM correction scheme must therefore be evaluated by comparing the distribution of results with the other methods (BM and FM) that were previously quantified on complete data sets including known SFT. 51

Figure 4-14. Decision tree for the choice of the BHT correction method dependent on the quality of the available input parameters. 52

Figure 4-15. Shut-in times versus depth and BHT values. 53

Figure 4-16. Distribution of solution after running Saltelli sampled FM (top) and 1BHTM (bottom) at high uncertainty of shut-in time with applied variance of ± 7200 s (left) and high confidence with applied variance of ± 900 s (right). 55

Figure 5-1. Completion of production well 1 (left) and injection well 2 (right) with equipped fiber optic cables in Munich with relevant depths and kick-off points (KOP). Blue: with bumper wires equipped flatpack cemented (gray) behind the casing in injector well. Yellow: tubular encased fiber (TEF) installed along sucker rods to TD in producer well. Turquoise: fiber optic P/T gauge. Sketches of TEF and Flatpack are shown in gray box........................ 64

Figure 5-2. Installation of the FO-cable in the producer well. (a): ¾ inch to 13 3/8-in. crossover. (b): Wellhead outlet. (c): TEF mounted on sucker rods with clamps. (d): Carrier at termination with centralizer. 67

Figure 5-3. Calibrated and non-calibrated DTS profiles of the Schäftlarnstraße site in comparison to P/T gauge data before and after software update. 68

Figure 5-4. P/T gauge data recorded during the first injection test of January 2020 (Inj1) and the second injection test of February 2020 (Inj2) with injection rates. 72

Figure 5-5. Schematic DTS velocity track analysis during injection of cold water. Dark gray and light gray lines are DTS temperature logs (TLog) at different times t1 and t2 and show the downhole propagation of injected cold water in the cased section of a well. Dark blue and light blue lines are DTS profiles at later times t3 and t4 below a feed zone. v_a and v_b are the velocities above and below the hydraulic active zone. 74

Figure 5-6. Interpreted flow zones in producer well together with flowmeter spinner data, temperature and logging speed, lithology and stratigraphic units. Zoom to top section is shown in green framed box..75

Figure 5-7. Temperature gradients from DTS profile at the geothermal Schäftlarnstraße site. Subplot (a) shows estimated temperature gradients with projected well trajectory and stratigraphy. Subplot (b) shows representative (rep.) DTS profiles from November 2019 to January 2020 at averaged over 6 hours and with a moving average of 2 m with the wireline temperature log and the approximate thermal gradient inside the reservoir. (1) and (2) mark zones where the DTS temperature deviates from the proposed gradient. 77

Figure 5-8. DAS strain measurements at the beginning of injection tests Inj1 (a) and Inj2 (b). The gray line marks the injection profile from flowmeter. DAS strain at the top of the reservoir is given in zoomed in sub plots. 78

Figure 5-9. Analysis of velocity of the injected cold water. (a) Vertical movement of cold waterfront of Inj1. (b1) Heat plot of Inj1. (b2) Heat plot of Inj2. Gray arrows: suggested 75 °C isotherm. The black arrow marks the proposed major hydraulic active zone. 79

Figure 5-10. DTS profiles during warm-back of Inj2. (a): Warm-back profiles at 4, 6 and 17 hours after shut-in together with the mean profile of January 2020 and the Shut-In profile over whole borehole in comparison to stratigraphic units and the well completion. (b): DTS peaks during long-term warm-back at top of the reservoir from 2810 m MD to 2840 m MD. The bold curves are raw DTS data, fine black curves are moving average over 2 m. The gray line indicates a vertical shift of about 1.5 m. 80

Figure 5-11 . Theoretical thermal expansion from DTS data and measured thermal expansion from DAS data after well shut-in, Inj2.. 81

Figure 5-12. Changing of temperature profiles over time in the first section. First subplot to the left shows the completion with tieback liner in blue and TEF/sucker rod in red. Second subplot shows the wireline temperature log that was recorded inside the tieback liner. Third to sixth subplots show DTS profiles that were recorded in the borehole as the tieback liner was pulled. Third subplot is the mean DTS profile until start of Inj1, fourth shows a DTS profile shortly before start of Inj1, fifth is 3 days after Inj1, sixth subplot shows a current DTS profile. Transparent lines are raw DTS data, sharp lines are moving average over 4 hours at a spatial resolution of 2 m. 84

Figure 5-13. Calculated strain from DTS and corrected pressure data. (a): Calculated Strain from DTS data to the depth of the P/T gauge in the first seven hours of injection of Inj2. Curves on the left y-axis are temperature deviations from the initial DTS profile. Curves on the right y-axis are the resulting strain for each DTS profile. (b): Measured gauge pressure data with correction factor to revise thermal caused displacement.. 85

Figure 5-14. Comparison of flowmeter injection profile and DTS and DAS response during Inj2. Transparent lines are raw DTS data, sharp lines are moving average over 10 m. (a): flowmeter profile with five DTS profiles in the first hour of cold water injection over from 2750 m MD to TD. (b): Zoomed to top of the reservoir. Flowmeter profile is shown together with three DTS profiles of injection start, each 20 min apart; and DAS strain at 1 min and 1.5 min after injection start. 88

Figure 5-15. Comparison of DTS warm-back profiles and flowmeter injection profile with interpreted injection zones from flowmeter interpretation. Transparent lines are raw DTS data, sharp lines are moving average over 10 m. (a): six DTS profiles taken at different times during the first 11 hours together with flowmeter inflow profile. A, B, C and D mark gradient change of DTS profiles. (b): Zoom to the top reservoir section............................ 89

Figure 6-1. Downhole cable configuration of the sucker rod with a centralizer (black) and the fiber-optic cable (yellow). 97

Figure 6-2. Static friction force Ff and normal force FN applying on a sucker rod contact point (nylon centralizer) as a function of the weight force Fw and the borehole inclination 90° - α. 100

Figure 6-3. DAS raw data examples over the scope of the cold-water injection phase for (a) the onset of fluid injection, (b) ongoing injection and (c) termination of fluid injection. Blue colors show relative compression and red colors relative extension. The color ranges are the same for all subplots.......... 102

Figure 6-4. Downhole monitoring data during the cold-water injection test. (a) DTS temperature profiles. (b) Comparison of strain profiles εDTS and εDAS. (c) Borehole inclination. (d) Wellbore schematic. 103

Figure 6-5. Sucker rod contraction event displayed by strain rate DAS data (a). The black arrows on the left y axis mark the depth location of time series used for the spectrograms in Figure 6-7. Line 'A' marks the move-out of the signal at a speed of 4000 m/s. The schematic drawing shows the inclination of the borehole with the fiber-optic cable (red) lying inside of the casing (b). The inflow profile from a wire line flowmeter measurement is shown by the blue graph. 104

Figure 6-6. Four raw DAS data examples of sucker rod events with the integrated strain rate (εDAS) over a period of 3 s. The timing of the events relative to the start of cold-water injection is as follows: A – +65 min; B – +110 min; C – +147 min; D – 210 min 105

Figure 6-7. Spectrograms for a 250 ms moving window at different depth along the well during the sudden vibrational event depicted in Fig. 5. Red colors indicate high amplitudes, blue colors low amplitudes. The relative amplitudes are displayed by the same color ranges for all subplots.......... 106

Figure 6-8. STA/LTA trigger algorithm applied as an automated detection method for vibrational events. Trigger start and end is marked with green and orange crosses.......... 108

Figure 6-9. Gray circles and black vertical lines indicate the spatiotemporal origin and spatial extent of vibrational events in the well, respectively. The shown period comprises the first 72 min of cold-water fluid injection. 109

Figure 6-10. Comparison of static friction F_f with applied forces F_{app} from thermal contraction of the rod within the first 72 min of cold-water fluid injection. The pale colors in F_{app} originate from measured DTS data, and the solid lines are constructed by a moving average over 15 m. 109

Figure 7-1. Chronological Overview of the FO monitored Well TH4 with Times of continuous DTS and P/T measurement marked in red. Modified from Figure 8-2. 115

Figure 7-2. Fiber Hook Diagram of FO cable in TH4 (left) and TH3 (right) showing the configuration of single-mode (SM) fibers and multi-mode (MM) fibers and the splice at the P/T gauge and surface splices. 116

Figure 7-3. Picture of the 2021 cable break when the control line was pushed into the high pressure chamber of the FO wellhead outlet, crushing and shearing the fibers. 120
Figure 7-4. Comparison of the evolution of the temperature below the pump (zenith sensor) and DTS readings 3 m below the zenith sensor during the first two weeks of operating the well. Data starts 3.5 h (0 h in the graph) after the pump was started. The data gap at 100 h is present on both measurements and can probably be explained by a power failure at the geothermal site. Temporal resolution of DTS data: 10 min, of zenith sensor: 5 min. 123
Figure 7-5. Results of Monte Carlo simulation of temperature at 760 m picked from a DTS profile measured about 300 h after the pump of SLS TH4 was started in 2021 with estimated uncertainties for the displacement and DTS temperature. (a) shows the temperature uncertainty. (b) shows the distributed displacement. 124
Figure 7-6. DTS profile taken about 300 h after pump start in 2021 at 10 min and 1 m resolution (black) with set of functions (grey) from Monte Carlo simulations taking into account DTS temperature and displacement uncertainties. The maximum standard deviations below 800 m are shown at 2900 m. 125
Figure 7-7. Optical losses during the lifetime of Single-Mode fiber no. 1 during the different intervals in the lifetime of the fiber optic cable in SLS TH4 from ground level to the P/T gauge, at the gauge and from the gauge to total depth (TD) in comparison at 1310 nm and 1550 nm wavelength. 126
Figure 8-1. Map of the Bavarian Molasse Basin, cropped to Bavaria, and the six well paths at the geothermal study site Schäftlarnstraße with inclination and well scheme of well completion of SLS TH4. 130
Figure 8-2. Timeline of fiber optic DTS measurements at SLS TH4. 131
Figure 8-3. (a) DTS profiles between July 2020 and July 2021 and a schematic of the wellbore with sketched fiber-optic cable (yellow line) clamped to sucker rod (grey line) and (b) temperatures at different depths plotted versus time. The grey DTS profiles in (a) are from the shut-in period before the ESP was installed and the blue DTS profiles were measured after installation. The displayed DTS data are averaged over 6 hours at a spatial resolution of 1 m. The temperature anomaly below 2750 m in (a) is a measuring fragment due to the inline splice from the downhole P/T gauge. 132
Figure 8-4. Results of DTS production profiling model inside the reservoir of SLS TH4. (a) Measured temperature (DTS, grey line) and modeled temperature (black dashed line) with estimated geothermal gradient (red line) versus depth, (b) modeled contribution of flow (grey) and cumulative flow in the bore (light blue) in comparison to surface pump rate (blue), (c) Inclination of the well, (d) well sketch of reservoir section. The olive band highlights the casing section. The shown results were generated with KAPPA Emeraude (v5.40). 135
Figure 8-5. Comparison of pressure loss at the main flow zone estimated as input for Emeraude modeling with analytically calculated pressure loss. 136
Figure 9-1. Histogram of the uncertainty range of all corrected BHT data sets in the NAFB..... 139

Figure 9-2. Synthetic BHT data sets (Points) at four different depths measured with the fiber optic monitoring system in the well SLS TH4 at different time intervals after a cold-water injection test and known static formation temperatures (dashed line) derived from a distributed temperature profile at undisturbed thermal conditions. The two transparent points shown on the right were not used in Table 9-1 to test the BHT correction methods. 141

Figure 9-3. Comparison of extrapolated BHT corrected p50 values (probabilistic workflow) and their uncertainties from p90 and p10 values with GeoMol and GeotIS temperatures at six wells from Supplementary 4-1, where SFT values were measured at top of the reservoir (red) with undisturbed temperature logs. 143

Figure 9-4. Calculated SFT compared to GeotIS and GeoMol temperatures at top of the reservoir of 15 exemplary wells dispersed in cardinal directions North, West, East and South (N, W, E, S) of the western NAFB, the middle (M, Munich area), eastern NAFB and northeast of the Landshut Neuoetting High (LNH) with uncertainties and measured outflow temperatures (red) available at six of the wells. 145

Figure 9-5. Summarizing comparison of the flow zone characterization in reservoir section of well SLS TH4. (a): stratigraphy in the reservoir with schematically drawn Karst in the Purbeck layer, (b): PLT flowmeter interpretation (Ch. 5.2.4) with cumulated flow contribution outlined in light blue zone, (c): DTS production profiling from invers model (Ch. 8.4) and interpreted zones in light blue and (d): exemplary DTS profiles during warm-back of the injection test (blue, see Ch. 5.2.7), during well production (red, see Ch. 8.4) and during shut-in (grey, see Ch. 8.3.1). The deviation of the cold and warm DTS profile from the assumed undisturbed (shut-in profile) is sketched in (d) as a blue and red area respectively. 149

LIST OF TABLES

Table 2-1. Average thermal conductivities of some exemplary materials and stratigraphic units in Bavaria. 8

Table 2-2. Comparison of conventional logging methods and tools with their limitations in terms of hydraulic and thermal reservoir characterization of hydrothermal geothermal wells. 16

Table 4-1. The BHT data set structured in steps of 500 m TVD regarding the shut-in time. 32

Table 4-2. Input requirements (marked with x) of six conventional BHT correction methods. .. 34

Table 4-3. Calculated minimum shut-in times for which the stability criterion is still met when κ is varied between $1.5 \cdot 10^{-7}$ and $6.8 \cdot 10^{-7}$ m²/s........ 39

Table 4-4. Applied ranges for all input parameters for the uncertainty analysis. The last column lists the respective input parameters with their individual designation. 41

Table 5-1. Excerpt of the well history of well 1 and well 2 64

Table 6-1 . Well design at geothermal site Schäftlarnstraße, Munich (see also Figure 6-3). 98

Table 6-2. Parameters used for the STA/LTA detection method........ 101

Table 7-1. Optical losses in dB at different sections of the installation and at different time intervals for single-mode fiber no. 1 together with calculated dB per km fiber length. The values were measured with different OTDR devices and at slightly different installation lengths of the cable system. 126

Table 8-1. Input parameter for the inverse DTS profiling with KAPPA Emeraude 133

Table 8-2. Comparison of flow zones interpreted from DTS production data with flow zone interpretation from flow meter data at injection taken from Schölderle et al. (2021). 136

Table 9-1. Synthetic BHT values at different depths from the fiber optic monitored well SLS TH4. The bold values t1, t2 and t4 at 12h, 18h, 178h shut-in time were used for BHT correction with Horner and Brennand method for a typical case (short shut-in times t1, t2) and an optimal case (t1, t4) to compare the results with the static formation temperature known from fiber optic sensing before the thermal disturbance. 141

Table 9-2. Comparison of extrapolated BHT corrected p50 values (probabilistic workflow) and their uncertainties from p90 and p10 values with GeoMol and GeotIS temperatures at 15 exemplary wells in the NAFB dispersed in cardinal directions North, West, East and South (N, W, E, S) of the western NAFB, the middle (M, Munich area), eastern NAFB and northeast of the Landshut Neuoetting High (LNH), see e.g., Figure 2-4. For six of these wells, wellhead (outflow) temperatures T_{Out} from operating data, provided by the Geothermal-Alliance Bavaria, were available that are listed as well for comparison. 145

Table 9-3. Theoretical heat output (th. power) for SLS TH4 at an assumed injection temperature of 50 °C and assuming that the production temperature corresponds to the mixing temperature $Temp_{Mix}$. $Temp_{Mix}$ was taken from a production DTS profile (Figure 8-4) for

both the original state as in Figure 8-4 and Table 8-2 and the well at a theoretical state where the upper most flow zone was packed off. 150
Table 9-4. Theoretical heat output for well SLS for different pump rate scenarios due to the removal of the upper most zone with imaginary packer at an assumed injection temperature of 50 °C and assuming a mixing temperature of 100.0 °C (see Table 9-3)........ 151

LIST OF ABBREVIATIONS

1BHTM:	1 BHT method
BHA:	Bottom hole assembly
BHT:	Bottom hole temperature
BM:	Brennand method
CBL:	Cement-bond-log
Cret.:	Cretaceous
DAS:	Distributed acoustic/dynamic strain sensing
DOFS:	Distributed optical fiber sensors
DPS:	Distributed pressure sensing
DSTS:	Distributed strain and temperature sensing
DSS:	Distributed strain sensing
DTS:	Distributed temperature sensing
ESP:	Electrical submersible pump
FBG:	Fiber Bragg grating
FPI:	Fabry-Perot interferometer
FIMT:	Fiber-in-metal-tube
FM:	Forward modeling method
FO:	Fiber optic
FO-WHO:	Fiber optic wellhead outlet
FORJ:	Fiber optic rotary joint
GAB:	Geothermal-Alliance Bavaria
GSA:	Global sensitivity analysis
HDF:	Heat flow density
HM:	Horner Method
IPCC:	Intergovernmental Panel on Climate Change
KOP:	Kick-off point
LBM:	Lachenbruch and Brewer Method

LM:	Linearization Method
LfU:	Landesamt für Umwelt (Environmental Agency of Bavaria)
MD:	Measured depth
MM:	Multi-mode
NAFB:	North Alpine Foreland Basin
NMR:	Nuclear magnetic resonance
OFDR:	Optical frequency domain reflectometry
OTDR:	Optical time domain reflectometry
PLT:	Production logging tool
RPS:	revolutions per second
SFT:	Static formation temperature
SM:	Single-mode
SMB:	South German Molasse Basin
SNR:	Signal-to-noise ratio
SRREN:	Special Report on Renewable Energy Sources and Climate Change Mitigation
STA/LTA:	Short-term/long-term average
TD:	Total depth
TEF:	Tubular encased fiber
TVD:	True vertical depth
VSP:	Vertical seismic profiling

1 INTRODUCTION

1.1 Overall Context – Mitigation of Climate Change

On November 4, 2016, the Paris Agreement came into effect, which legally bound 196 parties to keep the global average temperature increase as compared to pre-industrial levels "well below 2 °C while pursuing efforts to limit such a rise to 1.5 °C" (Delbeke et al., 2019). Following this, in 2019, the European Union formulated its European Green Deal, setting a clear target to reduce net carbon emissions (or equivalents) by at least 55 % by 2030 compared to 1990 levels and construct a "modern, resource-efficient and competitive economy where there are no net emissions of greenhouse gases in 2050 and where economic growth is decoupled from resource use" (European Commission, 2019). As more than 75 % of greenhouse gas emissions in the EU are related to energy production and consumption (European Commission, 2019), shifting energy supply from conventional to renewable alternatives is not only an important lever to reach the climate goals but is urgently needed. The IPCC Special Report on Renewable Energy Sources and Climate Change Mitigation (SRREN) classifies six renewable technologies regarding their high carbon mitigation potential. In addition to bioenergy, direct solar power, hydropower, wind, and ocean energy, geothermal energy is considered an important component of the future global energy system (Edenhofer et al., 2011).

When we speak of geothermal energy, we usually mean the amount of heat stored within the Earth's interior or the heat that can be extracted as a primary energy source from a reservoir by deep or shallow wells, borehole heat exchangers, or ground source heat collectors. Geothermal reservoirs at low bearing temperatures are suitable for heating and cooling commercial and residential areas directly or with heat pump systems (García Gil et al., 2022). Although not directly related to the depth of the reservoir, in practice these are usually referred to as 'shallow geothermal energy systems' (e.g., Stober and Bucher, 2020; García Gil et al., 2022). The term deep geothermal, in contrast, is often used to describe systems that store or extract heat at higher temperatures, which are often well suited for district heating networks or industrial heat directly or with large heat pumps. At sufficient temperatures, electricity production with e.g., binary cycle plants can become economical (e.g., Fink et al., 2022). In general, the amounts of thermal energy in the subsurface that are of interest for deep geothermal energy are enormous. Between the surface and 5000 m depth, they can be estimated at 56 to 140 · 10^6 EJ (1.6 to 3.9 · 10^{10} TWh) (Edenhofer et al., 2011). The use of this heat could theoretically easily meet global consumption demand, which was 22 848 TWh in 2019 (IEA, 2021). The actual realizable potential is certainly lower, but difficult to quantify due to lack of (borehole) data.

1.2 Deep Geothermal Energy Systems and Their Potential

Geothermal heat originates from the formation of the Earth but is also constantly produced in the crust and mantle due to radioactive decay (e.g., Zarrouk and McLean, 2019). The uppermost part of the Earth around 20 m depth is additionally affected by solar radiation, resulting in a seasonal varying temperature-depth profile that becomes important for shallow systems (e.g., Anderson, 2005; Stober and Bucher, 2020). According to Fourier's law of heat conduction, the stored heat flows from the depth to the surface, resulting in a temperature increase of 20 to 30 K per kilometer of depth (global average) and an average of 28 to 30 K per km in Europe (Zarrouk and McLean, 2019; Stober and Bucher, 2020). This geothermal gradient may be lower or higher depending on the thermal conductivity of the dry formation, which, if very low in hydrocarbon layers, for example, can act as a thermal barrier (Zarrouk and McLean, 2019). If the rock is very permeable and sufficient fluid is present, free or natural convection effects can occur, driven by the compensation of the density difference. These can lead to unstable thermal gradients and significantly higher temperatures. Likewise, advective processes are possible when forced convection occurs and fluid motion is initiated by gravity (Zarrouk and McLean, 2019).

A uniform system to categorize deep geothermal systems does not exist. Some authors sort systems according to the geological play type (Moeck, 2014), i.e. whether they are located in sedimentary rock or orogenic belt, in volcanic, crystalline, or magmatic rock. Others differentiate the settings depending on the temperature of the reservoir (Sanyal, 2005; Clauser, 2006). Regions with low temperatures, respectively low or average geothermal gradient are often categorized as low enthalpy systems, and regions that show a very high geothermal gradient and high reservoir temperatures as high enthalpy systems. Zarrouk and McLean (2019) refer to warm water systems or hot water systems when reservoir temperatures are below 120 and 250 °C, respectively, as the term enthalpy is then not entirely accurate. However, due to its widespread use in the literature (e.g., Majorowicz and Minea, 2015; Banks and Harris, 2018; Christiansen et al., 2021; Drews et al., 2022), the term 'low enthalpy' is used in this thesis. Another distinction can be made in the production system. Commercially established and well-operated for more than 100 years (e.g., Fridleifsson, 2001) are hydrothermal well systems for direct use or electricity production that produce natural fluid present in high permeable rock formations. Typically, at least two wells are required: one to pump the hot fluid and another to reinject the fluid back into the hydrothermal reservoir to allow it to reheat. At the surface, the produced fluid exchanges its heat with at least one other fluid circuit, e.g., in its simplest form the district heating network. In regions where permeability is too low to be hydraulically active and productive, petrophysical systems that use natural but dry well connections or artificially create such pathways are suitable. Such systems are not yet commercially established and are in operation at only a few sites, so those can be classified as being at the experimental and demonstration stage (Edenhofer et al., 2011).

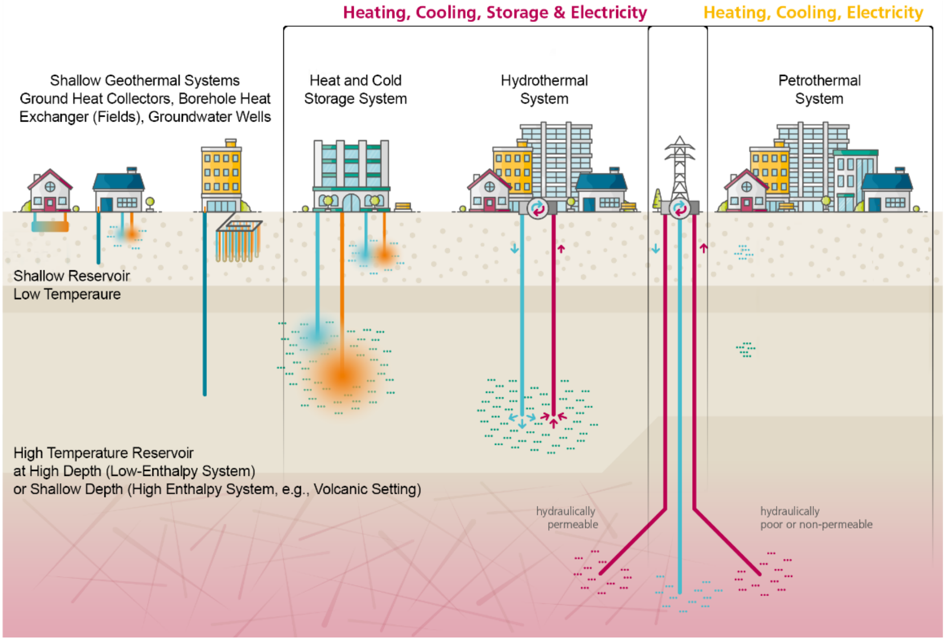

Figure 1-1. Shallow and deep geothermal systems for extraction of heat and cold/heat storage (modified after Fraunhofer-Gesellschaft and Helmholtz-Gemeinschaft, 2022).

Figure 1-1 illustrates the major geothermal systems with a rough distinction between shallow geothermal and deep geothermal systems. Regardless of the various classifications, knowledge of the regional geology is critical to determining whether an area is a potential reservoir for deep geothermal energy. Drilling a geothermal well is expensive, and without sufficient basic geological and geophysical data, the exploration risk is high and may even be too high for investors to start projects. Thus, comprehensive databases on key planning parameters and planning tools are essential for the further development of geothermal projects. These include, for example, forecasts of reservoir depths, permeabilities, reservoir temperatures, potential drilling risks, and monitoring data that demonstrate long-term sustainable management.

The efficiency of a deep hydrothermal well depends on the quality of the hydrothermal reservoir, mainly described by the chemical composition of the thermal water (Stober and Bucher, 2020) and the quantity of the reservoir that depends on the productive flow rate and the temperature of the produced water (Schulz et al., 2010). The thermal output P (J/s) of a hydrothermal doublet can be calculated as (Stober and Bucher, 2020)

$$P = \rho_F \cdot c_F \cdot Q \cdot (T_F - T_i), \qquad \text{(eq. 1-1)}$$

with T_F $(°C)$ the temperature of the produced fluid with pumping rate Q (m^3/s), T_i $(°C)$ the temperature of the fluid being reinjected and ρ_F (kg/m^3) and c_F $(J/(kgK))$ the density and specific heat capacity of the fluid. From this, it becomes clear that focusing on the production temperature, a few Kelvins can decide whether a hydrothermal project is economical, partly successful, or unsuccessful (Schulz et al., 2010; Flechtner et al., 2020).

Action against climate change requires the realization of geothermal potential to achieve a transition to renewable energy soon. Therefore, an improved framework is needed that reduces the exploration risk for future projects and assesses sustainable management of the geothermal heat resource. The temperature of the thermal fluid, which is directly related to the economic efficiency of a well, is crucial here and depends on the deep temperature of the rock inside the reservoir and the location of deeper flow zones at higher temperatures. Low production temperatures could require a heat pump, high temperatures could enable power generation, and in general, higher fluid temperatures allow for higher productivity. In addition, regions that have high temperatures at shallower depths are of greater interest, as this reduces drilling costs. Information on underground temperature is rare and the quality of available interpreted temperature data is often poor or unclear. Research is therefore needed to improve temperature prediction to provide planners and investors with a better risk assessment.

1.3 Hydrothermal Utilization in Germany and Bavaria

Germany is the fourth largest economy in the world in terms of gross domestic product (World Development Indicators database, 2023) producing high greenhouse gas emissions, which were 746 million tons as of 2022 (Umweltbundesamt, 2023). Subsequently, the country has a responsibility to rapidly reduce its high CO_2-equivalent emissions to meet the global climate targets. High potential for savings exists in the energy industry of which 56 % of the final energy consumption falls into the heat sector. Renewables cover only 15 % of the heat here (Fraunhofer-Gesellschaft and Helmholtz-Gemeinschaft, 2022). The potential to satisfy a large part of the heat demand with deep geothermal energy is given since there are three known regions in Germany with hydrothermal potential. In the west of Germany is the Upper Rhine Graben, in the north the North German Basin, and in the south the South German (Bavarian) Molasse Basin (SMB) or North Alpine Foreland Basin (NAFB). Although the NAFB also extends to Switzerland and Austria, in this paper the abbreviation only refers to the Bavarian part of it. The former two have not been much developed to date but several projects are in the planning or developing stages, according to recent press releases (e.g., Daimler Truck AG, 2023; Deutsche ErdWärme GmbH, 2023; Kunold and Zurawski, 2023; WEMAG AG, 2023). Of the currently active 42 plants in Germany, more than half are in the NAFB (BMWK, 2022), making it one of the most important low-enthalpy hydrothermal hotspots in Europe. Here, deep geothermal projects are developed for more than 15 years (Steiner et al., 2014), and a lot more are planned in the future, especially in the greater area of Munich to reach a CO2-emission-free district-heating network in Munich by 2040 (Kenkmann et al., 2017). As of 2022, a total of 24 geothermal plants are in operation in Bavaria (BMWK, 2022). Most of them have been drilled in the greater Munich area or in the eastern part of the NAFB, where good hydraulic conditions and temperatures above 80 – 90 °C are expected to be suitable for district heating networks. Today, colder regions are also becoming interesting exploration targets, as the integration of low temperatures with large industrial heat pumps is a promising alternative (Ahrendts et al., 2023). Further development of the reservoir requires improvements in terms of accuracy and uncertainty.

2 STATE OF THE ART

2.1 Thermal Processes in Geothermal Foreland Basins

2.1.1 Temperature Terminology

If speaking of temperature for geothermal utilization, one must differentiate between wellhead or production temperature, sometimes also called flowing temperature (e.g., Zhou, 2013; Steingrimsson, 2013), and static formation temperature.

In most cases, the preliminary geological investigation is based on the predicted static formation temperatures (SFT), the temperature in the natural conditions in the rock or formation, often specified at the middle or top of the reservoir. It is assumed that in a conductive dominated system, the temperature of a fluid entering a wellbore is equal to the SFT at the same depth (Kotlar et al., 2021). Not only is the SFT important as an estimate for the achievable production temperature or amount of heat stored in underground, but also for the interpretation of well logs, design of cement jobs, and derivation of thermal properties of the fluid and formation (e.g., Dowdle and Cobb, 1975; Andaverde et al., 2005; Liu et al., 2016). SFTs can be measured directly in a borehole (see Ch. 2.3.3) or estimated by applying different correction methods when only poor-quality temperature data is available (see Ch. 2.3.1).

The wellhead temperature in contrast is the temperature of the produced water at the surface. Prediction in advance is difficult because, on the one hand, the temperature of the fluid downhole is a mixed value from all inflows throughout a reservoir section (e.g., Steingrimsson, 2013), which may differ in temperature. On the other hand, the maximum wellhead temperature will always deviate from the temperature inside the reservoir because of conductive heat loss through the borehole to the formation during production (Tilley and Baumann, 2012; Zhou, 2013).

Ideally, planners would know the vertical temperature distribution in the reservoir while having a reliable estimate of the heat loss and the depths of the hydraulically active zones to determine the maximum fluid temperature that can be achieved.

2.1.2 Temperature Properties and Heat Transport

The temperature difference or gradient between the hot interior and the cool surface of the earth is the driving force for heat conduction. In a conductive dominated system, the thermal properties of the rock formation define the vertical temperature distribution according to Fourier's law (in its differential form, e.g., Eppelbaum et al., 2014):

$$HFD = -\lambda \cdot \nabla T, \qquad \text{(eq. 2-1)}$$

where HFD (W/m^2), is the heat flow density or heat flux which is the amount of heat flowing through an area in a specific time from warmer to cooler temperature and ∇T (K/m) the vertical temperature gradient. Theoretically, at constant λ for each rock type and known heat flow density, one could easily calculate the temperature at each depth following equation 2-1. However, usually at least two of the three parameters λ, HFD, and ∇T are not known. For providing an estimate of temperature/heat stored in a conductive underground system, different approaches are followed. Some attempt to calculate accurate geothermal gradients from borehole measurements (e.g., Dowdle and Cobb, 1975; Kutasov and Eppelbaum, 2003); others attempt to determine surface heat flow density (e.g., Fuchs et al., 2022), which can also be used as an indicator of a thermally well-suited drilling site. In the latter case, it is possible to create synthetic heat conductivity logs from other available logging data, e.g., Gamma Ray or Ultrasonic logs (Hu et al., 2021), and combine them with measured downhole temperature data to calculate the HFD.

Additionally, heat can be transferred by advection or convection. Advective heat transport is caused by pressure gradients and (natural or free) convection by density gradients (Kaiser et al., 2011; Zarrouk and McLean, 2019). Requirements for free convection are very good hydraulic properties of the rock, high temperature gradients and large thickness of the reservoir layer, (e.g., Kaiser et al., 2011), or in structures such as faults or fractures, which can allow the transfer of fluid. In general, convection processes affect the temperature distribution much more than conduction for their ability to carry more heat (Zarrouk and McLean, 2019).

The thermal properties of the rock determine the ability of the material to conduct or store heat. Of particular interest for hydrothermal systems and important for this thesis are the thermal conductivity, the specific heat capacity, and the thermal diffusivity.

The thermal conductivity λ ($W/(mK)$) can be understood as the resistance of the rock material to heat transfer. At a high λ, heat is well transferred and consequently, the temperature increase per meter depth is low and vice versa. Different rock types have different λ-values (see Table 2-1), e.g., higher sand content increases the conductivity, while a higher clay content decreases it.

Table 2-1. Average thermal conductivities of some exemplary materials and stratigraphic units in Bavaria.

Material	**λ (W/(mK))**	**Comment**	**Reference**
Air	0.025	-	(e.g., Eppelbaum and Kutasov, 2015)
Oil	0.15	at 20°C	(Eppelbaum and Kutasov, 2015)
Water	0.6	at 20°C	(Eppelbaum and Kutasov, 2015)
Claystone (Dogger)	1.6	Northeast Bavaria	(Kämmlein, 2019)
Granite (Crystalline)	3.2	Bavaria	(Homuth, 2014)
Sandstone (Gault, Low. Cret.)	5.23	East Bavaria	(Koch et al., 2009)
Limestone (Purbeck, Low. Cret.)	2.75	East Bavaria	(Koch et al., 2009)
Dolomite (Purbeck, Low. Cret.)	4.26	East Bavaria	(Koch et al., 2009)

However, in reality, λ is not constant throughout a stratigraphic layer as it is also dependent on various parameters, e.g., pressure, temperature, pore volume filled water, and chemical composition (Eppelbaum and Kutasov, 2015). Furthermore, it is an anisotropic value, which means that it is directional varying, especially if the rock is stratified directionally. Measuring thermal conductivity is therefore difficult because the true conditions downhole are hard to reproduce in the laboratory.

The heat capacity describes the amount of heat energy ΔQ necessary to heat a unit mass M [specific heat capacity c_p $(J/(kgK))$] or a unit volume [volumetric heat capacity c_v $(J/(m^3K))$] of a material by $\Delta T = 1K$. Mostly, the specific heat capacity is used to compare different materials:

$$c_p = \frac{\Delta Q}{\Delta T \cdot M}. \qquad \text{(eq. 2-2)}$$

Similar to thermal conductivity, the specific heat capacity of a material changes depending on other thermal and hydraulic conditions, e.g., temperature, porosity, and pressure. In general, λ and c_p decrease with depth. Both Clauser (2009) and Eppelbaum et al. (2014) provide a good overview and show examples of the relationships and dependencies of the various parameters in several graphs.

Related to the thermal conductivity, the thermal diffusivity κ (m^2/s) after all describes the change of the temperature distribution within a package of material/rock with time. Thus, it characterizes the thermal inertia of a system as (Clauser, 2006; Eppelbaum et al., 2014):

$$\kappa = \frac{\lambda}{\rho \cdot c_p}. \qquad \text{(eq. 2-3)}$$

For geothermal applications, it is an important factor for correcting disturbed temperature measurements, which is described in Ch. 2.3.1.

2.2 Specification and Characterization of the Hydraulically Active Zones

Rock formations in the hydrothermal reservoir filled with thermal fluid that can enter the wellbore, are hydraulically active and are often referred to as flow zones (e.g., Haffen et al., 2013) or feed zones (e.g., Horne, 2016). To understand the flow conditions in a well and the hydraulic behavior of the reservoir, characterizing and profiling these zones profiling has become one of the most important quantification methods in geothermal. Various approaches are used for this purpose.

During drilling, losses of drilling mud into the formation are recorded. The idea of using zones where this appears as possible indicators of hydraulically active zones seems reasonable, and correspondence with highly permeable layers is often observed (Birner, 2013). However, total mud losses can sometimes occur that cannot be related to hydraulically active zones at all, as observed in the dry well near Geretsried in the South of the NAFB (Dussel et al., 2021). Thus, there may be a relation, but profiling based solely on mud losses must be questioned.

More reliable and commonly used is running production logging tools (PLT) with a flow meter and/or a temperature measurement throughout the reservoir section (e.g., Kotlar et al., 2021; Schlumberger, 1997). The idea behind this tool is to disturb the hydraulic balance of a well (usually by injecting water) and run an impeller at constant speed along the axis of the well to measure its rotational velocity. If the velocity of the water stream in the well changes, for example, if the area flowed through changes or if water enters or exits the well, the velocity of the spinner also changes. By calibrating the spinner tool according to the movement of the tool at constant flow rates, and considering the borehole geometry (e.g., from Caliper measurements), it is possible to locate hydraulically active zones and calculate their hydraulic contribution. Zarrouk and McLean (2019) recommend a best-practice routine and evaluation software (e.g., KAPPA Emeraude: Anon, 2011; Kotlar et al., 2021) are designed according to this workflow: At minimum three different rates, beginning with the lowest, cold water is injected into the well with a surface pump system or freefalling from the wellhead. A PLT is run up and down the wellbore, and a spinner (and temperature) profile is measured for each of the three injection rates. There are different spinner types, for example, inline tools that have a very narrow diameter as small as the tool string diameter. They can thus be used in slim boreholes but must be centralized well. Also common are continuous flowmeters with larger impellers compared to the string that is mounted to the end of the tool. Even larger are full-bore flowmeters, which are more sensitive to flow changes (e.g., Kotlar et al., 2021). Since the rotational speed of a spinner depends on the blade diameter and the velocity profile of a tubular flow is not uniform, a correction factor is applied to account for the entire flow profile (Kotlar et al., 2021). To calibrate the spinner and determine its threshold value, measurement sections are selected that are believed or known to have no flow zones, such as a distinct cased section above the reservoir section or at the very

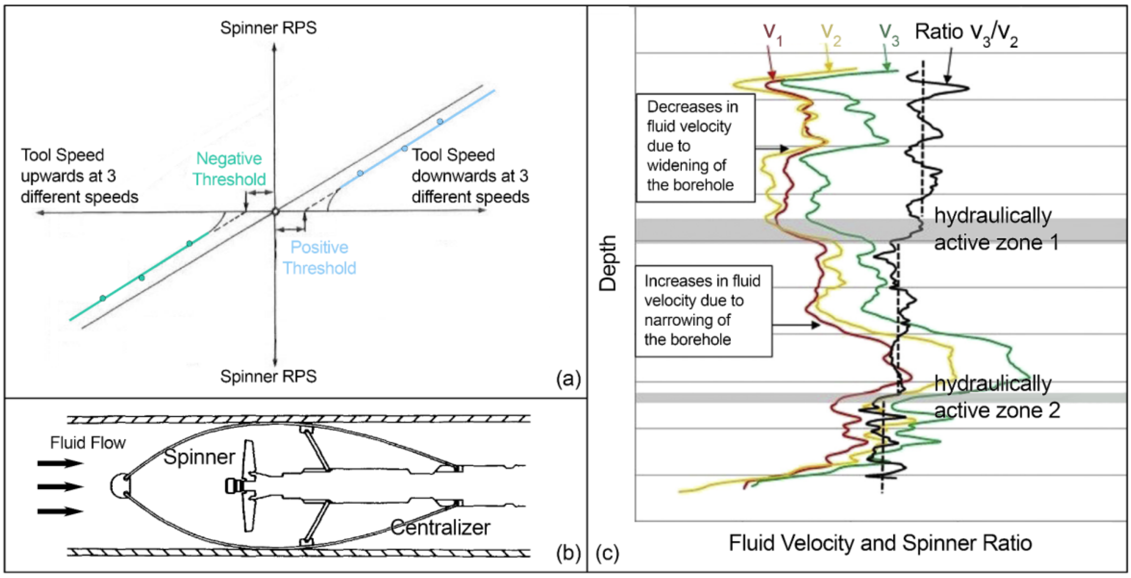

Figure 2-1. Flow meter analysis with (a) cross plot of spinner data to find calibration thresholds and (b) illustration of a conventional full-bore spinner tool (modified after Schlumberger, 1997) and (c) three exemplary spinner velocity profiles with interpreted spinner profile and resulting flow zones (modified after Zarrouk and McLean, 2019).

bottom of the borehole. The fluid flow is then plotted against the spinner revolutions per second (RPS), each for the up flow and down flow run for all three flow rates. An extrapolation of the data to the intercept of the diagram where the spinner speed is zero gives the moving speed of the tool at the same velocity as the flowing water. The calibration parameters are the positive threshold for the downward run and a negative threshold for the upward run as illustrated in Figure 2-1. Then, to the best of available knowledge, effects must be excluded that change the spinner velocity but are not related to flow zones, e.g., flow behind a perforated or slotted liner. The temperature profile of a PLT run can additionally help to qualitatively characterize the zones because sudden changes in the gradient are visible in zones where the injected water flows into the formation (Horne, 2016; Zarrouk and McLean, 2019; Steingrimsson, 2013). Unfortunately, often PLT surveys are not run according to the described workflow because multiple full PLT runs are time-consuming and thus costly (e.g., Brown, 2003). Often no or less than three complete runs are carried out, or multiple runs are only conducted in shorter lengths for calibration purposes. Additionally, many wells are inclined in the reservoir section to increase the length of the filter section. At very high inclination and in open hole completions, conventional wireline flow meter logging is becoming risky or not possible at all and therefore often not applied. Furthermore, the conventional analysis with flow meters is performed under injection conditions. Hydraulic tests or later operation of the same well have shown that regarding the hydraulics of a reservoir, injectivity, and productivity often differ (Zarrouk and McLean, 2019). Thus, it is not stated that the quantitative flow zone contributions from injection conditions can be transferred directly to production conditions.

Another method of flow zone profiling is heat-back monitoring. Here, several temperature profiles are measured wireline at increasing time intervals after cold water injection, e.g., as part of a PLT run (Zarrouk and McLean, 2019). Zones that heat very fast are regarded as major flow zones. If it is possible to measure pressure profiles along with the temperature profiles, they may show rotation about a pivot point, which is then likely to be very well connected to the reservoir and thus represent a dominant flow zone. In practice, multiple temperature and pressure profiles covering the whole reservoir section during the shut-in time of a geothermal well are very rare because of costs and because wireline measurements often fail at highly deviated wells.

In general, it is advisable to always put located hydraulically active zones into context with other geophysical logs or interpreted curves such as porosity, lithology, and fracture frequency.

2.3 Measuring the Temperature in the Development Phases of a Borehole

2.3.1 Drilling Phase: Geophysical Logging and Bottom Hole Temperatures

Most of the geological and geophysical information about the borehole if not gathered from surface seismic surveys or mud/cutting analysis is obtained during the drilling phase as part of the logging process. Downhole logging is an important step to understanding the subsurface and building a geological database for future development of the field. For such borehole measurements, tools are usually run from the surface at the drill pipe or with logging trucks that provide a spooler/cable drum from which the tool mounted on a wire can be suspended into the well (e.g., Schlumberger, 1997; Zarrouk and McLean, 2019). Some tools have an electrical connection to the truck so that the measurement can be monitored continuously, and others store a memory that can be read when the device is back on the surface. Conventional tools originate from the hydrocarbon industry and are usually transferred to geothermal applications with little or no adaptation. The geophysical logging program is usually performed only hours to a few days after one vertical or deviated section of a well has been completed. In most cases, a Gamma Ray log and/or a Spontaneous Potential measurement are made, which help to distinguish between permeable and impermeable layers and to characterize the lithology. Other important borehole information is provided by Sonic or Neutron logs from which porosity can be inferred, Caliper logs that provide variations in the diameter of a borehole, Image logs that allow visualization of outcrops in the rock, and many more. A good compilation of available tools is given in Schlumberger (1997, 1998) and Zarrouk and McLean (2019).

Usually several of these loggings are combined to save costs and downtime at the well site, but most often, a temperature probe is also integrated into the logging string. This was originally done in the hydrocarbon industry to locate possible oil or gas occurrences, as there are significant temperature changes when there are changes in the composition of multiphase fluids

(Schlumberger, 1998). Temperature was therefore a side product of other loggings and primarily mostly of qualitative interest. The resulting temperature information can be available as one continuous profile, but often only the highest temperature, usually located at the bottom end of the respective logging section is documented as the so-called 'bottom hole temperature' (BHT).

BHTs must be regarded as low-quality temperature data because they do not reflect the undisturbed condition in the rock or reservoir. This is due to the temporal proximity of the geophysical loggings to the preceding drilling, which thermally disturbs the conditions downhole. When a well is drilled conventionally, fluid ('drilling mud') is used to cool the drill bit, create sufficient drilling pressure to equalize the pressure in the formation, and transport the cuttings to the surface (Grant and Bixley, 2011). This changes the thermal condition inside the borehole drastically (e.g., Deming, 1989; Hermanrud et al., 1990; Zarrouk and McLean, 2019).

Figure 2-2 illustrates schematically on the left side the cooling of the thermal field during the drilling of the fourth section of an exemplary well. The temperature of the circulating drilling mud T_m $(°C)$ is lower than of the undisturbed static formation SFT $(°C)$, which depends on the duration of circulating the mud t_c (s) and the bulk thermal diffusivity κ (m^2/s). Bulk value means that κ here describes the thermal diffusivity of the combined system borehole/wellbore/reservoir rock as a mixing value (e.g., Middleton, 1982). Thus, κ must be estimated. Different approaches to this in the literature are discussed in Ch. 4.2.3.2. The second illustration from the left in Figure 2-2 shows the geophysical logging, performed after some time t_i (s), that past from stopping the mud circulation, removing the drill bit, and run in hole of the geophysical logging tool. During this time, the cooled borehole had some time to begin equilibrating towards the SFT, and the measured BHT value will be in between of T_m and the SFT. Note that this is true for deep parts of the reservoir where the mud temperature is lower than the temperature in the formation. At shallow depths, where the temperature in the formation is lower, the measured BHT will be higher than the actual SFT. Potential subsequent logging runs might lead to a series of BHT values with each increasing shut-in time. On the right side of Figure 2-2, the SFT is displayed as a vertical temperature profile as the geothermal gradient, which changes its slope depending on the thermal conductivity of the different layers according to Fourier's law. With knowledge of the thermal properties of the rock, the temperature of the drilling mud at the depth of the BHT measurement, duration of shut-in, and prevailing drilling circulation, an approximation of the SFT is possible with a wide range of different BHT correction methods. Sometimes other basic information about the well (e.g., drill bit size/diameter of the borehole) is additionally required. The correction schemes are strongly studied and compared for their suitability and accuracy (e.g., Deming, 1989; Hermanrud et al., 1990; Goutorbe et al., 2007), and new more advanced approaches are regularly added to the discussion (e.g., Zhou et al., 2015; Liu et al., 2016; Wang et al., 2019, 2021). The most common methods and their underlying equations are briefly described in Ch. 4.2.2. It should be noted that

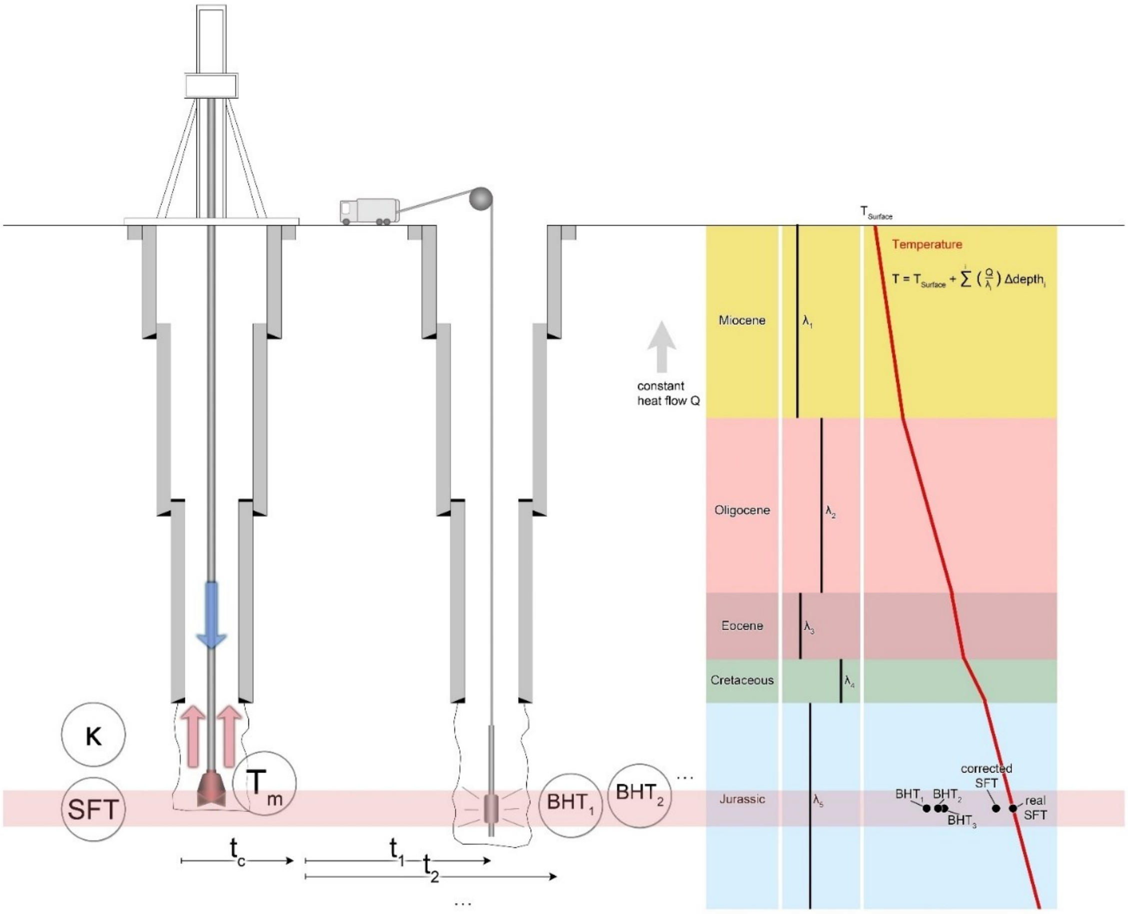

Figure 2-2. Schematic of thermal influences on the rock formation during drilling and during borehole measurements on the left with exemplary illustration of a conductive system where the geothermal gradient is changing its slope at layers with different thermal conductivity.

a good correction of the SFT using BHT data is highly dependent on the underlying database and remains inaccurate even with high-quality BHT data (Deming, 1989).

2.3.2 Hydraulic Testing Phase: Temperature at Top of the Reservoir

Hydraulic testing is the most important phase in the development of a geothermal well to predict its performance and derive reservoir properties. Baseline studies recommend a general approach to first perform a production logging (see Ch. 2.2), followed by an injectivity test and pressure transient analysis at different injection rates and lastly a heat-up survey (Sarmiento, 2011; Zarrouk and McLean, 2019). In low-temperature wells, hydraulic step-rate testing is also conducted under production conditions (Axelsson, 2013). Regardless of whether injection or production test, the reservoir properties can be derived using derivative log-log-analysis from pressure records (Bourdet, 2002). During a production test, a tool with a temperature probe can be hung in the well to record the temperature of the produced fluid at the top of the reservoir. This temperature is then a function of the entry temperatures in the different hydraulically active zones. Various examples of temperature profiles of flowing wells with varying numbers of feed zones are shown in Brown (2003). Although the measured mixing temperature at the top of the reservoir at the beginning of the test is still disturbed by the influence of the cold drilling fluid and other fluids injected (e.g. acidification), it provides an indication of the order of magnitude of the pumping temperature to be expected.

2.3.3 Shut-in Phase: Additional Geophysical Logging

In rare cases, the SFT can be measured accurately. Usually, the borehole is only accessible at times when the natural thermal field of the subsurface is disturbed by prevailing well construction work (see Ch. 2.3.1) or injection tests (see Ch. 2.3.2). A distinct amount of time, which is not known, must be given for the fluid inside the borehole and the cooled down formation to equilibrate back to undisturbed conditions. If this shut-in time is long enough, an undisturbed downhole temperature measurement can be carried out using wireline logging. Such continuous logs are regarded as high-quality temperature data. For these logs, simple thermistors, mechanical probes, and gauges along an electric line (Wisian et al., 1998; Steingrimsson, 2013) or more sophisticated fiber optic sensors (see Ch. 2.4) can be run downhole. If the shut-in time was not sufficiently long, the measured downhole temperatures would still be too low. For example, back in 1959, Lachenbruch and Brewer measured the thermal equilibration at a depth of 180 m in an 885 m deep study well over a period of 6 years and estimated that the temperature was still disturbed by 0.1 °C after this period (Lachenbruch and Brewer, 1959). There are approaches to correct such disturbed measured temperature profiles to undisturbed conditions (Schumacher and Moeck, 2020). However, to know exactly, repeated measurements or continuous measurements would be optimal.

2.3.4 Commissioning Phase: Development of the Outflow Temperature

Most simply, the wellhead temperature can be measured directly at the surface or in the system of a geothermal plant (e.g., near the heat exchanger) when a well is producing. In the early beginning of a project however, the well will not be fully heated up, and there will be radial heat loss from the wellbore to the cooler surrounding through casing, cementation, and formation behind (e.g., Ramey Jr., 1962; Kanev et al., 1997; Toth and Bobok, 2016). This heat flow is dependent on the overall thermal resistance of a section of the well, production parameters (pump rate), and the technical well design (e.g., cementation, radius) (Zhou, 2013; Eppelbaum et al., 2014). Heat loss is a transient process, as the thermal resistance shrinks with progressing well production because the cementation and near wellbore region of the formation will heat up. For wells in the NAFB, the magnitude of heat loss at the beginning of production (hydraulic testing works) can be more than 10 MW (Bauer et al., 2014), and the deviation of reservoir temperature to wellhead temperature can be up to 20 K. Zhou (2013) did extensive studies on heat loss in wells and improved the general heat flow model of Hasan and Kabir (2002) by e.g., supposing an equation for estimating the convective heat transfer coefficient of the wells annulus at the first well section. He concluded that heat loss is less at high flow rates and strongly sensitive to the pumping duration, however still present after final recovery.

Besides the heat loss and the temperature in the reservoir, a minor heat source in a producing well is given by the motor of the pump, if an electrical submersible pump (ESP) is used where the motor is stored downhole. In the NAFB, ESPs are the standard used pump, usually suspended to some hundred meters depth in the first well section. The ESP motor is cooled by the produced thermal water and consequently, the fluid gets heated when it passes the pump.

Despite these elusive influences, the outflow temperature can be considered a proxy for the mixing temperature of the fluid as it enters the cased borehole.

2.3.5 Wrapping up Conventional Downhole Tools

Table 2-2 summarizes the different conventional tools and methods. The limitations are listed, as well as a quality rating based on the limitations (see also literature outlined in Ch. 2.3.1, 2.3.2, and 2.3.3). Mud logging is always carried out because monitoring the density of the drilling mud, inflow and outflow rates, gas monitoring, and cutting analysis for lithological description is a fundamental process during drilling (Capuano, 2016). However, mud loss zones are only suitable for flow zone characterization to a limited extent (see Ch. 2.2) and must therefore be assessed as low quality for this purpose. The same applies to BHT measurements. BHTs are widely available but of poor quality (see Ch. 2.3.1). Most of the other methods are generally well qualified for characterizing the geothermal reservoir, and it is recommended to combine several of those (e.g., Zarrouk and McLean, 2019), but in practice they are often only partially and not completely carried out. This is due to the generally high costs of the tools, drilling rigs if required for the logging process, the sometimes high risks for the borehole, or the fact that running wireline tools is often not possible with today's modern geothermal borehole design (high deviation, open hole completions). High deviations can be a problem for all logging that is usually carried out wireline, such as PLT and temperature logging (see Table 2-2). Also, the downhole tools can only be carried out at an early or middle stage of a geothermal well during drilling or weeks to months after a well has been completed. They usually cannot be performed again after an ESP has been installed without well intervention. Therefore, detailed temperature data from the reservoir during the different cycles of a well (e.g., shut-in, testing, production) are usually missing, which is essential for predictions. Novel systems that enable permanent installation beyond the ESP to monitor the reservoir are thus needed to deepen the understanding of the temperature processes that control the temperature change in a production well and the thermal influence of hydraulically active zones.

Table 2-2. Comparison of conventional logging methods and tools with their limitations in terms of hydraulic and thermal reservoir characterization of hydrothermal geothermal wells.

	Tool/ Method	**Aim Parameter**	**Short Description**	**Limitations**	**Quality Rating**
Hydraulic Characterization (Flow Zones)	Mud logging	Mud loss	Analysis of returned drilling mud at the surface; zones of mud loss may indicate flow zones	The suitability for reservoir characterization must be doubted	Low
	Production logging tool PLT	Flow zones (quantitative contribution)	Measure changes in flow velocity along the wellbore with a flowmeter spinner after injection of water	Well established, but: Transferability from injection to production conditions is questionable Risky to run/can fail in open hole completions and high deviated wells Due to high costs (time-wise and economical) often not performed completely	Medium
	Heat-back monitoring	Flow zones (qualitative)	Repeatedly running a downhole Temperature probe wireline or at the drill pipe after injection of cold water	Repeated runs are rare due to high costs (time-wise and economically) Can fail in open hole completions and high deviated wells	High
Thermal Characterization (Natural, Flowing Temperature)	Geophysical logging	Bottom hole temperature BHT	Measure the temperature during geophysical logging after a well section has been drilled	Values are thermally highly disturbed due to the prevailing drilling	Low
	Flowing temperature	Production temperature	Measure the temperature of the pumped fluid during hydraulic testing at the top of the reservoir with a suspended temperature probe	The measured value is a function of the entry temperatures of the flow zones and in the early stage still influenced by the prevailing drilling and tests	Medium
	Wireline temperature logging	Vertical temperature profile	Measure the undisturbed temperature inside a well after a long shut-in time (at least several months)	Can fail in open hole completions and high deviated wells Required shut-in time until thermal equilibration is not known	High
	Measures during well operation	Production temperature	Measure the temperature at the surface at the wellhead or inside the system of the geothermal plant with a probe	Value at the surface differs from value downhole at the reservoir because of radial heat loss and waste heat of the pump	High

2.4 Downhole Fiber Optic Sensing as an Opportunity for Long-Term Monitoring

2.4.1 Fundamental Principle

Fiber Optic (FO) sensing can be considered as a novel downhole monitoring method. Applied for 30 years in the oil and gas business (Fenta et al., 2021), they are yet little applied in geothermal wells, although they were tested early on in the geothermal context (Hurtig et al., 1994; Förster et al., 1997). More recent studies are described in Ch. 5.1.1 and Ch. 6.1 of this work. For FO sensing, silica-based optical fibers are deployed in the environment and infrared light at a wavelength between 800 – 1600 nm is sent along the fiber (Smolen and Spek, 2003; Fenta et al., 2021). The velocity of the light inside the glass is less than the speed of light in vacuum because it is slowed down, which is described by the refractive index of the fiber. Most fibers have refractive indices of 1.5 to 1.7 (Smolen and Spek, 2003) that result in a velocity of light of $1.76 \cdot 10^8$ to $2.00 \cdot 10^8$ m/s. On the way through the fiber, a scattering process occurs that is influenced by the ambient conditions (e.g., temperature, pressure). The backscattered light can be analyzed at a sensor to infer different physical parameters. The position along the fiber can be derived from the two-way travel time.

2.4.2 Design of Optical Fibers and Fiber Optic Cables

Optical fibers consist of a silica glass core surrounded by a cladding made from silica glass. Around the core and cladding, various coatings of polymers with an optional carbon sublayer are required, primarily for mechanical protection and secondarily for chemical protection against hydrocarbons. Fibers are manufactured as single-mode fibers (SM) or multi-mode fibers (MM), in which one or several propagation modes exist. SM fibers allow only a single mode travel along the core fiber which has a diameter of typically 5 µm (Smolen and Spek, 2003) up to 10 µm (Fenta et al., 2021). The surrounding cladding has a refractive index that allows for total internal reflection inside the core. MM fibers on the other hand have about 10 times larger core diameter compared to SM fibers and therefore allow multiple modes to travel. The refractive index of the core and cladding can be split stepwise or graded, which is done for MM fibers to achieve a more uniform mode progression that allows for a better location during analysis (e.g., Fenta et al., 2021).

These fibers enable several FO technologies, allowing for measuring different geophysical properties at different scales and resolutions. Basic designs are single-point FO sensors (extrinsic sensors), that are connected to a fiber that acts in these forms only as a transmission medium, distributed fiber optic sensors (intrinsic sensors), and mixing forms where multiple-point FO sensors are connected in a chain.

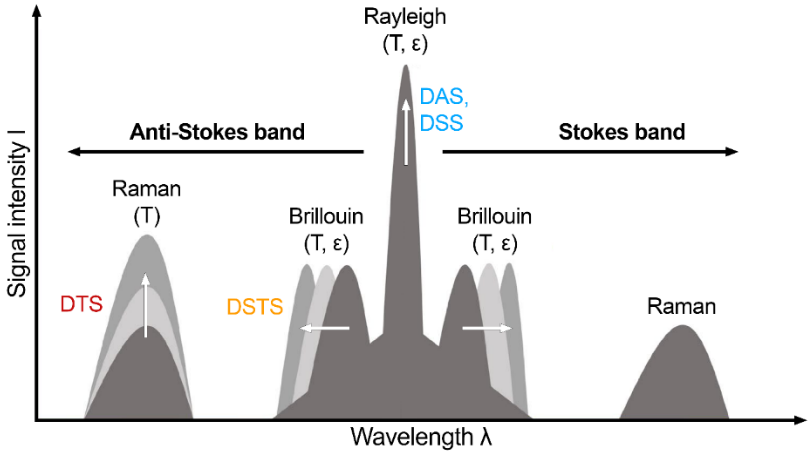

Figure 2-3. The back-scattered light spectrum with fiber optic technologies DTS, DSTS, DAS and DSS. T and ε are Temperature and strain, respectively. Modified from Ekechukwu and Sharma (2021).

2.4.3 Optical Fiber as a Transmission Medium

Extrinsic sensors are measuring devices connected to an optical fiber that acts only for transmission of the signal. A widely used type, favorable for its small but simple and cost-efficient design is the Fabry-Perot interferometer (FPI). FPIs are characterized by a small cavity (solid or air cavity) between two (semi-reflective) mirrors (Bremer et al., 2017; Zhu et al., 2023). This cavity varies in length depending on temperature or pressure. The light reflected from the cavity can be analyzed to determine the physical properties. FPI can be used to measure pressure, acoustic wave, acceleration, vibration at high resolution, strain, or even force (Zhu et al., 2023), and also temperature (Singh et al., 1995; Li et al., 2020). Another extrinsic type is Fiber Bragg Grating (FBG) sensors. For FBG sensors, the refractive index of the fiber is changed by the action of ultraviolet light at certain intervals. The gratings selectively refuse a certain wavelength of light passing through the grating. If the fiber changes due to strain or temperature in the optically active range, the grating constant also changes and the subsequent shift in the reflected wavelength can be measured (e.g., Sahota et al., 2020; Fenta et al., 2021).

2.4.4 Optical Fiber as Sensor Device – Distributed Sensing

Intrinsic sensors are fibers that act as measuring devices distributed over their entire length. This type of measuring is thus also called distributed sensing. It uses the three types of scattering - Rayleigh, Brillouin, and Raman - of the backscattered light spectrum to determine physical properties that change the amplitude, phase, and frequency of the scattering types as illustrated in Figure 2-3. The locations of the distributed sensing points along the fiber are determined using the two-way travel time in the time domain and determined using the optical time domain reflectometry (OTDR) or optical frequency domain reflectometry (OFDR) (Bense et al., 2008; Masoudi and Newson, 2016; Fenta et al., 2021).

In practical applications, a distinction is made between different distributed fiber optic technologies according to the measured properties and the measuring devices required for each technology, the so-called interrogators. Standard interrogators have both a laser to emit the light and a sensor to analyze the components of the backscattered spectrum. Brillouin-based interrogators are more complex because they launch a light pulse into both ends of a looped fiber.

Distributed temperature sensing (DTS) uses the ratio of Raman so-called Stokes (shifted to higher wavelength) and Anti-Stokes (shifted to lower wavelength) bands, the Brillouin component that is dependent on both temperature and strain or Rayleigh component (e.g., Ukil et al., 2012). Brillouin-based scattering in this context is therefore sometimes called distributed strain/temperature sensing (DSTS) (e.g., Tregubov et al., 2016). Compared to other FO technologies, DTS is rather old, first demonstrated in 1985 by Dakin and Pratt (1985) for practical applications.

Distributed pressure sensing (DPS) is enabled with special modified air-hole fibers (Zhang et al., 2021a) or by having multiple FBG sensors in an array (Arkwright et al., 2014). However, it was also demonstrated that prediction of the distributed pressure is possible by combining DTS and low-frequency distributed acoustic sensing (Ekechukwu and Sharma, 2021).

Measuring elastic waves along the fiber is possible with the analysis of the Rayleigh backscattered signal since this changes proportionally to an elastic wave. This enables distributed acoustic sensing (DAS) or distributed strain sensing (DSS). Downhole application of DAS is of major interest for its potential for seismic surveys and borehole integrity studies and those were subject to numerous research (Reinsch, 2012; Correa et al., 2017; Götz et al., 2018). Important for DAS is the so-called gauge length which corresponds to the physical distance between two positions along the fiber over which a measurement can be performed. Strain changes along the fiber induce a change in the phase difference of backscattered light at the two positions along the fiber (Jousset et al., 2018). This phase lag can be translated into strain along the fiber (Fenta et al., 2021). Besides the gauge length, the signal-to-noise ratio (SNR) is an important factor, describing the level of the wanted signal to the level of the ambient noise.

2.4.5 Measurement Setups and Downhole Deployments

Fibers can be either installed single-ended or double-ended. In a double-ended configuration, the fiber is looped at the bottom end of the cable with a turnaround and guided back to the surface inside the same cable, or the cable is looped at the bottom end and guided back. This design is often used for DTS systems by connecting both ends of the same fiber to the interrogator to shoot the light pulse alternating in both directions. This is advantageous for calibration and accuracy (Brown, 2003; Smolen and Spek, 2003). With single-ended fibers, only one fiber end is connected to the interrogator at the surface. Single-ended configuration is the standard configuration of DAS systems and for fibers connected to extrinsic sensors. Lastly, mixed forms are possible, where the fiber is looped at the bottom end, but only partially returned (Smolen and Spek, 2003).

2.4.6 Potential to Use Fiber Optics for an Improved Temperature Prediction

Recently, Khankishiyev et al. (2024) published a review on DTS in geothermal wells. They emphasize the benefits of the technology for improved reservoir characterization and optimization of reservoir management as well as monitoring of flow instabilities that might indicate casing/tubing leaks or scaling. Despite these known advantages, fiber optics is not yet an established standard method for reservoir monitoring in hydrothermal geothermal energy. Optical fibers could be particularly suitable for building a permanent reservoir monitoring system, as they enable measuring without electrical equipment downhole and can be installed flexibly beyond the pump.

2.5 The Hydrothermal Study Area of the North Alpine Foreland Basin

2.5.1 Geology and Classification

The NAFB is a hydrothermal reservoir extending from the Swabian and Franconian Alb in the north near the river Danube southward to the northern alpine rim (Meyer and Schmidt-Kaler, 1990). The basin descends to depths of over 5 km in the south, where the thermal water is up to 160 °C (Weber et al., 2019) in accordance with the average geothermal gradient of about 30 K/km (Stober and Bucher, 2020). However, some regions within the NAFB can be considered temperature anomalies, such as the Munich region, which has slightly higher gradients than average, or the so-called ‘Wasserburg Trough’ east of Munich, which is thought to have very low gradients according to heat transport modeling (Przybycin et al., 2017) and BHT data from old hydrocarbon wells (Agemar et al., 2012). With 24 geothermal sites to date (as of early 2024), the NAFB is one of the most important and most developed hotspots for low-enthalpy hydrogeothermal projects in Europe.

The reservoir, often referred to as Malm, was formed in the Upper Jurassic when sediments built up in the Tethys Sea, which today constitute a heterogeneous carbonate layer about several hundred meters thick, e.g., about 500 m in the Greater Munich Area (Steiner et al., 2014). It is characterized by an interplay of karst, fracture, and matrix porosity (Birner et al., 2012; Zosseder et al., 2022). The Malm rocks originate from the deposition of limestone, marl, and reef debris during a warm period in the Oxford to Tithon sequence (Meyer and Schmidt-Kaler, 1990). In the late Jurassic, the sea level of the Tethys Sea fell, presumably causing dissolution and karstification (Villinger, 1988; Mraz, 2019). In the early Cretaceous, carbonates of the Purbeck facies and other Lower Cretaceous formations formed due to evaporation when the shelf sea dried out (Meyer and Schmidt-Kaler, 1990; Mraz, 2019) on top of the partially eroded Upper Jurassic. The Purbeck layer today has similar hydraulic behavior as the underlying layers of the Upper Jurassic and thus can be counted as part of the hydrothermal reservoir (Böhm et al., 2013). In the Tertiary period, terrestrial sediments were deposited in the western part, while the eastern part retained its marine character. This followed a series of erosion, karstification, and deposition (Steiner et al., 2014). Since then, secondary processes such as dolomitization, recrystallization, and compaction have shaped the Malm reservoir into its present form.

In the year 1858, Quenstedt (1858) subdivided the Malm reservoir based on biostratigraphy from bottom up into Malm α, β, γ, δ, ε, and ζ, a classification that is still used today but not always helpful for prospecting. Therefore, the Malm is sometimes subdivided based on hydro stratigraphy into the heterogeneous Upper Malm, the relatively homogeneous Middle Malm, and the Lower Malm, which is less hydraulically active (Böhm et al., 2013). A further subdivision can be made into bedded facies, characterized by lower matrix porosity and massive (reef) facies with a high rock matrix porosity (Meyer and Schmidt-Kaler, 1990; Steiner et al., 2014).

In recent years, the Malm reservoir and the overlying Purbeck Formation have been the subject of numerous studies describing hydrochemically properties (e.g., Mayrhofer et al., 2014; Heine et al., 2021; Winter and Einsiedl, 2022), petrophysical properties (e.g., Bohnsack et al., 2020), hydraulic conditions and modeling approaches (e.g., Konrad et al., 2019, 2021), the potential for geothermal exploitation, or assessments to estimate drilling risk in the region (e.g., Drews et al., 2022). All these studies paint a picture of a complex and highly heterogeneous reservoir whose dynamics are not yet fully understood.

2.5.2 Temperature Models of the North Alpine Foreland Basin

Germany's most prominent geostatistical 3D temperature model is the Geothermal Information System 'GeotIS' that shows the formation temperature as a predicted value at the top of the reservoir and other layers for all regions in Germany that are relevant for deep geothermal prospecting (Agemar et al., 2014; Schulz et al., 2009; Agemar, 2022a). The model is accessible via an easy-to-use web interface and to date the best available temperature model for deep regions in Germany. GeotIS is continuously updated with new data and by adaption of applied methods (e.g., Agemar, 2022b). It accesses a database with temperature logs and values of over 11 000 boreholes in Germany, most of them lower quality BHT data (see Ch. 2.3.1). BHT data were corrected dependent on the database for each data set and then a model is estimated with 3D universal Kriging, a method that models the spatial (from 5000 m below sea level to surface) variety of a regionalized variable based on a variogram (e.g., Oliver and Webster, 2015). GeotIS' uncertainty is given as an estimated standard deviation based on Kriging variance (Agemar et al., 2014; Agemar and Tribbensee, 2018). This method has the advantage that it creates a full 3D model with which the geothermal gradient is automatically taken into account with high data density. However, it lacks the consideration of possible and expected errors due to the different forecasting methods applied and the uncertainty that lies in the input data and estimated data necessary for each method.

Another temperature model of the North Alpine Foreland Basin in Bavaria was created within the GeoMol project in the course of an Alpine Space program (Team GeoMol, 2015a, b, c). Similar to GeotIS, this model also relates to subsurface temperature measurements of different quality (BHT data and continuous temperature logs). The model shows the temperatures at the top of the Upper Jurassic layer, calculated from a simple linear gradient model, and the surface temperatures in the study area, which were determined by regression with the mean air temperatures. The uncertainty of the gradients is defined by the underlying BHT correction and extrapolation from measured depth to the top Upper Jurassic layer and is described by a two-stage quality classification. Indicator Kriging was then used to display the horizontal temperature in the area. Compared to 3D Kriging, indicator Kriging has the advantage that it is based on probability and does not constrain the data to be a normal distribution. Indicator variables represent the probability that the temperature at a location is greater or lower than defined threshold values and the value with the highest probability is selected depending on those (Hohn, 1999). One disadvantage is that this is not a complete 3D method and that the data must therefore be extrapolated to the respective depth beforehand. This entails an error that depends on the geothermal gradient applied, which is often unknown.

Both geostatistical models, GeotIS and GeoMol, do not consider the uncertainty that lies in the input data used for the calculation and estimation of the basic temperature data (e.g., BHT correction). It is likely that when this uncertainty is applied, the error of the corrected values exceeds the uncertainty reported in the existing models.

Another approach for a 3D basin temperature model for the NAFB was conducted at GFZ Potsdam based on first a purely conductive lithospheric model (Przybycin et al., 2015) and later refined by coupling fluid and heat transport simulations (Przybycin et al., 2017). With the purely conductive model, they concluded that conduction is the main heat transport mechanism for the NAFB, but their model is too warm and conduction alone cannot explain the thermal anomalies (e.g., South East of Munich). For their refined coupled model, they created a large-scale structural model with 12 lithostratigraphic units. As boundary conditions, they took a fixed temperature from 3D lithospheric-scale conductive mode at -7500 m above sea level and a mean annual surface temperature, and they considered conduction, advection as well as convection processes for the heat flow in between. The resulting temperature model shows the same trend as GeotIS, e.g., the positive thermal anomaly around Munich and the negative thermal anomaly southeast of Munich at the Wasserburg through. However, compared to BHT measurements and outflow temperatures, there are significant deviations of up to 40 °C in some areas, e.g., in the southeast of the NAFB and the northeast (Przybycin et al., 2017).

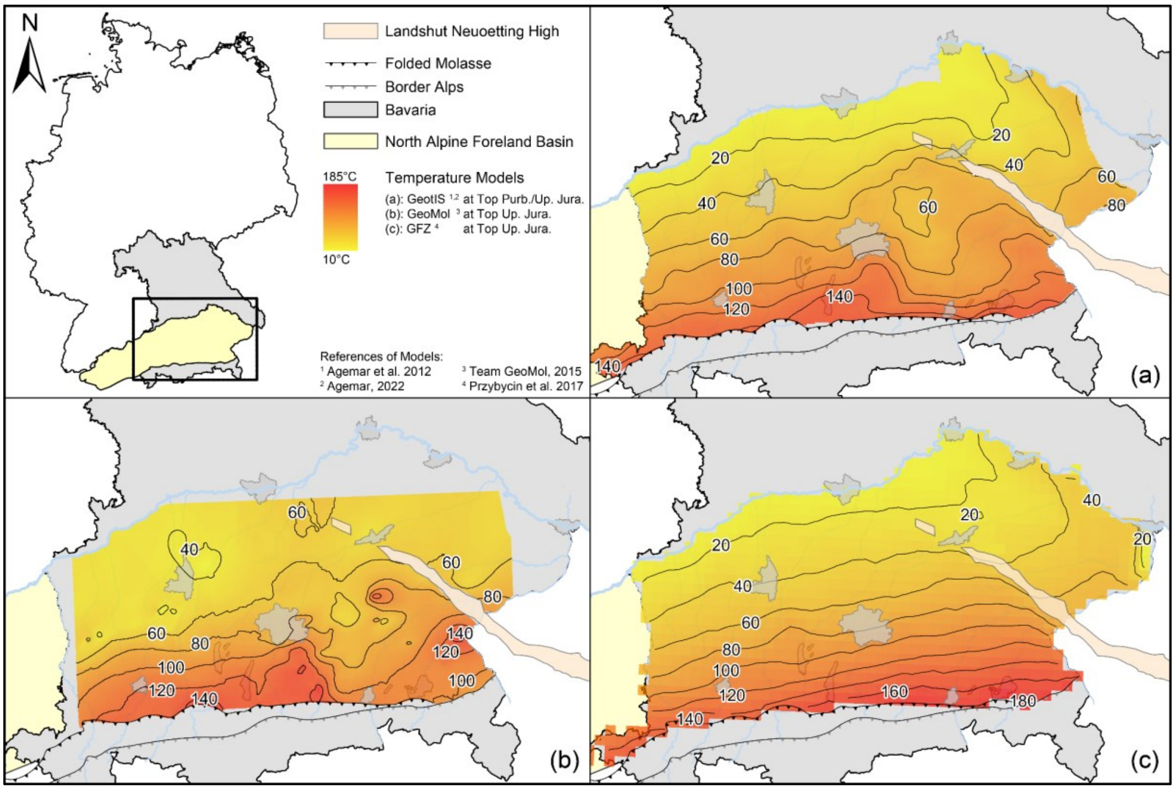

Figure 2-4. Comparison of three deep temperature models for the North Alpine Foreland Basin in Bavaria. The map was created with ArcGIS Pro 3.2.1. The visualized data were taken from (a): GeotIS temperatures at top of the reservoir, either Purbeck (Purb.) or Upper (Up.) Jurassic (Jura.) (Agemar et al., 2012; Agemar, 2022a). (b): GeoMol temperatures at top of Upper Jurassic (Team, 2015a). (c): Temperatures at top Upper Jurassic of the 3D basin model of GFZ (Przybycin et al., 2015). As the refined coupled model (Przybycin et al., 2017) was not available for this thesis at the top Jurassic layer, the purely conductive model is shown here. The legend shown in the upper left corner is related to the maps in (a), (b) and (c).

Figure 2-4 shows the temperature distributions of the three models GeotIS, GeoMol, and 3D basin model of GFZ at the top of the Upper Jurassic reservoir (GeoMol, GFZ), respectively the top of the Purbeck formation and if not available the Upper Jurassic (GeotIS). Note that for the GFZ model, only the purely conductive model (Przybycin et al., 2015) was available at the top of the reservoir and the coupled model reflects the negative anomaly South East of Munich and a positive thermal anomaly in the area of Munich much better.

Another approach was taken by Fuchs et al. (2022) by providing not subsurface temperature data, but the heat flow at the surface as heat flow densities. As part of the Global Heat Flow Database (Group Global Heat Flow Data Assessment, 2023), they did quality control of the available HFDs in Germany and gave reliable values for 170 locations in Germany. From those, they calculated an average terrestrial heat flow for Germany of 0.078 ± 0.007 W/m². The HFD value can be used to estimate whether the subsurface at a location is particularly warm or cold, i.e., whether higher temperatures are to be expected at depth than on average. Also, with knowledge of the HFD, it is possible to estimate the temperature at a specific depth following Fourier's law, if conduction is dominating and stratigraphic thickness and thermal conductivities are known. Unfortunately, only very few HFD data are available in the NAFB, and they are conglomerated at the Bavarian lakes, especially southwest of Munich. Regional statements can therefore not be made. Yet some areas are believed to show anomalies because of increased heat transport driven by advection (Fuchs et al., 2022).

In summary, due to its easy access and the fact that it is a full 3D model, GeotIS is the most used and best model available to date. It provides access to temperatures based on measurements in boreholes (BHTs and a few higher-quality measurements) at various depths. However, the underlying geostatistical approach with 3D Kriging must be questioned. It does not include a comprehensive error propagation from the uncertainty that lies on the input parameters of the BHT correction, through the correction itself to the extrapolation of the corrected values to the respective depth and then into the spatial representation.

3 AIMS AND SCOPE

The undisturbed, natural temperature in the subsurface is an important parameter for hydrothermal geothermal energy, especially in drilling planning and for the exploration prognosis. Prospecting is carried out in regions where high rock temperatures are suspected at the depth of the reservoir, and precise temperature forecasts are important for evaluating a geothermal heat reservoir and reducing the risk of exploration. In turn, the production temperature is of interest for the subsequent heat yield in addition to the quantity and quality of the pumped fluid. Given the background described in Ch. 2, the natural static thermal field and the dynamic production temperature are difficult to predict and there is a need and potential to improve the conventional predictions and monitoring procedures.

1. Regarding the static undisturbed temperature, it can be stated that the natural temperature field is insufficiently known and the existing models lack a holistic consideration of the uncertainty. Temperature models must refer to the correction of poor-quality temperature data such as bottom hole temperatures, which were mostly measured in old hydrocarbon projects where temperature was of subordinate interest. Consequently, the accuracy of those measurements must be questioned, and an improved model should focus on those uncertainties and error propagation.

   It is assumed that a temperature model that follows a comprehensible uncertainty assessment during the correction of BHTs will reveal that the common temperature models are too optimistic. Uncertainty-based methods are well suited to predicting the temperature of a poor-quality BHT data set. Therefore, in this work, the uncertainties of the input parameters of the common BHT correction methods will be specified, and a new correction workflow with Monte Carlo techniques will be developed for the temperature data set of the hydrothermal hotspot of the North Alpine Molasse Basin in Bavaria.

2. Regarding the dynamic production temperature, it can be stated that its prediction is still a challenge. The influence of hydraulically active zones on the production temperature is difficult to assess, even if it is estimated to be high. Sometimes, but unfortunately not always, production logging runs and other geophysical loggings are used to locate and characterize flow zones. Production tests are used to estimate the fluid temperatures in the reservoir.

However, during operation, monitoring the thermal conditions in the reservoir and the hydraulically active zones is not possible with the standard well design. As a result of the insufficient data available, the link between SFT and production temperatures remains unclear.

It is assumed that fiber optic technology is particularly suitable to build a permanent monitoring system in a geothermal reservoir. Such a system can be able to monitor inflows, verify standard methods such as PLT analysis, and improve the understanding of thermal conditions during different hydraulic states of the well. It is believed that too little emphasis is currently placed on hydraulically active zones during exploration, well design, and well logging and that the fiber optic monitoring system can reveal the presumably high importance for the subsequent hydraulics and thermals of the well. Therefore, a fiber optic cable for long-term monitoring is to be installed in the geothermal production well SLS TH4 in Munich in the center of the NAFB. The testing of this novel system is part of this work, as well as the investigation of the hydraulically active zones of the wellbore using the fiber optic data and the evaluation of their contribution to the mixed production temperature.

4

Uncertainty Assessment of Corrected Bottom-Hole Temperatures Based on Monte Carlo Techniques

This chapter was published as:

Schölderle F., Götzl, G., Einsiedl, F., Zosseder, K. (2022). Uncertainty Assessment of Corrected Bottom-Hole Temperatures Based on Monte Carlo Techniques. Energies, 15(17). https://doi.org/10.3390/en15176367

Abstract: Most temperature predictions for deep geothermal applications rely on correcting bottom hole temperatures (BHTs) to undisturbed or static formation temperatures (SFTs). The data used for BHT correction are usually of low quality due to a lack of information and poor documentation, and the uncertainty of the corrected SFT is therefore unknown. It is supposed that the error within the input data exceeds the error due to the uncertainty of the different correction schemes. To verify this, we combined a global sensitivity study with Sobol indices of six easy-to-use conventional correction schemes of the BHT data set of the Bavarian Molasse Basin with an uncertainty study and developed a workflow that aims at presenting a valid error range of the corrected SFTs depending on the quality of their input data. The results give an indication of which of the investigated correction methods should be used depending on the input data, as well as show that the unknown error in the input parameters exceeds the error of the individual BHT correction methods as such. The developed a priori uncertainty-based BHT correction helps to provide a real estimate of the subsurface temperatures needed for geothermal prospecting and probabilistic risk assessment.

4.1 Introduction

Knowledge of the static formation temperature (SFT) is essential for both geothermal and hydrocarbon projects for optimal borehole design (drilling and completion, e.g., Eppelbaum et al., 2014), for exploring heat deposits, as a basis for interpreting geophysical loggings, e.g., Schlumberger (1998) and for calculation and correction of geothermal and hydraulic parameters (Eppelbaum et al., 2014). It is of special importance for geothermal projects in low-enthalpy regions, since the SFT directly correlates with the amount of energy produced by a geothermal well, which is crucial for reaching the minimum production temperature (Schulz et al., 2010). Small differences in expected formation temperature therefore have large impacts on the estimated efficiency and economics of geothermal systems and, consequently, on exploration risk and insurability. Statistically validated temperature forecasts are consequently of high interest for geothermal prospecting and to reduce the risk of successful exploration. To obtain an approximation of subsurface temperatures, isothermal maps and temperature distribution models are used. The quality of these temperature predictions is influenced by the data density, the heterogeneity of data including disturbed and undisturbed temperatures and the applied inter- and extrapolation (Cressie, 1993). Disturbed temperatures represent data that are measured immediately or shortly after the drilling process and are therefore thermally affected by the drilling process, while undisturbed temperatures represent the actual rock temperature. Direct measurement of undisturbed temperatures is costly and time consuming, as well as challenging due to the unknown, proportionally long shut-in time that must be waited for. This is possible with a temperature logging tool, which is usually operated via a wireline, or with fiber optic temperature measurements, which are either wireline or permanently installed. Therefore, the SFT is rarely known and in most cases must be estimated from poor quality temperature data.

Most common sources of downhole temperature data are bottom hole temperatures (BHTs) that are measured during or after drilling as a byproduct of geophysical logging runs and are usually documented at the lowest point of a logging run across a well section. Usually, the drilling fluid cools the formation, but at shallow depths at around 1000 m, the rock temperature is low and therefore BHT measurements may exceed the SFT, e.g., Team GeoMol (2015c) (see Figure 4-1).

In the early stages of geothermal projects, BHTs are often the only downhole temperature information available as documented, e.g., by Poulsen et al. (2012) for their Denmark data set. BHTs are well known to be highly influenced by mud circulation (temperature of the drilling mud, duration and pumping rate), the time that passed since circulation stops, the geometry of the borehole, the geothermal gradient, and the thermal properties of the borehole fluid and the surrounding formation, e.g., Eppelbaum et al. (2014).

An estimation of the SFT from BHT data is possible by analytical or numerical extrapolation of the temperature buildup during the shut-in period of the respective well. Reviews of the most prominent existing conventional correction methods highlighting their differences are given by

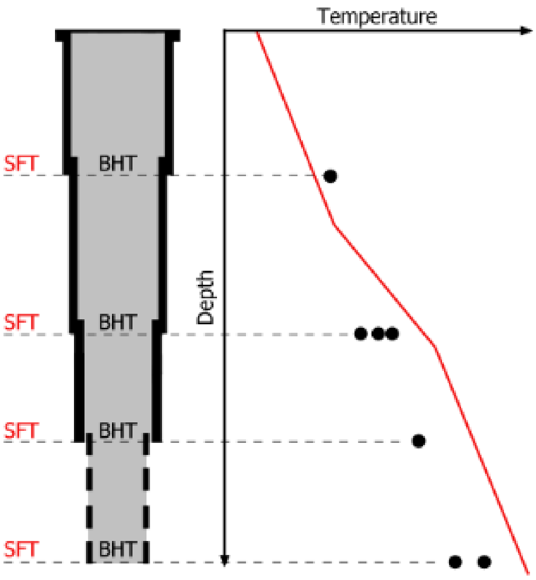

Figure 4-1. Schematic of exemplary bottom hole temperature (BHT) measurements in a borehole. The BHTs (black dots) can be present single or, if several were measured at one depth, as a series of measurements. Due to the thermal influence of the previous drilling, BHTs deviate from the static formation temperature (SFT), which can be derived by the geothermal gradient (red line).

Deming (1989), Hermanrud et al. (1990) or Zarrouk and McLean (2019). Widely used are the Horner Plot method (Horner, 1951) adapted by Dowdle and Cobb (1975), the correction according to Lachenbruch and Brewer (1959), as well as the generalized Kutasov-Eppelbaum method (Kutasov and Eppelbaum, 2005). These methods represent BHT-correction procedures based on a line source approach that determine the equilibrium temperature as the intersection point with the temperature-axis. A mathematical issue with these models is that they inadequately represent the borehole as they ignore the spatial dilatation (borehole radius). Other methods that are solved graphically are the spherical-radial heat flow model of Ascencio et al. (1994) or the radial heat source Brennand method (1984), which is recommended by several authors due to its accuracy (Sarmiento, 2011; Horne, 2016; Zarrouk and McLean, 2019). The numerical and analytical methods following Leblanc et al. (1982) are based on a cylindrical source model considering the spatial dimensioning (radius ≠ 0) (Poirier and Poirier, 2016; Hermanrud et al., 1990). By estimating the initial temperature disturbance and thermal diffusivity, one can also calculate the SFT for only one available BHT at fixed values for the borehole radius and thermal diffusivity (e.g., Schulz, R. & Werner, 1987; Agemar et al., 2012). The latter method was refined by Agemar (2022b) by correlating the thermal disturbance with the borehole radius.

More advanced and more complex methods were introduced by several authors in recent years, such as a two-component model that respects the thermal interactions between drilling mud and formation due to their different thermal properties (Shen and Beck, 1986) or an artificial neural network approach to empirically derive the SFT (Bassam et al., 2010). Other available approaches include Wong-Loya's rational polynomial functions (Wong-Loya et al., 2012), the stochastic method of particle swarm optimization algorithm (Liu et al., 2016), the multicomponent approaches on the basis of geochemical data (Nitschke et al., 2017; Ystroem et al., 2020), or a numerical wellbore simulator and numerical inversion of temperature logs during injection (Wang et al., 2019, 2021).

However, conventional methods are still widely used (e.g., Barba et al., 2021), because they are easier to apply and require less information about the geophysical properties of the drilling fluid and the formation, as well as less computational effort than the more complex methods. Thus, they are often applied at wells with poor documentation where the accuracy of the information may be doubted or where the necessary parameters for the correction methods are often not known at all. This is particularly true for old hydrocarbon wells. In general, BHT data found in older logging reports and logging headers is not reliable, as the values often suggest incorrect documentation and rounding of relevant parameters (Deming, 1989). A validation of different conventional BHT correction schemes versus field data was executed by, e.g., (Hermanrud et al., 1990; Förster, 2001), who estimated errors up to about 8 to 10 °C, or Andaverde et al. (2005) who studied different regression schemes for the solution of graphical BHT correction. Förster (2001) concluded that, due to high standard deviations, corrected BHT reflect the undisturbed formation temperature not better than ± 16 °C. These authors focused on the different mathematical correction methods but did not include the likely interactions of varying input parameters in their studies. We suspect that the inaccuracy of the input data has a much greater impact on the correction than the methodological weakness of the generalized conventional methods. This was also highlighted by, e.g., Deming (1989), who stated that the accuracy of the corrected BHT does not necessarily lie in the method used for the correction, but rather in the quality of the available data. Aabø and Hermanrud (2019) also found that the results of different correction methods differ a lot and that the errors are generally of importance, with up to 10 to 20 °C. They see the different mud circulation practices as a main trigger. For a holistic consideration of the true error of the corrected BHTs, the errors in all input parameters are relevant.

For prospecting and risk assessments prior to the start of new geothermal projects and for a general assessment of a region's geothermal potential, tools that present reservoir temperatures as a reliable business case are needed. To date, a quantitative consideration of the error of BHT-corrected values has been lacking but is crucial for a risk assessment of the temperature forecast. Therefore, in this study, we investigate how BHT-corrected values can be provided as a distribution dependent on the quality of the input data and their errors, rather than as a distinct corrected temperature value that ignores error propagation, as is commonly done (e.g., Poulsen et al., 2012; Liu et al., 2016; Agemar, 2022a). To do so, we study the sensitivity of typically used correction schemes and their error considering different parameter assumptions. Based on the results of the sensitivity study, a new workflow that accounts for the likely errors in the input parameters and provides a probabilistic alternative to existing temperature estimates to assess business, as well as the worst- and best-case scenarios, is described.

4.2 Materials and Methods

We applied a variance-based global sensitivity analysis (GSA) using Sobol indices (Sobol, 2001) and Saltelli sampling (Saltelli et al., 2010) on the temperature data set of the Bavarian Molasse Basin to show possible sources of error of BHT correction and provide recommendations on the favored methods to be applied. The focus was on six conventional BHT correction schemes that are commonly used and can be applied on a large data set with partly poor or unknown quality, and thus large uncertainty of the available data. Therefore, the uncertainties in all input parameters were studied and the outcome's uncertainty based on the given input parameter set and its error-proneness was evaluated. Using undisturbed temperature logs, also derived from fiber optic distributed temperature sensing measurements (DTS) from the data set, the BHT correction schemes were compared with respect to their uncertainty. For this purpose, the possible deviations of the corrected SFT from the actual temperature conditions were calculated from the temperature logs and the DTS measurements, respectively. By combining the results of the sensitivity study and the uncertainty analysis, we developed a workflow that yields a corrected SFT with statistically valid uncertainty depending on the quality of the individual BHT data sets. Since conventional correction methods are based only on conductive heat transfer, we also investigated the performance of these BHT corrections in a well at known inflow zones.

4.2.1 Study Area and Data Set

The main exploration target in the conductive-dominated hydrogeothermal study area is the fractured and karstified carbonate rocks of the Upper Jurassic Malm aquifer. The production temperatures range between under 50 °C in the north, where the aquifer is at shallow depths, and over 160 °C in the south, where the Upper Jurassic is in depths of 4000 – 6000 m (Weber et al., 2019; Flechtner et al., 2020). We used this temperature data set of drillings in the Bavarian Molasse Basin in Southern Germany, which includes both hydrocarbon and geothermal wells. In the 1950s and 1960s, multiple gas and oil wells were being drilled there, exposing layers of the Cretaceous and deeper in layers of the Upper Jurassic. In the last 15 years, a lot of geothermal projects were developed, making the Bavarian Molasse Basin one of Europe's most important low enthalpy geothermal hotspots today (Steiner et al., 2014; Eyerer et al., 2020). Extensive studies were conducted during the geothermal buildup to characterize the reservoir of the Molasse Basin in detail as well as regionally, hydrochemically (Heine et al., 2021), petrophysically (Bohnsack et al., 2020a), and geothermally (Konrad et al., 2019; Zosseder et al., 2022).

In the study area, a total of 65 geothermal wells and 870 hydrocarbon wells exist. Of those, BHT data with associated reported shut-in times from logging reports and headers are available from 346 wells (292 oil and gas wells and 54 geothermal wells). Fourteen wireline temperature logs (TLogs) of both geothermal and hydrocarbon wells were available, of which eleven were

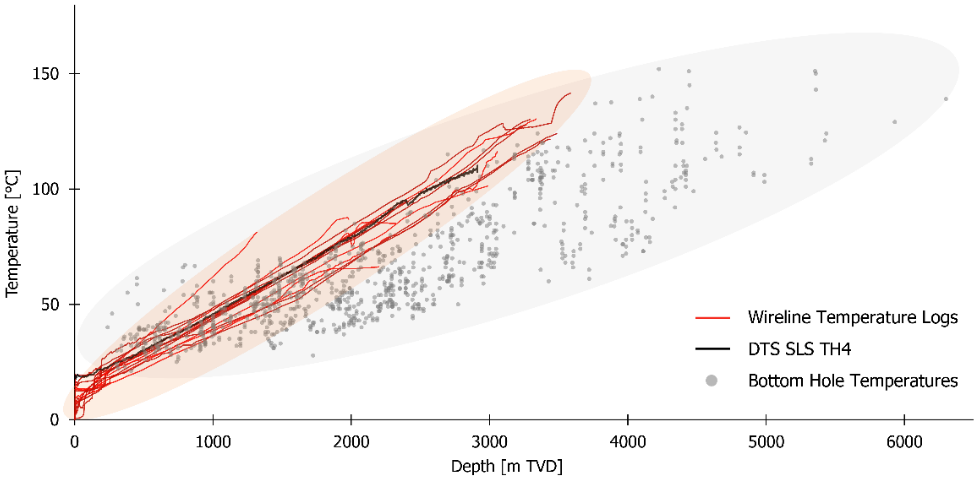

Figure 4-2. BHT values and temperature profiles available for the Bavarian Molasse Basin temperature data set versus depth. The black profile is from a fiber optic DTS measurement in well SLS TH4 at the Schäftlarnstraße geothermal site.

measured after a shut-in period of at least two months. In addition, a time series of continuously measured high-quality temperature profiles was available at the well TH4 of the Schäftlarnstraße (SLS) site in Munich. This well is equipped with a permanent fiber optic monitoring system, installed inside of the borehole over its entire length along a steel sucker rod (Schölderle et al., 2021). There, distributed temperature sensing (DTS) was used to collect temperature profiles over a 16-month period during the shut-in and to monitor the equilibrating borehole temperature. The DTS temperature profiles were acquired every 10 minutes at a spatial resolution of 1 m. With the exception of a dominant hydraulically active zone at top of the reservoir, thermal dynamics (warm back) are no longer evident in the profiles after 16 months of shut-in (Schölderle et al., 2021). Therefore, we suspect that this profile reflects the geothermal gradient with great accuracy. Further details on the background of downhole fiber-optic temperature measurements, the installation of the monitoring system in SLS TH4, and the technical specification can be found in Schölderle et al. (2021).

Table 4-1. The BHT data set structured in steps of 500 m TVD regarding the shut-in time.

TVD (m)	Number of Wells	Valid Bottom-Hole Temperature at One Depth						Average Shut-in Time (s)	Temperature Range (°)
		1 BHT	2 BHT	3 BHT	4 BHT	5 BHT	6 BHT		
≤ 500	39	36	7	0	0	0	0	30 600	21.0 – 61.3
- 1000	98	78	25	7	1	0	1	29 880	22.0 – 67.0
- 1500	104	63	32	12	9	2	0	33 120	30.0 – 70.0
- 2000	103	82	26	10	5	1	0	32 200	27.8 – 82.0
- 2500	95	79	22	9	3	3	1	48 960	39.0 – 92.0
- 3000	66	47	18	5	5	3	0	60 480	47.0 – 116.7
- 3500	37	25	10	6	2	3	1	61 200	60.0 – 124.0
- 4000	27	17	11	3	3	0	1	76 680	61.0 – 137.5
> 4000	35	30	14	7	3	1	0	57 960	73.0 – 167.7

A summary of all available continuous temperature logs is given in Supplementary 4 - *1*. Figure 4-2 depicts all available temperature logs (wireline and DTS) and the BHT data of the Bavarian Molasse Basin.

As can be seen in Figure 4-2, the disturbed BHT readings generally tend to overestimate the undisturbed temperature profiles at shallower depths and underestimate them at greater depths. For 165 cases, we had to assume copying errors of the BHT (i.e., the same BHT values were written down for different shut-in times), and in some other cases we noticed errors copying the shut-in time. These data were not used for further analysis. In total, there were 730 cases with one or a series of BHT measurements with reported shut-in times that could be corrected to SFT. For 155 wells, only a single BHT was available at a depth layer of the respective well. This means that more than one BHT may be measured in a well, e.g., from different logging runs at different depths/borehole sections of the respective well, but not consecutively in a series of logging runs in a borehole section. In the following, such data are then referred to as 'one BHT'. Data for one BHT is generated if only one logging run was performed per borehole section or if a series of logging runs was performed but only one valid BHT was reported. If multiple consecutive logging runs have been performed, but the reported BHT data does not increase over time, this BHT data is classified as invalid. Table 4-1 shows the evaluable BHT data in increments of 500 m TVD. Even for wells drilled in recent years, the vast majority have only one BHT that can be corrected. A reason for this lies in the fact that often only a few expensive logging runs are performed and the BHT and corresponding shut-in time are reported only as a byproduct to the actual logging parameters and are thus often imprecise or missing.

In nine cases, a complementary data set of undisturbed temperature data was available from TLog or fiber optic DTS data (well SLS TH4) and BHT data with reported shut-in times. Unfortunately, only in two of these cases was a set of measurements from at least two BHTs at the same depth with different shut-in times available. The unperturbed temperature information was used as the target value in the uncertainty study in these nine cases.

4.2.2 Applied Correction Schemes

We applied the six conventional and commonly used correction techniques of the Horner Method (HM), the Lachenbruch & Brewer Method (LBM), the Brennand Method (BM), the linearization Method (LM), forward modeling (FM) and the 1BHT Method (1BHTM). HM and LBM are based on a linear heat source, disregarding the radius of the borehole. These methods, as well as BM, based on a radial heat source, are solved graphically by interpolation of a time equivalent versus the measured BHT values. The LM, FM and 1BHTM schemes, in contrast, are based on Leblanc's cylindrical heat source model following eq. 4-1 (Leblanc et al., 1982):

$$BHT\ (0,t) = SFT + \Delta T\left(e^{\frac{-a^2}{4\cdot\kappa\cdot t_s}} - 1\right), \Delta T = SFT - \ T_m \qquad \text{(eq. 4-1)}$$

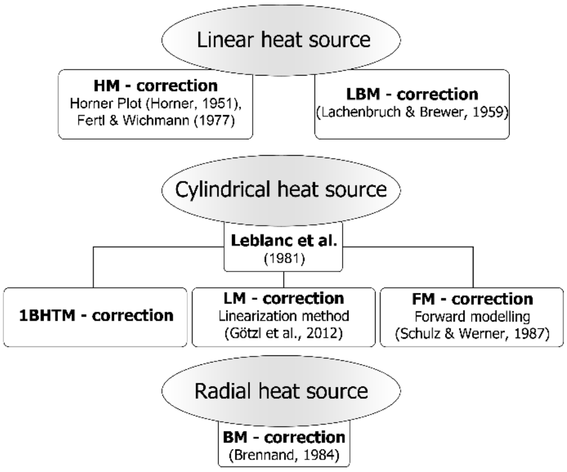

Figure 4-3. BHT correction methods applied for quantifying uncertainty.

where $BHT\ (°C)$ represents the thermally disturbed in situ temperature, $SFT\ (°C)$ the undisturbed rock temperature measured at equilibrium conditions, $\Delta T\ (K)$ the initial temperature disturbance, $a\ (m)$ the borehole radius, $\kappa\ (m^2/s)$ the bulk thermal diffusivity of the system drilling mud and formation, $t_s\ (s)$ the shut-in time (time since drilling fluid circulation stopped), and $T_m\ (°C)$ the mud temperature (temperature of the drilling fluid during circulation). The analytical solution of Leblanc's correction technique of a cylindrical explosion heat source was designed for at least three BHT-data per depth. The method can be applied if the following stability criterion is met:

$$a^2 < 4 \cdot \kappa \cdot t_s. \qquad \text{(eq. 4-2)}$$

The six applied methods are shown in Figure 4-3 subdivided by their mathematical approach.

We can also distinguish the six methods by how they are solved, i.e., analytically, or graphically. Table 4-2 gives an overview over the six methods with their respective required input parameters.

Table 4-2. Input requirements (marked with x) of six conventional BHT correction methods.

Name	Number of BHTs per Depth Layer	Shut-in Time	Mud Temperature	Borehole Radius	Circulation Time	Thermal Diffusivity
Graphically Solved						
LBM	≥ 2	x				
HM	≥ 2	x			x	
BM	≥ 2	x			x	
Analytically Solved						
LM	≥ 3	x		x		
FM	≥ 2	x		x		x
1BHTM	1	x	x	x		x

4.2.2.1 Lachenbruch & Brewer Method (LBM)

The correction according to Lachenbruch and Brewer (1959) determines the SFT as the intersection point of the BHTs with the temperature axis. Therefore, we used linear regression considering the reciprocal value of the shut-in time as $\ln(1/t_s)$ on the x-axis. For this method, at least two BHT values with associated shut-in time are required.

4.2.2.2 Horner Method (HM)

In contrast to LBM, the correction method according to Horner, originally developed for pressure build-up (Horner, 1951) and adapted for temperature build-up (Lachenbruch and Brewer, 1959; Dowdle and Cobb, 1975), additionally considers the circulation time t_c (s) in the form of $\ln((t_c+t_s)/t_s)$ on the axis of abscissa. In Goutorbe et al. (2007) it was shown that Horner's method gives poor results for large borehole radii and short shut-in times, but reliable ones when the following criterion is met:

$$a^2 \ll 4 \cdot \kappa \cdot t_s. \qquad \text{(eq. 4-3)}$$

4.2.2.3 Brennand Method (BM)

The Brennand method is based on a radial heat source and is written as (Brennand, 1984):

$$\begin{gathered} BHT(a,t) = SFT - m \cdot log(t_B),\ t_B = \frac{1}{t_s + p \cdot t_c}, \\ m = \beta \cdot (\mathrm{SFT} - T_m) \cdot n,\ n = \frac{c_{p,r} \cdot \rho_r \cdot a^2}{\lambda}, \end{gathered} \qquad \text{(eq. 4-4)}$$

where t_B (s) is the Brennand time, $p = 0.785$ and $\beta = 6.28$ are constants derived from field data of a Philippines data set, and $c_{p,r}$ $(J/(kgK))$, ρ_r (kg/m^3), and λ (W/(mK)) are the specific heat capacity, density, and thermal conductivity of the formation rock. The solution is derived when at least two BHTs recorded at different shut-in times are plotted versus their respective Brennand times. The intersection at zero Brennand time of a linear fit through all points represents the undisturbed formation temperature SFT.

4.2.2.4 Linearization Method (LM)

LeBlanc's formula (eq. 4-1) can be solved inversely by numerical optimization of the thermal diffusivity (Goetzl et al., 2010; Götzl et al., 2013). Transformation and logarithmic calculus of Equation (1) generate the linear equation according to the scheme C = a – b · t*:

$$\begin{gathered} \underbrace{\ln(BHT - T_m)}_{C} = \underbrace{\ln(\Delta T)}_{a} - \underbrace{\left(\frac{a^2}{4}\right) \cdot \frac{1}{\kappa}}_{b} \cdot \underbrace{\frac{1}{t_s}}_{t*}, \\ \text{where}\ \ SFT = T_m + \Delta T. \end{gathered} \qquad \text{(eq. 4-5)}$$

Eq. 4-5 can be transformed to an inverse linear optimization problem in case at least three independent BHT measurements are available. In that case, initial guesses need to be made for the mud temperature T_m and the bulk thermal diffusivity of the drilling mud and the nearby rocks κ, while the borehole radius a, the shut-in time t_s and the measured BHT values are given. As a first approximation, T_m can be set at 30 °C or at 50 % of the maximum observed BHT value.

During the iterative linear optimization procedure applying standard LSQ methods, the correction vector adapts ΔT and κ until a convergent solution is found or a maximum number of iterations has elapsed. The resulting value for κ can be used for quality control measures to evaluate if thermal conduction is the major process of the thermal balancing observed inside the borehole regarding the observed BHTs. In addition, this method delivers the total fitting error (predicted versus observed BHT values) for all iteration steps.

4.2.2.5 Forward Modeling (FM)

In contrast to the Linearization method, Forward Modeling is an analytical solution that disregards mud temperature. The method can be used for at least two BHTs per depth. The following eq. 4-6 represents the calculation of undisturbed rock temperatures by analyzing the temperature increase with raising shut-in times (Schulz and Werner, 1987):

$$SFT = BHT(t_{s,1}) + \left(BHT(t_{s,2}) - BHT(t_{s,1})\right) \cdot \frac{1-f(t_{s,1})}{f(t_{s,2})-f(t_{s,1})}, \qquad \text{(eq. 4-6)}$$
$$f(t_s) = e^{\left(-\frac{a^2}{4\cdot\kappa\cdot t_s}\right)}.$$

4.2.2.6 1BHT Correction Scheme (1BHTM)

All the methods described above have in common that they are applicable only when at least two BHTs have been measured at the same depth at different time intervals. In most boreholes (see Table 4-2), only one BHT is available at a depth layer. Leblanc's eq. 4-1 can be simplified to also account for the correction of a single BHT. The transformed equation writes as follows (Leblanc et al., 1982):

$$SFT = \frac{BHT + T_m(f(t_s)-1)}{f(t_s)}, \qquad \text{(eq. 4-7)}$$
$$f(t_s) = e^{\left(-\frac{a^2}{4\cdot\kappa\cdot t_s}\right)}.$$

4.2.2.7 Constraints

There are two restrictions to the correction schemes. First, a basic requirement for all methods is that each consecutive temperature measurement and the corresponding time since circulation stopped is higher than the previous one. Second, as some of the applied methods are valid only if the stability criteria $a^2 < 4 \cdot \kappa \cdot t_s$ (eq. 4-2) or $a^2 \ll 4 \cdot \kappa \cdot t_s$ (eq. 4-3) are fulfilled, we applied the respective criterion to all methods to keep the results of the sensitivity study comparable. Fulfillment of the stability criterion is dependent on borehole radius a, shut-in time t_s and estimated thermal diffusivity κ. We therefore applied the sensitivity study at typical borehole radii, as they are typical for the Bavarian Molasse Basin, and calculated the limits of minimum and maximum shut-in time and thermal diffusivity with respect to the criterion. The typical diameters of the well sections in the data set were 23 inches (0.58 m), 17.5 inches (0.44 m), 12.25 inches (0.31 m), 8.5 inches (0.22 m), 6.25 inches (0.16 m) and 6 inches (0.15 m). For each section, we considered a possible widening of 1 inch (~0.03 m) due to outcrops in the rock.

4.2.3 Global Sensitivity Analysis (GSA)

The quality of input parameters to the BHT correction methods within the data set varied. For example, even-numbered shut-in times without a decimal digit frequently occurred in logging headers, which indicated to us that these values were often rounded or not measured precisely. In other cases, the values were more accurate to one decimal place, implying that they are more reliable. We applied a global sensitivity analysis (GSA) using Sobol method with the open source Python library SALib (Herman and Usher, 2017) and Saltelli sampling (Saltelli et al., 2008, 2010) to the BHT correction methods (HM, LBM, BM, LM, FM, 1BHTM) to investigate the qualitative influence of parameter assumptions or empirical approaches. Sobol method is a robust and high-performance (Burhenne et al., 2011) variance-based GSA for which all input parameters are varied over the whole parameter space (Sobol, 2001). The analysis produces first-order indices that determine the impact (percentage) of the variance of an input parameter on the model output, second-order indices that measure the interaction between two parameter variances, and total-order indices that determine the overall effect, including interactions that a parameter variance has on the entire model output. The suitability and strength of GSA for geoscience applications with the Python library SALib has been demonstrated in several studies, e.g., (Jessell and Valenta, 1996; Konrad et al., 2021). To formulate the problem for Sobol analysis, we defined uncertainty ranges for each input parameter set, then chose a realistic statistical distribution for each set and sampled it according to Saltelli's extension of the Sobol sequence (Saltelli et al., 2008, 2010). SALiB allows to specify the parameter sets as four basic distributions, which are rectangular, if all parameters within the set are equally likely, or triangular, normal or lognormal, if the parameter is non-uniformly distributed.

4.2.3.1 Parameterization of Borehole Radius a

For the borehole radius, a triangular distribution was assumed, with the minimum and mean value as the borehole radius resulting from the respective well section diameter and the maximum value being an additional 0.03 m, which is possible due to outcrops but rare in our study area.

4.2.3.2 Parameterization of Thermal Diffusivity κ

The applied correction methods FM and 1BHTM require the thermal diffusivity κ as a bulk value for the whole borehole system (drilling mud/formation). κ is dependent on the specific geological setting and cannot be measured downhole. Thus, it must be estimated. To choose a realistic min/max range we researched literature values for the bulk thermal diffusivity of carbonate and sedimentary rocks as found in our study area of the region of the Bavarian Molasse Basin. Of those we found a minimum value of $1.5 \cdot 10^{-7}$ m²/s assumed from numerical tests and statistical data in (Agemar, 2022b) and a maximum value of $6.8 \cdot 10^{-7}$ m²/s in (Goutorbe et al., 2007). Other values we researched (Team GeoMol, 2015; Leblanc et al., 1982; Middleton, 1979; Luheshi, 1983; Bullard, 1947) lie in between these extrema.

We varied κ between $1.5 \cdot 10^{-7}$ m²/s and $6.8 \cdot 10^{-7}$ m²/s in agreement with the researched literature values and distributed them uniformly by a rectangular type.

4.2.3.3 Parameterization of Shut-in Time t_s

The shut-in time t_s is a required parameter for any correction scheme. From the selected range for κ, we calculated the minimum shut-in times for which the stability criteria eq. 4-2 is still met. This is true if the squared radius a^2 in the left term of eq. 4-2 is smaller than four times the product of t_s and κ in the right term of eq. 4-2. The calculated minimum shut-in times are shown in Table 4-3 for the extrema of the κ range.

Figure 4-4 shows that the data set is represented well at the smaller borehole sections (8.5 inches, 6.25 inches, 6 inches) for which the majority of reported shut-in times exceeds the calculated minimum shut-in time at minimum κ. For 12.25 inches 25 %, for 17.5 inches only 3 % and for 23 inches no BHT data are represented.

The recorded maximum shut-in time of all BHTs in the data set was 170 000 s, and the minimum and maximum hold-up times between a previous and a subsequent recording were 1800 s and 125 000 s, respectively. For GSA, we therefore varied the first recorded shut-in time between each minimum value of Table 4-3 (depending on the borehole radius used) and 170 000 s. For every subsequent measurement, the respective shut-in time must be larger than the previous. To represent this in the GSA, we filtered the data set for cases showing more than one BHT per depth and calculated the deltas and implemented the second and third values as a positive delta (*delta_ti*) to the respective preceding value. The range for *delta_t1* and *delta_t2* were subsequently set to minimum waiting time from the previous measure of 1800 s and maximum waiting time 125 000 s and distributed uniformly.

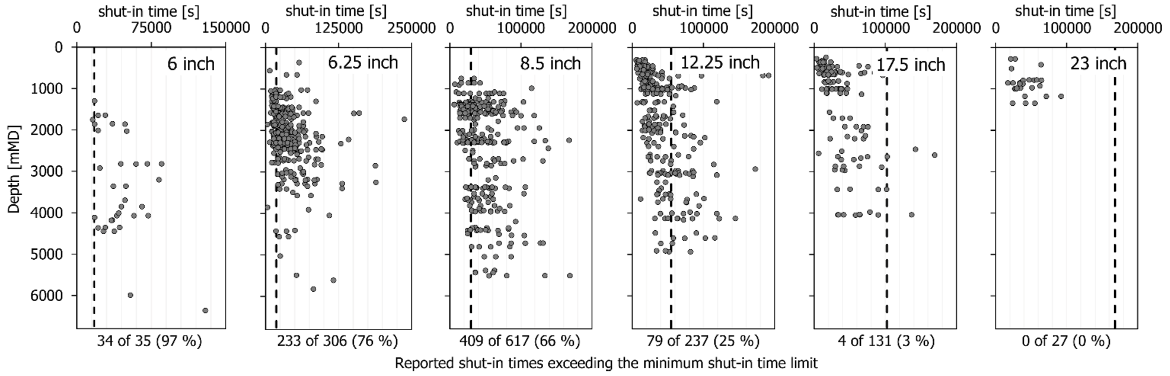

Figure 4-4. Shut-in times versus depth for the different borehole sections with varying radius a of the Bavarian Molasse Basin data set. The black dashed line marks the calculated limit over which the BHT correction stability criterion $a^2 < 4 \cdot \kappa \cdot t_s$ is still met for the respective borehole diameter when κ is $1.5 \cdot 10^{-7}$ m²/s. Below each subplot, the representation of the data set for the stability criterion is indicated by a percentage.

4.2.3.4 Parameterization of Measured In Situ Temperature BHT

The BHT value is a required input for any correction scheme. Although the BHT was correctly and accurately reported in the field after the geophysical logging run was performed, it is still subject to a measurement error due to the uncertainty of the tool. The uncertainties of common temperature gauges used at logging tools are in the range of ± 2 °C (Steingrimsson, 2013) or ± 3 % (kind note of the service company Weatherford). For the GSA, we chose each initial BHT as a representative value for each well section from the data set (6 inches: 90 °C, 6.25 inches: 70 °C, 8.5 inches: 66 °C, 12.25 inches: 55 °C, 17.5 inches: 49 °C), and set the ranges for the input parameters in a conservative manner with an assumed error of ± 3 %. We distributed the BHT uniformly as a systematic measurement error is equal likely within the error range. As in a row of measurements, subsequent BHTs are expected to be higher than those previously measured, we had to reflect this in the GSA.

Consequently, we implemented subsequent BHTs as a positive delta (*delta_iBHT*) to the respective preceding BHT with a range of 0.5 K to 36 K, which was derived from the data set after filtering for cases showing more than one BHT per depth.

Table 4-3. Calculated minimum shut-in times for which the stability criterion is still met when κ is varied between $1.5 \cdot 10^{-7}$ and $6.8 \cdot 10^{-7}$ m²/s.

Φ Bit Size (inch/m)	**a^2 (m²) (with Additional 1 Inch Due to Outcrops)**	**t_{min} (s) for $\kappa_{min} = 1.5 \cdot 10^{-7}$ m²/s**	**t_{min} (s) for $\kappa_{max} = 6.8 \cdot 10^{-7}$ m²/s**
23.00/0.58	0.1008	168 010	37 061
17.50/0.44	0.0613	102 218	22 548
12.25/0.31	0.0328	54 587	12 041
8.50/0.22	0.0178	29 637	6538
6.25/0.16	0.0110	18 296	4036
6.00/0.15	0.0103	17 204	3795

4.2.3.5 Parameterization of Circulation Time t_c

The circulation time t_c is a required parameter for HM and BM. For the given data set of the Bavarian Molasse Basin (see Figure 4-2 and Table 4-1), the circulation time has been reported in very rare cases. From the few drilling reports on hand, it appears that the average minimum circulation time is about two hours and increases with the depth of a well. A relation of depth and circulation time seems to be recognizable, since we know that a higher volume requires a longer cleaning period and in general a longer subterranean intervention, which increases the thermal disturbance. In previous studies, an estimation in the form of eq. 4-8 was applied, assuming an increase in t_c by two hours per 1000 m depth (Team KLIP, 2012):

$$t_c\ (s) = depth\ (m\ MD) * 7200\ (s). \qquad \text{(eq. 4-8)}$$

However, in order to represent a broad spectrum of possible circulation times in the GSA, we initially chose a wide range with 3600 s and 144 000 s as extrema and the 7200 s as the most frequent value known from drilling reports as the peak of a triangular distribution.

4.2.3.6 Parameterization of Mud Temperature T_m

The mud temperature T_m is one of the input parameters for the LM and 1BHT-correction scheme. In rare cases, mud reports that provided information about the inlet and outlet temperatures of the drilling mud, the respective drilling depths, and pumping rates, were available. As Figure 4-5 shows, a linear regression is in our case not suitable for the prognosis of the mud temperature, as only little of the data are represented by the regression.

The mean of all mud outflow temperature values at hand is 54 °C. As the heat loss or gain between drilling depth and the surface is unknown, an estimation of the mud temperature from the outflow temperature is prone to unknown errors. Therefore, we applied a broad range of 24 to 80 °C, covering the known drilling fluid outflow temperatures from the data set and implemented the distribution of the parameter in a triangular form with 54 °C as the peak value and 24 and 80 °C as the minimum and maximum values, respectively.

4.2.3.7 Summary of the Variation of the Input Data

The resulting variances of the inputs built the basis of the parameter space for the Sobol analysis. Table 4-4 summarizes the origin of the uncertainty of the different input parameters and their designation in the model.

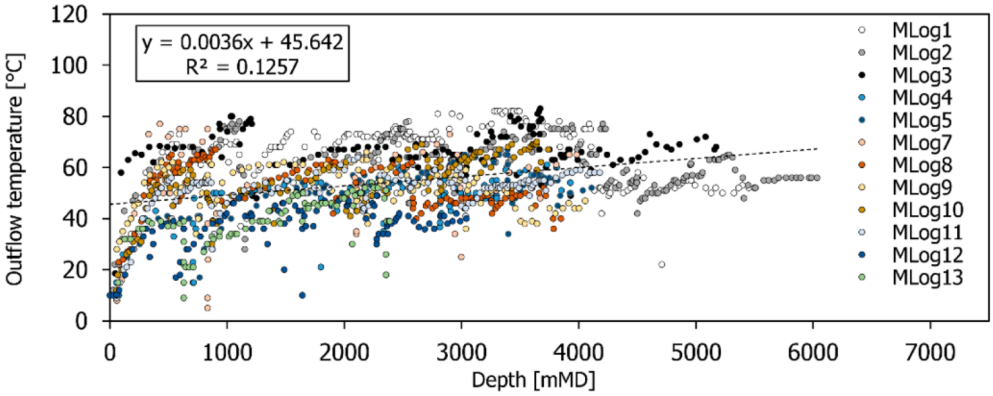

Figure 4-5. Outflow temperatures from mud logs in the Bavarian Molasse Basin. The different colors represent 13 different wells.

4.2.3.8 Sampling and model convergence

The convergence of the GSA model solution had to be proven after every Sobol model run. For this, we repeated the Sobol analysis for increasing sample numbers until we found a stable solution (e.g., where the Sobol total order index did not change anymore as depicted in Figure 4-6). The required number of samples to achieve convergence varied between 10 000 and 90 000 for our models, depending on the number of input parameters, see, e.g., (Herman and Usher, 2017).

Table 4-4. Applied ranges for all input parameters for the uncertainty analysis. The last column lists the respective input parameters with their individual designation.

Parameter	Applied Uncertainty	Variance Range as [;]	Labelling for Analysis
BHT value	Accuracy of measurement tool and rounding error	[BHT · 0.97 ; BHT · 1.03]	*1st_BHT, delta_1stBHT, delta_2ndBHT*
First shut-in time	Minimum: shut-in time for which stability criteria are still fulfilled, Maximum: from data set	[minimum time ; 170 000 s]	*t1*
Subsequent shut-in times	From data set	[1800 s ; 125 000 s]	*delta_t1, delta_t2*
Radius	+ 1 inch possible due to possible outcrops	[radius ; radius + 0.0254 m]	*radius*
Circulation time	Unknown, parametrization over whole parameter space of data set (Drilling reports at hand)	[3600 s ; 144 000 s]	*tc*
Mud temperature	Unknown, parametrization over whole parameter space of data set (Mud reports at hand)	[24 °C ; 80 °C]	*Tm*
Thermal Diffusivity	Unknown, parametrization over a wide range from literature	[$1.5 \cdot 10^{-7}$ m²/s ; $6.8 \cdot 10^{-7}$ m²/s]	*kappa*

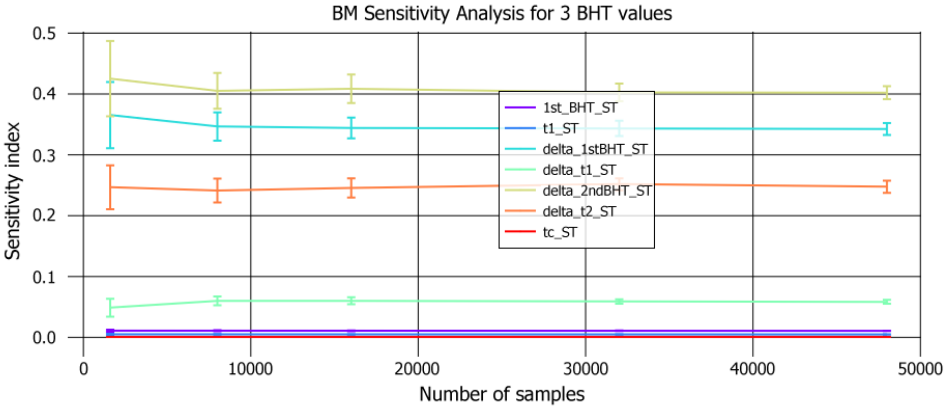

Figure 4-6. Proof of convergence of a Sobol model run using Brennand's method for three BHT values. The abbreviations in the legend refer to the total order index of the first measured BHT and respective shut-in time (1st_BHT_ST, t1_ST), the increase in temperature from first to second BHT and the respective shut-in time gone by (delta_1stBHT_ST, delta_t1_ST), the increase in temperature from second to third BHT and the respective shut-in time gone by (delta_2ndBHT_ST, delta_t2_ST) and the circulation time (tc_ST).

4.2.4 Uncertainty Study

To quantify the uncertainty for each method, wells were chosen for which both the target value (the SFT from available continuous TLog, respective DTS data from SLS TH4) and the quality of the input data set were well known. The available TLogs were measured after a minimum of 2 months of no circulation. With such long shut-in times, we assumed that temperature equilibration was at an advanced stage and the logs reflect the approximate undisturbed formation temperature in the well. We developed the Python Script BHT_Unct that contains the introduced correction schemes HM, BM, LBM, FM, LM and 1BHTM and uses Saltelli's extension of Sobol sequence sampling to create the parameter space. We proceeded with a parameterization of the input parameters similar to that for the GSA (Table 4-4), except in cases where additional or more detailed information was available. For example, if there were drilling reports available, we took the circulation time from there with an estimated uncertainty of 3600 s to respect rounding and imprecise reporting. If there were mud reports at hand, the mud temperature was estimated from the reported outflow temperatures. For shut-in time, we took the reported values from the respective BHT measurements and rated the accuracy of the reported values. In the absence of a decimal place, it was assumed that the value was imprecisely documented. Then an uncertainty of ± 7200 s was applied to make a conservative estimate and to account for possible rounding errors. Shut-in times reported with a decimal place seem to be measured with more caution, and we respected this by specifying a higher quality with a lower uncertainty of ± 3600 s. This was the case for well no. 3 and no. 7.

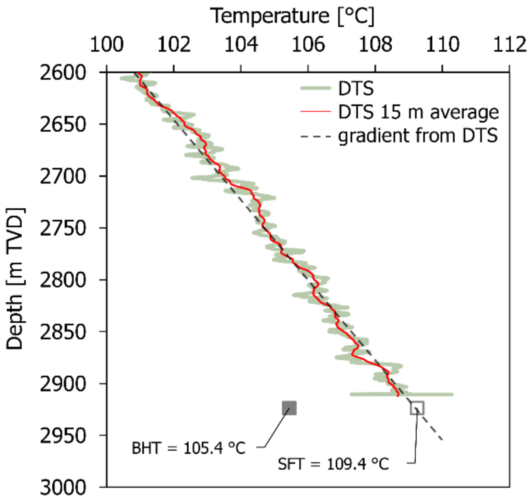

Figure 4-7. Fiber optic temperature log in SLS TH4 with BHT data at 2950 m with shut-in time of 86 400 s. The bold red line is a DTS profile measured after the well has been shut for 16 months with a spatial sampling of 1 m. The thin red line is the same DTS profile averaged over 30 m. The dashed line is the assumed reservoir gradient, derived from DTS.

The criterion that consecutive BHT measurements increase in temperature and shut-in time had to be met. After the uncertainty ranges are created, the parameter spaces may overlap, which may result in the parameter space sampled by Saltelli not satisfying this constraint. In this instance, the overlap region was therefore trimmed equally from both sides.

After we ran the different models, we studied the distribution of the model result space to find the uncertainty as the deviation from known SFT. The percentiles for which 10 %, 50 % or 90 % of the data lie within (p_{10}, p_{50}, and p_{90} limits) were chosen to describe the distribution of the values in a probabilistic way. In this context, the p_{50} limit describes the median of all calculated values in the distribution and can be used as the expected value. The p_{10} and p_{90} value can be used as a worst-case and best-case prediction, respectively.

We examined seven wells (well no. 1 to well no. 7) with known SFT from TLogs and DTS for 1BHTM, for which only one BHT value was measured, and the stability criterion eq. 7-2 was met. An overview of the wells, the available BHT and SFT data, is given in Supplementary 4 - 1. Figure 4-7 shows exemplary the data set of the well SLS TH4 with fiber optic temperature data (16 month of shut-in well) and one BHT (105.4 °C) with a reported shut-in time of 86 400 s available at the bottom of the reservoir section.

From these data, it is concluded that the SFT at the respective depth is 109.4 °C. To provide a more robust analysis, BHT data from a nearby well at the Schäftlarnstraße site was also included. To investigate the uncertainty of methods that require more than one BHT per depth, the available data limit the analysis to two wells (no. 8 and no. 9, see Supplementary 4 – 2) for which a long-term temperature log over the shut-in period is available and for which the reported shut-in time is large enough to meet the stability criterion. The temperature log of well no. 8 was measured two years after the last circulation; for well no. 9 a temperature log of a nearby well in

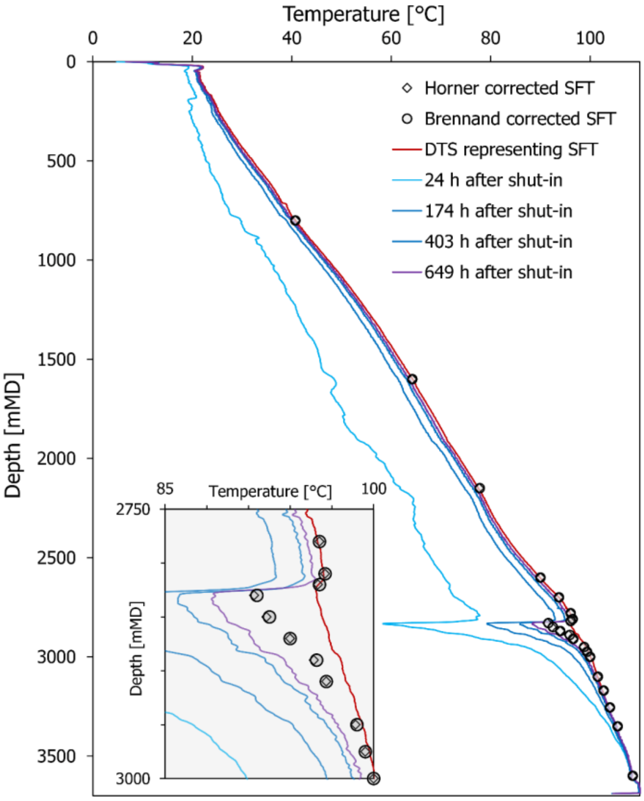

Figure 4-8. DTS profiles measured before (red line) and after (blue lines) a cold-water injection test at the well SLS TH4. The grey box shows the profiles at the top interval of the reservoir section. Point data are Horner corrected (diamonds) and Brennand corrected (circles) temperatures from temperatures read from the blue DTS profiles.

2300 m distance was used that was measured after 2 months of shut-in. For well no. 8, the two BHTs were measured at 2240 m depth, where the SFT from TLog is assumed at 66.50 °C; for well no. 9, two BHTs were available at 1492 m MD depth, where an SFT of 81.25 °C was derived from the nearby TLog.

The application of the LM is restricted for these examples as it is designed for at least three BHTs at one depth. Therefore, a series of four BHTs at 2355 m MD in well no. 8 was used to analyze the uncertainty of LM. The TLog available in well no. 8 is incomplete and does not cover the depth at which the four BHTs were measured. Without known SFTs the uncertainty of the LM method cannot be quantified, but it can be estimated in a qualitatively way by comparison with other correction methods applied to the four BHT series (e.g., FM and BM that have been studied before at well no. 9 and the two available BHTs in well no. 8 at 2240 m depth and known SFT).

4.2.5 BHT Correction at Flow Zones

We studied correction methods that are based on conductive heat transport process only. It is well known that, for example, Horner's method fails in the presence of strong convective processes, since the formation then takes longer to reach complete temperature equilibrium

(Ascencio et al., 1994; Sarmiento, 2011; Poulsen et al., 2012). To conclusively assess the quality of a BHT correction using conventional methods, one should consider convective zones in the wellbore to ensure that the corrected BHT is not within one. To do so, the fiber-optically monitored well SLS TH4, which has a highly active hydraulic zone between 2820 m MD and 2900 m MD (Schölderle et al., 2021), was studied. We took DTS profiles that were measured after a 24 h lasting cold-water injection and applied Horner's and Brennand's method on temperatures at different depth intervals from different times after injection (10 800 s to about 2 340 000 s shut-in time). As Figure 4-8 shows, the corrected values above 2800 m MD and below 2950 m MD are close to the undisturbed DTS profile but have a high deviation (up to 4.2 K) from the undisturbed DTS profile in the known convectively dominated zone.

4.3 Results

We applied the GSA at the borehole sections 6 inches, 6.25 inches, 8.5 inches and 12.25 inches, as the underlying parametrization is not representative for our data set at the 17.5-inch section and 23-inch section (see Figure 4-4). We completed the GSA for all six methods for up to three available BHT per depth. The total order indices are shown in Figure 4-9, classified by the graphical methods (HM, BM, and LBM) and the analytical methods (LM, 1BHTM, and FM).

For all graphical methods, the circulation time has low sensitivity (total order index < 0.1). The sensitivity of shut-in time is in general higher (the total order index of second and third recorded value is between 0.25 and 0.5 for HM, BM and LBM) than the BHT value (the total order index is maximum 0.3 for the second BHT measured for HM). For the 6-inch, 6.25-inch, and 8.5-inch radii, the results are very similar, whereas for 12.25 inches, the first measured shut-in time appears to be less sensitive than for smaller borehole radii. In general, the chosen range/uncertainty of the shut-in times has a larger impact than that of the BHT values (especially the second and third measured shut-in times, which have a total order index for HM and BM between 0.25 and 0.5, and the first measured shut-in time for LBM, which has a total order index of about 0.6).

For all analytical methods the borehole radius has low sensitivity (total order index < 0.1). In general, the FM tends to be more sensitive to the shut-in time (especially the third measured one with a total order index up to 0.7) at the chosen range/uncertainty of the input, whereas the LM tends to be more sensitive to especially the second measured BHT value (total order index up to 0.62). The outcomes of both methods are stable for each section where the GSA was applied. In contrast, we see a varying sensitivity of 1BHTM in the different sections. The sensitivity of the mud temperature is lower at the 6-inch section (total order ~0.25) and higher at larger radii (e.g.,

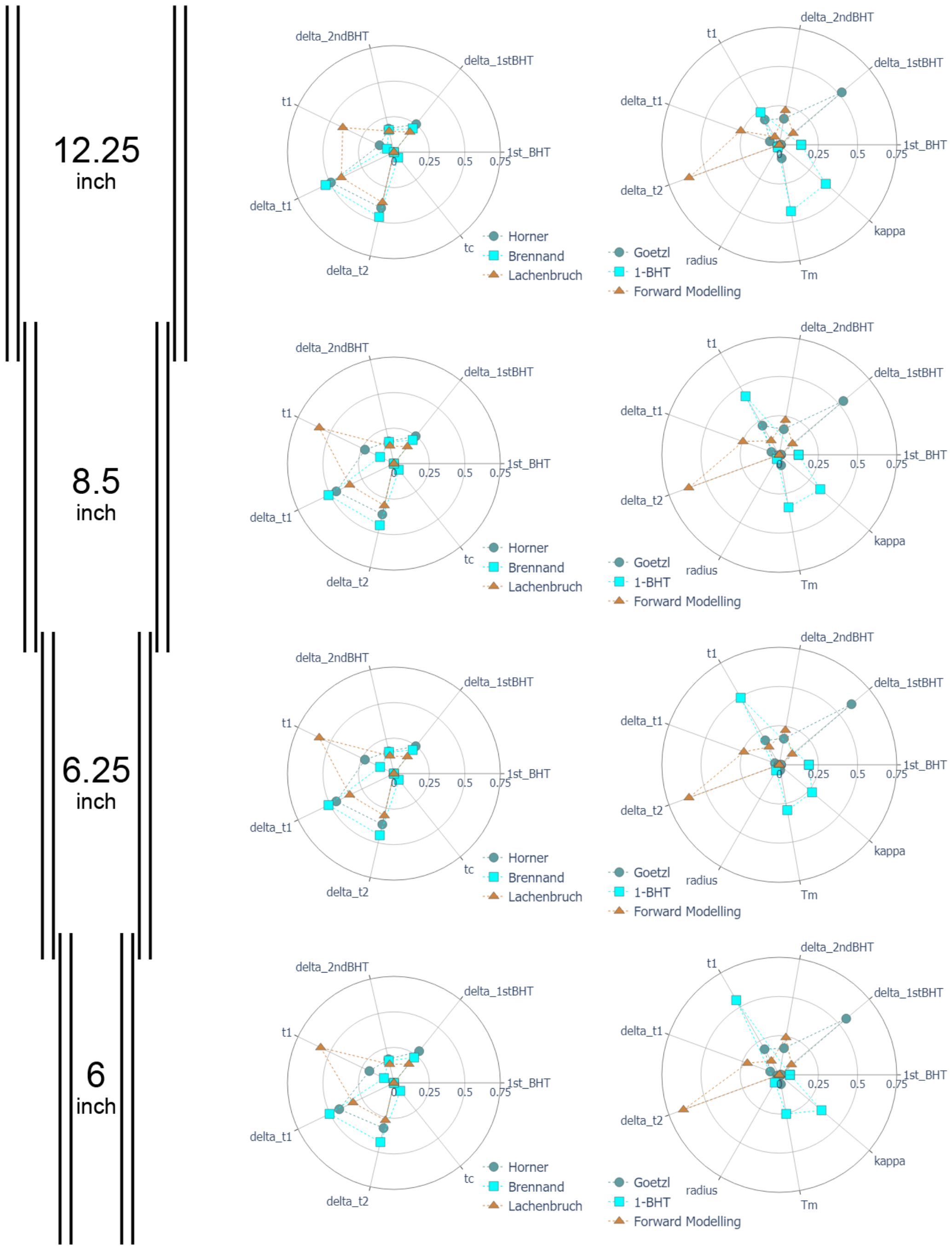

Figure 4-9. Results of the GSA structured by borehole sections. Shown are Sobol total indices for each relevant input parameter. The margin of the total order index corresponds to the importance of the respective parameter to the model output. The diagrams on the left show the methods that are solved graphically, those on the right the analytical methods. The abbreviations refer to the first measured BHT and respective shut-in time (1st_BHT, t1), the increase in temperature from first to second BHT and the respective shut-in time gone by (delta_1stBHT, delta_t1), the increase in temperature from second to third BHT and the respective shut-in time gone by (delta_2nd^{d}BHT, delta_t2), the circulation time (tc), the mud temperature (Tm) and the bulk thermal diffusivity of the system mud/borehole (kappa).

at 12.25 inches total order ~0.4). The reverse is true for the measured shut-in time (total order > 0.5 at 6 inches and ~0.25 at 12.25 inches). The sensitivity of the thermal diffusivity is between total order 0.25 and total order 0.38 for all sections. Compared with those three input parameters, the BHT as an input value has less influence on the result (total order < 0.25 at all sections).

4.3.1 Uncertainty of 1BHTM

Input parameters to 1BHTM were the measured BHT, the shut-in time, the borehole radius, the thermal diffusivity and the mud temperature. Given the uncertainties that must be assumed for the individual inputs, we can describe the total uncertainty of each solution as a deviation from the static formation temperature. The resulting ranges of the Sobol uncertainty analysis are shown as density and box plots in Figure 4-10 for the seven observed wells at different variances for the thermal diffusivity κ.

For the first plot from the left in Figure 4-10, κ was varied as in the GSA ($1.5 \cdot 10^{-7}$ m^2/s to $6.8 \cdot 10^{-7}$ m^2/s); in the second and third plot κ was set to different base values and varied by 50 %. In all observed cases, the SFT lies in between the p10 and p90 limit of the results. The maximum deviation of the result at base values from the respective SFT for $\kappa = 3.0 \cdot 10^{-7}$ m^2/s is 8.3 K for well no. 6 and the minimum deviation is less than 0.5 K for well no. 4. The largest range between p10 and p90 limit was modeled at 31 K for well no. 5.

4.3.2 Uncertainty of Corrections for at Least Two BHT at One Depth

To investigate the uncertainty of the HM, BM, LBM and FM correction schemes, we performed model runs for two geothermal wells (no. 8 and no. 9), for each of which two BHTs and an undisturbed TLogs covering the depth of the measured BHTs were available. Figure 4-11 and Figure 4-12 show box diagrams and density plots of the result spaces for each model with its p10, p50 and p90 limits (first, second and third black dashed line), its modal value (gray line), the respective SFT (red dashed line), and the calculated value when the particular model is run without varying the input parameters (blue dashed line).

From the graphical methods shown in (a), (c) and (d) of Figure 4-11 and Figure 4-12, it can be observed that BM outperforms HM and LBM as the p50 value has a smaller deviation of 1.4 K (well no. 8), respective 2.05 K (well no. 9) from the SFT compared with 3.1 K and 3.5 K for LBM and HM. The range between p10 and p90 however, is larger at 10.3 K (well no. 8) and 13.6 K (well no. 9) for BM compared to 7.5 K (well no. 8) and 11.8 K (well no. 9) for LBM and HM.

The ranges between p10 and p90 for FM are in the same order of magnitude as for BM, as well as the deviation of p50 from SFT, which is 2.0 K at well no. 8, respectively 2.1 K at well no. 9.

The Linearization method LM was tested in well no. 8 on a BHT data set with four independent measurements in comparison to the BM and FM correction schemes, as shown in Figure 4-13.

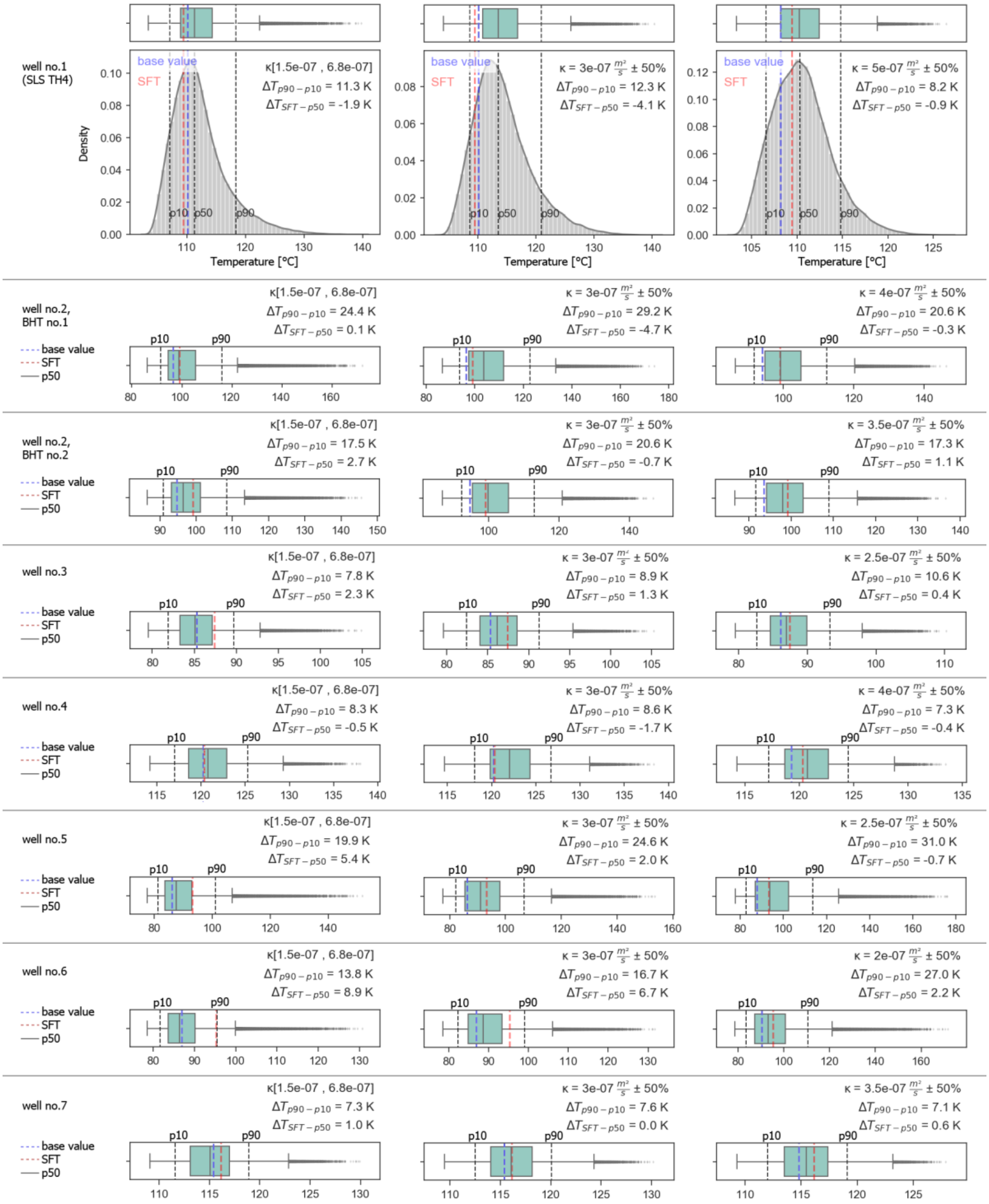

Figure 4-10. Corrected BHTs after running the 1BHTM with Saltelli sampling displayed as box plots. For well no. 1, the results are also shown in a density plot. SFT is shown as red dashed line. p10, and p90 value are shown as first and second black dashed line. p50 (median) is displayed as grey line in each box plot and the result at base value is displayed as blue dashed line.

Since the four BHTs were taken at a depth where there was no TLog, as this extended to only 150 m above the measured values, the accuracy of the LM method was evaluated in comparison to the FM and BM methods. Their uncertainty was previously investigated in the same borehole

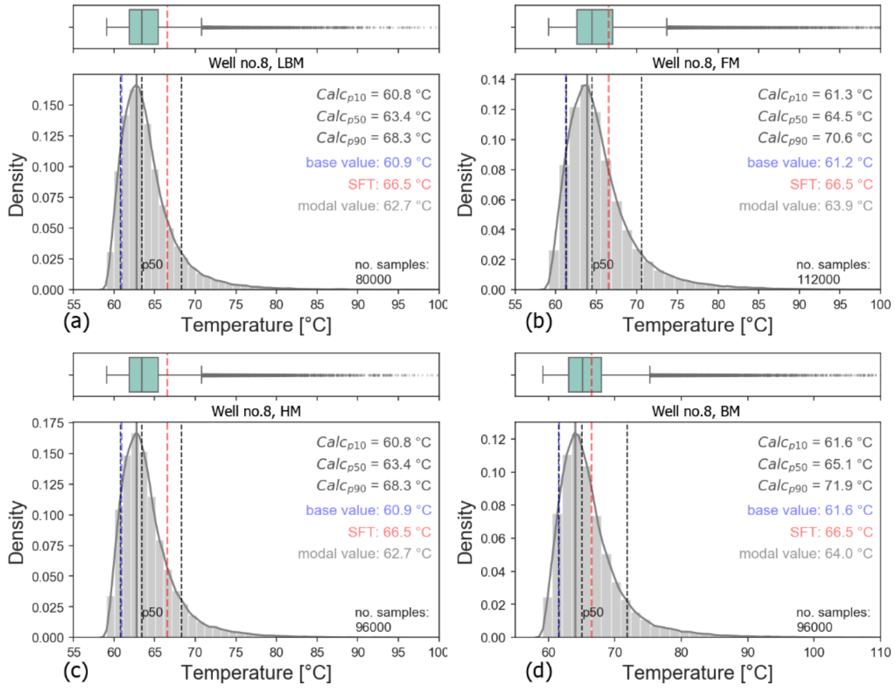

Figure 4-11. Distribution of corrected SFT at well no. 8 for five conventional methods (a): Lachenbruch and Brewer method LBM, (b): Forward modeling FM, (c): Horner plot method HM, (d): Brennand method BM. The SFT has been read from an undisturbed TLog with a shut-in time of approximately 2 years. A boxplot is included above every subplot with the SFT as the red dashed line.

using a series of measurements with two BHTs (Figure 4-11 and Figure 4-12). LM appears to have the closest p10 – p90 range of the three methods with 5.4 K in comparison to 5.5 K for BM and 6.7 K for FM. The calculated base value is of the same order of magnitude for all three methods; however, BM and FM seem to tend toward a higher deviation of the value at p50 limit from the base value.

4.4 Discussion

By combining the findings of the GSA and the uncertainty analyses, we can make recommendations for temperature prediction from BHT data. From the sensitivity study (Figure 4-9), it can be concluded for the Bavarian Molasse Basin that the choice of the correction method to be applied should be made depending on the quality of the input data set of the individual wells. If the reported shut-in time is assumed to be reliable, both Forward Modeling FM and Brennand method BM work well. If the reported shut-in time is likely to have a high uncertainty, it is recommended to use the Linearization method LM if at least three valid BHT values are available. The 1BHTM correction scheme should be used only if there is not more than one consecutive BHT available. Figure 4-14 shows proposed decision-making as to which method to apply depending on the number of available consecutively measured BHT values and uncertainty of the given input parameters.

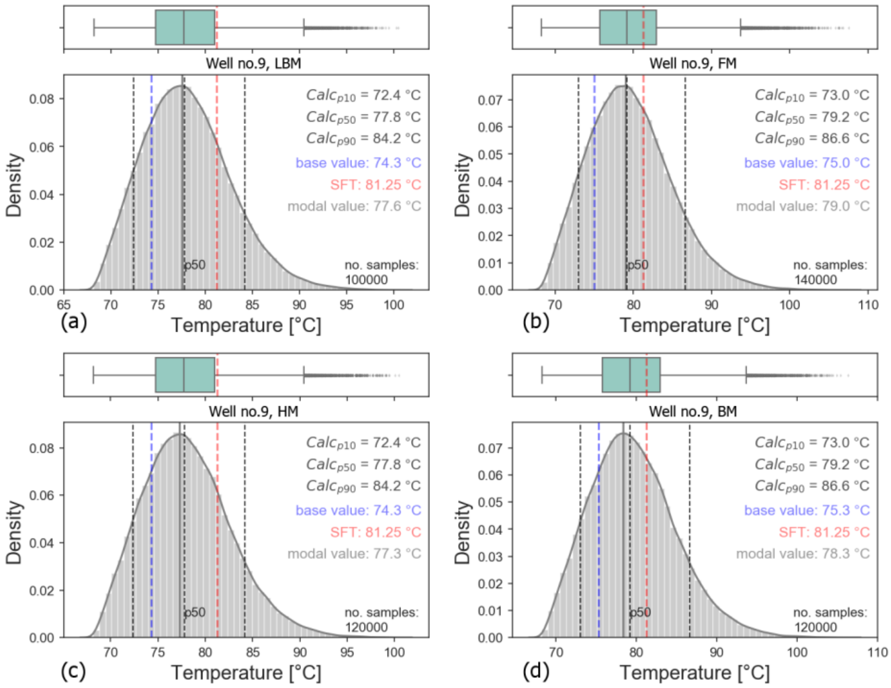

Figure 4-12. Distribution of corrected SFT at well no. 9 for six conventional methods (a): Horner method HM, (b): Forward modeling FM, (c): Lachenbruch and Brewer method LBM, (d): Brennand method BM. The SFT has been estimated from a nearby (2300 m distance) undisturbed TLog with a shut-in time of 2 months. A boxplot is included above every subplot with the SFT as the red dashed line.

The correction schemes used work only under conductive conditions (see Figure 4-8). Thus, we suggest that corrected BHT values measured in the reservoir at depths where flow zones were suspected or interpreted should not be corrected using conductive BHT correction schemes.

After a method is selected according to Figure 4-14, the BHT values can be corrected with the Sobol method for given uncertainties of the input parameters. This procedure was implemented into the Python tool BHT_Unct, which is based on the Python library SALiB and can be obtained via GitHub (https://github.com/Flix-S/BHT_Unct) under an open-source GPL-3.0 license. The advantage of this approach is that the corrected values can be represented as a distribution function (as in Figure 4-10, Figure 4-11, Figure 4-12, and Figure 4-13), so that the statistical values of the density plot can be used to describe a business case (p50 of density plot), worst-case prediction (p10) or a best-case prediction (p90).

4.4.1 Sensitivities of Parameters and Correction Schemes

The results of the GSA (Figure 4-9) show that one should evaluate the data set for the accuracy of the input parameters before choosing a method to correct BHT to SFT. The different input parameters contribute to the model results as follows.

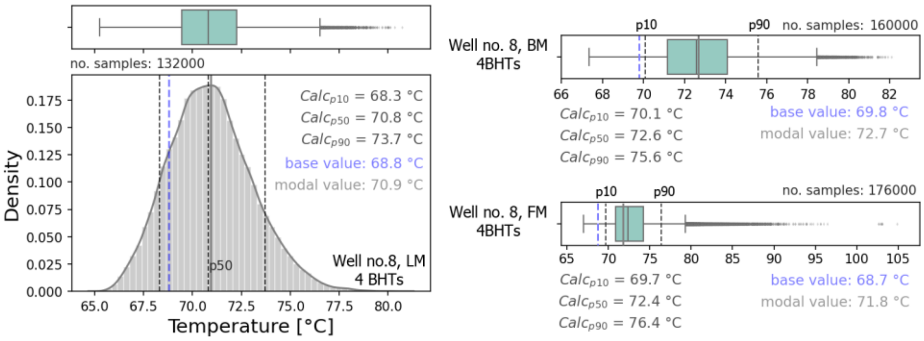

Figure 4-13. Distribution of corrected SFT at well no. 8 for the three corrections: linearization method LM (left), Brennand's method BM (middle), and forward modeling FM (right). A boxplot is included above every subplot. Due to an incomplete wireline TLog, there is no SFT information available at the depth of the BHT measurements and therefore it is not shown in the plots. The uncertainty of the LM correction scheme must therefore be evaluated by comparing the distribution of results with the other methods (BM and FM) that were previously quantified on complete data sets including known SFT.

In Figure 4-9, we showed that the shut-in times are highly sensitive in all graphical methods (HM, BM, and LBM). For HM, this is in accordance with the findings of e.g., (Shen and Beck, 1986) or (Goutorbe et al., 2007), which state that the method becomes more precise the longer the waiting time between shut-in and BHT measurement. In some studies the shut-in time was estimated using linear regression if no time was reported for the respective measurement, e.g., Agemar (2022) based on Bolotovskiy et al. (2015). This seems reasonable, since longer shut-in times can be assumed for greater depths and higher temperatures, because the duration for extracting the drilling tool and then retracting the measurement tool increases correspondingly. However, Figure 4-15 shows that a linear regression based on depth, i.e., BHT measurement, does not represent the data set of the Bavarian Molasse Basin.

Giving this fact and the high sensitivity, the use of the graphical correction schemes is not recommended if the reported shut-in time has a high uncertainty or if it is unknown.

The circulation time, which is required as input for HM and BM, has a marginal relevance with total order index < 0.1 (see Figure 4-9). Therefore, a rough estimation of this parameter following eq. 4-8 seems acceptable. Regarding the measured in-situ temperature, we showed that the second measured BHT value is more sensitive to the graphical solutions than is the first measured one. This is explained by the fact that the second value significantly influences the slope of the regression line from which the SFT is estimated (see Figure 4-9).

For the analytical methods LM, 1BHTM, FM, we can see a more diverse spread of sensitivities. The 1BHTM scheme is sensitive to t_s, T_m and κ. The borehole radius and BHT value are of minor sensitivity. As the sensitive parameters, T_m and κ are usually unknown and hard to predict, the 1BHT method should in general be avoided in cases that other methods could be applied. T_m must be estimated accurately, especially for corrections at larger radii. For FM, the shut-in times are important, especially the shut-in time of the latter measured BHTs. For LM, shut-in times have a minor role, but the measured BHT value, especially the second measured one is sensitive

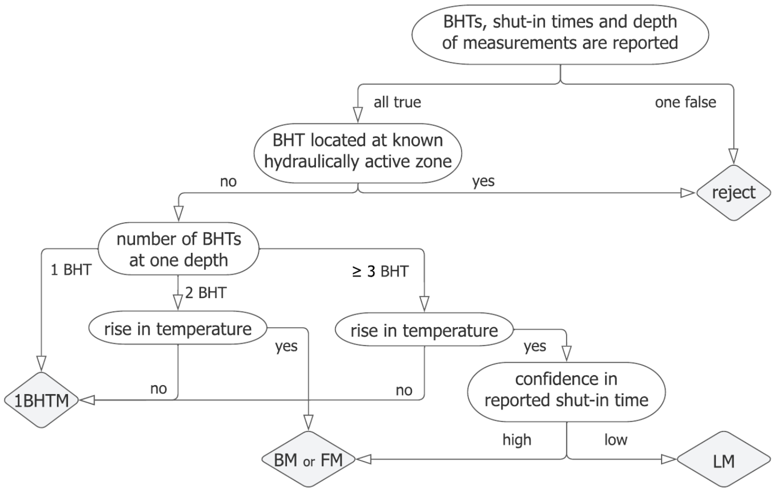

Figure 4-14. Decision tree for the choice of the BHT correction method dependent on the quality of the available input parameters.

to the model output. As an error of 3 % can always be assumed in temperature measurement (see Chapter 4.2.3.3), it is recommended to use FM or BM and, if there are doubts about the accuracy of the reported shut-in times, LM.

4.4.2 Uncertainty

For the seven wells at which the 1BHT-method was applied, we found that an underestimation of the thermal diffusivity leads to an overestimation of the SFT (Figure 5-10). An excessively low assumed thermal diffusivity means a slower assumed spread of the temperature wave during drilling. This results in too high a correction. For the exemplary studied wells in the Bavarian Molasse Basin, $3.0 \cdot 10^{-7}$ m²/s had the best fit for the thermal diffusivity. At this value, the mean of all Sobol results seems to be the estimation with the lowest uncertainty of the SFT.

The methods using two or more BHTs were tested at well no. 8 and well no. 9. In general, the maximum error of the graphical methods is high. These methods calculate the intersection of a regression line through the BHT values and the respective calculated representative time (Brennand time, Horner time, Lachenbruch time) at zero (BM, LBM) or one (HM). When two shut-in times or BHT values are varied up to their maximum assumed error (e.g., BHT1 –3% error and BHT2 +3 % error), the resulting slope of the regression line changes on large scales.

For the two studied wells we can support the statements that Brennand method performs well (Zarrouk and McLean, 2019; Sarmiento, 2011; Horne, 2016) as it outperforms HM and LBM (see Figure 4-11 and Figure 4-12). Based on the results of only the two wells, it is not possible to deduce if BM or the analytical method FM should be preferred. At well no. 8, the deviation of p50 from

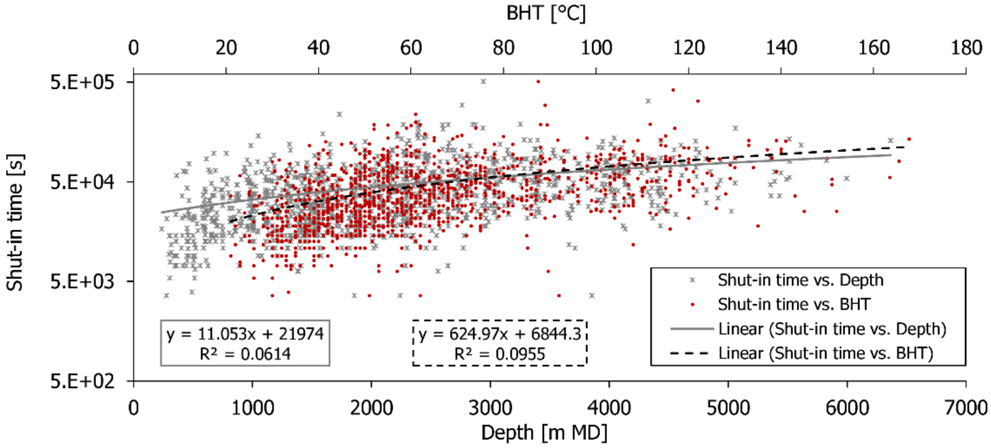

Figure 4-15. Shut-in times versus depth and BHT values.

the SFT is 2 K for FM and 1.4 K for BM, and at well no. 9, the deviations of FM and BM are equivalent at about 2 °C.

A deeper BHT data set in well no. 8, for which there was no SFT, was used to study the uncertainty of LM in comparison to FM and BM at the same data set. The distribution of results from FM and BM is similar, with a p50 value of 72.4 °C and 72.6 °C, respectively, and an 80 % uncertainty range at 6.7 K and 5.5 K (Figure 4-13). LM, in comparison, has a similar uncertainty range of 5.4 K, but its p50 value is lower by 1.6 °C and 1.8 °C, respectively (Figure 4-13).

From the uncertainty analysis, we can conclude that very large errors are possible when an unfavorable combination of input parameter variances occurs. This is most evident in the tailing of the density plots, which are up to 60 K for 1BHTM (Figure 5-10, well no. 2, BHT no.1) and about 30 K for BM at well no. 8 (Figure 4-11) for example. Such situations, however, should be recognized in the field if the available data is evaluated with caution, e.g., by filtering for temperature data or reported times that seem unrealistic for the completed logging runs or the known geological conditions at the site. Therefore, we expressed the likely error of the correction as the deviation of the most frequent value (modal value) or mean or p50 case from p10 and p90 cases, which should cover all realistic combinations.

4.4.3 Implications for Temperature Predictions in the Bavarian Molasse Basin

Only two TLogs were available at wells with more than one reported BHT per depth, and there was an incomplete data set of a well in the Molasse Basin with four BHTs at one depth and known SFT from TLog or DTS. This emphasizes the importance of the 1BHTM correction scheme for this data set. The workflow used in this study proposes to use the p50 value of the distribution of corrected temperature as a business case for temperature predictions, p10 as a worst-case, and p90 as best-case scenario. This procedure means that the corrected SFT at p50 can be specified at 80 % with an uncertainty equal to the deviation at p10 and p90.

Thus, for the wells we studied with 1BHTM at best fit for κ ($3.0 \cdot 10^{-7}$ m²/s, see Figure 5-10), 80 % of the corrected values are within a range of 29.2 K maximum (well no. 2, BHT no. 1) and at 7.6 K minimum (well no. 7). An example illustrates the relevance of these ranges of error. Assuming that the formation temperature is equal to the temperature of the produced water and that there are no heat losses along the production well, the SFT equals the production temperature T_p. With an exemplary pumping rate of Q = 0.1 m³/s, a fixed injection temperature T_i assumed to be 50 °C, and an assumed heat capacity c_f and density ρ_f of the fluid of 4181 J/((kgK)) and 998 kg/m³, the significance of the temperature uncertainty for the heat output P (W) can be calculated according to, e.g., Schulz et al. (2010):

$$P = Q \cdot \rho_f \cdot c_f \cdot (T_p - T_i). \qquad \text{(eq. 4-9)}$$

If the best-case SFT prediction (p90) is assumed to be 100 °C, the output according to eq. 4-9 is 20.9 MW. For a maximum uncertainty range of 29.2 K, the worst-case scenario (SFT p10 at 70.8 °C) is then 8.7 MW. This means a clear reduction of thermal power by 58.4 % if the worst case occurs instead of the best case. For the minimum observed uncertainty range at well no. 7, the reduction in thermal power calculates analogously to 15.2 %. The ranges for HM and LBM are lower in wells no. 8 and no. 9, at 7.5 K and 11.8 K, respectively, representing a 15.0 % and 23.6 % reduction in thermal power when the same assumptions are made for eq. 7-9 as before. The 80 % uncertainty ranges of BM and FM are in the same order of magnitude at about 10 K (20 % output reduction) for well no. 8 and 13.6 K (27.2 % output reduction), respectively. For the lower BHT data set of well no. 8, the uncertainty ranges of LM, BM and FM are also in the same order of magnitude of about 5 - 7 K, implying a reduction in thermal output of about 10 – 14 %. Such scales are of clear importance for economic and planning aspects.

However, comparing the methods is not possible by the 80 % ranges alone. Figure 4-16 examined how the 80 % ranges for the different methods change when the input parameters are assumed to have different uncertainty.

For the calculated cases on the right side of Figure 4-16, we assumed that the shut-in time was reliably documented and an uncertainty of 900 s was applied to it (shut-in time ± 900 s). The plots on the left show the calculated density plots for a higher uncertainty (shut-in time ± 7200 s). The 80 % range for 1BHTM (Figure 4-16 bottom) remains almost unchanging (15.4 K at low confidence of shut-in time and 14.5 K at high confidence), while the 80 % range of FM decreases clearly by about 7 K. This shows the overall high uncertainty of 1BHTM, even if the quality of the input data set is satisfactory. On the other hand, it also shows the applicability of 1BHTM for BHT data sets of low quality, since the uncertainty of the other methods is then not significantly higher.

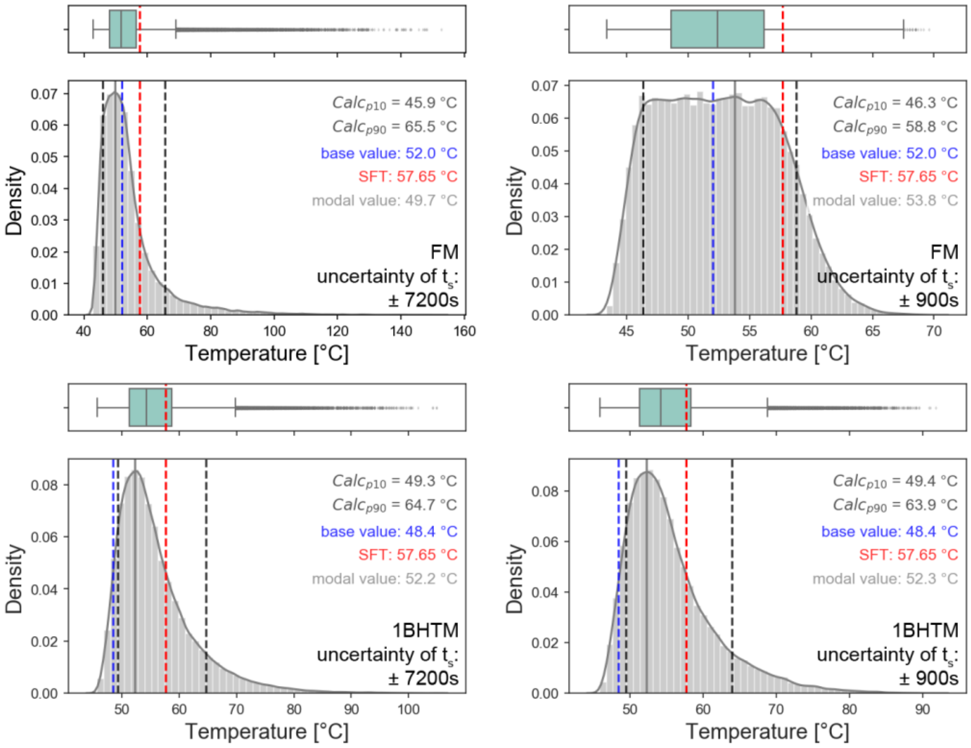

Figure 4-16. Distribution of solution after running Saltelli sampled FM (top) and 1BHTM (bottom) at high uncertainty of shut-in time with applied variance of ± 7200 s (left) and high confidence with applied variance of ± 900 s (right).

In contrast, if there is low confidence in the reported shut-in time, it is recommended to use the Linearization method LM. As the circulation time is not sensitive to the studied models HM and BM, we propose to use the simple estimation of eq. 7-8 with the approach that the circulation time should last longer with rising depth. The thermal diffusivity and mud temperature are important input parameters when applying the 1BHTM. By comparing corrected BHTs with undisturbed TLogs and DTS in the Bavarian Molasse Basin (Figure 5-10), we found a κ of $3.0 \cdot 10^{-7}$ m^2/s as a best fit.

4.5 Conclusions

The results obtained confirm the finding of former studies that accurate correction of BHT data is in most cases not possible due to the unknown errors in the input parameters. By studying the sensitivity of the commonly and widely used conventional BHT correction methods of Horner Plot, method of Lachenbruch & Brewer, Brennand's method, Forward Modeling, Linearization method and 1BHT method, we developed a workflow to adjust BHT to SFT considering parameter availability and uncertainty. Usually, the BHT-corrected values are given as defined temperatures, ignoring the error that lies within the input parameters. Instead, our method aims to provide probability scenarios (e.g., p10, p50 and p90 limits) that can be used as expected value, worst-case and best-case scenario that can be used as a business case for the successful implementation of geothermal projects. Since the thermal output of a hydrothermal well depends on production temperatures, the large uncertainty ranges that can occur are a serious concern in estimating the expectable risk to economic efficiency. In addition, the probability scenarios can be used in the evaluation of borehole data, e.g., in the correction of hydraulic parameters or calculation of hydro-geothermal parameters for which the borehole temperature must be known.

In the future, a regional representation of predicted formation temperatures can build on this approach as it allows for a valid propagation of the likely errors to be considered. Furthermore, the error-based correction workflow can be transferred to other geothermal settings when tested on known static formation temperatures that can be estimated from drill stem tests, fiber optic temperature sensing or wireline temperature logs.

Author contributions: Conceptualization, F.S. and K.Z.; methodology, F.S. and G.G.; software, F.S.; validation, F.S., G.G., F.E. and K.Z.; writing—original draft preparation, F.S.; writing—review and editing, K.Z., F.E. and G.G.; visualization, F.S.; supervision, K.Z. and F.E.; project administration, K.Z.; funding acquisition, K.Z. All authors have read and agreed to the published version of the manuscript.

Supplementary Materials: The data is available on request from the authors. The Python Script for the error based BHT correction BHT_Unct using Saltelli Sampling is available from (https://github.com/Flix-S/BHT_Unct) under an open source GPL-3.0 license.

Funding: This study has been supported by the Bavarian Environmental Agency LfU (Bayerisches Landesamt für Umwelt) in the framework of the project KompakT (grant no. not applicable).

Acknowledgments: Thanks to Stephan Haug from the Research group Mathematical Statistics of TUM for statistical consulting. Many thanks also to Florian Konrad for his help in writing and improving the Python script.

5

Monitoring Cold Water Injections for Reservoir Characterization Using a Permanent Fiber Optic Installation in a Geothermal Production Well in the Southern German Molasse Basin

This chapter was published as:

Schölderle, F., Lipus, M., Pfrang, D., Reinsch, T., Haberer, S., Einsiedl, F., Zosseder, K. (2021). Monitoring cold water injections for reservoir characterization using a permanent fiber optic installation in a geothermal production well in the Southern German Molasse Basin. Geotherm Energy, 9(21). https://doi.org/10.1186/s40517-021-00204-0

Abstract: Fiber optic sensing has gained importance for wellbore monitoring and reservoir characterization in geothermal fields as it allows continuous, spatially highly resolved measurements. Distributed acoustic sensing (DAS) and distributed temperature sensing (DTS) technologies, among others, enable monitoring of flow regimes and heat transport inside the wellbore to describe the dynamical behavior of the reservoir. The technically challenging installation of a permanent fiber optic monitoring system in a geothermal production well over the entire wellbore length was conducted for the first time at the geothermal site Schäftlarnstraße in Munich, Germany. One cable with two DAS fibers, two DTS fibers, and one fiber for a downhole fiber optic pressure/temperature gauge were clamped to ¾-in. sucker rods and installed to 3.7 km measured depth to collect data from the wellbore after drilling, during testing, and during operations. We present DTS profiles during 3 months of well shut-in and show the results of two cold water injection tests conducted to localize inflow zones in the reservoir and to test the performance of the fiber optic setup. A vertical displacement in temperature peaks of approximately 1.5 m was observed during the injection tests, presumably resulting from thermal contraction of the sucker rod–cable setup. This was verified by analyzing the strain information from the DAS records over 1 h of warm-back after cold water injection with the calculated theoretical thermal contraction of DTS of the same period. We further verified the flowmeter measurements with a gradient velocity analysis of DTS profiles during injection. Intake to the major inflow zone was estimated to 93.5 % for the first injection test, respective 94.0 % for the second, intake of flowmeter was calculated to 92.0 % for the same zone. Those values are confirmed by analyzing DTS profiles during the warm-back period after the well was shut.

5.1 Introduction

The role of renewable energy sources gains importance for climate change mitigation strategies today. About 40 % of Europe's energy demand comes from the heating sector (Kavvadias et al., 2019), for that, regions with high geothermal potential have gained much interest in recent years. To ensure the sustainable use of the geothermal reservoir, a reliable production must be ensured for which well integrity, microseismicity, or thermo-hydraulic interactions inside the reservoir are essential. Understanding subsurface formation conditions is important during drilling, as well as during the production phase, to maintain the system's integrity. Besides that, an accurate reservoir characterization remains one of the most important tasks within a geothermal project to reduce the risk of drilling unsuccessful wells (IGA Services GmbH, 2014). Hence, also a reliable regionalizing of determined geophysical properties is essential for further geothermal exploration, defining a productive drilling target, and reducing exploration and drilling risks. In this framework important geophysical properties are, e.g., permeability and porosity of the reservoir matrix and the structure of the reservoir such as fractures. Suitable conditions of these properties create influx zones that feed the geothermal well and make it productive (e.g., DiPippo, 2015). To identify and characterize hydraulic active zones, production logging tools (PLTs) are usually run after drilling. Thus, it is possible to identify the location of the flow zones as well as the quantitative contribution of flow from distinctive zones (Grant and Bixley, 2011). Most important for flow zone characterization today are spinner flowmeter that measure flow velocities in different depths of a well, from which a flow profile can be calculated. PLTs often also contain temperature tools that can support flowmeter by indicating fluid flow by temperature slope change (Schlumberger, 1997). Production logging in open-hole sections and highly deviated wells is difficult to conduct and evaluate (Ben Haoua et al., 2015) and is often not or only incompletely performed due to a high risk of getting stuck. Further characterization and spatial representation of the data can be accomplished by setting the observed hydraulically active zones in the context of lithology, porosity, and fracture analysis. Schlumberger (1997) gives a broad overview of most logging techniques which can be used to interpret feed zones and their application and interpretation. But all of these logs need well intervention and, in the case of high deviations, a rig during measurements to push the tool into the well. During production, such logs are not possible to acquire. Usually, the deepest monitoring system is the pressure gauge installed below the electrical submersible pump (ESP), which is the commonly used in offset wells for this study. Reservoir pressure commonly must be interpolated from ESP measured gauge pressure and estimated reservoir temperature and salinity data (Zarrouk and McLean, 2019). Monitoring in the reservoir is not possible for standard well designs.

To combine the concerns of a sustainable and secure reservoir management with the detailed characterization of the reservoir, comprehensive well monitoring is required that can be permanently conducted in a borehole without well intervention, hence the reservoir can be monitored even during operation. Sudden changes in pressure or temperature, e.g., thermal breakthrough) and changes of the chemical composition of the geothermal fluid, e.g., scaling processes (Baticci et al., 2010; Köhl et al., 2020) can reduce or even disrupt successful productivity and affect at least the efficiency of the operation (Zarrouk and McLean, 2019). Another important aspect is the observation of dynamic processes in flow zones, as characteristics of such zones can irreversibly change after longer production or sudden changes in pressure (Blöcher et al., 2015). Hence, monitoring the reservoir's behavior and the mentioned processes becomes important for plant operators and is also significant for production licenses provided by authorities.

However, implementation of permanent monitoring systems is challenging in production wells with an ESP, as simple wireline constructions do not allow an installation below the pump. Such type of installation must not disturb production, and well intervention must be allowed for ESP changeover without damaging or harming the monitoring system or the well itself. Permanent monitoring can be provided by fiber optic (FO) sensing, which can continuously measure physical parameters with high temporal and spatial in-depth resolution. Additionally, a FO-monitoring system installed inside the borehole to the reservoir offers the possibility of integrating a punctual pressure gauge to measure the reservoir pressure at depth and allows to avoid rough estimations based on the ESP-gauge pressure. Hence, FO-sensing enables comprehensive short- and long-term monitoring to characterize the reservoir, as well as monitoring of spatial and punctual pressure and temperature changes in the well and reservoir without intervention.

Distributed optical fiber sensors (DOFS) provide near real-time data that capture the dynamics of spatially and temporally varying downhole parameters. In addition to DOFS, fiber optic point sensors can be used to acquire relevant information at the position of the sensor with high accuracy (e.g., Kersey, 2000; Qi et al., 2002). Downhole point sensors are typically used to monitor pressure and/or temperature (P/T) at a specified depth in or above the reservoir. Point sensors are often used to acquire high accuracy data at distinct depth in downhole applications. Commonly, combined pressure and temperature sensors are applied (Kersey, 2000; Qi et al., 2002). One common type of FO sensors is Fabry–Perot interferometer (FPI) that can be used as a combined pressure and temperature gauge. The sensing principle is based on the reflection of an incident and coherent pulse generated by laser that is reflected at the interface upon entry and exit of a Fabry–Perot cavity. The reflected light interferes, and the interference pattern is linearly related to the length of the cavity (Bremer et al., 2010; Qi et al., 2002). If the cavity length changes upon pressure or due to thermal expansion, the interference pattern changes and can be analyzed. Multiplexing, e.g., two cavities in a single fiber, one insulated from ambient pressure and a second subjected to pressure and temperature, allows decoupling both phenomena if properly calibrated. Another sensor type is the fiber Bragg grating (FBG). Liang et al. (2018) give a good description of FBG type sensors - and also combinations of FPI and FBG type sensors exist (Zhou et al., 2012; Bremer et al., 2010). Fiber optic point sensors can be combined with DOFS in a single cable.

For DOFS, distributed temperature sensing (DTS) and distributed acoustic or vibration sensing (DAS) data are acquired in most existing downhole installations. Other applications are static or long-term fiber deformation using distributed strain sensing (DSS) and pressure measurements with distributed pressure sensing (DPS). DSS and DPS will not be discussed in detail here, as only DAS and DTS were realized for this study.

DTS was developed in the 1980s by Dakin and Pratt (1985), who demonstrated that Raman scattering in an optical fiber can be used for measuring temperatures. Based on either optical time domain reflectometry (Raman-OTDR) or optical frequency domain reflectometry (Raman-OFDR), temperature profiles can be acquired with a spatial resolution of about one meter and a temporal resolution of several seconds. For DTS, mostly multi-mode fibers are applied, which usually have a core diameter of 50 µm and are suitable for ranges up to 10 km (e.g., Bense et al., 2008; Smolen and Spek, 2003).

Rayleigh and Brillouin scattering have been used to measure the strain changes in an optical fiber, which is the underlying physical principle of DAS systems (Masoudi and Newson, 2016). The fibers usually used for DAS are of the single-mode type, which has a smaller diameter of usually 5 µm compared to the multi-mode type. It is suitable for longer distances, but more difficult to design and thus more expensive (e.g., Daley et al., 2013; Smolen and Spek, 2003).

5.1.1 Application of Fiber Optic Sensing in Geothermal Wells

For reservoir monitoring, accurate pressure and temperature measurement at reservoir level is key. FO-sensing is widely used in wells in the oil and gas industry for production surveillance (Bücker and Grosswig, 2017) but is still a rare technology for geothermal applications. Thus, FO-systems in geothermal wells are of concern to several scientific studies but are not yet established as a standard monitoring procedure.

5.1.2 DAS

Distributed acoustic sensing has been used in downhole applications for structural underground investigations and reservoir monitoring (Barberan et al., 2012; Cox et al., 2012). DAS has also been used to complement and substitute classical geophones in vertical seismic profiling (Daley et al., 2013; Hartog et al., 2014; Madsen et al., 2016; Götz et al., 2018) and has also potential in the field of monitoring production zones (Williams et al., 2015; Naldrett et al., 2018) and flow characteristics (Bukhamsin and Home, 2017). A broader review of DAS applications in wells is given by Lipus et al. (2022).

5.1.3 DTS

DTS temperature measurements in oil and groundwater wells, production pipelines, and mining areas are well documented in previous studies (Majorowicz and Smith, 1999; Kersey, 2000; Johnson et al., 2006; Nath et al., 2006; Brown, 2009; Inaudi and Glisic, 2010; Frings and Walk, 2011; Sanders, 2011; Ukil et al., 2012; Banks et al., 2014; Lumens, 2014; Hartog, 2017) as well as the use within the scope of borehole heat exchanger installations for distributed thermal response tests (Fujii et al., 2006, 2009; Acuña and Palm, 2013; Latal et al., 2011; Hartog, 2017; Franco and Conti, 2020). Regarding the use of DTS in geothermal wells, laboratory and field tests were carried out in the late 1980s to prove the ability of FO-techniques for temperature and pressure measurements (Angel and Hirschfeld, 2020). After that, DTS has been installed in geothermal wells for various applications, such as for testing DTS systems or assessing lithology in boreholes (Hurtig et al., 1994, 1996; Reinsch and Henninges, 2012; Reinsch et al., 2013; Förster et al., 1997; Wisian et al., 1998; Henninges et al., 2005c; Freifeld et al., 2008; Siska et al., 2016). Further, a few studies have shown that DTS-measurements in geothermal wells can identify hydraulically active zones and fracture characteristics and measure pressure profiles (Sharma et al., 1990; Sakaguchi and Matsushima, 2000; Smithpeter et al., 1999). With the same aims, DTS measurements were conducted in combination with cold water injections (Henninges et al., 2005c; Patterson et al., 2017). The installation of DTS in a geothermal production well was firstly carried out by Smithpeter et al. (1999) using small diameter stainless steel tubing. However, the measurements failed in general due to hydrogen diffusion and a low repeatability. Permanent DTS-measurements are successfully realized by installing the fiber cable behind the borehole casing, but they are then generally limited to the first borehole section (Henninges et al., 2005c; Hartog, 2017).

For monitoring the wellbore during a longer period of operation, a successful permanent deployment of a DTS system or a general FO-sensing system in a geothermal production well down to the reservoir section would be preferable.

To establish such a continuous measurement of pressure, temperature and acoustic data for monitoring the temperature development in the wellbore and in the hydraulically active zones in the Upper Jurassic reservoir of the Bavarian Molasse Basin in Southern Germany, the present study investigates the set-up of a permanent installation of a fiber optic cable in two wells (producer and injector well) at the geothermal site 'Schäftlarnstraße' in the City of Munich. Apart from the challenge of leading the FO-sensing cable beyond the ESP to the bottom of the deep borehole in order to monitor the entire reservoir section, the production well used was additionally highly deviated. Distributed temperature sensing (DTS) and distributed acoustic sensing (DAS) are successfully implemented along with temperature and pressure data from a fiber optic FPI sensor in the producer well located directly above the reservoir. Two cold water injections were conducted in this study to test the performance of the installed FO equipment and to ascertain inflow zones and compare the results with identified zones from existing flowmeter measurements. Other areas of focus included investigating the warm-back from drilling inside the reservoir to the geothermal gradient during flow-off periods, estimating the reservoir parameters with inverse methods, and testing the ability of the FO sensing setup to detect microseismicity, in case any microseismicity events occur, and to assess well integrity with respect to cementing.

5.2 Methods

We installed fiber optic cables into a geothermal production and injection well and used DTS data measured after drilling and during shut-in after cold water injection to observe the temperature distribution within the production well. To test the overall performance of the FO-installation and characterize the flow zones in the reservoir, we analyzed DTS and DAS data during two injection tests that were performed in early 2020. We further estimated an inflow profile by analyzing flowmeter data from July 2019 together with FO-DTS data from injection tests. We used temporally integrated DAS strain rate data to detect whether and how the FO-system is subject to thermal contraction/expansion.

5.2.1 Description of the Study Site Conditions and Wells

Since about two decades, the Upper Jurassic carbonates of the Bavarian Molasse Basin in Southern Germany are the target for geothermal exploration as they provide favorable geological conditions for hydro-geothermal projects (Steiner et al., 2014). The sedimentary layers of the aquifer partly show very good hydraulic properties, providing hot water with temperatures up to > 160 °C (Weber et al., 2019). Accordingly, many geothermal projects were realized in recent years, most of them in the Munich metropolitan region, which together deliver a thermal output of 322 MW and an electrical power of 35 MW — as of 2020 (Flechtner et al., 2020). Further geothermal projects are planned in the greater Munich area to reach the vision of the City of Munich having a CO_2 emission-free district heating network by 2040 (Kenkmann et al., 2017).

The Bavarian Molasse Basin is an alpine foreland basin extending from the northern alpine rim northward to the Swabian and Franconian Alb where it emerges (Meyer and Schmidt-Kaler, 1990). In the Upper Jurassic, carbonates were deposited on a carbonate platform in the Tethys Sea. Today, sequences of limestone, marl and dolostone form two different facies types, a massive reef facies with a high rock matrix porosity and a bedded facies that is composed by lower matrix porosity (Meyer and Schmidt-Kaler, 1990). As a potential aquifer, dolomitized massive facies is a preferable geothermal exploration target in the Molasse Basin (Böhm et al., 2013) and can be explored in the middle layers of the Upper Jurassic (referred to as Malm Delta and Epsilon), as well as in the uppermost layers (referred to as Malm Zeta 1 – 6). Malm Zeta is overlaid by carbonates of the Purbeck facies that formed due to evaporation as the shelf sea dried out at the end of late Jurassic (Meyer and Schmidt-Kaler, 1990; Mraz, 2019) and can also bear a potential hydrothermal reservoir (Böhm et al., 2013).

Multiple studies of the reservoir, comprising hydrochemistry analyses, overpressure conditions, and hydraulic and geophysical characterizations, pointed out that the Malm geothermal reservoir shows partly strong heterogeneous conditions in terms of changing porosity, permeability, and variable flow zones from matrix-dominated flow to prevalent fracture and karstic flow (Birner, 2013; Drews et al., 2018; Bohnsack et al., 2020b; Heine et al., 2021; Konrad et al., 2019, 2021).

Moreover, analyses of the geothermal wells in the Malm have shown that karstification and a reasonable matrix permeability, existing preferentially in the reef facies, are key factors for productivity. Faults and/or associated fracture zones seem to play a subordinate role for well productivity in the greater Munich area, but may play a dominant role in the southern part of the Molasse Basin (Wolfgramm et al., 2009; Böhm et al., 2013; Konrad et al., 2021). Hence, the identification and monitoring of flow zones and their contribution to the productivity in a geothermal well is an important factor to further characterize the reservoir and improve targeting and reservoir engineering in the Malm reservoir.

The geothermal site Schäftlarnstraße in downtown Munich, Germany, located in the middle of the Bavarian Molasse Basin, consists of six wells (three producers and three injectors) and explores the carbonates of the Upper Jurassic Malm reservoir described above as well as the overlying Purbeck formation. Malm Zeta reservoir is in a depth of 2250 to 2550 m depth below surface and the expected production temperature is about 100 °C. To improve the exploitation of the reservoir and keep distance between production and injection, all wells in this project are deviated. Two of six wells at the site were used for the installation of fiber optic monitoring systems. In well 1 (production well) cables were installed from top to the end of the reservoir section inside the wellbore and in well 2 (injection well) in the top section behind the 20-in. casing. Well 1 is completed with a 20-in. anchor casing, a 13 3/8-in. casing, a 9 5/8-in. liner and a perforated 7-in. production liner. Kick-off points of the deviated well are at 250 m MD (4° inclination), 880 m MD (44° inclination), 2220 m MD (42° inclination) and 2850 m MD (58° inclination). The total measured depth of the well is 3741 m, which corresponds to a true vertical depth (TVD) of 2947 m.

Well 2 has a depth of 4443 m MD (2722.8 m TVD) and is completed with a 20-in. anchor casing, a 13 3/8-in. casing and a 9 5/8-in. liner. The reservoir section that was drilled with an 8.5-in. bit is a completed open-hole. An overview of the completion of both wells including kick-off points is given in Supplementary 5 - 1.

Table 5-1 shows the well history for the relevant sections where the FO-system was installed in both wells. After completion, several logging runs were conducted in the reservoir section of well 1, including Resistivity Micro Image Log, Caliper, Gamma Ray, Sonic Log and Nuclear Magnetic Resonance (NMR) (only in the upper 100 m of the reservoir). Hydraulic testing with airlift started shortly afterwards. Thereafter, a production logging flowmeter temperature run was performed. The well was shut and a wireline temperature log run was performed after 3.5 months. This temperature log reaches only to 2819 m, as the tool could not pass the 7-in. liner hanger.

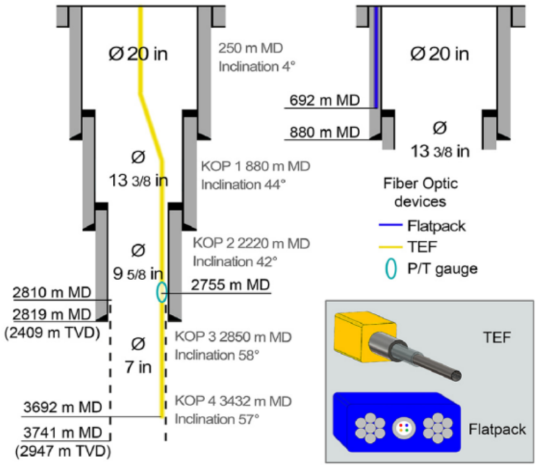

Figure 5-1. Completion of production well 1 (left) and injection well 2 (right) with equipped fiber optic cables in Munich with relevant depths and kick-off points (KOP). Blue: with bumper wires equipped flatpack cemented (gray) behind the casing in injector well. Yellow: tubular encased fiber (TEF) installed along sucker rods to TD in producer well. Turquoise: fiber optic P/T gauge. Sketches of TEF and Flatpack are shown in gray box.

5.2.2 Implementation of the Fiber Optic Monitoring System

The completion of the production well and the relevant well section of the injection well with fiber optic cables are shown in Figure 5-1.

Due to the high deviation, reaching total depth (TD) with the FO-installation was challenging. To minimize the risk and successfully land the cable, a perforated liner was installed in the reservoir section of well 1, unlike the open-hole completions done in most of the other five wells at the site. In advance of the installation, a conventional wireline temperature log was performed for comparison. At this time, a temporarily 13 3/8-in. 'tieback' liner was inside the first section of the well, which was pulled just before installing the FO downhole cable. After successful FO-installation to TD in well 1, the drilling rig was skidded to well 2. After drilling the first section, a second fiber optic cable was permanently installed behind the casing and cemented in place in well 2 (see blue 'Flatpack' line in Figure 5-1).

Table 5-1. Excerpt of the well history of well 1 and well 2

Well 1 (producer)		**Well 2 (injector)**	
Completion of drilling open hole	4 June 2019	Completion of drilling first section	24 November 2019
Logging in reservoir section	15 to 21 June 2019	Construction of FO cable	28 to 29 November 2019
Hydraulic testing	June and July 2019	Cementing first section	30 November 2019
Flowmeter logging	10 July 2019		
Wireline temperature log	23 October 2019		
Installation of FO cable	24 to 31 October 2019		
Cold water injection test 1	23 January 2020		
Cold water injection test 2	22 February 2020		

To achieve the objectives mentioned above, the installation in the second well was used to investigate the temperature distribution and evolution while cementing and the warm-back of the borehole to the geothermal gradient until the start of injection. Also the temperature distribution while injecting, as well as acoustic measurements to monitor potential microseismicity were investigated. The analysis of these measurements in well 2 are not part of this study, as it focuses on the overall performance of the FO-system and reservoir characterization, respectively, the detection of the flow zones. Hence the measurements presented and discussed in this study were carried out in producer well 1. Nevertheless, construction of the cemented FO-cable is described, as the fibers of both wells producer and injector, form one monitoring system at the site.

5.2.2.1 Downhole Cable

An installation in a geothermal well to total depth poses specific challenges to the FO-cable, as it is exposed to harsh conditions like chemical and physical stress from the high pressure and high-temperature thermal water (e.g., Smithpeter et al., 1999). To withstand these conditions, the single-mode and multi-mode fibers were specially designed for applications in oil and gas fields, providing high resistance to the harsh environment in boreholes and ensure long-term reliability, e.g., resistance to hydrogen darkening (Smithpeter et al., 1999). The fibers are protected by a 1/4-in. stainless steel tube. This tubing encased fiber (TEF, see sketch in gray box in Figure 5-1) in producer well 1 is encapsulated with 11 × 11 mm polypropylene for ease of installation and additional protection. The TEF was designed for a maximum temperature of 150 °C and pressures up to 20 kpsi (1375 bar) as per the expected well and reservoir conditions. It contains two double-ended multi-mode fibers for DTS, two single-mode fibers for DAS (one of those as backup) and one single-mode fiber for the fiber optic P/T gauge located right at the top of the reservoir (2755 m MD, see Figure 5-1). For the FO-installation outside the casing in the injector well, additional cable protection was chosen to withstand the high potential drag torque forces of the 20-in. casing during installation. This was achieved by packaging the 0.25-in. TEF with two protective 0.375-in. bumper wire in a so-called 'flatpack' (see sketch in gray box in Figure 5-1). The TEF in the flatpack contains two single-mode and two multi-mode fibers for DTS. To allow a double-ended fiber configuration, the fibers are bent 180° at a low profile. This 'mini-bend' at the bottom end of the cable enables measuring in both wells in one daisy chain system (e.g., Götz et al., 2018).

Since the fibers are subjected to less physical and chemical stress once they are routed out of the borehole, the downhole cables are connected to a simpler surface cable at the wellheads of wells 1 and 2.

5.2.2.2 Installation behind the Casing of the Injector Well

Special clamps were used to provide mechanical protection at each connection of the casing. Also, special non-rotating centralizers were used to prevent damaging the TEF during installation. During installation, cable integrity was monitored with continuous OTDR measurements. After run in hole, the casing was cemented in, with this cementing process being recorded using both DAS and DTS. The downhole TEF is connected to the surface cable using a vent-box, which protects the fiber splices is mounted to the wall of the borehole cellar.

5.2.2.3 Installation Inside Producer Well

The installation of the TEF to total depth of the producer well was planned in close cooperation with the geothermal operator. The major challenge was to design a monitoring system that would cover the entire length of the borehole, including the reservoir section, without interfering with well production and with proper routing below the ESP as well as beyond the liner hangers of each casing section. During the planning phase, the additional pressure loss due to friction of the FO-construction and narrowing of the effective flow area inside the borehole was estimated at worst case 3.5 bar. For a reservoir pressure of around 215 bar, as measured by pressure logs and confirmed by the FO-P/T gauge (see Chapter 5.2.3), this results to around 1.5 % additional loss. The main components of the FO-construction are shown in Figure 5-2.

To ensure the TEF reaches TD in a nearly straight line as well as for mechanical protection, while minimizing flow restrictions, the TEF was mounted to sucker rods (see (c) in Figure 5-2). For the first phase, these sucker rods were suspended from the tubing hanger via a crossover (see (a) in Figure 5-2). For the ESP-installation, the top sucker rods will be pulled and removed, with the remaining sucker rods then being connected to below the ESP and production tubing, ideally without breaking the TEF.

The 3/4-in. sucker rods are each 30 foot in length with four pre-installed nylon-centralizers to guide the TEF along the rods. To ensure controlled routing of the TEF from the cable drum to the rig floor, it was run over a sheave held by a crane, while the sucker rods were installed using the rigs top-drive and were torqued together via couplings to install the FO-cable from bottom to top. At every sucker rod connection, the TEF was fixated with special clamps (see (a) and (c) in Figure 5-2) and with heat-resistant plastic strips, leaving a bit of excess length to the cable to allow for thermal expansion of the sucker rods. Therefore, sucker rod length and cable length differ, requiring careful localization of the measurements. At the downhole end of the sucker rods, a carrier (length 1.42 m, diameter 0.15 m, see (d) in Figure 5-2) protects the termination of the DAS fibers as well as the pre-installed mini-bend for looping the multi-mode fibers. The centralizer at the carrier allowed a successful run-in-hole across all liner hangers. To install the P/T gauge at the desired depth directly above the reservoir, the sucker rod installation was interrupted, the TEF was cut, and the fibers were spliced to the gauge. The sensitive fiber splices were protected in a specially designed splice-carrier. The gauge and the splice carrier were

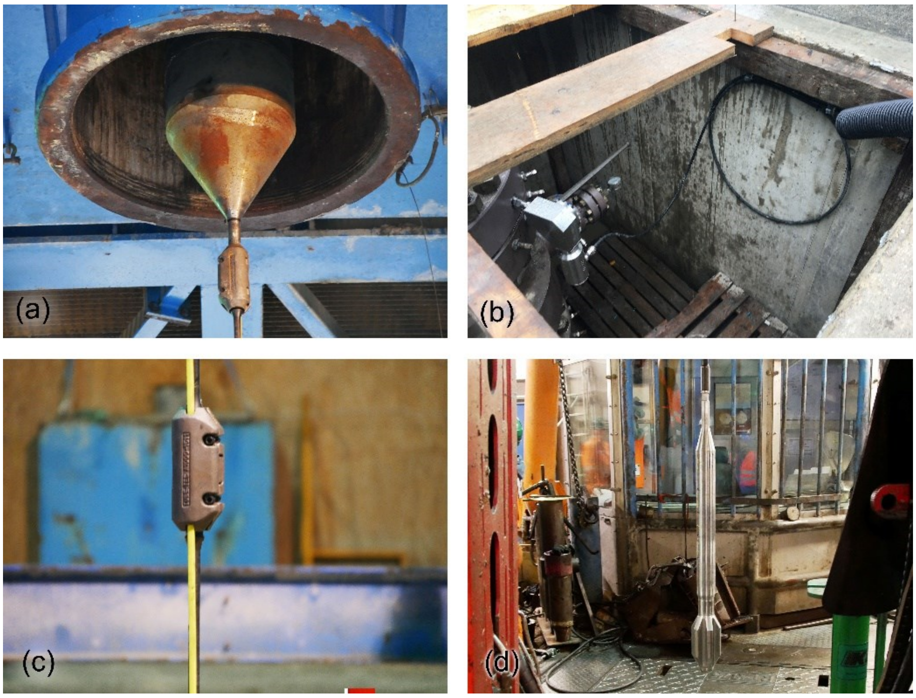

Figure 5-2. Installation of the FO-cable in the producer well. (a): ¾ inch to 13 3/8-in. crossover. (b): Wellhead outlet. (c): TEF mounted on sucker rods with clamps. (d): Carrier at termination with centralizer.

inserted in a 1.59-m-long carrier that was torqued to the sucker rods. At the top of the sucker rod string, the crossover (see (a) in Figure 5-2) was suspended from the tubing hanger. The TEF was guided on the outside of the tubing and passed through the hanger. There it was bent 90° in a controlled manner so that it could exit horizontally from the wellhead collar through the specially designed fiber optic wellhead outlet (FO-WHO, see (b) in Figure 5-2). The FO-WHO is installed on the side of the wellhead and allows the downhole fibers in the stiff TEF to be connected to the more flexible surface fiber cable via a pressure barrier. To ensure that the TEF was not damaged during run-in hole, the fibers were continuously monitored via OTDR and a 'fiber optic rotary joint' (FORJ), a connection that allows free rotation along the cable axis.

Additional direct OTDR and DTS measurements were performed at regular intervals to check the fibers' integrity, as the FORJ added noise. This surveillance detected a deteriorating splice at the P/T gauge, thus the string was pulled and the splice redone.

The installation was successfully completed in November 2019 and a first DTS profile fits to the wireline temperature log recorded 1 week before (see light gray curve in comparison to red curve in Figure 5-3 in Chapter 5.2.3).

5.2.3 Performance of the FO-System and Calibration

Repeated OTDR measurements were conducted whenever necessary to check the integrity of the fiber optic system, e.g., after completion of the installation, after repair works, or prior to specific

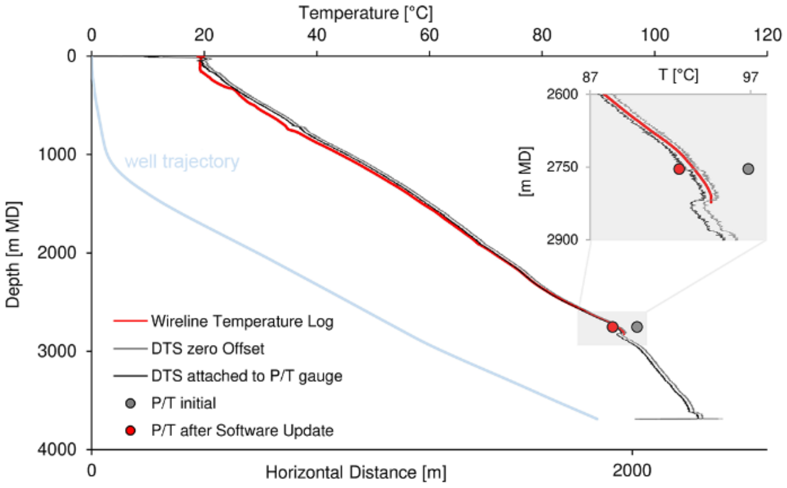

Figure 5-3. Calibrated and non-calibrated DTS profiles of the Schäftlarnstraße site in comparison to P/T gauge data before and after software update.

tests at the site. The OTDR tests showed a uniform loss of the optical power level between the splices and fiber connectors along the fiber, indicating good backscattering behavior of the cable. The splice at the *P*/*T* gauge and the splices at the wellhead produce about 0.8 dB loss. A higher loss can be observed at the mini-bend in the injector well, which is about 1.3 dB. This mini-bend had to be installed on site in comparison to the mini-bend of the TEF in producer well 1 that was pre-installed in the workshop under controlled conditions. Overall, the loss along the multi-mode fibers inside the producer well is about 0.7 dB/km, in the injector well higher with 1.18 dB/km (due to the higher loss at the mini-bend). Along the single-mode fiber, the loss is approximately 0.75 dB/km. Exemplary OTDR measurements of the multi-mode (DTS) fibers in the producer well and of the daisy-chained single-mode (DAS) fibers ending at total depth of the producer well are attached in

Supplementary 5 - 2. The OTDR measurements show that the fiber optic system allows precise DTS and DAS measurements in the deviated production well.

5.2.3.1 Resolution of FO-Measurements

A DTS interrogator, a P/T interrogator, and a DAS interrogator are installed as measurement devices at the study site. The performance of DTS depends on the temperature resolution and the spatial resolution. The laser pulse width specifies the minimum sampling interval, defined as the length increment, for which traces can be recorded. Spatial resolution, on the other hand, is the integrated distance a system needs to fully represent a temperature change (e.g., Smolen and Spek, 2003). The DTS interrogator at the study site is an AP Sensing Linear Pro Series N4386B unit with a maximum measuring range of 12 km. The unit works on Raman-OTDR backscattering. With the given configuration (double-ended fiber and measuring range of about 8 km), the interrogator allows a spatial sampling of 0.25 m at a spatial resolution of 1 m. The temperature resolution is mainly dependent on the acquisition time and increases with longer measurement times (e.g., Brown, 2003; Smolen and Spek, 2003). In our case, DTS traces are acquired every 10 min. At this temporal resolution and spatial resolution of 1 m the dispersion of DTS values in field shows to be ± 0.6 K. After averaging the data over time intervals of 6 hours the temperature resolution is about 0.13 K. This is roughly on the same order of magnitude as other reported DTS installations in geothermal wells, e.g., Henninges et al. (2005) gave a resolution of 0.06 K for their DTS installation in the Groß Schönebeck borehole (where temperature data were averaged over time intervals of 2 hours). The P/T interrogator installed at the study site is a SureView PT Gen3 unit. P/T data are acquired every second and averaged over 10 s. Resolution of the data in field shows to be 0.06 K, respectively 0.8 bar. The absolute accuracy of the P/T gauge as specified by the manufacturer is ± 5 psi (~0.34 bar). The DAS interrogator was a Silixa iDAS device that uses Rayleigh backscattered photons (phase-OTDR) by measuring the phase difference changes between the beginning and end of any section of the optical fiber (Masoudi et al., 2013). Key parameters to the performance of DAS are sampling frequency, gauge length, and spatial sampling, which were 1000 Hz, 10 m, and 1 m, respectively.

5.2.3.2 Depth Allocation

For fiber optic distributed sensing, each measurement trace needs to be located at depth (Smolen and Spek, 2003). The recorded DAS and DTS traces begin at the respective interrogator. As there are several meters of surface cable between the interrogator and the wellhead (146 m to production well, 143 m to injector well), the exact position of the well inlet on a FO-measurement must be determined. For DTS, a cooling spray was used to mark specific points on the measurements, located at short known distances from the wellhead outlet. For the injector well, the temperature marker was set 6 m before the inlet to the cementation at the bottom of the drilling cellar, 2.5 m below ground level. For the producer well, the temperature marker was 1.5 m before the wellhead outlet, which is 0.5 m below ground level. The end of the DTS traces is located at total well depth, which is known from drilling tally. For well 1, this is the length of the installed sucker rod construction, which is 3690.2 m. For well 2, the end of the traces is given as the length of the casing along which the flatpack was installed, which is 692.0 m. The recorded DTS traces are separated into surface and downhole section and further processed. Depth locations were set by linear interpolation between the wellhead and the bottom of the installation. For DAS, an acoustic knocking noise (‘tap test’) on the FO-WHO was recorded to exactly determine the surface depth reference (Götz et al., 2018). At a gauge length of 10 m with a spatial sampling of 1 m, the acoustic signal related to the tabs is spread out over several meters, which leads to a smearing over a few meters at the wellhead, resulting in an error of approximately ± 2 m.

5.2.3.3 Temperature Calibration

At the beginning of the project, it was planned to use the P/T gauge as a temperature calibration point for the DTS in the downhole section. However, first gauge measurements showed temperature values exceeding those of DTS by almost 4 K (see the deviation of the red circle and gray circle in Figure 5-3). Figure 5-3 shows the first DTS profiles compared to the incomplete wireline temperature log (the logging tool could not pass the 7 inch liner hanger, see Chapter 5.2.1) and the P/T gauge temperature data.

As DTS profiles showed good agreement with the conventional wireline temperature log run one week prior to the completion FO-installation (see Table 5-1), it was considered that the measurement of the gauge was inaccurate and there might be a problem with the gauge's hard- or software or the P/T interrogator. In early 2020 the manufacturer of the gauge delivered a software update which improved the P/T data by -4.3 K and +0.73 bar. After this, the DTS was calibrated to the gauge data at the respective depth (see dark gray curve in Figure 5-3). With that, DTS data on top of the reservoir showed to be 0.7 °C lower than the wireline temperature log. The software update of the gauge shifted the temperature values to better agreement with DTS and the independent wireline log. By aligning the wireline temperature log with repeated DTS measurements, the previous readings of the P/T gauge could be verified and corrected.

5.2.4 Flowmeter Logging

We used flowmeter analysis for hydraulic active zone characterization and compared the results with DTS and DAS data of the FO-monitoring system. Raw flowmeter data (uncalibrated) were available from a full-bore flowmeter run on 11 July 2019, with three calibration runs of each of the first and last 60 m of the reservoir section, one flowmeter log over the entire section, and corresponding temperature runs. Injection rate during the flowmeter run was 50 l/s.

Usually, flowmeter logs are run when a stable injection rate and pressure is reached, but this can sometimes not be achieved due to operational constraints. The recording of spinner responses at different logging speeds (at least three) enables to calibrate the spinner and to allow quantitative interpretation (Schlumberger, 1997). As the injected fluid enters karstified, porous and/or fractured zones, the impeller motion of the flowmeter can point to inflows and outflows at the respective depth of the tool. For this study, flow zone interpretation was done following the basic workflow of the commonly used petrophysical software environment KAPPA Emeraude (v5.20.03), which is based on interpretation techniques as described, e.g., in Schlumberger (1997). As common, only the smoother upwards run was used for interpretation. First the spinner was calibrated in a zone with constant cable speeds and spinner velocities, resulting in a spinner threshold of ± 0.818 m/min. Based on this calibration and by considering the exact borehole diameter from the caliper curve, the revolutions per second (RPS) measured by the impeller were translated into continuous rate calculation profile as a function of depth. From this injection profile, schematic inflow zones were inferred considering geological background knowledge from geophysical loggings, as a sonic interpretation using the petrophysical software package Interactive Petrophysics (4.5.5). Since no other porosity tool, e.g., density, neutron, was performed over the entire borehole section, the sonic log was used to calculate the matrix porosity of the formation. The resulting matrix porosity was cross-checked against available laboratory porosity measurements of 19 sidewall core samples from this borehole using Wyllie's equation (Wyllie et al., 1956) with matrix interval times of 47.6 µs/ft for limestone and 43.5 µs/ft for dolomite (Cannon, 2015). In addition, the flowmeter temperature log was considered, since inflows are reflected in a slope change on the temperature profile (Grant and Bixley, 2011; Zarrouk and McLean, 2019).

5.2.5 Cold Water Injection Tests

After more than 6 months of shut-in (after flowmeter run, see Table 5-1), fresh water was injected freefalling into the well to artificially disturb the temperature equilibrium of the well. The focus was to verify flowmeter data with a high temperature gradient and to record the warm-back profile with DTS, as well as listening to the acoustic response with DAS. The initial water level was about 170 m on 23 January 12:00.

The first hydraulic test took place on 23 January at 14:22. Altogether 1350 m^3 of about 10 °C fresh water were injected into the borehole without pressure increase at the wellhead, using two standard hoses connected to the mains water supply. The injection duration was 24 hours and the pumped volume was monitored every two hours. The mean injection rate was about 16 l/s. Due to memory and connection problems, DAS data could only be collected at the beginning, but not for the entire duration of the test. To obtain a complete data set for both DAS and DTS, a second injection test was performed on 22 February from 00:56 to 23 February 01:00. The test setup was the same as in January, except for a higher flow rate of about 23 l/s compared to the first injection test. Pumped volume was monitored every hour to assure a constant flow rate. In total, 1995 m^3 fresh water were injected. No pressure increase was recorded at the wellhead throughout the entire test. In the following, the two injection tests are named Inj1, which is the first test carried out in January, and Inj2, which represents the second test in February.

Gauge data and flow rates are depicted in Figure 5-4 for the two injection tests, including a shut-in time of 41 hours. Initial pressure at the gauge was 215.3 bar. The recorded temperature data clearly reflect a rapid cooling of the fluid inside the borehole from surface to top reservoir immediately after start of cold-water injection. After two hours of injecting, the water was cooled down by 35 K and 45 K for Inj1 and Inj2, respectively. The temperature decline during the second test was faster, indicating a faster cooling, probably due to the higher injection rate during Inj2. After 6 hours, the temperature curves of Inj1 and Inj2 remain almost constant. As the well was shut, the water temperature quickly increased at the P/T gauge and began to equilibrate back to formation temperature. At this time, the well was cooled at reservoir level during Inj1 by 65.5 K

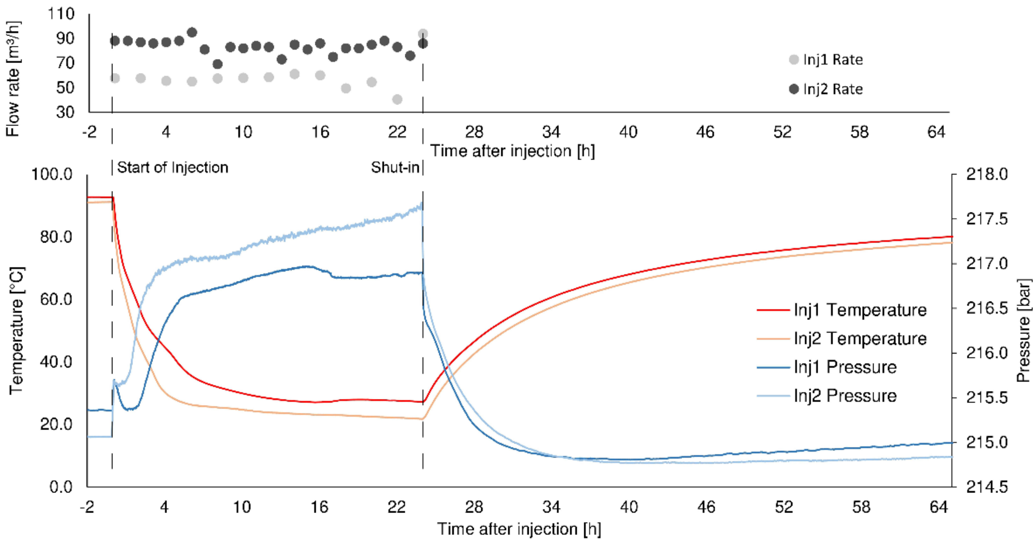

Figure 5-4. P/T gauge data recorded during the first injection test of January 2020 (Inj1) and the second injection test of February 2020 (Inj2) with injection rates.

and during Inj2 by 69.5 K. As there were only 29 days between the shut-in of Inj1 and the start of Inj2, the well temperature was not in equilibrium with the undisturbed formation temperature. Therefore, the initial temperature of Inj2 was 1.5 K lower compared to the initial temperature measured before Inj1.

5.2.6 Thermal Dynamics of the FO-Construction

To test if the sucker rod/FO-cable construction has been subject to thermal contraction (due to cold water injection) and thermal expansion (heating after shut-in), we calculated a theoretical thermal strain from DTS and compared this with DAS measured and temporally integrated strain rate along the fiber. The theoretical contraction/expansion, respective strain ε_{DTS} (με) to which the downhole FO-construction is exposed due to the cooling or heating can be calculated with equation 1 by multiplying the temperature deviation of two DTS profiles ΔT_{DTS} (K) with a thermal expansion coefficient α_{th} (μ(ε/K)) of the relevant material according to (James et al., 2001):

$$\varepsilon_{DTS} = \alpha_{th} \cdot \Delta T_{DTS}. \qquad \text{(eq. 5-1)}$$

The downhole construction consists of sucker rods, TEF, centralizers and clamps. To simplify the calculations, we neglected the thermal-mechanical properties of centralizers and clamps and assumed the sucker rod and steel of the cable to be the main construction part. A thermal expansion coefficient α_{th} of 13 με/K was applied for the sucker rod 4332 SRX nickel-chrome-moly steel (Cverna, 2002). The resulting strain profile shows the theoretical expansion of the sucker rod due to heating. Negative strain can be translated as contraction, positive strain as expansion.

To check if this expansion is actually experienced by the fiber or if the fiber remains in place and thermal stresses build-up, the DAS strain rate data were integrated over the same time period to a cumulative strain ε_{DAS}. DAS, as used in our application, analyses the phase of elastically backscattered photons by measuring the phase difference between the beginning and end of any section of the optical fiber. External forces (e.g. strain) that perturb this section result in phase difference changes (Masoudi et al., 2013). Raw measured strain rate can be converted to a DAS strain ε_{DAS} at a distinct location by integrating in time. This integration entails the risk of systematic error due to a drift of the acquisition unit. Lipus et al. (2022) referred to this and relativized the risk of such error as they saw no strain accumulation to the very end of the installation where no thermal contraction is expected.

5.2.7 Temperature Interpretation and Warm-Back Analysis

When cold water is injected, the temperature equilibrium of a well gets disturbed. The cooling process in the reservoir section differs according to the characteristics of the wellbore environment. Low permeability zones are getting cooled by the conduction of heat from the fluid to the formation, while high permeability zones are cooled due to the heat advection current of the fluid that flows into these zones. Major temperature responses can be seen in such zones (Sakaguchi and Matsushima, 2000; Brown, 2003; Henninges et al., 2005c; Hole, 2008; Patterson et al., 2017).

To localize hydraulically active zones with the FO-system, we analyzed the cooling within the reservoir during the injection period and analyzed the propagation of the cold front of the injected freshwater. As we follow the cold water down the borehole we expect a moving cold front along the borehole axis. Figure 5-5 shows a scheme of the performed DTS velocity track analysis with the gray and blue lines representing DTS profiles at different times after the start of cold water injection above a hydraulically active zone (gray lines) and below the zone (blue lines).

From the distance covered by the injection front, a velocity (v_a and v_b in Figure 5-5) can be estimated. At zones with high permeability (hydraulically active zones), the vertical moving thermal front should change in terms of velocity and a slowdown should be noticeable (Ali et al., 2014). In Figure 5-5, this is reflected by the fact that the velocity below the hydraulic active zone v_b is lower than the velocity above in the cased section v_a. We applied this graphical analysis to both injection tests Inj1 and Inj2. For verification, the flow velocities inside the well were also estimated from the injection rates and the area inside the borehole. For simplifications, the flow area was assumed as a concentric circular ring. With hydraulic diameter $d_h = d_{C,i} - d_{FO}$ and assuming uniform turbulent pipe flow, the mean flow velocity for such is given by eq. 5-2 (Bohl and Elmendorf, 2005):

$$v_i = \frac{Q \cdot 4}{({d_{C,i}}^2 - {d_{FO}}^2) \cdot \pi}, \qquad \text{(eq. 5-2)}$$

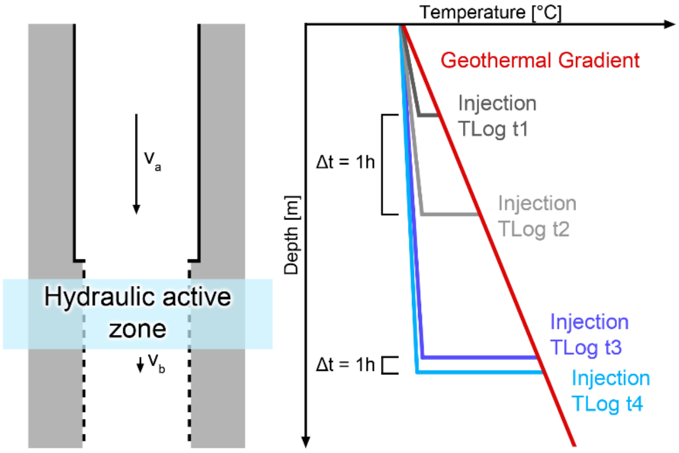

Figure 5-5. Schematic DTS velocity track analysis during injection of cold water. Dark gray and light gray lines are DTS temperature logs (TLog) at different times t1 and t2 and show the downhole propagation of injected cold water in the cased section of a well. Dark blue and light blue lines are DTS profiles at later times t3 and t4 below a feed zone. v_a and v_b are the velocities above and below the hydraulic active zone.

where v (m/h) is the velocity, the index i is the respective borehole section, Q (m^3/h) is the flow rate, d_C (m) is the inner diameter of the casing, and $d_{FO}(m)$ is the diameter of the installed FO-construction. The cross-section of the sucker rod/TEF was simplified as a circle with a diameter of 0.03 m (0.43-in. TEF mounted to the 3/4-in. sucker rod).

To qualitatively characterize the located hydraulic active zone, we calculated the ratio I (%) of velocities above v_a (m/h) and below v_b (m/h) the zone that were estimated from the DTS velocity track analysis (see Figure 5-5) and derived from velocity calculations (see eq. 5-2) according to equation

$$I = (v_a - v_b)/v_a. \qquad \text{(eq. 5-3)}$$

In analogy to the flowmeter analysis, the total volume injected into the formation was estimated from the flow rate and calculated ratio I.

To analyze the dynamics of the reservoir in a time-resolved manner, in particular located hydraulic active zones, we observed the warm-back of the water column to the initial formation temperature after well shut-in. This was essential to provide information about the temperature distribution inside the well that is dependent on time, the rock's thermal properties and its hydraulic properties.

5.3 Results

The downhole FO-monitoring system was successfully installed in the highly deviated well without damaging the fibers or the wellbore. Continuous monitoring started 11 days afterwards (see Table 5-1). With exception of one-month downtime in March 2020 during the rig-down of the drilling rig, P/T gauge data and DTS data were recorded from November 2019 until August

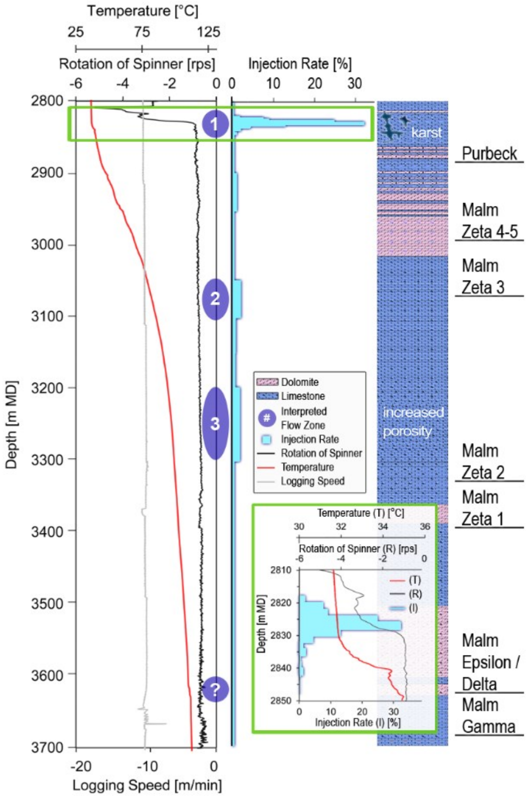

Figure 5-6. Interpreted flow zones in producer well together with flowmeter spinner data, temperature and logging speed, lithology and stratigraphic units. Zoom to top section is shown in green framed box.

2020. DAS was only recorded during the injection measurement campaign, as well as other testing works on the site. For Inj1, the DAS dataset is incomplete, and only covers the beginning of the test. For Inj2, a complete DAS dataset is available.

The results presented here are structured in flowmeter interpretation for a comparison with the DTS/DAS dataset, DTS-measurements as the well was shut, outcomes of the cold water injection tests and verification of the hypothesis of the dynamical behavior of the FO-structure to thermal stress.

5.3.1 Flow Zone Detection by Flowmeter Logging

Flowmeter measurements were conducted to identify hydraulically active zones in the reservoir section, and they were used to match the DTS/DAS measurements to the results. Figure 5-6 shows the raw flowmeter data (logging speed, rotation of spinner and corresponding temperature log, all from July 2019), the resulting injection rate profile (light blue), and the interpreted injection zones (purple zones).

The interpreted main injection zone (1 in Figure 5-6) is located in the stratigraphic formation Purbeck in the uppermost of the reservoir section. This karst dominated zone has a length of 15 m MD (see green box inside Figure 5-6). Here, the flowmeter measurements detected that about 92 % of the injected water flowed into the formation. Although the flowmeter temperature curve shows a rapid increase below 2900 m, the rotation of spinner curve does not highlight an additional injection zone, as the spinner response was quite low (< 1 % inflow). This behavior might be related to a slight change in logging speed. Only about 8 % inflow could be assigned to regions in deeper reservoir sections. One can be located at the transition of Malm Zeta 3 to Zeta 2 (zone 2 in Figure 5-6) and another one from 3200 to 3300 m MD in Malm Zeta 2 (zone 3 in Figure 5-6). By comparison with sonic-log measurements, both zones correlate to an increase of porosity. Further down, the spinner signal becomes unstable. In this part, a slight step in the flowmeter temperature profile indicates an additional zone (questionable zone below 3600 m in Figure 5-6).

5.3.2 Initial Temperature Log from DTS

From the start of FO-measurements in November 2019 to the end of January 2020 (prior to the start of injection testing), the P/T gauge and DTS data show that the well has not reached thermal equilibrium [see Figure 5-7 (b)]. The temperature increase in that period extended from 0.15 to 0.2 K for the complete reservoir section except for a 100 m section in the upper part of the reservoir at 2500 m (TVD) that has heated up by about 0.35 K. Above the reservoir section, changes in temperature profile throughout November were less than 0.5 K, and no or very little (lower than detection limit of DTS) changes were observed in January. To create a representative continuous temperature profile with low data noise from which temperature gradients can be derived, all DTS profiles from January 2020 were taken as mean values. Figure 5-7 (a) shows this profile together with the thermal gradients, approximated from the averaged DTS profile for specific depth regions [labelled A, B, C and D in Figure 5-7 (a)] showing a constant gradient. The mean geothermal gradient is 3.3 K/100 m, A is 2.7 K/100 m, B is 3.2 K/100 m, C is 4.7 K/100 m and reservoir gradient D is 2.6 K/100 m. Furthermore, we can see some anomalies in the otherwise smooth course of the DTS profile. At point A in Figure 5-7 (a), there is a sudden step in temperature of about 1 K from 710 m to 720 m. Two other deviations from the assumed geothermal gradient are in the reservoir section [referred to as zone (1) and (2) in Figure 5-7 (b)].

The first deviation [zone 1 in Figure 5-7 (b)] is in the upper 100 m of the reservoir between 2815 m MD (2,405 m TVD) and 2885 m MD (2460 m TVD) and deviates with $\Delta T = 1.2$ K from the assumed thermal gradient. The second deviation [zone (2) in Figure 5-7 (b)] is below 3600 m MD (2850 m TVD) and is also present in the flowmeter temperature log at the level of Malm Gamma (see questionable zone in Figure 5-6). It deviates with $\Delta T = 0.8$ K from the assumed thermal gradient. Zone 2 in Figure 5-7 (b) shows little thermal dynamics, as in contrast to zone 1, for which ΔT decreases from November 2019 to January 2020, ΔT of (2) is remaining constant [see gray box in Figure 5-7 (b)].

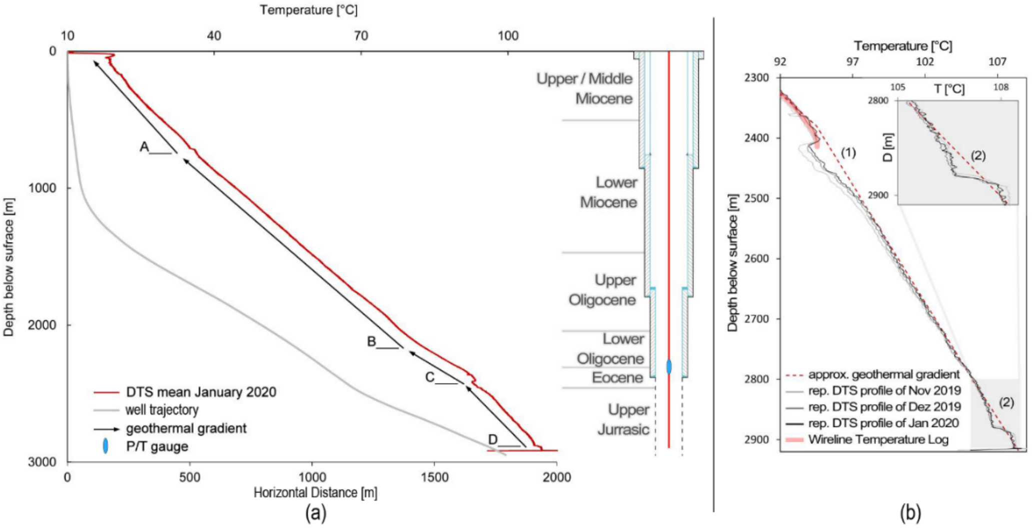

Figure 5-7. Temperature gradients from DTS profile at the geothermal Schäftlarnstraße site. Subplot (a) shows estimated temperature gradients with projected well trajectory and stratigraphy. Subplot (b) shows representative (rep.) DTS profiles from November 2019 to January 2020 at averaged over 6 hours and with a moving average of 2 m with the wireline temperature log and the approximate thermal gradient inside the reservoir. (1) and (2) mark zones where the DTS temperature deviates from the proposed gradient.

5.3.3 FO-Sensing during Injection Tests

The two injection tests Inj1 and Inj2 were performed with the same duration (24 h). Inj2 differs from Inj1 in terms of a higher flow rate (23 l/s in comparison to 16 l/s for Inj1) and a short shut-in time (28 days in comparison to more than 6 months for Inj1) as shown in Figure 5-4.

5.3.3.1 Acoustic Sensing

Significant DAS signals were recorded immediately after the start of testing. Figure 5-8 shows temporally integrated DAS strain rate data for the first minutes of both injection tests. At the very beginning of the tests (1 min after the start of injection), deep regions of the well are not yet affected by the cold water, as we find almost no acoustic response along the rods. For Inj1, the strain between 2000 m and 2800 m is about -1 $\mu\varepsilon$ [see Figure 5-8 (a)], while no significant strain is observed for Inj2 [see blue line in Figure 5-8 (b)]. Along the first 200 m, the water is freefalling until it encounters the water table. Here, the rods are cooled by the injected water. At 750-800 m, a step of 0 to -1 $\mu\varepsilon$ for Inj2 at +1.5 min and -0.5 to -3 $\mu\varepsilon$ for Inj1 at +3 min is evident. A second step is at 1900 - 2000 m (-0.5 to -2 $\mu\varepsilon$ for Inj2 at +1.5 min). Both steps are at the location of the 13 3/8-inch hanger (770 m) and 9 5/8-inch hanger (1907 m), respectively. A third step can be found at 2,800 - 2,850 m with local high negative and positive strain rates for Inj2 (-10 to 20 $\mu\varepsilon$). From

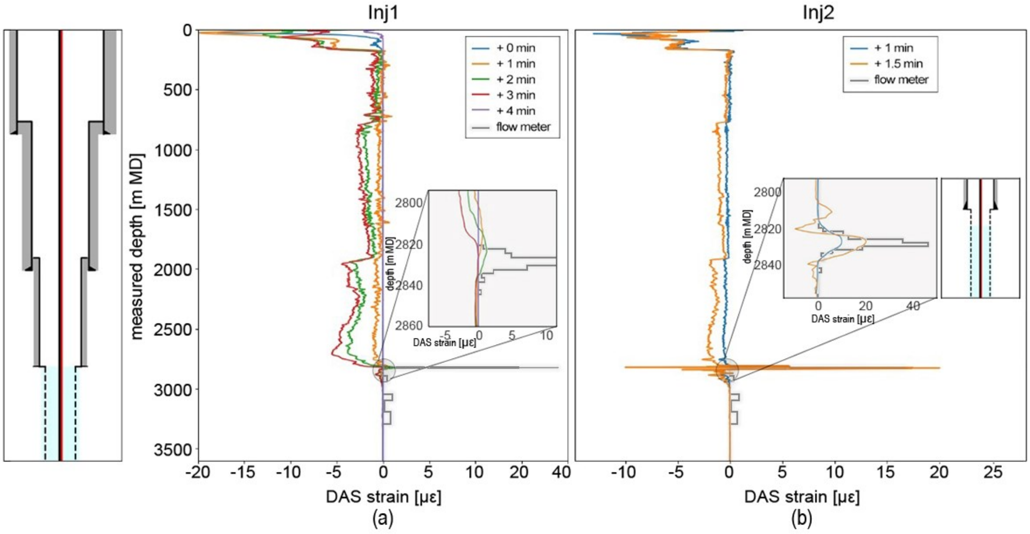

Figure 5-8. DAS strain measurements at the beginning of injection tests Inj1 (a) and Inj2 (b). The gray line marks the injection profile from flowmeter. DAS strain at the top of the reservoir is given in zoomed in sub plots.

2850 to TD at 3700 m, the strain is zero. The stepwise change of the strain rate from 250 to 2800 m can be interpreted with respect to the well completion. As the inner diameter decreases at the liner hanger, flow velocity rises and the volume of water per meter depth decreases, which means a higher cooling rate.

5.3.3.2 Temperature Sensing during Cold Water Injection Tests

The DTS profiles recorded during the injection tests (one every 10 minutes) were used to estimate the water flow velocities inside the well. Figure 5-9 (a) shows how the thermal front of the injected water of Inj1 (analogous plot for Inj2 is attached in Supplementary 5 - 3 moved vertically down the well. In the first section, velocity of the thermal front is of about 360 m/h, when the calculated theoretical velocity (see eq. 4-2) at an injection rate of 16 l/s is 345 m/h. At top of the slotted 7-inch liner, the calculated velocity is 1537 m/h. Right on top of the reservoir section, we can see a slowdown of the cold front, indicating that the majority of injected water got lost to the formation. The vertical movement of the cold front is then about 100 m/h.

Roughly estimated from the velocity change and by applying eq. 4-3, we can assume that the zone took up about 93.5 % of the water. For Inj2 the percentage inflow is accordingly calculated to 94 % (see Supplementary 5 - 3).

Figure 5-9 (b1) and (b2) show the temperature DTS injection profiles in the upper reservoir section from 2810 m MD to 2898 m MD for both tests. Since the flow rate of Inj1 was lower than for Inj2, the movement of the cold front was much slower, which is why the heat plots show a higher gradient for Inj2 than for Inj1. It took about 6 hours of injection for Inj1 to cool by 40 °C at 2898 m MD; this happened twice as fast for Inj2 due to the larger amount of flowing cold water.

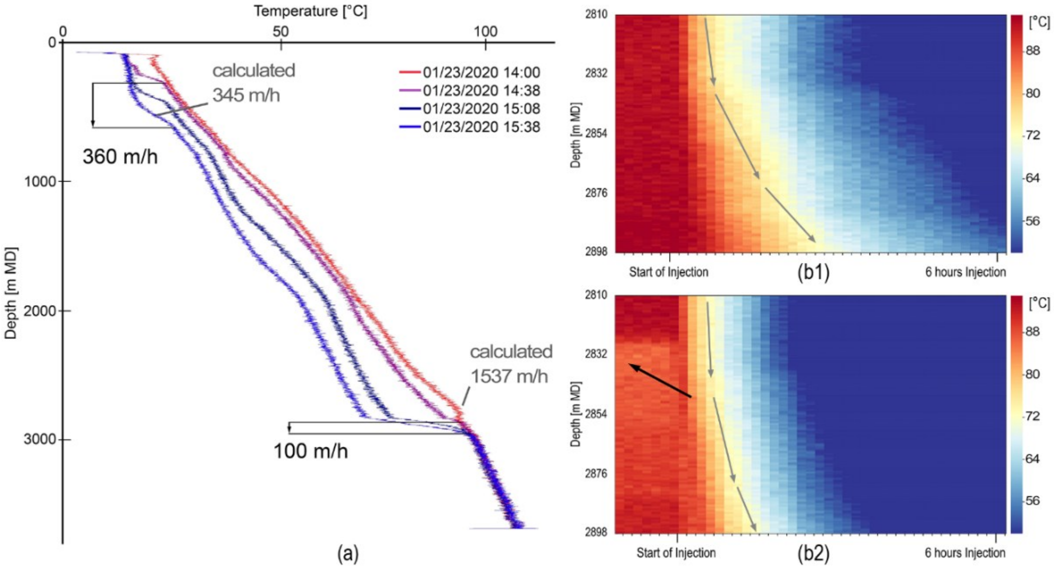

Figure 5-9. Analysis of velocity of the injected cold water. (a) Vertical movement of cold waterfront of Inj1. (b1) Heat plot of Inj1. (b2) Heat plot of Inj2. Gray arrows: suggested 75 °C isotherm. The black arrow marks the proposed major hydraulic active zone.

In both cases, we see near-vertical isotherms to a depth of 2830 m MD, below the slope changes, indicating that the formation took the injected water at this location. Furthermore, we can recognize a colder region at Inj2 [indicated by brighter color in Figure 5-9 (b2)] before the start of injection, beginning at 2827 m MD that fades out below. This is due to the cold water the formation took up when Inj1 was performed. For Inj1, the temperature deviation is much smaller ($\Delta T = 1.2$ K, see Figure 5-7) because the shut-in time was large (> 6 months) and the fluid was able to warm towards the formation temperature.

5.3.4 DTS during Warm-Back

As the well was shut-in, the water in the wellbore began to heat up back to the undisturbed formation temperature. Figure 5-10 (a) depicts DTS profiles during the warm-back after Inj2 (see supplement D for Inj1) at different time stamps (4, 6, 17 hours after shut-in) together with DTS at shut-in and the mean DTS profile of January 2020. Interesting steps and changes are present in the warm-back profiles. One is located in 200 m depth that divides a strong uniformly heating section above from a less strong heating below. A second one is between 750 m and 900 m, a third one at around 1500 m [marker (A) in Figure 5-10 (a)], a fourth one at 2135 m [marker (B) in Figure 5-10 (b)] and another one at the top of the reservoir. Warm-back profiles in the Upper/Middle Miocene, the Lower Miocene and the Lower Oligocene are relatively uniform, while the profiles in the Upper Oligocene showing higher variation. Below 2380 m, with beginning of the reservoir section, warm-back profiles change significantly. Throughout the profiling a slower warm-back was recorded at 2830 m MD, followed by a sharp increase of slope

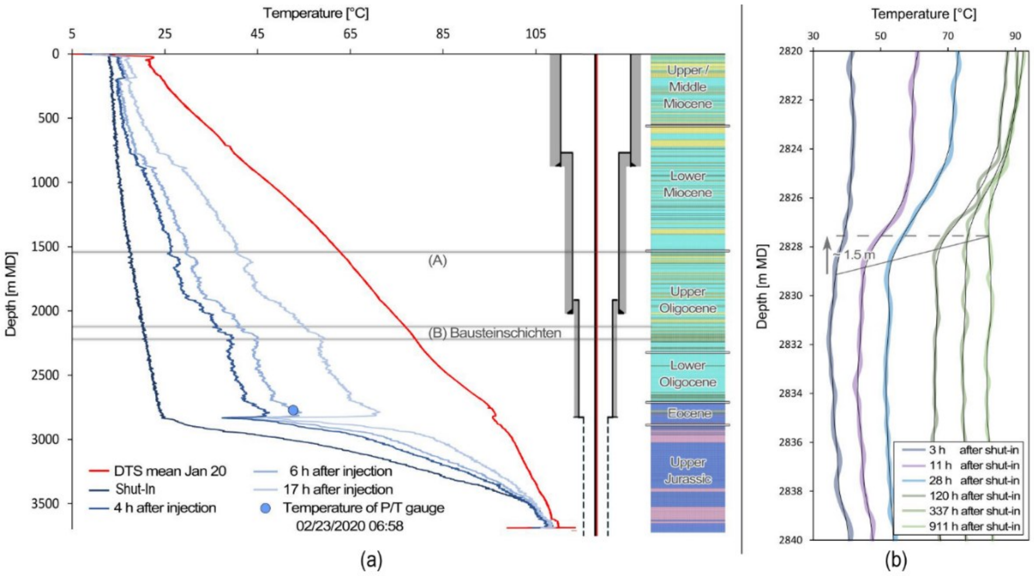

Figure 5-10. DTS profiles during warm-back of Inj2. (a): Warm-back profiles at 4, 6 and 17 hours after shut-in together with the mean profile of January 2020 and the Shut-In profile over whole borehole in comparison to stratigraphic units and the well completion. (b): DTS peaks during long-term warm-back at top of the reservoir from 2810 m MD to 2840 m MD. The bold curves are raw DTS data, fine black curves are moving average over 2 m. The gray line indicates a vertical shift of about 1.5 m.

of the DTS profiles below. For long shut-in times, we noticed a vertical shift of the temperature profiles of about 1.5 m compared to the injection profile [see gray shift line in Figure 5-10 (b)].

5.3.5 Thermal Contraction

DAS was used to evaluate whether the vertical shift in the data [see gray line in figure 10(b)] was caused by a thermal expansion or contraction of the sucker rod/TEF structure during the warm-back process. Figure 5-11 (a) shows two DTS profiles, one during shut-in and one 60 min after shut-in of Inj2. Figure 5-11 (b) demonstrates the temperature difference between these two profiles. The third subplot [Figure 5-11 (c)] shows the theoretical expansion of the fiber/cable/sucker rod due to heating, calculated with eq. 4-1 and the DAS strain rate, integrated over the same 60 min period. A clear match is visible between the calculated theoretical thermal expansion from DTS data ε_{DTS} and the actual measured expansion from DAS data ε_{DAS}. In the depth interval from 2200 to 2800 m a larger expansion (up to 25 με) was measured from DAS than would be expected from ε_{DTS}.

5.4 Discussion

After the successful implementation in the deviated production well, the FO-monitoring period during shut-in and the two injection tests showed that reservoir characterization and detailed correlation and comparison with other measurement devices can successfully be conducted.

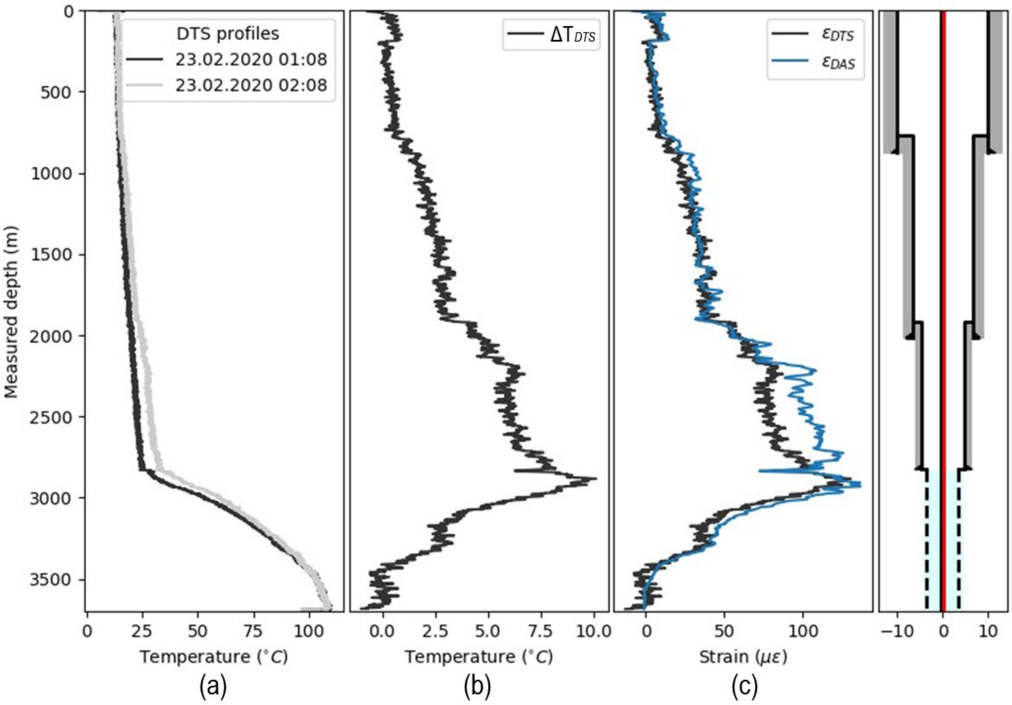

Figure 5-11 . Theoretical thermal expansion from DTS data and measured thermal expansion from DAS data after well shut-in, Inj2.

However, the results of the FO-system need to be evaluated in terms of the mechanical dynamics of the system design along the sucker rod structure.

5.4.1 Dynamic Temperature Development in the Monitored Well

The 3-month shut-in monitored by DTS (November 2019, installation of the FO-system to end of January 2020, start of the first cold water injection test) showed that the well had not yet reached thermal equilibrium in this period [see Figure 5-7 (b)]. However, dynamic zones that were still warming up were found mainly in the reservoir section. There was little heating in the cased sections of the well in November and no noticeably heating, respectively heating lower than the detection limit of DTS in January. Thus, we assume that DTS profiles of January are close to the geothermal gradient, apart from the dynamic zones within the reservoir section. The graphically derived mean geothermal gradient is 3.3 K/100 m, which is a typical value for the Bavarian Molasse Basin (Bauer et al., 2014). A more detailed analysis revealed four different thermal gradients, labelled A, B, C and D in Figure 5-7 (a). Up to 800 m, gradient A is 2.7 K/100 m, which is also typical for the Southern Molasse Basin (Casper et al., 2014; GeoMol Team, 2015). Second, B is higher at 3.2 K/100 m down to 2000 m depth, near the boundary between the layers of the Upper and Lower Oligocene. Third, C up to top reservoir is the highest gradient with 4.7 K/100 m and lastly 2.6 K/100 m for the reservoir section itself. Assuming a constant heat flow, according to Fourier's law, a high gradient indicates low thermal conductivity of the rock (e.g., Eppelbaum et al., 2014; Zarrouk and McLean, 2019), which means that the most prominent gradient (C) is due to the low thermal conductivity of the shaly Rupel rock of the Lower Oligocene that is delimited from the sandy Chatt rock of the Upper Oligocene. For example, Homuth (2014) proposed thermal conductivities of about 2.53 W/(mK) for Rupel rock and up to 3.15 W/(mK) for Chatt rock.

The two cold water injection tests, Inj1 and Inj2, ended the shut-in period after FO-construction. We artificially disturbed the nearly equilibrated temperature distribution inside the well and measured the warm-back to initial conditions. For both Inj1 (see supplement D) and Inj2 [see Figure 5-10 (a)], we saw that the uppermost 200 m in the well heated more rapidly than those below. 200 m is about the expected depth of the water table. Up to this depth, the TEF mounted on the sucker rods is likely hanging in the middle of the borehole, with no contact to the casing. Here, the cable is surrounded by air with a lower heat capacity of about 1.0 kJ/(kgK). Thus, the cable heated much faster than below, where the ambient medium is water, having a heat capacity at 20 °C of about 4.2 kJ/(kgK). Irregularities in the warm-back profiles were found at the top liner hanger of the anchor tubing (750 m). It is likely that the combined effects of cementing and casing of the liner hanger affected the heat transfer here. From 900 m to about 1,500 m, a uniform heating behavior can be seen when getting through the layers of the shaly Lower Miocene. At the change of the shalier Lower Miocene to the sandier Upper Oligocene, there is a notable temperature drop in the warm-back profiles. Here [marker A in Figure 5-10 (a)], we find a 50 m thick clay marl layer that might act as a hydraulic barrier or indicate a local lower thermal conductivity of the rock. The Upper Oligocene reaches to a depth of about 2330 m (2050 m TVD) and shows to be more heterogeneous than the layers above. This is also reflected by the warm-back DTS profiles as they increase in variance. Notable is a sudden temperature step at 2135 m (1960 m TVD), which is on the horizon of the Bausteinschichten [marker B in Figure 5-10 (a)]. Below this is a 70 m thick layer of clay marl with less heating. From 2330 m to 2710 m we see uniform heating in the shaly Rupel layers of the Lower Oligocene. Koch et al. (2006) studied samples from 14 wells of the Molasse basin and found that thermal conductivity of the Bausteinschichten ranges from 1.57 W/(mK) to 3.81 W/(mK) with a mean of 2.88 W/(mK). The Rupel formation has lower mean thermal conductivities, e.g., Homuth (2014) gave a value of 2.53 W/(mK), and shows to have a thermal insulation effect during warm-back.

5.4.2 Construction and Design Issues

5.4.2.1 FO-Installation

Running logging tools in highly deviated wells is challenging. At the study site, this was shown when a conventional wireline temperature log could not pass the 7-in. liner hanger. The design of the downhole FO-construction was focused on minimizing this risk. The installation along sucker rods to the reservoir was successful. However, the design of the FO-system posed challenges in both the installation and the analysis of the FO-measurements. Installation was performed with a triple drilling rig. Designed for heavy weights, no significant hook load could be recorded on the driller's console because of the low weight of the sucker rods. As the fiber optic rotary joint was noisy (see Chapter 5.2.2), checking the integrity of the sucker rod string during installation turned out to be challenging. The final installation showed losses at the wellhead splices and connectors, at the splice at the P/T gauge and at the mini-bend. Apart from those, no unexpected anomaly in the attenuation profile occurred. The combined losses were however demanding for the daisy-chained DAS measurements across both wells, mainly due to the relatively high loss at the mini-bend in the injector well.

5.4.2.2 DTS Anomaly

First DTS measurements after installation showed a temperature anomaly inside the borehole that is a 1 K temperature step above the transition of section 1 to section 2 from 710 m to 720 m [see Figure 5-7 (a)]. This is about 50 m above the liner hanger and can be found in every DTS profile recorded before Inj1 (November 2019 to end of January 2020). The anomaly disappeared with Inj1 and cannot observed in DTS profiles recorded afterwards. Figure 5-12 shows the mean DTS profile from January 2020, the wireline temperature log and three exemplary profiles that were recorded before and after Inj1. As neither the independent wireline temperature log does show a similar anomaly, nor is there evidence of bad cementing or other influences, e.g., a rock layer with little thermal conductivity (Wisian et al., 1998), it is obvious that the temperature step might relate to the FO-installation. OTDR measurements do not show suspicious loss in the respective depth that would indicate a damage of the fibers. One hypothesis is that the DTS temperature step reflects a stratification of the water column, possibly triggered by the pulling of the 13 3/8-in. tieback, which happened immediately prior to FO-installation (see Chapter 5.2.2). The tieback was initially placed after cementing the second section of the well and the following purging. Thus, the drilling mud remaining in the annulus, behind the tieback, would not be mixed with the short-term air-lift production tests that were performed with the installed tieback after well completion. With pulling the tieback, mud residues might accumulated at 710 to 720 m, which might cause an insulation effect and a thermal stratification.

5.4.2.3 Depth Displacement

One challenge of the sucker rod construction for permanent monitoring might be its dynamic behavior. The two injection tests carried out in January and February 2020 indicated that temperature changes cause thermal contraction and expansion of the sucker-rod/fiber cable installation [Figure 5-10 (b) and 4-11 (c)] along with a vertical shift of the fibers and the P/T gauge. Such behavior is well known, for example, for conventional wireline measurements (Grant and Bixley, 2011; Zarrouk and McLean, 2019).

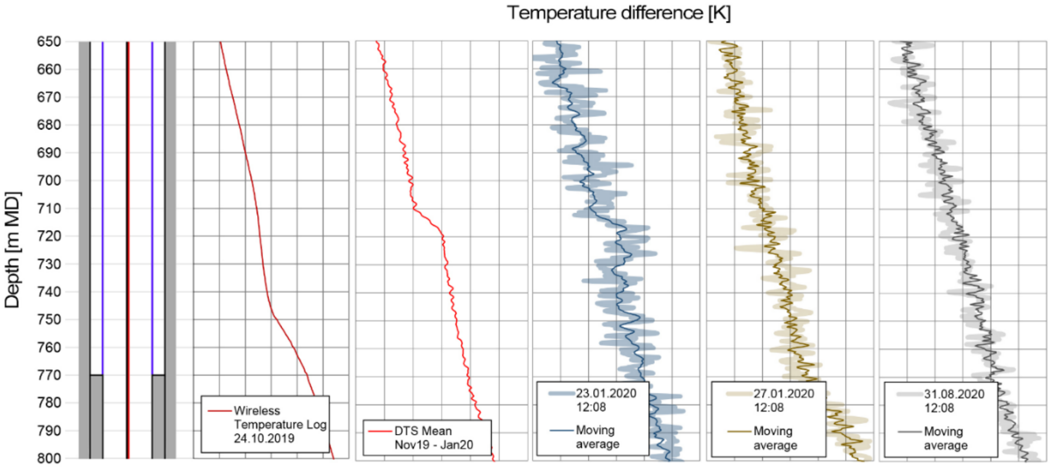

Figure 5-12. Changing of temperature profiles over time in the first section. First subplot to the left shows the completion with tieback liner in blue and TEF/sucker rod in red. Second subplot shows the wireline temperature log that was recorded inside the tieback liner. Third to sixth subplots show DTS profiles that were recorded in the borehole as the tieback liner was pulled. Third subplot is the mean DTS profile until start of Inj1, fourth shows a DTS profile shortly before start of Inj1, fifth is 3 days after Inj1, sixth subplot shows a current DTS profile. Transparent lines are raw DTS data, sharp lines are moving average over 4 hours at a spatial resolution of 2 m.

Depth calibration is essential for interpreting DTS values (e.g., Smolen and Spek, 2003). Therefore, different temperature profiles require their own post-processing to correctly assign measured temperatures. As a consequence, all of the DTS and DAS profiles of the cold water injection tests shown in this study have a slightly incorrect depth assignment since the depth calibration refers to the less disturbed temperature profile as it was after FO-installation. The relevance of the displaced P/T and DTS measurements can be estimated by calculating the theoretical displacement of each measurement point along the downhole FO-construction caused by the thermal contraction related to the cold water injection. According to e.g., Zarrouk and McLean (2019) this is given by:

$$\Delta L = \int_{x_1}^{x_2} \Delta T_{DTS}(x) \cdot \alpha_{th} \cdot dx, \qquad \text{(eq. 5-4)}$$

where ΔL (m) is the expansion length due to the temperature deviation ΔT_{DTS} (K) of a DTS injection profile from the undisturbed DTS profile, x (m) is the respective depth and α_{th} $(1/K)$ is the thermal expansion coefficient for the construction, that again is assumed to 13^{-6} K^{-1} (see Chapter 5.2.6). The maximum calculated displacement at the end of the construction is about 1.5 m for both Inj1 and Inj2. Such a scale does not play a major role for DTS, considering that depth assignment and the exact location of TD are subject to a certain error, as for example the accuracy of drillers tally, as well as the fact that the downhole temperature does generally not change rapidly at the scale of few meters, which is also shown by the common geothermal gradient of 0.033 K/m in the Bavarian Molasse Basin (Bauer et al., 2014; Casper et al., 2014 and proposed thermal gradient in Figure 5-7a).

The calculated displacement of the P/T gauge at 2755 m MD is shown in Figure 5-13 for the first 7 hours of the injection period of Inj2. After 4 hours of injecting, temperature profiles and the

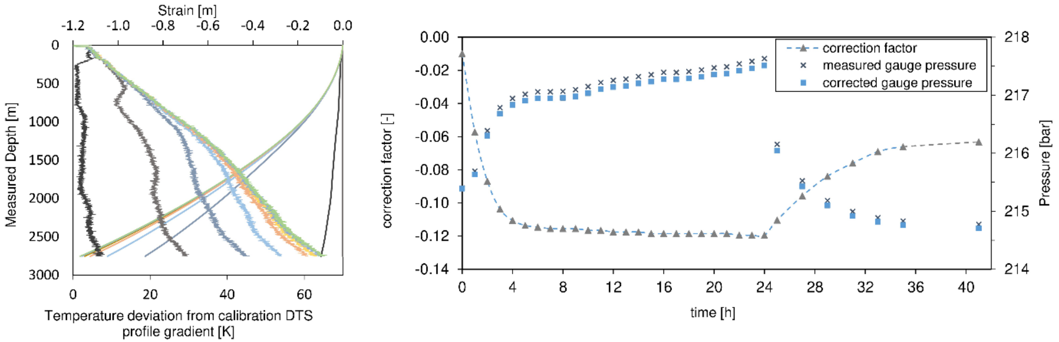

(a) (b)

Figure 5-13. Calculated strain from DTS and corrected pressure data. (a): Calculated Strain from DTS data to the depth of the P/T gauge in the first seven hours of injection of Inj2. Curves on the left y-axis are temperature deviations from the initial DTS profile. Curves on the right y-axis are the resulting strain for each DTS profile. (b): Measured gauge pressure data with correction factor to revise thermal caused displacement.

resulting thermal stress change only very slightly. The vertical displacement is around 1.2 meters to the end of Inj2. The pressure at the correct position of the P/T gauge can be recalculated by applying a correction factor to the measured gauge pressure:

$$\Delta p = \rho \cdot 9.81\frac{m}{s^2} \cdot \Delta h, \tag{eq. 5-5}$$

where Δp (bar) is the hydrostatic pressure of the water column between the correct and the dislocated gauge with height Δh (m) (vertical displacement) and ρ (kg/m^3), the density of water column in the well. The density of the fluid of the water column was assumed to be 1005 m^3/kg in accordance with Eppelbaum (2014), who reported values for water at 25 MPa and 25 °C, which approximates the conditions at the respective depths during cold water injection. At the beginning of the injection test, the correction factor Δp is low, but after the borehole was cooled down almost completely (4 hours of injection), the calculated measurement deviation is about -0.12 bar.

Initial P/T gauge pressure before Inj2 was 215.1 bar. The pressure increase throughout the test was 2.5 bar and the maximum recorded pressure was 217.6 bar at shut-in. With maximum deviation of 0.12 bar due to the displacement, the resulting error of pressure increase is therefore 5 %.

Consequently, the FO depth calibration should be reconsidered when the well starts to produce, because this will cause a different temperature profile inside the well to be recorded. Up to now, DTS is calibrated with respect to the temperature profile after FO-installation that shows little heating apart from the hydraulic active zone (see 5.2.3 and Figure 5-7). In production, the thermal stresses in the reservoir will not play as large a role as in the injection tests performed.

The top sucker rod will be located below the ESP, thus most of the sucker rods in the top section will be replaced by the production tubing. Subsequently, the sucker rod string will be shortened by around 700 to 800 m. Additionally, temperature gradients between production temperature and shut-in temperature in the reservoir will be lower, and thus the thermal stress at the sucker rods in the reservoir will be less than during the injection tests. A similar FO-installation design in injection wells should consider relevant temperature changes and subsequent displacements.

Open questions remain concerning the excess of about 25 µε (ε_{DAS}) over the theoretical expansion (ε_{DTS}) between 2200 m and 2800 m [see Figure 5-11 (c)]. The excess may be due to the fact that ε_{DTS} only relates to the time period between two DTS profiles, while the strain evolution during temperature changes also includes information from previous events. For example, the initial stresses 'stored' inside the rod may not exceed frictional forces and are therefore not measured by DAS. Another possible error-proneness of the method lies in the nature of the procedure for generating DTS data in our system. The timestamp of a DTS profile is set to the end of one measurement, which means that the profile can be understood as an averaging temperature over the last 10 minutes. The well was shut at 23.02.2020 00:56, the first DTS profile of the considered 60 min period was recorded at 01:08. Consequently, the sucker rod/TEF construction has already been subject to warm-back and thermal expansion. Cumulative strain ε_{DAS} covers exactly the 60 min period from 01:08 to 02:08, although the comparison of ε_{DAS} and ε_{DTS} is liable to shift. Further research about the relation of measured DTS and DAS data to friction forces inside the well is discussed in Lipus et al. (2022).

The consequence of the above findings is that all DTS profiles of the injection tests have a shift in depth due to thermal contraction. However, the vertical displacement at the top of the reservoir (near to the P/T gauge at 2755 m MD) is no more than 1.2 m, which is about the 1 m spatial resolution of the processed DTS data (see Chapter 5.2.3). This is a small magnitude relative to the distance over which significant temperature changes take place (e.g., major flowmeter zone that flowmeter data showed over a distance of 15 m).

5.4.3 Reservoir Characterization

While monitoring the temperature in the reservoir section showed high dynamics of the thermal distribution over the reservoir section, the questionable zone near TD at 3630 m MD [see Figure 5-6 and Figure 5-7 (b)] was unaffected by the hydraulic tests. Here, all available temperature profiles (flowmeter temperature and DTS before, during and after injection tests) show a temperature anomaly with little dynamic behavior [see Figure 5-7 (b)]. The fact that this is also present in the measurements that are independent from DTS (flowmeter) shows that the anomaly is not a FO-system design related factor. The observed anomaly can either be interpreted as minor hydraulically active zone, in form of a fault zone (that is unclear from geological model) or as insulation effect from drilling residues (drill fluid, ingress of material, sludge) that accumulated at the bottom hole (Zarrouk and McLean, 2019). As there is no evidence for either of the two hypotheses up to now, no reliable interpretation can be made. The origin of the anomaly can be clarified when the well produces.

To localize hydraulic active zones, flowmeter analyses were compared with DTS and DAS data. Flowmeter is the preferred tool for locating flow zones inside the reservoir. However, interpreting flowmeter measurements in highly deviated wells with perforated liner is difficult (Ben Haoua et al., 2015), as flow regimes become more complex than for vertical wells and fluid velocity behind the liner tends to change apparently without context to feed zones (Zarrouk and McLean, 2019). In this study, both are present (deviation of 58° in the reservoir section and perforated 7-inch liner). Additionally, the most prominent flowmeter response (92 % interpreted inflow, see Figure 5-6) was at the very top of the reservoir section from 2820 to 2838 m MD, where flow might have been disturbed due to turbulence of the narrowing of the diameter at the transition of section 3 to the perforated liner. Minor flow zones were interpreted below where there is an increase of porosity of the formation (see Figure 5-6).

The cold water injection experiments were performed to test the newly installed FO-system and to confirm the flowmeter interpretation. Assumed flow velocities from thermal front movement from DTS [see Figure 5-9 (a)] confirm flowmeter results by giving a percentage inflow of 93.5 % (Inj1), respective 94 % (Inj2) at 2830 m MD. This is in accordance with the inflows interpreted from flowmeter (92 %). Further down in the reservoir section, no vertical movement is evident in the DTS profiles, indicating that the injected water was lost above, or that fluid flow velocities were below the detection limit of the DTS analysis. Ali et al. (2013) also used fluid velocity analysis when they monitored DTS during an injection of water to the carbonatic reservoir of a test well in the South-West of the USA. Similarly to the Schäftlarnstraße well considered in our study, the major feed zone they investigated was a highly permeable karstic zone. They found that increasing the injection rate resulted in a relatively higher contribution from the karstified zone – likely due to the opening of fractures – and a relatively lower contribution from the minor feed zones. A similar behavior cannot be indicated for our tests, but this may be due to the dominance of the main inflow zone, which contributes with 92 % (flowmeter) respectively 94 % (velocity analysis of Inj2). Figure 5-14 summarizes the results of flowmeter interpretation (Figure 5-6) and FO-measurements during the injection period of Inj2 (Figure 5-8 (b) and Figure 5-10). During the analyses of the DAS data (Figure 5-8), we found that the strain profiles tend to negative values with progressing time, thus cooling of the well. However, shortly after begin of the injection test Inj2 (+1 min), a positive DAS strain is seen at 2820 to 2840 m that agrees very well with the flowmeter inflow profile. For this profile, we can see close to 0 με above or below the active zone, except for the uppermost 200 m where the water was freefalling until it hit the water table (see Figure 5-8). We assume that there was no or very little thermal or mechanical effect on the sucker rod/downhole cable at this time. Hence, the local DAS signal at the hydraulically active zone cannot be interpreted as positive strain (extraction of the rod), after that no heating process is conceivable here. Thus, the DAS signal indicates that fluid flow between borehole and reservoir rock might induced an acoustic response that was later obscured by the mechanical/thermal stress. However, this could only be observed in the first minute after injection start and only for Inj2. Figure 5-8 shows that there is no comparable recording for Inj1. The reason for this is

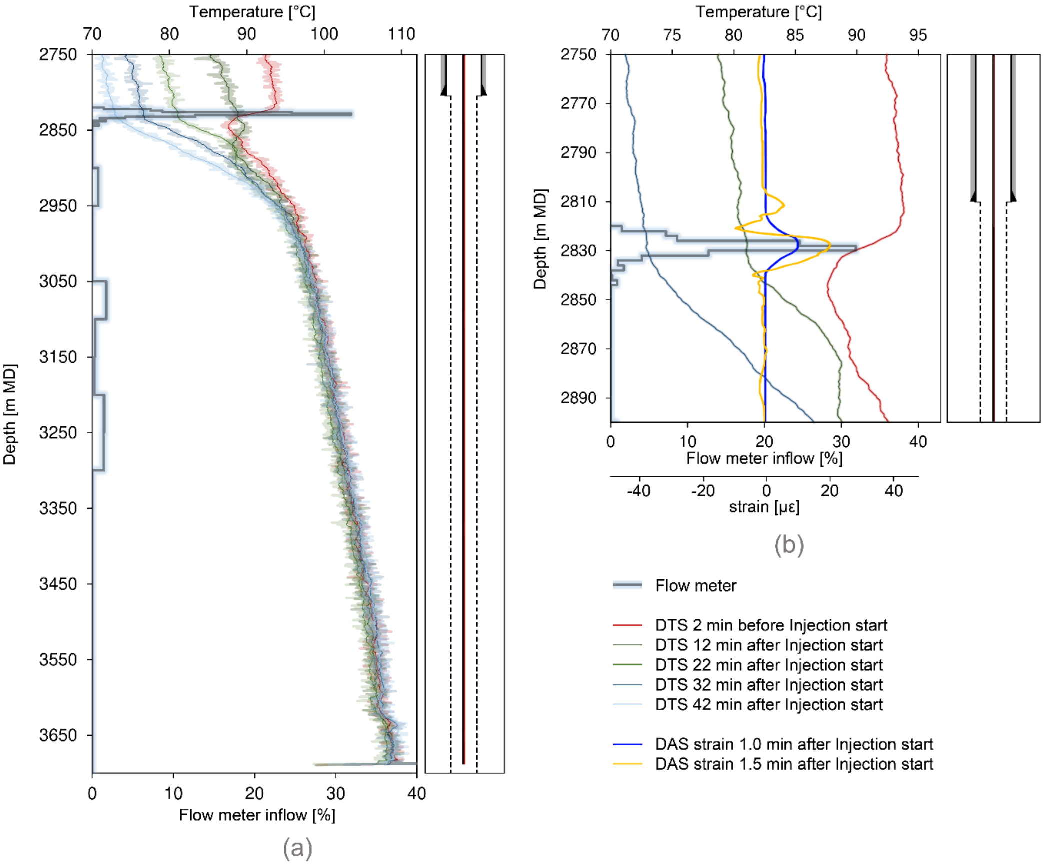

(a)

(b)

Figure 5-14. Comparison of flowmeter injection profile and DTS and DAS response during Inj2. Transparent lines are raw DTS data, sharp lines are moving average over 10 m. (a): flowmeter profile with five DTS profiles in the first hour of cold water injection over from 2750 m MD to TD. (b): Zoomed to top of the reservoir. Flowmeter profile is shown together with three DTS profiles of injection start, each 20 min apart; and DAS strain at 1 min and 1.5 min after injection start.

unknown, however the differences from Inj1 and Inj2 in terms of flow rate (16 l/s in comparison to 23 l/s) and shut-in time (34 weeks in comparison to 4 weeks) are obvious.

Just a little later (+1.5 min), strain built up and negative strain, thus contraction, was present throughout the cased sections, which is related to thermal stress (see Figure 5-8). To verify whether in fact the DAS signal +1 min is related to the noise of flowing fluid, a detailed description of the signal, e.g., analysis of the frequency information needs to be executed. Paleja et al. (2015) used Fourier transformation to directly evaluate flow velocities from DAS. Such is beyond the scope of this study and can be addressed in a future study. However, it is apparent that the DAS data at the hydraulically active zone at 2830 m MD show high dynamics. As testing time progresses, abrupt and spatially defined acoustic signals occur, mostly below 2800 m, more rarely above from 2000 to 2800 m. Lipus et al. (2022) referred to those as “sucker rod events” and gave an analysis of the complete DAS dataset that was created throughout the entire injection test Inj2. DTS profiles show that the same zone took the injected cold water rapidly during the first 42 minutes of injection. The inflection point of the DTS curves is at 2835 m MD, which is very

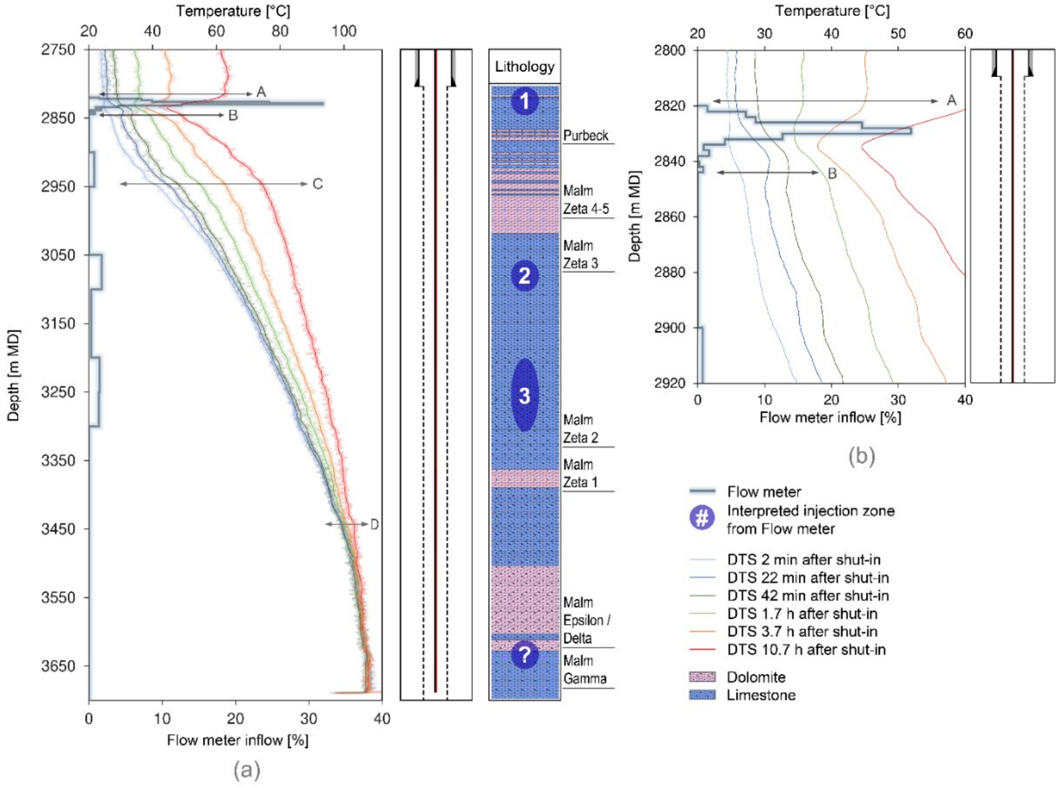

Figure 5-15. Comparison of DTS warm-back profiles and flowmeter injection profile with interpreted injection zones from flowmeter interpretation. Transparent lines are raw DTS data, sharp lines are moving average over 10 m. (a): six DTS profiles taken at different times during the first 11 hours together with flowmeter inflow profile. A, B, C and D mark gradient change of DTS profiles. (b): Zoom to the top reservoir section.

near to the major contribution zone from flowmeter at 2828 m MD to 2830 m MD. Below 2835 m MD, the slope of the DTS profiles increases strongly, indicating less cooling, and below 2950 m MD no difference in the DTS curves of the first 42 minutes of Inj2 is present.

After 24 h of injection, the section from 3500 m MD to TD was the only one unaffected by the cold water injection. As the temperature recovers towards the undisturbed equilibrium, the transient temperature distribution gives evidence of hydraulically active zones (Henninges et al., 2005c; Ali et al., 2014).

Figure 15 shows a comparison of the flowmeter injection profile (Figure 5-6) with DTS profiles at irregular intervals from shut-in to 10.7 h after shut-in. Additionally, the interpreted injection zones of flowmeter (see Figure 5-6) and interesting slope changes of warm-back profiles (A, B, C and D in Figure 5-15) are shown.

Above A, which is at 2820 m MD, heating is uniform, indicating mainly conductive heat transfer (Ali et al., 2014). From A to B there is slow heating, suggesting that most of the injected cold water infiltrated within this zone. This also strongly agrees with the observed major inflow from the flowmeter measurements (zone 1). The gradient of the DTS profiles increases towards B, which may indicate less inflow to the formation near B at 2840 m MD. Below B (2845 m MD to 2950 m

MD), there is a gradient change that indicates minor inflow, most clearly visible in the first 42 minutes after shut-in. Flowmeter did not show any evidence of such at 2845 to 2880 m MD, but a minor spinner response was seen at 2900 to 2950 m MD (< 1 % inflow). During injection, an inflow between B and C is not clearly evident, however some scattered DTS profiles indicate hydraulically activity at 2890 m MD (e.g., 12 min and 22 min after injection start, see Figure 5-14). Between C (2950 m MD) and D (3450 m MD), warm-back profiles are uniform and do not indicate further hydraulically active zones. At D, a locally defined further gradient change is evident over a distance of about 10 m, indicating minor inflows. The questionable zone at 3650 m MD (see zone marked with question mark in Figure 5-6) is not represented by the warm-back profiling.

In contrast to Sakaguchi and Matsushima (2000), who found in hydraulic tests that their DTS system detected flow zones more clearly during injection than during warm-back, in our case the first hours of temperature recovery indicate a hydraulically active zone between B and C (2850 m MD to 2950 m MD) that was not clearly perceived during the injection period. The injection and temperature recovery profiles of the well SN-8R, Sakaguchi and Matsushima (2000) studied, suggest that the different fractures took a relatively similar amount of the injected fluid. In our case, the upper flow zone is very dominant. It is likely that this masks the contribution of the minor hydraulic active zones and that higher flow rates would have caused more response at fractures below the major flow zone during the injection period.

Flowmeter results suggest minor inflow zones between 2900 and 2950 m MD (< 1 % inflow), from 3050 to 3100 m MD (~1.7 %), from 3200 to 3250 m MD (~1.5 %), and from 3250 to 3300 m MD (~1.5 %) that were not visible in neither DAS nor DTS data during injection. Warm-back profiles indicate a minor hydraulically active zone at 2900 to 2950 m MD, but no statement is possible on the zones below. One explanation lies in the different flow rates of the flowmeter injection and Inj1 and Inj2. To keep the hydraulic stress on the reservoir and the mechanical/thermal stress on the sucker rod/cable construction low, flow rates of Inj1 and Inj2 were relatively low (Inj2 with 23 l/s was less than half of that of flowmeter with 50 l/s). From velocity analysis [Figure 5-9 (a)], we have seen that the major inflow zone took almost all of the cold water. It is possible that a higher injection rate would have led to a noticeable reflection of the minor inflow zones detected by the flowmeter. As temperature changes in below 3000 m MD during short-term injection are small, thermal anomalies caused by the injection zones are below the detection limit of DTS. However, it is expected that the DTS-temperature profile during the production will provide answers as soon as the well produces.

The acquired FO-data enhance and verify the flowmeter interpretation and show that flowmeter can still give good results under the given uncertainties – high deviation, close to liner hanger and perforated liner as described above.

5.5 Conclusion and Outlook

The feasibility of installing a permanent fiber optic cable for a permanent monitoring along sucker rod into the reservoir of a deep and deviated geothermal production well was successfully demonstrated at the study site. A comprehensive database could be created that combines conventional logging data with the continuously recorded pressure, acoustic and temperature data of the innovative FO-system, allowing a long-term study of the geothermal reservoir. The FO-monitoring system enables a dynamic monitoring of the thermal distribution in the borehole and the reservoir when the well is set to operation, as well as acoustic studies which can be additionally addressed to the subject of monitoring the pump or micro seismicity. First results that were obtained from the installed FO-monitoring system during the shut-in time and during two cold water injection tests lead to the following conclusions.

The DTS data enabled an observation of the dynamic change of thermal water temperature in the reservoir and explained the origin of an anomaly detected at the end of the wireline temperature log after well completion to be cold water remaining in the hydraulic active zone from the flowmeter test.

Conventional downhole measurements could be complemented by the FO-monitoring-system, e.g. the temperature gradient was derived by the FO-monitoring system over the whole borehole length, hence also in the reservoir, while a wireline temperature logging tool got stuck and was not able to run into the reservoir at the present well deviation. Additionally, DTS measurements were used to crosscheck and correct the wireline temperature log and the P/T gauge for which a processing error could be detected. Flowmeter measurements were also verified with DTS monitoring by successfully comparing the temperature response during a cold water injection and subsequent warm-back period with flowmeter data from the flow zone detection and percentage of inflow in the reservoir at the major zone. However, the flowmeter interpretation showed some uncertainties because the reservoir section is highly deviated and not open hole, but completed with a perforated liner. In addition, a major flowmeter spinner response is at a karstified zone very near to the liner hanger, where turbulence of the fluid is possible due to the well design. Hence, DTS measurements can significantly enhance the flow zone characterization qualitatively as well as quantitatively. By the dynamic long-term monitoring it is speculated that also the uncertainty of flow zone characterization can be more precisely interpreted.

Additionally, a cold water injection test revealed vertical displacement of the FO structure. DAS data were used to verify that the thermal contraction and expansion of the sucker-rod/fiber cable installation was indeed caused by the temperature decrease from cold water injection. Such thermal stress must be considered for calibration issues during future installation and installations of such FO-monitoring system with sucker rod design. These results give advice on how DTS and P/T data should be processed once the well is in operation and the temperature distribution in the well changes significantly.

Although DAS monitoring of the cold-water injection test Inj2 shows primarily thermal/mechanical stress on the sucker rod construction, a reasonable DAS response was observed at the very beginning of Inj2 that agrees well with the injection profile from the flowmeter. However, further research is needed to determine if the signal can be translated into a velocity/injection profile.

Author contributions: FS conceptualized this work, was involved in the installation works and calibration works of the FO-system, and did DTS analyses, flowmeter interpretation, visualization, and wrote the original Draft. ML and TR measured DAS during the injection tests and analyzed and interpreted DAS data. They further calculated the theoretical thermal expansion from DTS. DP was involved in planning, and installing the FO-monitoring system, as well as calibrating DTS. She further contributed to flowmeter interpretation. SH was responsible for planning and executing the installation of the fiber optic cable inside the wells. FE and KZ supervised the project and were involved in conceptualization. KZ was furthermore engaged in review and writing work. All authors read and approved the final manuscript.

Availability of data and materials: The datasets used and/or analyzed during the current study are available from the corresponding author on reasonable request.

Funding: Open Access funding enabled and organized by Project DEAL. This work has been performed in the framework of the project Geothermal Alliance Bavaria and is funded by the Bavarian Ministry of Science and Art.

6

Dynamic Motion Monitoring of a 3.6 km long Steel Rod in a Borehole during Cold-Water Injection with Distributed Fiber-Optic Sensing

This chapter was published as:

Lipus, MP., Schölderle, F., Reinsch, T., Wollin, C., Krawcyk, C., Pfrang, D., Zosseder, K. (2022). Dynamic motion monitoring of a 3.6 km long steel rod in a borehole during cold-water injection with distributed fiber-optic sensing. Solid Earth, 13(1), 161-176. https://doi.org/10.5194/se-13-161-2022

Abstract: Fiber-optic distributed acoustic sensing (DAS) data find many applications in wellbore monitoring such as flow monitoring, formation evaluation and well integrity studies. For horizontal or highly deviated wells, wellbore fiber-optic installations can be conducted by mounting the sensing cable to a rigid structure (casing/tubing) which allows for a controlled landing of the cable. We analyze a cold-water injection phase in a geothermal well with a 3.6 km long fiber-optic installation mounted to a 3/4 in. sucker rod by using both DAS and distributed temperature sensing (DTS) data. During cold-water injection, we observe distinct vibrational events (shock waves) which originate in the reservoir interval and migrate up- and downwards. We use temperature differences from the DTS data to determine the theoretical thermal contraction and integrated DAS data to estimate the actual deformation of the rod construction. The results suggest that the rod experiences thermal stresses along the installation length – partly in the compressional and partly in the extensional regime. We find strong evidence that the observed vibrational events originate from the release of the thermal stresses when the friction of the rod against the borehole wall is overcome. Within this study, we show the influence of temperature changes on the acquisition of distributed acoustic/strain sensing data along a fiber-optic cable suspended along a rigid but freely hanging rod. We show that observed vibrational events do not necessarily originate from induced seismicity in the reservoir but instead can originate from stick–slip behavior of the rod construction that holds the measurement equipment.

6.1 Introduction

Fiber-optic distributed sensing in borehole applications has gained a lot of attention in recent years. Distributed temperature sensing (DTS) has been used to assess rock thermal properties and locations of water-bearing fractures (Hurtig et al., 1994; Förster et al., 1997). DTS was used to perform cement job evaluations and wellbore integrity analysis during and after production tests (Pearce et al., 2009; Bücker and Grosswig, 2017). The performance of a borehole heat exchanger was monitored with DTS to evaluate the heat input along the wellbore and to measure the regeneration time after a heat extraction period (Storch et al., 2013). While DTS has found its way as a standard tool for wellbore monitoring over the last 2 decades, the utilization of distributed acoustic sensing (DAS) is still subject to many research questions. Johannessen et al. (2012) introduced the potential and capabilities for acoustic in-well monitoring applications based on DAS systems which range from, e.g., flow measurements, sand detection, gas breakthrough and leak detection to vertical seismic profiling (VSP). Daley et al. (2013), Mateeva et al. (2014), Harris et al. (2016), Daley et al. (2016) and Henninges et al. (2021) compare traditional geophone with DAS recordings acquired during a vertical seismic profiling campaign (VSP). Götz et al. (2018) on a multi-well VSP campaign at a carbon dioxide storage site by using only one single DAS interrogator. Finfer et al. (2014) performed an experiment to study DAS applications for turbulent single-phase water flow monitoring in a steel pipe. Bruno et al. (2018) investigated the potential to use downhole DAS data for cross-hole monitoring between two adjacent wells by inducing low-frequency pressure pulses to detect high-conductivity zones by measuring characteristic vertical strain patterns. Naldrett et al. (2018) compare fiber-optic technology to traditional production logging tools and provide field data examples of flow monitoring based on both DTS and DAS with wire-line-type installations. Ghahfarokhi et al. (2018) analyze an extensive data set including borehole geophone and DAS during hydraulic fracturing (cable behind casing) to study microseismicity and low-frequency events in the borehole. Raab et al. (2019) show that DAS data from a behind casing installation can be correlated to conventional cement-bond-long (CBL) recordings by analyzing the acoustic data in noisy drilling and testing operations. Chang and Nakata (2020) and Martuganova et al. (2021) report on reverberating signals in DAS recordings which can occur on free-hanging cables in geothermal wells during fluid injection and which are probably caused by bad cable-to-well coupling. In all reported cases, the coupling of the sensing glass fiber to the surrounding media plays a crucial role for the application of DAS technology.

Especially for the monitoring of deformations occurring over longer time periods, i.e., from minutes to hours to days, the coupling of cable and surrounding environment becomes essential to derive any meaningful result from fiber-optic strain sensing. Whereas Reinsch et al. (2017) provide a theoretical approach to describe the response of the sensing fiber in dependence of the specific cable design, the coupling of the cable to the rock formation strongly depends on the specifics of a measuring experiment. Lipus et al. (2018) compare data from fiber-optic strain sensing and data from a conventional gamma–gamma density wire line log during a gravel packing operation in a shallow well for heat storage. Sun et al. (2021) demonstrate with a laboratory and field test that the extent of a deformed reservoir sandstone and silt caprock by injected CO2 can be quantitatively evaluated using static distributed strain sensing over periods of 42 h (cable behind casing). Zhang et al. (2021b) provide an attempt to use distributed strain sensing to monitor elastic rock deformation during borehole aquifer testing to derive hydraulic parameter information. Miller et al. (2018) compare DTS and time-integrated DAS recordings from a borehole and find a correlation between DTS recordings and very low-frequency DAS strain recordings. In their work, they report on repeating "slip events" seen in the DAS data as short and confined vibrational events upon temperature changes in the well.

The study at hand observes similar slip events and shows their causal connection to the thermo-mechanical response of the borehole construction to water flow therein.

Installing a fiber-optic cable in a borehole requires specialized equipment. Depending on the aim of the fiber-optic monitoring campaign, different cable installation types are possible. One way is to permanently install the cable by mounting it to the outside of a casing and run it together with the casing into the well and cement it in place (Henninges et al., 2005a; Reinsch, 2012; Lipus et al., 2021). A cemented fiber-optic cable generally provides a thorough mechanical coupling to the surrounding structure which is favorable for DAS data quality. Due to its placement behind the casing, the fibers do not interfere with well operations and monitoring of the well can be performed at any time. However, the cemented annulus of a well is a crucial secondary barrier element for well integrity, which is compromised by the installation of a fiber-optic cable. A fluid pathway could potentially be created along the cable. Cases where the well completion design includes liner elements, a permanent cable installation behind casing to the end of the well is technically not possible or, at least, very challenging. In such cases, other installation types are available. A semi-permanent installation along, e.g., production tubing or a temporary installation via a wire line cable or coiled tubing allow cable placements inside the borehole after drilling is finished. Munn et al. (2017) present a field test of a novel "flexible borehole coupling technique" that allows deploying fiber-optic cables in boreholes after completion has finished with an improved mechanical coupling compared to loosely installed fiber-optic cables. Due to physical constrains, this technology is best suited for shallow boreholes (< 425 m). Becker et al. (2017) provide an analysis of borehole fracture displacements using such a cable coupling technique. Another method to place a fiber-optic cable in a well is by mounting it to a rigid rod (e.g., a pump sucker rod). The stiff sucker rod acts as a centralizer and guides the flexible fiber preventing it from coiling up. Such a type of installation is especially advantageous if the cable should be placed in a deep and deviated well.

To utilize acquired fiber-optic data from a free-hanging/free-lying rod with the highest possible confidence, it is important to understand the behavior of such a long and stiff structure inside a well. Heating and/or cooling of the well will lead to thermal stresses in the material which potentially result in contraction or expansion of the sucker rod and fiber-optic cable construction. As the fiber-optic cable is firmly attached to the rods, these dynamics influence the distributed strain and temperature sensing. From DTS monitoring, Schölderle et al. (2021) found that measurement equipment in the previously described setting does indeed contract upon the injection of cold water and that the points spatially sampled by the distributed sensing change their position. Besides a detailed analysis based on DAS and DTS data of the rod's dynamics in response to temperature changes during a cold-water injection, we show that the resulting thermal stresses are released by the observed vibrational events thus indicating stick–slip-like behavior of the rod–borehole wall compound.

6.1.1 Well Description and Cable Installation

The fiber-optic cable is installed within a production well at the geothermal site Schäftlarnstraße in Munich, Germany. A detailed description of the geothermal site and the cable installation procedure is presented in Schölderle et al. (2021). The well was completed with a 20 in. anchor casing, a 13 3/8 in., a 9 5/8 in. liner and a perforated 7 in. production liner. An overview of the landing depths is presented in Table 1. The design of the borehole completion is schematically shown in Fig. 3d. The well is vertical to a depth of 250 m. Below 250 m, the well is slightly inclined to 4° down to a depth of 879 m TVD (true vertical depth) (880 m MD, measured depth). A number of kick-off points (KOPs) are located along the well path. These are also listed in Table 2. In the Results section, a survey shows the well path. From a flowmeter log it is known that the most prominent feed zone in the well is just below the transition from 9 5/8 in. liner to 7 in. perforated liner in the depth interval between 2825 – 2835 m MD.

The downhole fiber-optic cable is a tubing-encapsulated fiber (TEF) that contains two multi-mode and two single-mode fibers. In this fiber-in-metal-tube (FIMT) construction, the sensing fibers are embedded in gel and placed in a metal tube. At elevated strain levels, the gel deforms plastically and allows for a relative motion between fiber and cable. Also, creep between cable construction and optical fibers can occur. Strain measurements with such a type of cable are typically applicable for dynamic strain changes (high frequencies) and low deformations (Reinsch et al., 2017). For longer periods and higher deformations, fiber-optic strain sensing with FIMT cables is still possible but it becomes less localized due to deformation of the material. A laboratory experiment on the relative motion between cable structure and optical fiber in a FIMT cable at higher mechanical stress over time is presented in the literature (Lipus et al., 2018). The cable has a total nominal diameter of 0.43 in. (1.1 cm) and the cable mantle is made of polypropylene. The cable was landed in the well after drilling was finished. To safely and effectively navigate the placement of the fiber-optic cable down to the end of the almost 3.6 km long well, the cable was strapped to steel rods (sucker rods) which were installed in the well together with the cable. The steel sucker rod also helps to retrieve the cable from the borehole when needed. Due to the high deviations in the well at depth, the cable needs to be gently pushed into the well. Therefore, the rigid sucker rod is used for the installation instead of a wireline-type installation. The final landing depth of the sucker rod construction is 3691 m (MD). Figure 6-1

Figure 6-1. Downhole cable configuration of the sucker rod with a centralizer (black) and the fiber-optic cable (yellow).

depicts the configuration of the sucker rod/fiber-optic compound. Together with a number of crossover elements and the final landing joint, more than 400 individual sucker rod elements were installed in the well. In the following, we refer to the sucker rod/fiber-optic cable construction as ‘the rod’. The depth reference for the DTS (spot warming) and DAS (tap test) is set to surface.

A fiber-optic pressure/temperature (P/T) gauge was installed with the rod and positioned at the top of the reservoir section at 2755 m (MD).

6.1.2 Monitoring Campaign

The data shown in this study were measured before and during a cold-water injection test in a geothermal well. Before the start of fluid injection, the well was shut-in for 29 d, so that the initial temperature profile is close to the natural geothermal gradient of the Bavarian Molasse basin (see Schölderle et al., 2021). The temperature at the well head was 17 °C and increasing up to 110 °C at the bottom of the well just before the injection start (see profile ‘00:48’ in Figure 6-4a). Cold-water fluid injection started on 23 January 2020 at 00:56 CET by pumping water through the wellhead which leads to a cooling of the well. With an initial water table at a depth of 170m below surface, water was injected from the surface without pressure built-up at the wellhead. The cold-water injection was maintained for 24 h at a flow rate of 83 m^3/h. In this study, we analyze the transient phase of well temperature change for the first 72 min of cold-water fluid injection.

6.2 Data Analysis

The analysis in this study is based on the comparison of strain derived from fiber-optic distributed temperature sensing (DTS) on the one hand and distributed acoustic sensing (DAS) on the other.

Table 6-1 . Well design at geothermal site Schäftlarnstraße, Munich (see also Figure 6-3).

Drill bit Ø	Type	Casing/liner Ø	Top (TVD/MD) (m)	Bottom (m TVD/MD)
	standpipe	30 in.	surface	59.1/59.1
26 in.	anchor casing	20 in.	surface	866.2/867.5
17 ½ in.	liner	13 3/8 in.	766.0/767.0	1812.3/2010.0
12 ¼ in.	liner	9 5/8 in.	1740.0/1907.2	2408.7/2819.0
8 ½ in.	perforated liner	7 in.	2412.2/2810.1	2932.7/3716.0
	KOP	**Inclination (°)**	**Depth (TVD/MD) (m)**	**Direction (°)**
	no. 1	44	879/880	287
	no. 2	42	1819/2220	250
	no. 3	58	2432/2850	250
	no. 4	57	2775/3432	231

6.2.1 Derivation of Strain from DTS

DTS uses each location of a glass fiber as a sensor for temperature (Hartog, 1983; Hartog and Gamble, 1991). This is achieved by coupling laser-light pulses into a glass fiber and analyzing the Raman spectrum of the backscattered light whose origin along the fiber is determined by the two-way travel time of the light. In this study, we use a system based on Raman backscatter. Temperature profiles were acquired every 10 min with a spatial sampling of 0.25 m. Detailed information about the performance of the fiber-optic system m and the calibration procedure are presented in Schölderle et al. (2021).

We calculate the change in temperature from DTS at the start of fluid injection and the profile later during fluid injection. From DTS measurements we may predict thermomechanical deformation according to

$$\varepsilon_{DTS}\,(x) = \alpha_{rod} \cdot \Delta T\,(x), \qquad \text{(eq. 6-1)}$$

where α_{rod} is the thermal expansion coefficient and $\Delta T\,(x)$ is the temperature difference at two subsequent points in time at some location x of the fiber. The rod construction as a whole consists of many different materials with different thermal expansion coefficients, such as the sensing fibers, gel filling, metal tubes, polypropylene mantle, and steel rod and nylon centralizers. However, the steel of the sucker rod and the steel of the fiber-optic mantle are the dominant material by weight and the most relevant for any thermal stresses. The sucker rod consists of 4332 SRX nickel–chromium–molybdenum steel with a thermal expansion coefficient of 10 – 13 $\mu\varepsilon/K$ (Hidnert, 1931), where 1 $\mu\varepsilon = 10^{-6}$ m/m, and a modulus of elasticity of 200 GPa (Engineering ToolBox, 2004). The second-most dominant material is the polypropylene cable mantle with a modulus of elasticity of 1.5–2 GPa (Engineering ToolBox, 2004). The proportion of steel on the thermal stresses in the rod construction are 99.8 %. For simplicity, we assume that thermal expansion coefficient α_{rod} = 13 $\mu\varepsilon$/K for the sucker rod/fiber-optic cable construction and neglect the other materials.

6.2.2 Direct Measurement of Strain via DAS

Similar to DTS, DAS also analyses the backscatter of light coupled into a fiber from one end. Upon contraction or dilatation, the strain rate of the fiber, i.e., the temporal derivative of relative change in length, can be derived from the temporal change in the interference pattern of coherent light elastically scattered (Rayleigh scattering) from adjacent points within a certain interval of fiber called the gauge length (Masoudi et al., 2013). The centroid of the gauge length is defined as a sensor node. The location (x) of a sensor node along the fiber is again determined by the two-way travel time of light from its source to the node and back. In our study, DAS data are acquired at 10 000 Hz and down-sampled to 1000 Hz. The gauge length and spatial sampling are 10 and 1 m, respectively. No additional filtering was applied in post-processing (no high-pass and no low-pass filtering).

In contrast to DTS, DAS directly yields the temporal derivative of strain. In order to convert the measured strain rate $\dot{\varepsilon}(x,t)$ data to strain $\varepsilon_{DAS}(x)$ at each location, we integrate in time:

$$\varepsilon_{DAS}(x) = \int_{t1}^{t2} \dot{\varepsilon}\,(x,t)dt, \qquad \text{(eq. 6-2)}$$

where *t1* and *t2* delineate the time window and $\dot{\varepsilon}(x,t)$ the recorded strain rate at position x. In the following we speak of ‘measured strain’ ε_{DAS} in contrast to ‘predicted or expected’ strain ε_{DTS}.

We compare ε_{DTS} with ε_{DAS} measurements. We then use the ε_{DTS} data to compute the contractional forces along the rod which occur due to cooling. We compare the result with a static friction curve that was estimated from the sucker rod tally and borehole inclination.

6.2.3 Stick–Slip Approach

As the thermal contraction of the cooled sucker rod inflicts a sliding movement of the rods along the borehole wall, we must consider the friction of their relative motion. This friction would yield a stick–slip motion, which is observed almost everywhere when two solid objects are moving relative to one another. A detailed review of the origins of stick– slip behavior in mechanical parts as well as an experimental and theoretical analysis on stick–slip characteristics is presented in the literature (e.g., Berman et al., 1996). In the simplest case, a stick–slip motion appears when the static friction force F_f between two stationary solid bodies is overcome. A schematic drawing of the forces on an interval of the sucker rod construction at a depth with borehole inclination is presented in Figure 6-2.

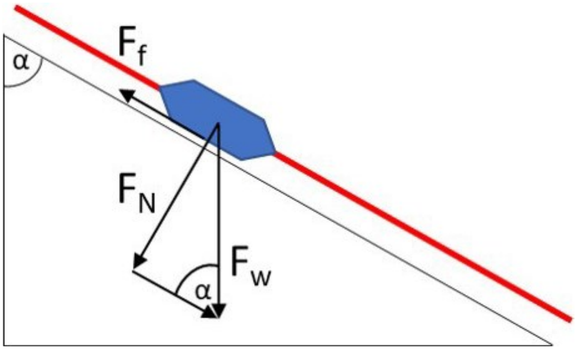

Figure 6-2. Static friction force F_f and normal force F_N applying on a sucker rod contact point (nylon centralizer) as a function of the weight force F_w and the borehole inclination 90° - α.

The static friction force F_f can be calculated according to

$$F_f = \mu \cdot F_N, \qquad \text{(eq. 6-3)}$$

where F_N is the normal force and μ the static friction coefficient. The value for μ = 0.36 was obtained from a plateto-plate experimental analysis on the stick–slip behavior between steel and a glass-fiber-reinforced nylon specimen (Muraki et al., 2003). The force F_N is calculated according to

$$F_N = F_w \cdot \sin\alpha = \mathrm{g} \cdot \mathrm{m} \cdot \sin\alpha, \qquad \text{(eq. 6-4)}$$

where F_w is the gravitational weight force and α the borehole inclination. Each sucker rod element is 9.1 m long, weights 15.7 kg and is equipped with four nylon centralizers and the fiber-optic cable (20 g/m). Therefore, the weight force for each contact point of the rod construction yields F_w = 9.81 m/s² · 15.9 kg/4 = 39.0 N. Regarding the lowermost part of the rod construction as an example, this means that for the last nylon centralizer (borehole inclination of 54°), a static friction force of F_f = 0.36 · 39.0 N · sin (54°) = 11.3 N is calculated. With respect to contraction of an initially unstressed rod construction, for each subsequent nylon centralizer towards the surface, the friction force of the rod at the given depth is calculated by the cumulative sum of all friction forces from the nylon centralizers below. The friction force increases with decreasing well depth. Two further weights are added to the friction force profile: the bottom end of the sucker rod is a 1.4 m long steel piece with a weight of 64 kg and the carrier of the P/T gauge at 2755 m MD is a 2.2 m long steel piece with a weight of 105 kg. Here, we applied a static friction coefficient for steel on steel of μ = 0.8 (Lee and Polycarpou, 2007).

The expected thermal contraction ε_{DTS} can also be translated to a force. Assuming a Young's modulus for stainless steel of E = 200 GPa (Cardarelli, 2018) and given the cross-sectional area of the rod (A_{rod} = 2.9 cm²), we can calculate the applied force F_{app} at each location along the rod which was thermally induced within the investigated 1 h cold-water injection period:

$$F_{app} = \sigma \cdot A_{rod} = E \cdot \varepsilon_{DTS} \cdot A_{rod}. \qquad \text{(eq. 6-5)}$$

For simplicity, we assume that the elasticity from the fiber-optic cable and the nylon centralizers are neglectable and that the steel dominates the mechanical behavior of the structure. Furthermore, we make the assumption that no mechanical stresses are exerted on the rod prior to the cold-water injection. This allows us to set a zero-force baseline before injection start for the stick–slip analysis.

6.2.4 Stick–Slip Event Detection and Picking

In the DAS data we monitored repeating vibrational events with ongoing cold-water injection in the deeper part of the well. These events are characterized by a sudden DAS amplitude peak at some depth and an up- and downward directed move-out. With time, the spatiotemporal distribution of these vibrational events changes. To automate the detection of depth location and move-out of an event, we employ a short-term/long-term average (STA/LTA) trigger (Allen, 1978; Vaezi and Van der Baan, 2015) using the Python toolbox ObsPy (Beyreuther et al., 2010). The parameters used for the STA/LTA analysis can be found in Table 6-2.

6.3 Results

Figure 6-3 shows examples of raw and unprocessed strain rate data measured with the DAS unit in the well at the start of cold-water injection (first subplot), 1 h after start of fluid injection (second subplot) and shortly after the end of the 24 h water injection period (third subplot). Each subplot depicts 10 s of data with the same data color scaling. A number of features can be recognized in each of the data examples. At the depth marked with the arrow ‘A’, there is a transition from a noisy depth interval above to a rather quiet one below. The transition marks the location of the water table in the well. From the wellhead, the water free-falls down to the water table at about 170 m below surface. In the cased hole section down to the depth of the transition to the perforated liner, high-velocity tube waves (around 1500 m/s) are present which are reflected at the liner shoe of the 9 5/8 in. casing at ca. 2810 m MD (arrow ‘B’ in first subplot).

Table 6-2. Parameters used for the STA/LTA detection method.

Parameter	Value
STA window length (N_S)	1 s (1000 samples)
LTA window length (N_L)	3 s (3000 samples)
Trigger start threshold τ_1	2
Trigger end threshold τ_2	0.8

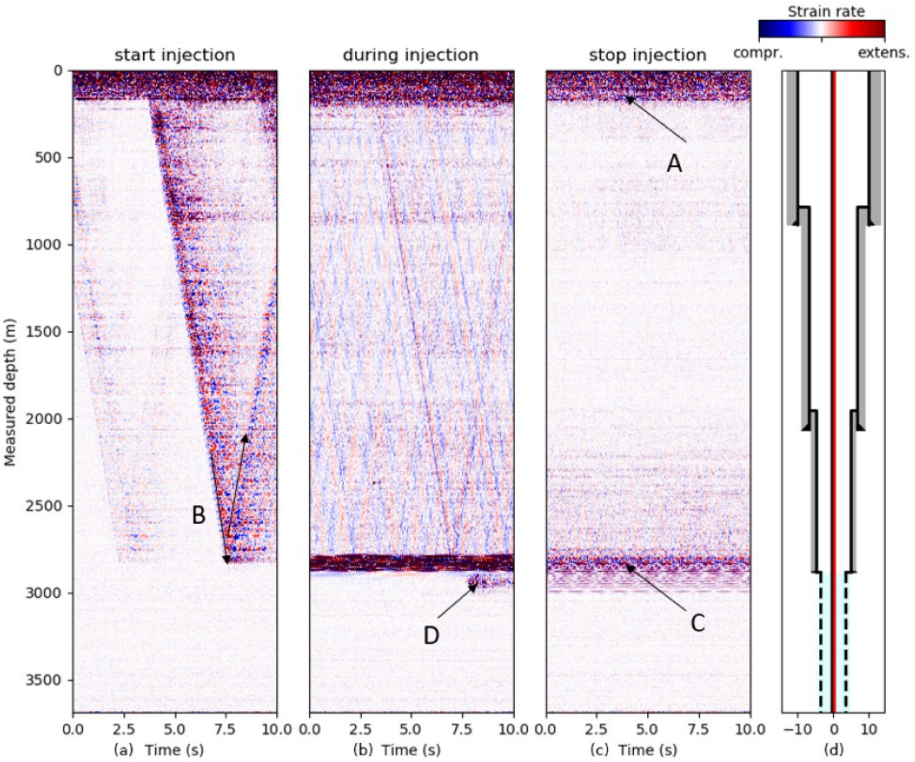

Figure 6-3. DAS raw data examples over the scope of the cold-water injection phase for (a) the onset of fluid injection, (b) ongoing injection and (c) termination of fluid injection. Blue colors show relative compression and red colors relative extension. The color ranges are the same for all subplots.

Below B, the cable is located inside the perforated liner. The tube waves are not further guided in this interval and the noise level is rather low. This abrupt and localized signal is interpreted as a sudden contraction of the sucker rod. In the uppermost 100 m of the perforated liner section (2810 – 2900 m MD), a strong signal is present in the second and third subplot (arrow 'C'). The arrow 'D' marks another common characteristic feature in the DAS data which was observed over the analyzed cold-water injection period. This abrupt and localized signal is interpreted as a sudden contraction of the sucker rod.

6.3.1 Sucker Rod Contraction

Figure 6-4 shows fiber-optic data from DTS and DAS for the first hour of cold-water fluid injection testing. The first subplot shows three DTS profiles at 00:48, 01:18 and 02:08, which are −8, +22 and +72 min relative to the cold-water injection testing. The first subplot shows three DTS profiles at 00:48, 01:18 and 02:08, which are −8, +22 and +72 min relative to the cold-water injection start. The entire rod from surface to 3100 m experiences cooling. Below the most prominent feed zone of the well at 2830 m MD, the cooling of the well decreases. This is because most of the injected cold water flows into the formation (2825 – 2835 m MD) and the fluid column below remained rather undisturbed. A theoretical tensile strain from thermal contraction of the

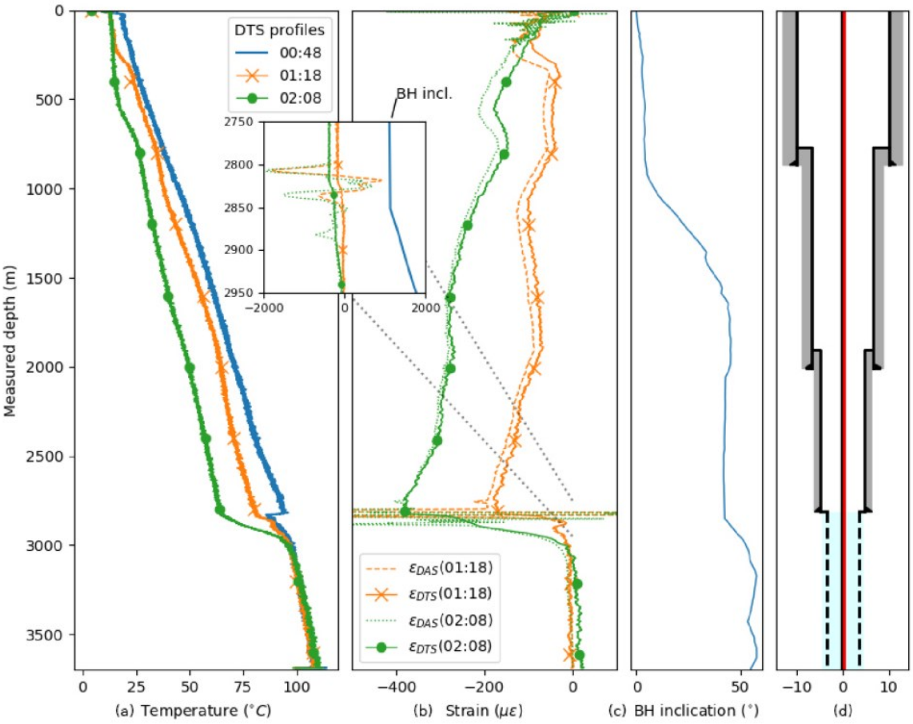

Figure 6-4. Downhole monitoring data during the cold-water injection test. (a) DTS temperature profiles. (b) Comparison of strain profiles εDTS and εDAS. (c) Borehole inclination. (d) Wellbore schematic.

steel rod (and the fiber-optic cable) ε_{DTS} can be derived from the temperature difference between the two profiles for a certain depth relative to the profile at 00:48. The second subplot compares the 15 m moving average of ε_{DTS} calculated after eq. 5-1 with the local strain (ε_{DAS}) calculated after eq. 5-2 during the same time interval. The third subplot shows the borehole inclination from the deviation survey. On the fourth subplot, a schematic representation of the casing/liner landing depths is shown together with the location of the rod.

In general, a clear match is visible between ε_{DTS} and ε_{DAS} for the entire well which means that the strain the steel rod experiences (ε_{DAS}) follows the predicted thermal contraction (ε_{DTS}). However, there are depth intervals where the experienced strain (ε_{DAS}) exceeds and others where it falls short on the predicted strain (ε_{DTS}). Until 2825 – 2835 m MD, where the most prominent injection interval is located, ΔT increases with increasing depth. At the injection interval ΔT rapidly increases. Below this zone, no thermal contraction is expected.

Along the 13 3/8 in. casing interval (from top liner hanger 13 3/8 in. at 768 m MD to top liner hanger 9 5/8 in. 2010 m MD), ε_{DTS} and ε_{DAS} are negative and show the same trend, thus indicating the expected contraction. In absolute values expected strain ε_{DTS} exceeds the measured strain ε_{DAS}. Over this depth interval, the well inclination increases from nearly vertical to 45°.

At the transition to the 7 in. perforated liner at 2810 m MD (top liner hanger packer) a notably different ε_{DAS} pattern is measured compared to ε_{DTS} (box plot in Figure 6-4). In the depth interval 2795 – 2815 m MD, the expected contraction from ε_{DTS} at 01:18 yields –170 με (–380 με at 02:08),

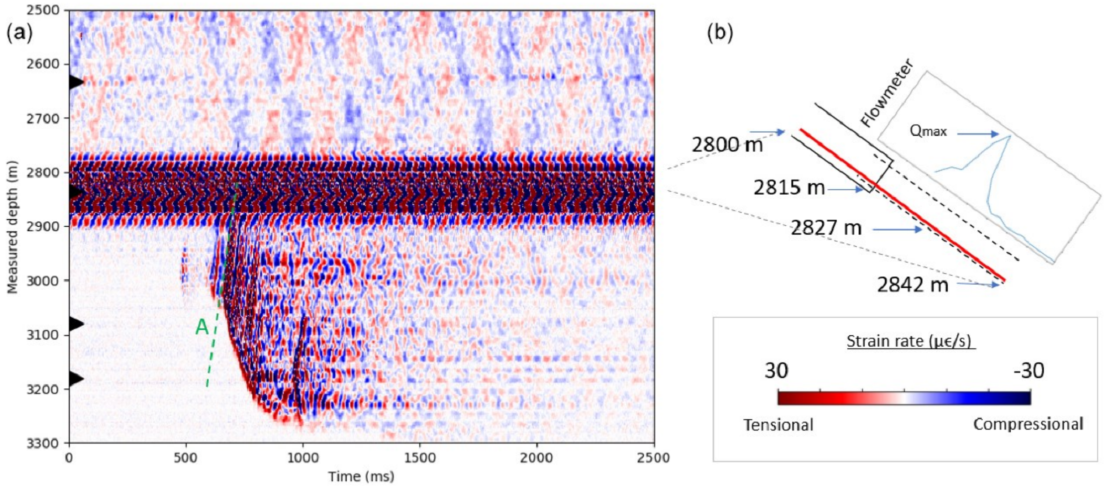

Figure 6-5. Sucker rod contraction event displayed by strain rate DAS data (a). The black arrows on the left y axis mark the depth location of time series used for the spectrograms in Figure 6-7. Line 'A' marks the move-out of the signal at a speed of 4000 m/s. The schematic drawing shows the inclination of the borehole with the fiber-optic cable (red) lying inside of the casing (b). The inflow profile from a wire line flowmeter measurement is shown by the blue graph.

while the estimated contraction from ε_{DAS} at 01:18 results in –1740 με (–1950 με at 02:08) με between 2805 – 2810 m MD, which is more than a factor 10 higher (factor 5 at 02:08). In the depth interval 2815 – 2830 m MD, ε_{DAS} shows an extension of the rod with a maximum of 900 με at 01:18, while ε_{DTS} decreases from –160 με at 2815 m MD to –55 με at 2835 m MD. This is the only locations in which the integrated strain rate from ε_{DAS} shows extension instead of the predicted contraction. At 2830 – 2850 m MD, another interval with extraordinary high ε_{DAS} readings relative to ε_{DTS} is present. Below 2850 m MD, ε_{DAS} and ε_{DTS} again follow the same trend at 01:18. At 02:08, the ε_{DAS} and ε_{DTS} show a discrepancy down to 2890 m MD and the same trend below. The gyro data show a sudden increase in the inclination of the borehole at 2850 m MD. Between 2900 – 3100 m MD, the temperature difference between the two DTS profiles rapidly decreases (see Figure 6-4, first and second subplot). At 02:08, the DTS profile shows slightly increased temperatures (+1 ◦C) with a constant offset from 3100 m to the end of the cable compared to the DTS profile at 01:18. This leads to a constant offset of a positive expected strain ε_{DTS}. The measured strain ε_{DAS} shows no offset in this depth interval.

6.3.2 Sudden Contraction Events

6.3.2.1 Event Description

A close-up of raw DAS data is shown for the depth interval 2500 – 3300 m MD around the transition from cased hole to perforated liner 52 min after the start of the cold-water fluid injection (see Figure 6-5). At this time, the DAS records a transient strain rate anomaly. Similar events are repeatedly observed in the course of the measurement during the cold-water injection

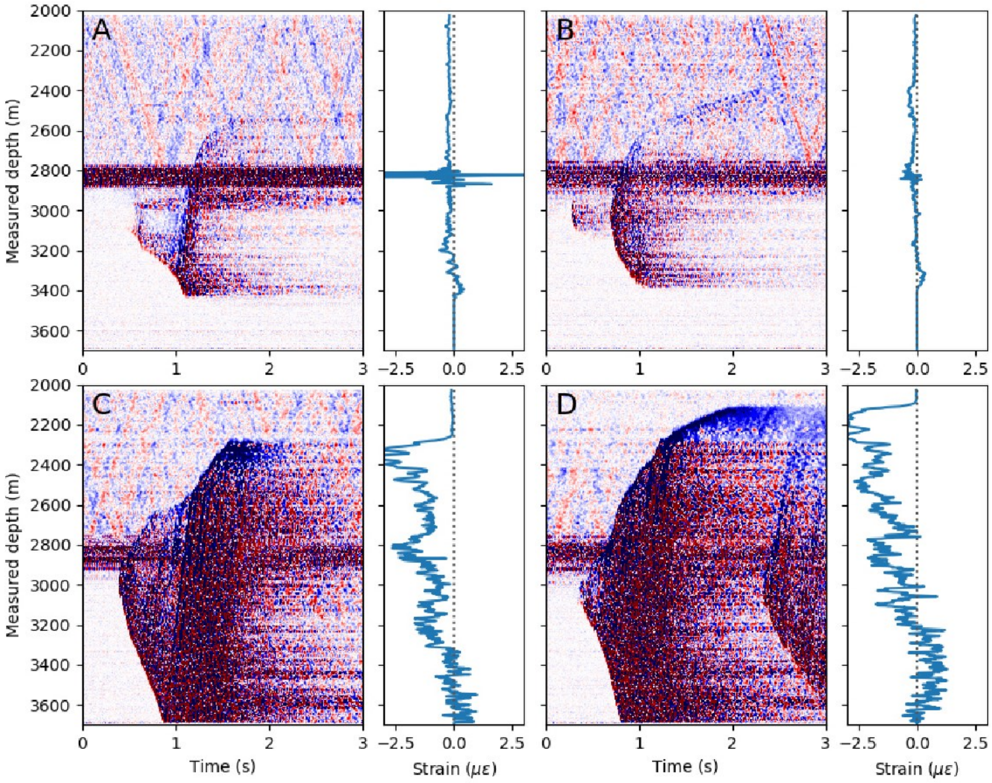

Figure 6-6. Four raw DAS data examples of sucker rod events with the integrated strain rate (εDAS) over a period of 3 s. The timing of the events relative to the start of cold-water injection is as follows: A – +65 min; B – +110 min; C – +147 min; D – 210 min

periods. Using the event shown in Figure 6-5 as a representative example, we describe common features of these events in the following. Its origin lies at 600 ms and 3000 m MD and is characterized by an abrupt increase in the measured strain rate. The sudden increase in strain rate amplitude propagates both up- and downwards along the well with a compressional and tensional sign of amplitude, respectively, where the propagation velocity upwards is approximately 3900 m/s (green line A in Figure 6-5). In contrast, the downward propagation velocity is slower and shows irregularities from 650 – 1260 m/s. Most striking is the decay of the velocity from 3200 m MD onwards and the eventual stop of propagation slightly above 3300 m MD. In an upward direction, this event is halted somewhere in the noisy interval where the reservoir section of the borehole begins. The event is followed by elastic reverberations that decay after approximately 0.5 s.

Further examples of such events are plotted in Figure 6-6 (events A, B, C and D). They all have in common that they originate below 2900 m MD and trigger a contraction above and an extension below. The previously discussed event is characterized by a smaller precursor 100 ms before the origin of the large event at the same depth. Precursors and successors can also be observed in the examples in Figure 6-6 (in particular in Figure 6-6, event B), yet the events shown here are distinguished by the fact that their upwards propagation extends beyond the noisy reservoir

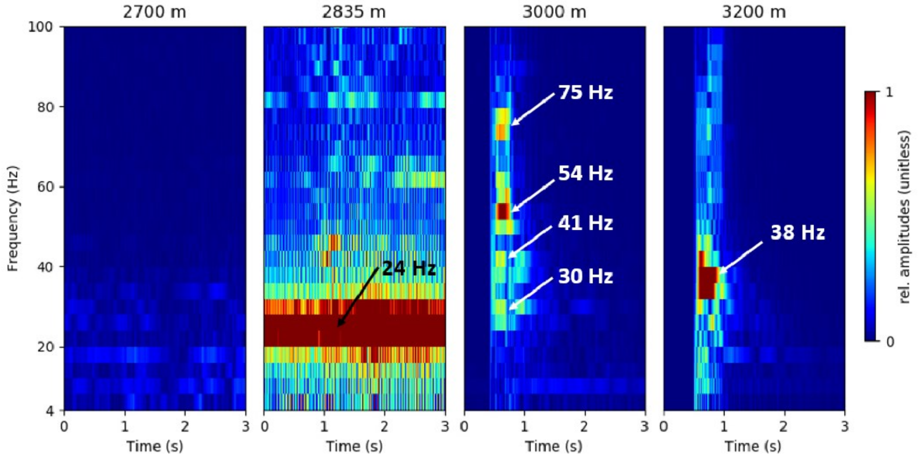

Figure 6-7. Spectrograms for a 250 ms moving window at different depth along the well during the sudden vibrational event depicted in Fig. 5. Red colors indicate high amplitudes, blue colors low amplitudes. The relative amplitudes are displayed by the same color ranges for all subplots.

section. All exemplary events except event A, whose downward propagation is arrested rather suddenly, have in common that the up- and downward propagation slow down before coming to a halt. Another striking observation in all of the events is that the initial onset propagates slower than the reverberations in the coda.

While the exact shape of the spatial propagation and length varies (length between 20 – 1600 m), the duration of these events is mostly in the range of 0.5 s with some fading noise/reverberation afterwards. These events typically show a tensional signal at the energy front in the downward direction, while the initial energy front upwards is mostly compressional. As the vibrational signal propagates along the rod, a succession of compressional and tensional waves is created which moves with a velocity of about 3900 m/s along the rod (as shown by the green line A in *Figure 6-5*). The downward propagation of the first arrival changes its velocity from the onset of the event towards the end of the vibrational event. In the first 50 ms, it increases in velocity; then it stays constant before it gradually decreases in velocity at around 700 ms below 3200 m MD.

The four black arrows on the left y axis in Figure 6-5 indicate the time series for which the four spectrograms shown in Figure 6-7 were calculated with a moving window of 250 ms. The DAS strain rate time series at 3000 and 3200 m MD show the onset of the slip event at 0.5 s with dominant frequencies of the first break between 30 and 75 Hz. The slip only lasts approximately 0.5 s, but reverberations of different duration and different frequencies can be observed in the band below 30 Hz depending on the rod segment. For instance, at 3000 m MD long-lasting reverberations occur at ~10 Hz, whereas at 3200 m MD they occur at 20 Hz. As can be seen from the spectrogram from the DAS strain rate recordings at 2700 and 2835 m MD, the slip event does not penetrate into and beyond the feed zone, whose characteristic noise at 24 Hz remains undisturbed just as the low-frequency pattern of the tube waves above.

6.3.2.2 Event Detection over Time

We applied a STA/LTA algorithm to automate the detection of the sudden vibrational events within the first 72 min of cold-water fluid injection. Three attributes are obtained for each event: (a) the depth location where the event starts; (b) the lower end and (c) the upper end of the event according to the STA/LTA algorithm. Figure 6-8 shows one example of the automated detection with the STA/LTA trigger. The upper subplot shows an example trace of raw DAS data at a depth of 3120 m MD (marked by the black arrow in the lower subplot) and the corresponding STA/LTA characteristic function. Beginning and end of the detection are marked by the green and orange crosses, respectively. The lower subplot shows spatiotemporal DAS data and the detection of two vibrational events.

All vibrational events which occurred within the first 72 min of cold-water fluid injection are plotted in Figure 6-9. Gray circles mark the spatiotemporal origin of vibrational events. The corresponding vertical black line indicates the spatial extent of the respective event. In this representation, events with a spatial extent of less than 20 m are neglected. Such small events occur between 4 – 10 times per minute in the depth region from 1250 – 2750 m MD over the entire investigated 72 min after fluid injection start. Within the first 15 min, only a relatively small number of bigger vibrational events occur, i.e., events which extend over more than 20 m. Early events (within the first 5 min relative to injection start) appear in the depth region between 1250–1900 m MD. Except for two large events (4 min: 2260 – 2730 m MD; 6 min: 2040 – 2700 m MD), the spatial extent of the vibrational events is rather small. One single event was recorded at a depth of 3540 – 3580 m MD close to the shoe of the installation. With time, the depth of vibrational events increases to 2900 m MD. From 17 min onwards, the occurrence of vibrational events is mostly constrained in the depth region from 2900 – 3100 m MD. The maximum spatial extent of large vibrational events increases with time. From 01:18 (+22 min after injection start) onwards, most of the events extend into the depth region of 2835 – 3080 m MD. At 02:08 (+72 min to injection start), the spatial extent of the events is 2500 – 3470 m MD.

With time, the frequency of the occurrence of the events decreases: 4 – 5 h after injection start, large events (such as in Figure 6-6 c and d) appear every 10 – 15 min; 8 h after injection start, large events appear approximately every 25–40 min.

6.3.3 Friction Force Model

The static friction force F_f after eq. 6-3 is compared to the applied force from thermal contraction of the rod F_{app} after eq. 6-5, which was evaluated for the period from injection start to 01:18 (+22 min after start of injection) and to 02:08 (+72 min after start of injection) (Figure 6-10). The gravitational weight force F_w per nylon centralizer is constant for every contact point of the rod. The force needed to overcome the cumulative static friction F_f is a function of the borehole

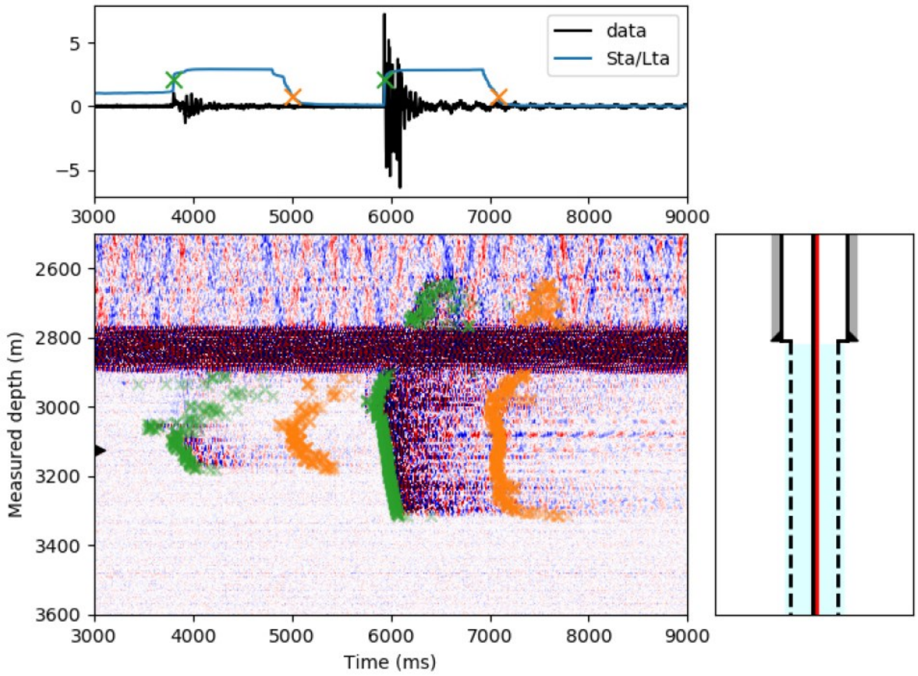

Figure 6-8. STA/LTA trigger algorithm applied as an automated detection method for vibrational events. Trigger start and end is marked with green and orange crosses.

inclination. F_f increases from the bottom of the rod installation at 3691 m MD towards 1000 m MD. The bottom end of the sucker rod and the carrier of the P/T gauge at 2755 m MD create an additional static friction force of 0.4 and 0.5 kN, respectively. Above 1000 m MD, the well is nearly vertical and only little static friction is expected. The static friction F_f at 1000 m MD yields 26.1 kN. F_{app} at 01:18 is lower than F_f for the entire installation length. Only in the depth interval 2731 – 2820 m MD does F_{app} approach a force of 10.5 kN, which is close to F_f. This indicates that forces are sufficient to initiate relative motion between sucker rod and casing at that depth. With ongoing cold-water fluid injection, the applied forces F_{app} increase with further decreasing temperatures. At 02:08, F_{app} surpasses the frictional forces in the depth range from 2150 – 2912 m MD. F_f and F_{app} intersect at 17.0 and 9.3 kN, respectively. At the depth interval from 2732 – 2820 m MD, the applied force peaks at 22.0 kN (shown in Figure 6-10). For all estimates given above, it is assumed that the sucker rod did not move relative to the casing; i.e., thermal stresses can build up but will not be released by relative motion.

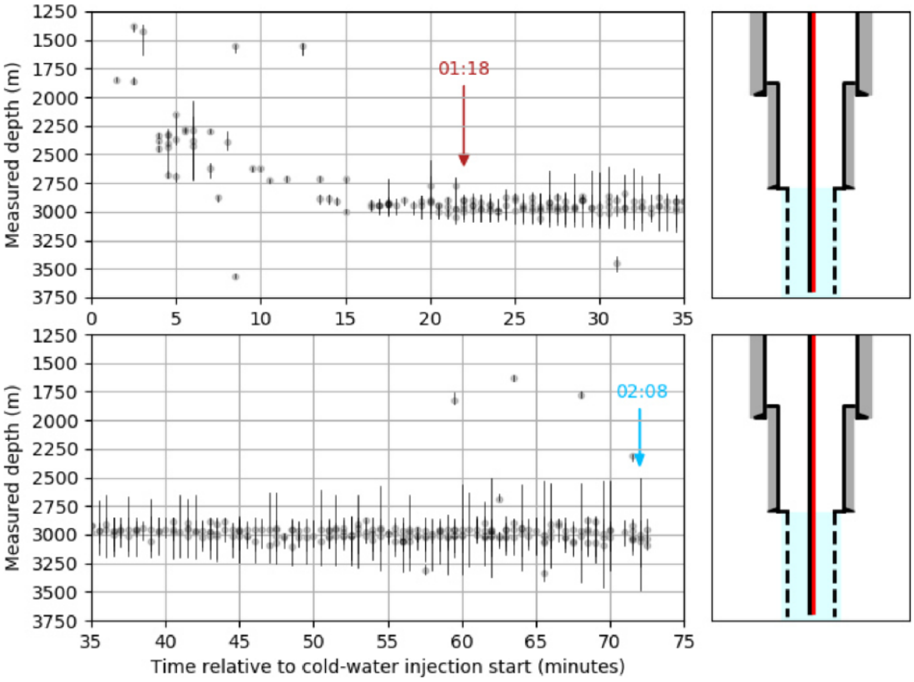

Figure 6-9. Gray circles and black vertical lines indicate the spatiotemporal origin and spatial extent of vibrational events in the well, respectively. The shown period comprises the first 72 min of cold-water fluid injection.

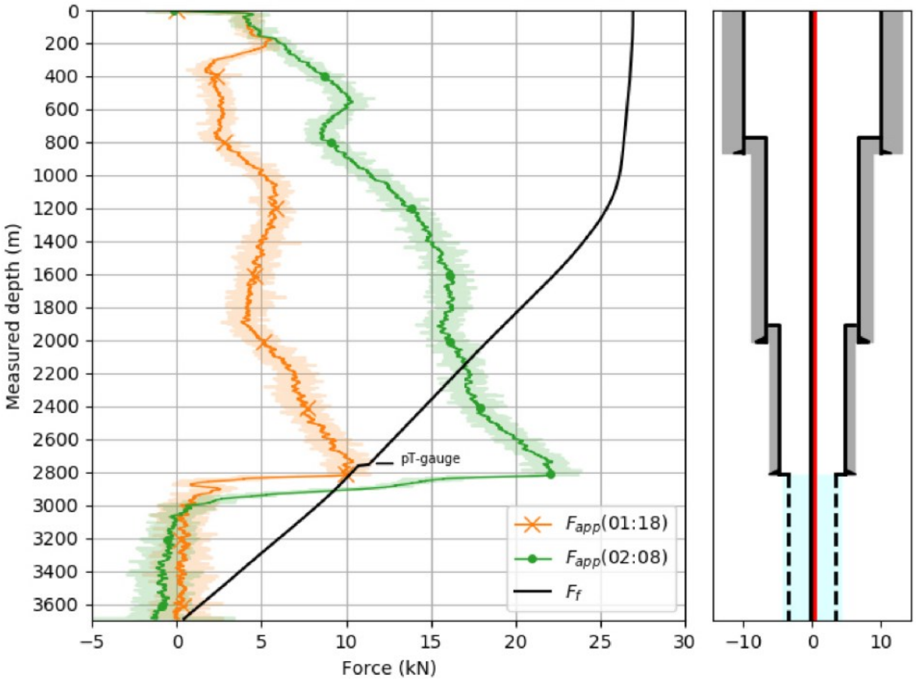

Figure 6-10. Comparison of static friction F_f with applied forces F_{app} from thermal contraction of the rod within the first 72 min of cold-water fluid injection. The pale colors in F_{app} originate from measured DTS data, and the solid lines are constructed by a moving average over 15 m.

6.4 Discussion

With the help of distributed fiber-optic temperature and acoustic data, we monitored a cold-water injection period in a geothermal well at the site Schäftlarnstraße, Munich. The downhole monitoring data allow for an analysis of the deformation of the 3.6 km long sucker rod/fiber-optic cable construction due to cooling. We observe numerous localized episodes of large strain rates that nucleate along the inclined stretch of the borehole and propagate both towards greater depth and the surface. Such events induce quickly declining elastic vibrations along the entire extent of the affected interval. The emergence of these vibrational events strongly correlates with the beginning of the fluid injection. In the following, we thus argue that the vibrational events are a result of the substantial temperature changes which the sucker rods with the optic fiber are exposed to. The contraction of the sucker rods upon cooling induces stress where the sucker rod is held to the borehole wall by frictional forces. On the basis of a simple mechanical model we show that accumulated stresses may eventually exceed the friction giving rise to sudden stress release and the observed strain changes.

6.4.1 Assessment of Measuring Errors

Our monitoring data analysis is based on a debatable approach of integrating DAS data over longer time periods. To obtain the ε_{DAS} profile over the period of 1 h, a total number of 3.6 million strain rate profiles are integrated (sample rate: 1000 Hz). Such a numerical operation has a high risk of creating numerical errors due to, e.g., rounding off or value truncation. In addition, the smallest systematic error in the DAS measurement system results in a significant drift over time which would misrepresent the strain profile measured by the sensing fiber. Also, it is well known that for FIMT-type installations, the gel filling allows for creep and differential movement of fibers with respect to its surroundings, which makes strain sensing unreliable for greater deformations and longer periods (e.g., Lipus et al., 2018; Becker et al., 2020). However, creep over many meters or even kilometers is most likely improbable. To strengthen the meaningfulness of our integrated strain profile, we analyzed the ε_{DAS} for a deeper section of the well, where little temperature change (ca. 1 °C) was measured by the DTS. In 3500 m depth, we do not observe any strain accumulation after temporal integration of strain rate data over a period of 60 min. This indicates that the measured strain rate has no significant drift during the time of interest. For measurements with higher amplitudes such as within the depth interval 2800 – 2900 m, non-linear effects influencing the temporal integration of the data cannot be excluded.

6.4.2 DAS Data Integration

We integrated DAS data in time over 72 min to assess the absolute contraction of the rod construction prior to the cold-water injection start (see Figure 6-4). For the well interval from the water table to the transition to the perforated liner, the results show a good match to the contraction that was theoretically assumed from the cooling of the well. However, from 2800 – 2900 m MD, we obtain much higher deformation from the DAS data than what we expected. We cannot give an unambiguous explanation for that but see two likely reasons for that observation. Firstly, the DAS integration process might result in a drift when integrating high-amplitude DAS data. Especially from 2800 – 2900 m MD, constantly high energy is recorded by the system. The second explanation could be that the integrated DAS data measured a true deformation of the construction. In the depth region around 2800 m, the annular space of the borehole is rather irregular (transition to 7 in. liner interval, localized increase in the borehole inclination; see Figure 6-4 c). The repeating sudden sucker rod events might lead to an uneven distribution of the thermal stresses along the rod. Interestingly, the most prominent feed zone of the well coincides with the one single DAS interval which shows an extensional signal.

The sudden slip events presented in this study show some similarity to the slip events which were previously observed in FIMT-type fiber-optic installation in a geothermal well (Miller et al., 2018). In the reported DAS campaign, a fiber-optic cable was installed in a geothermal well, and it is argued that repeated thermal cycles led to a loss of frictional coupling between fiber-optic cable and the borehole wall. Miller et al. (2018) reported that a sudden loss triggered a movement of the cable with a first arrival speed of 4600 m/s (we measured a first arrival speed of 4000 m/s). The integrated strain of the reported event shows a balance towards absolute contraction which we also observe in our events. Another similarity is given by the frequency content of these events. They recorded a dominant frequency of 45 Hz with some harmonics in both directions which we also observed in our data (see Figure 6-7 at 3000 m MD).

6.4.3 Stick-Slip Rod Behavior

We calculated the static friction force F_f along the rod construction by a cumulative sum of the friction of each nylon centralizer with the borehole inner wall. Independently of that, we computed the applied force F_{app} on the rod construction by thermal contraction using the DTS monitoring data. By comparing both curves, we can distinguish depth regions where the rod remains immobile ($F_f > F_{app}$) and depth regions where the applied forces overcome the static friction force ($F_f < F_{app}$). The temperature difference in the course of the investigated time period is particularly high over the 9 5/8 in. liner interval (depth region from 2485 – 2890 m MD), which in consequence also means that F_{app} is high. According to our model calculation, the contraction forces surpass the frictional forces at 2800 m MD around 01:18 (22 min after injection start). This result implies that after this time, the construction can contract in this depth interval. In other words, the thermal stresses on the rod construction in this depth region are high enough that the rod starts to move and to contract. Hence, the literature values assumed for the static friction between sucker rod and steel liner are assumed to approximate the real values.

With ongoing cold-water injection and further cooling of the well, the applied forces F_{app} increase. This leads to a continuous growing of the depth interval where F_{app} surpasses the static friction F_f of the rod. The STA/LTA detections match the predictions of the friction fore model. After a rather quiet initial phase of low-energetic events (before 17 min in Figure 6-9) which could be caused by the relaxation of previously accumulated stress anomalies along the sucker rods, repeated vibrational events start to concentrate in the region 2800 – 3100 m MD. As the region with $F_f < F_{app}$ increases, the length of the vibrational events increases. From our friction force model, we would expect vibrational events (more specifically: the contraction part of the movement) at 02:08 in the depth region 2150 – 2910 m MD. However, the observed events extend from 2500 – 3500 m MD. Regarding the upper limit, we can see in Fig. 10 that there is a significant change in slope for F_{app} at 02:08 at 2500 m MD. The friction force model is based on numerous assumptions (i.e., static friction coefficient nylon steel, Young's modulus for stainless steel, neglecting fiber-optic cable, stress-free initial conditions) which might not accurately depict the downhole conditions. This could mean that either the calculated applied force F_{app} is too high and/or the static friction force F_f is too low.

With respect to the lower limit of the vibrational events, we predict the contraction part (F_{app}(02:08) Figure 6-10) of the vibrational events down to a depth of 2912 m MD from our friction force model. However, we record vibrational events down to a depth of 3480 m MD. This discrepancy can partly be explained by the fact that the model prediction only shows the contraction part of the vibrational event. As seen in the cumulative strain ε_{DAS} (see Figure 6-10 events A and B), the lowest part of a vibrational event yields extension. The most likely reason is that the contraction above results in a pulling of the rod from a lower-lying region to compensate for the missing rod length. Therefore, the events can be traced down to a greater depth than predicted.

The constant temperature offset by +1 °C in the DTS profiles from 02:08 (relative to 01:18) in the depth interval from 3100 m MD to the end of the cable is unlikely to be caused by any fluid movement. While DTS temperature measurements did show a variation, no additional offset was recorded from the measured strain ε_{DAS}. This could mean that the rod builds up thermal extensional stresses without actual movement taking place ($\varepsilon_{DTS} > 0$, $\varepsilon_{DAS} = 0$). However, we speculate that the temperature anomaly is related to the processing of the DTS data. DTS temperature was measured in a double-ended configuration. A temperature profile is created by overlaying the DTS signal from both directions which are measured consecutively for both fiber branches. Close to the folding location (at the bottom of the well), an asymmetry in the temperature reading was observed between both fiber branches, which does not seem to be caused by any fluid motion. Averaging this difference between both branches led to a temperature offset. This offset was only visible if strong temperature changes were observed.

6.5 Conclusion

The field test at the geothermal site Schäftlarnstraße demonstrates that simultaneous recording of DTS and DAS data can be used for a detailed analysis of the deformation of a sucker-rod-type fiber-optic cable installation in a 3.6 km deep well. By comparing the theoretical contraction of the rod structure from DTS with an estimated contraction from DAS, we can distinguish depth intervals with higher and lower thermal stresses in the material. We introduce a friction force model which accurately predicts the onset and extent of sucker rod events releasing accumulated thermal stress. This is an important finding for DAS monitoring in geothermal settings because it shows that localized high-energetic vibrational events must not necessarily be related to micro seismic events occurring in the rock formation but can originate in the subsurface construction and the way in which the fiber-optic monitoring equipment is installed in the well. Moreover, the friction force model is useful to predict the data quality for DAS measurement campaigns for deep sucker-rod-type fiber-optic installations. Especially for the recordings of weak acoustic signals that are, e.g., induced by fluid movement in the annulus, it is essential to know the potential sources of errors and artifacts in the data. During operations which introduce a temporal temperature gradient, the thermo-mechanical response of freely hanging steel parts in the borehole may introduce stick–slip events that must be distinguished from any other relevant seismogenic source. Potentially, the vibrational energy from the sucker rod events can also be used to study the formation velocity in the nearfield around the borehole. Furthermore, the large-scale contraction along certain sucker rod and fiber intervals must be considered with respect to the location of the distributed sensor nodes. Our description also serves as a starting point for a more detailed dynamic description of the observed processes. This can be of use to predict the onset and depth interval of such sucker rod events and to contain their destructive potential in case of too quick a cooling of the construction.

Author contributions: TR and KZo conceptualized, planned and coordinated the monitoring campaign. MPL, FS, CW, TR and DP conducted the field measurement. MPL performed the DAS data processing. CMK helped in the interpretation of the DAS data. All authors contributed in the interpretation of the results. MPL prepared the first draft of the paper with contributions from all authors.

Code and data availability: Python scripts and data are available upon request to the corresponding author.

Competing interests: At least one of the (co-)authors is a member of the editorial board of Solid Earth. The peer-review process was guided by an independent editor, and the authors also have no other competing interests to declare.

Special issue statement: This article is part of the special issue 'Fibre-optic sensing in Earth sciences'. It is not associated with a conference.

Acknowledgments: This work would not have been possible without the continuous support from our partners involved in the project. The authors are thankful to Stadtwerke München, owner and operator of the geothermal site Schäftlarnstraße, for providing access to the well site, their premises and well data. The authors would also like to thank the drilling contractor Daldrup for accessing the site during the drilling and well completion operation. Moreover, we would like to give credit to our colleagues at Erdwerk GmbH and Baker Hughes for the close collaboration and fruitful discussions. From GFZ, the authors are thankful to Christian Cunow and Tobias Raab who supported the field work and acquisition of fiber optic data. The authors would like to thank Ryan Schultz and the second anonymous referee for reviewing and improving this paper.

Financial support: The fiber-optic cable was installed in the framework of the Geothermal Alliance Bavaria project, funded by the Bavarian Ministry of Economic Affairs, Energy and Technology. A part of this work was financed by the GeConnect project (Geothermal Casing Connections for Axial Stress Mitigation), coordinated by ÍSOR, which is funded through the ERANET cofund GEOTHERMICA (project no. 731117), from the European Commission, Technology Development Fund (Iceland), Bundesministerium für Wirtschaft und Energie aufgrund eines Beschlusses des Deutschen Bundestages (Germany) and Ministerie van Economische Zaken (the Netherlands).

The article processing charges for this open-access publication were covered by the Helmholtz Centre Potsdam – GFZ German Research Centre for Geosciences.

Review statement: This paper was edited by Zack Spica and reviewed by Ryan Schultz and one anonymous referee

7

TECHNICAL NOTE - INTEGRATED FIBER OPTIC MONITORING IN A GEOTHERMAL PRODUCTION WELL: LESSONS LEARNT

7.1 History of the FO System: Implementation and Operation

During this study, a novel fiber optic (FO) monitoring system was installed in a geothermal production well. This chapter is intended to share the experience gained during the installation and four years of supporting and conducting measurements. Figure 7-1 shows the chronology of the FO system from installation until late 2023.

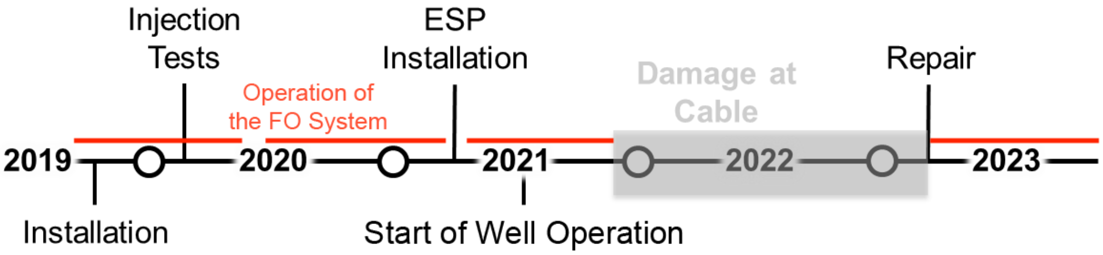

Figure 7-1. Chronological Overview of the FO monitored Well TH4 with Times of continuous DTS and P/T measurement marked in red. Modified from Figure 8-2.

In 2019, two wells of the Schäftlarnstraße geothermal site in Munich (owner Stadtwerke München) were permanently equipped with fiber optic cables. In the injector well TH3, one cable was installed behind the surface casing of the first section and cemented in place. In the nearby producer well TH4, a novel monitoring system in the geothermal sector was implemented by suspending a fiber optic (FO) cable for permanent use inside the casing and liner down into the reservoir. This was enabled by a comparably light sucker rod (each sucker rod is about 10 m long and weighs less than 16 kg), to which the cable was attached by clamps and bendings. Its load is sufficiently low for suspension from the wellhead and later the pump. The cable was installed in two configurations at the site. First, it was suspended from a blind flange during a temporary 1.5-year shut-in phase before the start of the well operation then converted with the installation of the pump by suspending it below the ESP.

7.2 Technical Design

7.2.1 Overall Fiber System and Downhole Cable

Figure 7-2 shows the overall design of the cables and fibers in the two wells at the Schäftlarnstraße site. From a server room storing the interrogators and measuring computers, the cables are guided over a length of about 150 m to the wellheads of TH3 and TH4. There, the surface cables are spliced to the downhole cables in a splice box (TH3) and inside of a pressure-proved wellhead outlet (TH4). This outlet serves as a pressure barrier to separate potentially rising gases in the cable from the surface system. The cable cemented in TH3 is a flatpack cable design with two single-mode (SM) and two multi-mode (MM) fibers which are looped via a minibend at the

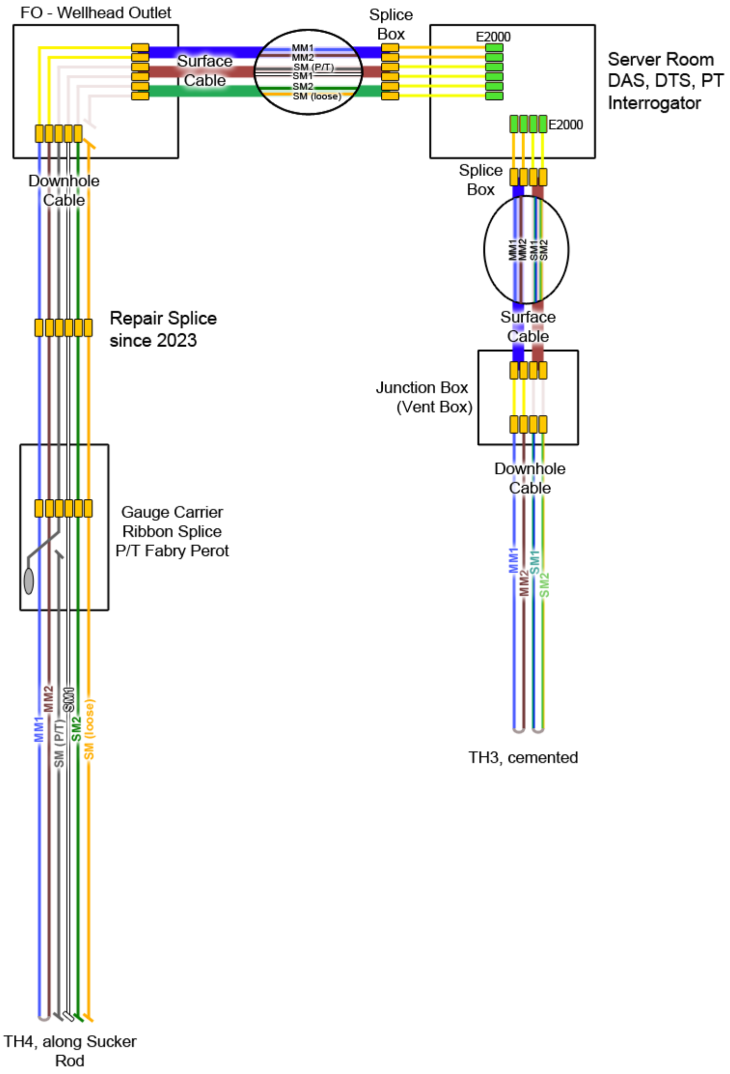

Figure 7-2. Fiber Hook Diagram of FO cable in TH4 (left) and TH3 (right) showing the configuration of single-mode (SM) fibers and multi-mode (MM) fibers and the splice at the P/T gauge and surface splices.

bottom end. The SM fibers are used for distributed acoustic/dynamic strain sensing (DAS) and the MM fibers for distributed temperature sensing (DTS). The cable installed in TH4 is a tubular encapsulated fiber (TEF) design with 11 mm x 11 mm polypropylene encapsulation containing two multi-mode fibers and four single-mode fibers. The cable is rated to 150 °C and 1379 bar (20 kpsi) to cover the downhole conditions of the thermal fluid. At the approximate depth of the top reservoir plus a safety distance of around 50 m, a fiber optic pressure/temperature (P/T) gauge, which works according to the Fabry-Perot principle, was spliced into the cable during installation. The cable contains six fibers, two of which are multi-mode and four are single-mode. The MM fibers are used for distributed temperature sensing, two of the SM for distributed acoustic sensing (one in use, one as a backup) and the remaining two SM for P/T gauges (one is installed at the top reservoir, the other was initially planned below the pump but not installed in the end). A bottom hole assembly (BHA) with a conical-shaped centralizer forms the bottom end of the installation, housing the end of the single-mode fibers and the mini-bend used to loop the multi-mode fibers.

7.2.2 Sucker Rod

Sucker rods are poles up to 10 m long with connectors at both ends that can be screwed together. They are usually used in the oil industry to connect the downhole and surface equipment of a piston pump. Such sucker rods were used as support elements for the cable. Downhole components such as the BHA and the gauge carrier were screwed into the rod and the cable was clamped to each sucker rod connection and tightened in between with cable straps. The rod was suspended in the upper part of the borehole, initially from a tubing during shut-in times and later from the bottom end of the electric submersible pump. With higher deviation at higher depth of the well, the cable/sucker rod lies loosely at the low side of the borehole.

The design's advantages are the simple integration of downhole components (BHA, gauge, and gauge carrier) supporting these in terms of their weight, and the possibility of pushing the entire string from the surface at high deviations. In the case of highly deviated wells, installation of cables alone due to gravity only can be difficult, especially if there are cross-sectional constrictions, e.g., at casing junctions. In the Schäftlarnstraße TH4 well, the maximum deviation is 58 °, and gravity-driven wireline logs, got stuck at 2810 m MD, the transition of the 9 5/8-in. casing shoe to the 7-in. slotted liner in the reservoir section. However, a disadvantage of the suspended steel sucker rod/cable design is its susceptibility to thermal contraction and the relative motion of the sucker rod/cable system to the casing, and the resulting displacement in the measuring points. In addition, more space is required in the borehole than with a cable alone, which reduces the cross-sectional area and increases the pressure loss to some extent.

7.2.3 Pressure Loss due to the Reduced Flow Area

If a section through the borehole with the sucker rod/cable inside is regarded as a circular ring with an outer diameter $D\ (m)$ (casing or tubing) and the inner diameter $d\ (m)$ (sucker rod/cable), the pressure loss $\Delta p\ (bar)$ of a 1 m long section of the system can be roughly estimated using the standard hydromechanical equation with the density of the fluid $\rho\ (kg/m^3)$, its velocity $v\ (m/s)$ and the pipe friction coefficient $\lambda_f\ (-)$ (eq. 7-1)

$$\Delta p = \frac{\lambda_f \cdot 1m \cdot \rho \cdot v^2}{d_h \cdot 2},\ d_h = D - d \qquad \text{(eq. 7-1)}$$

or by using one of the numerous online pipe flow calculators (e.g., Pressure Drop Online-Calculator for Mobile and PDA), which was done here. In the reservoir section, the outer diameter is defined by the 7-inch slotted liner. Assuming that the ¾ inch sucker rod with the FO cable has a total diameter of 1.2 inches, with an assumed roughness of the liner of 0.205 mm (Codo et al., 2012), and assuming a water temperature of 100 °C, the corresponding density of the fluid of 968 kg/m² and its dynamic viscosity of $2.88 \cdot 10^{-4}$ (Ns)/m², calculated according to the IAPWS-IF97 formulation (IAPWS, 2011), and a pumping rate of 100 l/s, the pressure loss Δp with and without the FO cable calculates to 12.11 mbar and 9.02 mbar, respectively. Summed up over 900 m of reservoir section (as in SLS TH4), this results in an additional pressure loss of 2.8 bar for the reservoir section due to the fiber optic cable and sucker rod. This is not immense, but for wells that are already hydraulically limited, such an additional pressure loss can lead to a reduction in pumping capacity. It then remains to be seen whether this disadvantage is outweighed by the additional information gained through reservoir and pump monitoring.

7.3 Technical Challenges and Recommendations

7.3.1 Monitoring the Installation and the Integrity of the Cable

To complete the sucker rod installation as safely as possible, the installation was conducted from a drilling rig. Installation with a crane seems also possible, but the axial rotation of the sucker rod line should be avoided as far as possible to minimize the mechanical stress on the cable. Barriers to implementation that were considered in advance of the installation are the deviation of the well, narrowing of the diameter, e.g., at the liner hanger, and the axial stress/tension on the material during run in hole and pull out of hole. In the well TH4, a slotted liner is installed, but a lot of geothermal wells are also completed open hole. In such cases, analysis of caliper runs, and image or other logs is strongly recommended to locate critical zones with major breakouts or karstified intervals which could lead to the sucker rod line getting stuck. Slowing down run in hole is recommended here. Using the hook load at the rig to measure sudden stress on the downhole components turned out to be too imprecise for the relatively lightweight and flexible sucker rod string. As a consequence, repeated control measurements of the fibers are required to check the integrity of the cable downhole.

For such, it is recommended to do optical time domain reflectometry (OTDR) or comparable measurements on all fibers in previously defined intervals to control the integrity of all fibers. In the event of a cable break, a decision must be made as to whether the cable should be brought back to the surface to repair the damage or whether the installation should be aborted. It may be necessary to abort the installation if the rig time no longer permits repair. It is generally not advisable to leave a broken cable in the borehole, as the integrity of the borehole may no longer be guaranteed and fluids could penetrate the inside of the cable, which could lead to rapid blinding of the fibers. Time intervals of control measurements should be shortened at critical depths and the end of the installation. Unfortunately, continuous monitoring is difficult to apply, i.e., we tried with a fiber optic rotary joint, but this added too much noise to the data.

7.3.2 Splicing

The most critical point of the installation was the mounting and associated splicing of the P/T gauge. To integrate the P/T gauge into the system at the depth of the top reservoir, all fibers at that installation depth had to be cut and spliced together with a ribbon splice. This turned out to be time-consuming and challenging because of the different fiber types (multi-mode and single-mode) inside the cable and the technical difficulties with the splicing device. An alternative to ribbon splicing would be to splice the individual fibers one after the other, but this presents some other challenges, as the fibers have to be set down to the same length. A prefabricated splice would be optimal to save costs and minimize the risk to the cable, but that would create other problems. Firstly, the already installed length of the cable up to the sensor must then be exactly adapted to the sucker rod length, which is difficult due to the loose attachment to the rod (excess length) and the factory length tolerance of the sucker rods (the sucker rods we used varied in length from 9.14 to 9.18 m). Secondly, the gauge and protective sleeve for the splice would then have to be attached to or on the cable reel, which represents an additional obstacle in handling and transportation. Producing the downhole splice on site therefore seems to be the most feasible option. We recommend having at least two alternating teams for splicing and to provide protection from the weather and cold, e.g., with a tent or find a safe way to operate with prefabricated splice and gauge. Alternatives to the complicated ribbon splices should also be considered, e.g., the installation of a small volume to allow for the excess length of the fibers so that the fibers can be spliced one after the other and in different lengths.

To ensure good measurement quality later, we recommend setting limit values for the losses at the splice points. We suggest 0.3 dB at splices and 1 dB at the mini-bend (SM, at 1310 nm), for MM 1.2 dB (at 1300 nm). If there are several downhole splices, the limit values should be lowered slightly to prevent the loss over the entire system from becoming too large.

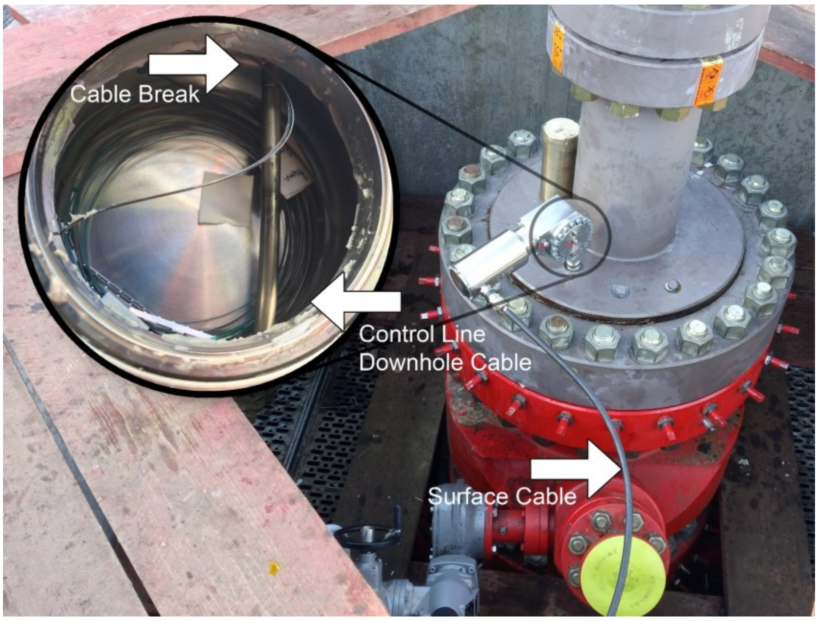

Figure 7-3. Picture of the 2021 cable break when the control line was pushed into the high pressure chamber of the FO wellhead outlet, crushing and shearing the fibers.

7.3.3 Well Interventions

As of early 2024 and since the initial installation in 2019, there have been four well interventions in which the FO cable had to be partly removed. The first was planned for 2021 with the installation of the ESP, the others took place due to ESP failures in 2021 and 2023. With the first ESP change, a problem occurred at the screw connection of the cable's outlet at the wellhead and the cable loosened and was pushed into the FO wellhead outlet, where it broke only hours after the new pump was set to production (see Figure 7-3). As the pump could not be changed for over a year for operational reasons, the fiber optic monitoring system was offline in 2022 until the ESP failed again in early 2023. With the subsequent change of the ESP, the cable was repaired.

The workovers/well interventions were carried out with a small mobile workover rig or cranes alone. We found that the weights were higher than expected when pulling out of hole, which was probably due to higher frictional force between the rod and the wall of the inner radius of the deflected hole. Preliminary pull out of hole torque-and-drag analyses for a slightly different system (neighbor well with similar completion and deviation) estimated that the load is unlikely to exceed 13.8 tons, but about 18 % more hook load was required to pull the sucker rod/cable system under high tension. We therefore recommend including a greater safety factor.

With every intervention, the installed cable length changes as on the one hand the cable must be disconnected when the wellhead is opened, and every new splice consumes some meters of downhole cable. On the other hand, installation depths downhole may change, e.g., because the pump string might change in length, or one or more sucker rods must be removed to gain enough cable length to prepare the splices when the cable is connected again.

To maintain the consistency of the measurements before and after an intervention, it is essential to know the exact installation lengths and any cable lengths that have been removed. Tubing installation lists are therefore as important as a detailed installation protocol. A reference point in the borehole would be ideal in this context, for example, the definition of a temperature point at a certain depth. Unfortunately, this is not yet possible due to inaccessibility.

With the installation of the ESP in 2021, some hundred meters of sucker rod were removed, and the cable was mounted at the production string and attached together with the power cable by metal bends. Those turned out to be too sharp for the polypropylene encapsulation of the cable and it became peeled open by it. At a subsequent ESP change in 2023, the damaged cable broke during removal as it got stuck on a guide wheel. It was replaced with around 500 m contingency length from the initial installation and Teflon mats were clamped between cable and metal bends to prevent such damage in the future. In the course of this, a new splice had to be added to the system which was housed in a special casing (in stock for such eventualities) and mounted to the production tubing.

For well interventions, we therefore recommend having splicing devices and personnel at hand, as well as redress kits and appropriate splice housing, in case the cable breaks and has to be repaired.

7.4 Measuring, Calibration and Accuracy

7.4.1 Depth Calibration

The installed system is designed to measure downhole temperature via distributed temperature sensing (DTS) along a double ended (looped over mini-bend in the BHA) multi-mode fiber. Pressure and temperature are measured at high resolution at one point at the top reservoir via a Fabry-Perot P/T gauge connected to a single-mode fiber, and distributed strain/acoustics (DAS) via single-mode fiber.

For distributed sensing, the position of individual measurement points along the cable needs to be calibrated. This is because the fiber has an excess length in the cable and the cable itself is mounted relatively loose to the sucker rod. Additionally, the downhole equipment is subject to thermal expansion and contraction. It is assumed that the share of excess length in the actual length is continuous and allocate the measuring points along the fiber to the correct location according to the two fixed points which are the wellhead and the bottom end of the installation which is known from the list of installed elements. Good depth allocation is possible if the installation depths are well known from tubing lists and optional alignments with geophysical logging. The upper part of the downhole installation can be defined by cold or hot anomalies at the cable near the wellhead (e.g., cold spray or with a hot air dryer) which can be seen in the DTS traces. The surface extension from the measuring device to this temperature mark can be removed from the measurements and should be saved separately. For DAS, calibration can be done with acoustic tap tests at the wellhead.

7.4.2 Temperature Calibration

Temperature calibration of downhole cables is a challenge due to the inaccessibility of the system. In TH4, a Fabry Perot P/T gauge and a wireline temperature log run before the cable installation were used to determine the necessary calibration shift on the DTS data. However, the gauge temperature after installation was 4 k higher and after a software update 0.7 K lower than the wireline log at the respective depth (see Ch. 5.2.3.3). The overall uncertainty of the P/T gauge is unknown. The error of the temperature gauge used for the wireline log was specified in a friendly message from the executing company (LIAG) to a maximum of 0.6 K, tested in a liquid bath. An additional unknown error is given by the inertia of the gauge at the wireline measuring speed and the fact that over 13 days of installation between the wireline log and the first measurements with the fiber optic system.

During this time, the borehole could change thermally, not least due to the mixing of the water column during run out of hole of the wireline log and run in hole of the fiber optic cable/sucker rods. We calibrated the DTS at this gauge. However, the wireline log turned out to be very helpful as it revealed an incorrect calibration ($\Delta T = 4$ K, see Ch. 5.2.3.3) of the P/T probe.

7.4.3 Accuracy of the DTS

In 2021, the well was set into operation and wellhead temperatures and temperature values at the zenith sensor of the ESP were available to compare and recalibrate the DTS data. These data allow the accuracy of the DTS data to be determined assuming that the zenith sensor provides the true values. This can be done by calculating the standard deviation and confidence interval for the differences between the reference (zenith sensor located at 757 m) and the DTS data directly below the ESP at 760 m. Figure 7-4 shows the comparison of DTS data with a resolution of 10 minutes and a spatial resolution of 1 m with the temperature measured by the electrical zenith sensor 3.5 h after the pump was started and over the following two weeks. From this, the mean difference of the DTS to the reference temperature is -0.12 K and the standard deviation is 0.26 K. The maximum error can be specified as +0.64 K at 95 % confidence.

Next to the DTS-measured temperature value, the location of the measuring points is not accurately known. In this context, uncertainties that can be considered are the position of the cable in relation to the cross-section of the borehole, the overstuff or excess length of fibers inside the cable, the excess length of the cable at the sucker rod, the position of the calibration point at

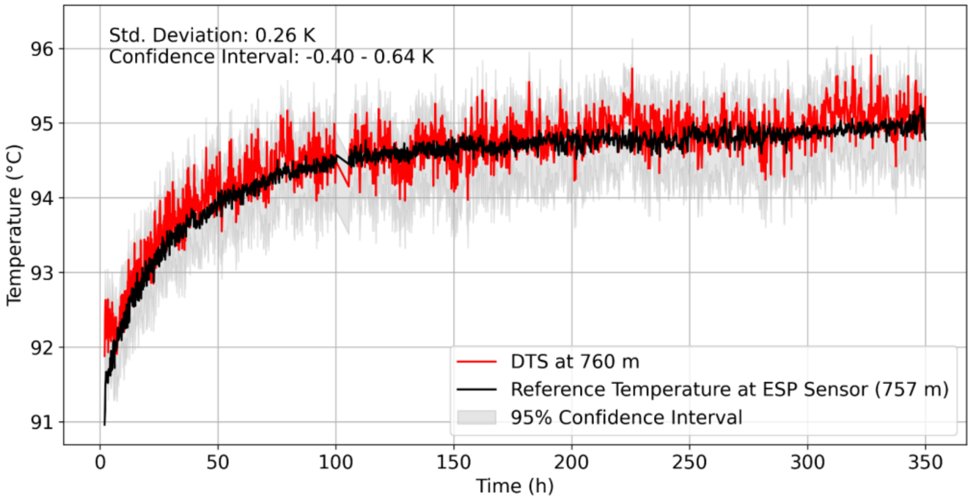

Figure 7-4. Comparison of the evolution of the temperature below the pump (zenith sensor) and DTS readings 3 m below the zenith sensor during the first two weeks of operating the well. Data starts 3.5 h (0 h in the graph) after the pump was started. The data gap at 100 h is present on both measurements and can probably be explained by a power failure at the geothermal site. Temporal resolution of DTS data: 10 min, of zenith sensor: 5 min.

the wellhead defining the beginning of the DTS profiles, and the installation length of the sucker rods (maximum installation depth). To estimate the accuracy of a processed DTS profile regarding depth allocation, a Monte Carlo simulation can be performed with the key parameters defining the depth calibration's uncertainty which are estimated as follows:

1) The uncertainty given by an eccentric position of the cable inside the circular borehole is negligible as it is at high deviations at a maximum insignificantly larger than the distance from the borehole axis to the inner wall. At the 57° high inclined reservoir section with the 7-inch slotted liner, this is less than 0.1 m.

2) The overstuff (relation of fiber length to cable length) was specified and tested by the manufacturer of the cable to be 2.6 – 3.1 %. The excess length of the cable along the sucker rods can be calculated from the installation tally by relating the installed sucker rod length to the readings from the installed cable (having length markers on it). From the bottom end to the P/T gauge (splice), the excess length is 1 %, from the gauge to the wellhead it is with 0.3 % significantly lower. During processing the DTS profiles, linear interpolation is done between the wellhead and BHA, assuming a continuous excess length of fiber in cable of (3.1 % + 2.6 %)/2 = 2.85 % and cable at sucker rods of (1 % + 0.3 %)/2 = 0.65 %. However, as can be seen from the calculations, a certain tolerance should be taken into account. With an additional safety factor of 0.15 % due to possible uncertainties in the tally list, the uncertainty of both overlengths can be estimated to be negligible (zero) near the wellhead and increasing linearly with depth up to (3.1 % - 2.85 %) + (1 % - 0.65 %) + 0.15 % = ± 0.75 %.

3) The position of the calibration point on the surface was determined by a thermal marking on the cable near the wellhead, which was done about 1.5 m away from the wellhead by spraying 1 m of cable with a cold spray. The position of the thermal marker is accurate within

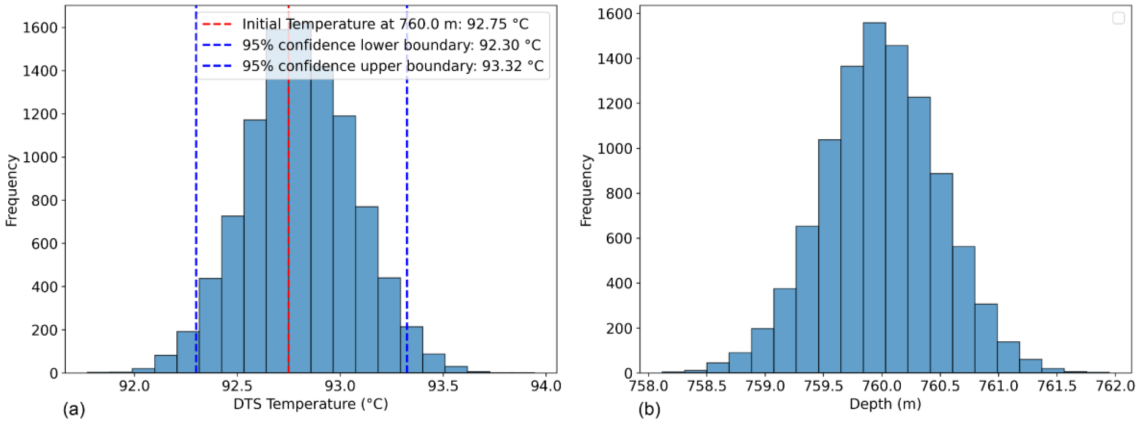

Figure 7-5. Results of Monte Carlo simulation of temperature at 760 m picked from a DTS profile measured about 300 h after the pump of SLS TH4 was started in 2021 with estimated uncertainties for the displacement and DTS temperature. (a) shows the temperature uncertainty. (b) shows the distributed displacement.

the spatial resolution of the measurements, which is also 1 m. However, the distance of cable from the marker to the hanger (depth zero of DTS profiles) underlies an estimated measurement error of ± 0.2 m.

4) Lastly, the position of the sucker rods along the borehole axis depends on the accuracy of the installation list of sucker rods and tubings. The total number of sucker rods installed in 2019 agrees with the number listed in the tally, so a larger error e.g., missing to count one rod can be excluded. Each installed sucker rod was length measured before installation. However, the sucker rods have a length tolerance of ± 0.2 m. Taking into account the uncertainty due to manual measurement and a possible change in length due to thermal stress of up to +1.2 m (see Ch. 5.4.2.3), the uncertainty is estimated as zero at the wellhead and linear increasing with depth up to ± 2 m.

Figure 7-5 shows the results of the Monte Carlo simulation at 760 m of an exemplary DTS profile (at 300 h from Figure 7-4) with the applied uncertainties of depth displacement in Figure 7-5b and the subsequent temperature shift in Figure 7-5a if additionally the standard deviation of 0.26 K derived from Figure 7-4 is applied. For this profile, a displacement of ± 1 m results in a temperature uncertainty of around ± 0.5 K at 95 % confidence.

In Figure 7-6, a set of functions is shown that results from Monte Carlo simulations with all estimated uncertainties over the whole DTS profile (same DTS as taken in Figure 7-5). In the upper 700 m, the noise on the data is high as the cable is clamped outside the production tubing. For the part below, the maximum standard deviation of the displacement $\Delta D\ (m)$ = 3.61 m and the resulting maximum standard deviation of the temperature $\Delta T\ (K)$ = 1.6 K at 2900 m can be determined for the set of functions. This is in the region of the major flow zone of the reservoir, thus a large temperature change is present over a short distance. At other intervals in the well, ΔT is well below ± 1 K.

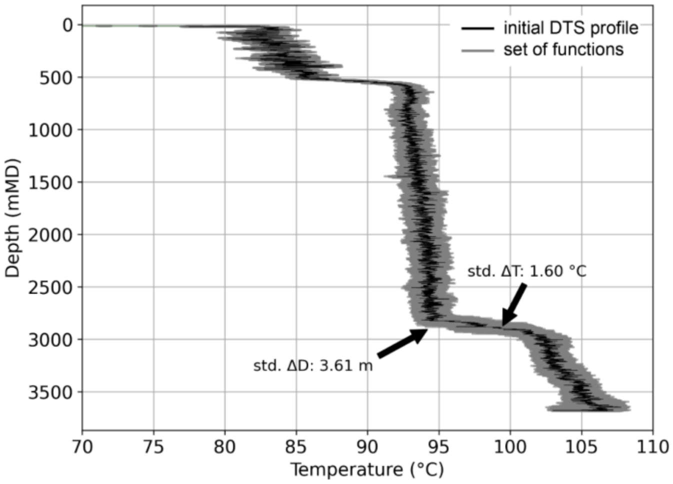

Figure 7-6. DTS profile taken about 300 h after pump start in 2021 at 10 min and 1 m resolution (black) with set of functions (grey) from Monte Carlo simulations taking into account DTS temperature and displacement uncertainties. The maximum standard deviations below 800 m are shown at 2900 m.

In summary, the accuracy of the DTS system can be considered good in detecting the slope changes in temperature profiles that seem to occur in deep geothermal boreholes. The DTS was initially calibrated at the P/T gauge at the top of the reservoir in 2019. At this configuration, a comparison to production temperatures in the upper part of the well during the start of the pump in 2021 showed a standard deviation of ± 0.26 K (Figure 7-4). An independent wireline temperature log conducted one day before the FO installation took place, was taken as verification of both P/T and DTS. In our case, these measurements showed significant differences, and an incorrect configuration of the P/T probe was found, which was subsequently corrected by a software update. We therefore strongly recommend carrying out measurements independent of the fiber optics that can be used to correct a temperature shift. It would be best to calibrate the DTS interrogator to the actual downhole cable. This is planned with a defined length (10 to 20 m) of cable in the laboratory under constant, monitored temperature conditions, e.g. in a thermostat.

7.5 Long-Term Stability

As of 2024 and since the first installation in late 2019, the setup was adapted during subsequent well interventions four times. Every intervention to the system is a risk to the integrity of the fiber optic cable installation. A damage occurred twice but could be repaired. OTDR measurements were performed after each intervention to test the integrity of the fiber system.

Figure 7-7 and Table 7-1 show OTDR measured losses at different times throughout the lifetime of the system at different locations along the cable exemplary for one of the SM fibers. The values on the different fiber sections and the gauge vary, as it was not possible to maintain constant test conditions. For example, several OTDR devices from different manufacturers were used, the lead

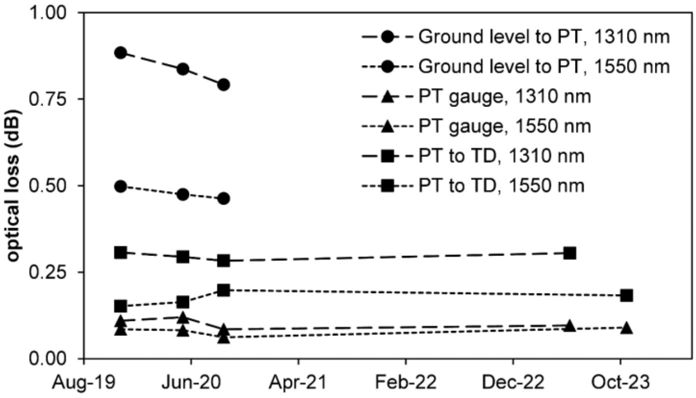

Figure 7-7. Optical losses during the lifetime of Single-Mode fiber no. 1 during the different intervals in the lifetime of the fiber optic cable in SLS TH4 from ground level to the P/T gauge, at the gauge and from the gauge to total depth (TD) in comparison at 1310 nm and 1550 nm wavelength.

lengths and cable types of the pigtails varied and the surface system was subject to several changes (such as the laying of the surface cable in 2020). In addition, the length of the subsurface cable also changed slightly during well interventions and an additional splice point was brought into the system due to repair work in 2023. However, Figure 7-7 shows that the losses at the P/T gauge and the fiber sections downhole did not get significantly worse.

Considering that the cable is pulled out of the hole a little and pushed back in again with each intervention and is subjected to thermal and mechanical stress when the pump is switched on and off without any loss of measurement quality, it can be concluded that the technical design is well suited for long-term use. The system concept has thus proven itself.

Table 7-1. Optical losses in dB at different sections of the installation and at different time intervals for single-mode fiber no. 1 together with calculated dB per km fiber length. The values were measured with different OTDR devices and at slightly different installation lengths of the cable system.

Date	**Fiber Section GOK to P/T gauge**		**P/T gauge**	**Fiber Section P/T gauge to TD**	
	dB	**dB/km**	**dB**	**dB**	**dB/km**
			SM Fiber 1, 1310 nm		
Dez-19	0.884	0.303	0.110	0.307	0.325
May-20	0.837	0.293	0.120	0.294	0.312
Sep-20	0.792	0.276	0.085	0.283	0.302
May-23			0.096	0.305	0.323
			SM Fiber 1, 1550 nm		
Dez-19	0.498	0.171	0.085	0.152	0.162
May-20	0.475	0.166	0.082	0.164	0.174
Sep-20	0.463	0.165	0.062	0.198	0.198
Oct-23			0.090	0.183	0.196

8

Inverse flow Zone Characterization using Distributed Temperature Sensing in a Deep Geothermal Production Well located in the Southern German Molasse Basin

This chapter was published as:

Schölderle, F., Pfrang, D., Zosseder, K. (2023). Inverse flow zone characterization using distributed temperature sensing in a deep geothermal production well located in the Southern German Molasse Basin. Adv. Geosci., 58, 101-108. https://doi.org/10.5194/adgeo-58-101-2023

Abstract: The localization and characterization of hydraulically active zones in a geothermal well is a major task in understanding the hydro geothermal reservoir. This is often done based on interpretations of spinner flow meter measurements that are performed at the end of the well test while injecting cold water. Once a production well is equipped with an electric submersible pump, data collection inside the reservoir and monitoring of the flow zones is usually barely possible. In a 3.7 km (MD) deep geothermal production well in Munich, Germany, it was successfully demonstrated in 2019 that a permanently installed optical fiber cable could close this measurement gap. We used this fiber-optic monitoring system to collect distributed temperature data once the well was set into production. We inversely modeled the inflow from the formation into the borehole from the production temperature data with an energy and mass balance model. The derived flow profile correlates with previous flow meter analysis and indicates that a karstified region at the very top of the reservoir is the driving factor for hydraulics and obtained production temperature. Qualitatively, the two profiles acquired by distributed temperature sensing (DTS) and flow meter are matchable, yet the production inflow profile by DTS logging is more differentiated compared to spinner flow meter logs interpretation during injection.

8.1 Introduction

Reservoir characterization is a key for ensuring secure and sustainable usage of geothermal resources. One major task is the localization of productive zones in the reservoir, respectively flow zones inside a well and the quantification of the contribution of the single zones to the produced amount of thermal water. Typically, production logging tools equipped with flow meter spinners are used in geothermal wells to estimate hydraulically active zones during injection of water (Schlumberger, 1997). Additionally, wireline temperature runs can be analyzed for non-linearity indicating potential high permeable zones inside a well (Lim et al., 2020).

During production, data logging in the reservoir is difficult, as permanent deep monitoring tools are rare and in case the well is a production well and equipped with an electric submersible pump (ESP), the deepest measurement point is usually located directly at the bottom of the pump. Monitoring tools below the ESP are not yet standard, but are feasible, as demonstrated in 2019 in a geothermal production well in Munich, Germany, where a fiber-optic cable was installed along a free hanging sucker rod in the middle of the wellbore (Schölderle et al., 2021). This cable enables seismic campaigns via distributed acoustic sensing (DAS) technology, temperature monitoring via distributed temperature sensing (DTS) and measuring point pressure and temperature (P/T) at a gauge spliced into the cable on top of the reservoir. Due to its high spatial and temporal resolution, DTS technology, often via cemented cable or wireline designs, has become increasingly popular in geothermal applications in recent years, for both monitoring wellbore stability (Reinsch, 2012) and reservoir characterization (Sakaguchi and Matsushima, 2000). Wellbore temperature, respectively heat can be used as a tracer for flow in porous and/or karstified and/or fractured aquifers. With the knowledge of the thermal properties of the reservoir rock and pressure conditions, a flow profile can be back calculated from the temperature data. This was shown by e.g., Pouladiborj (2021) who used the classical approach of energy balance for a control volume inside the producing well of Ramey (1962) and Hasan and Kabir (2010) to inversely derive flow profiles of DTS data of a well in Brittany, France. In addition, there are commercial solutions that allow production profiling by calculating a flow profile from DTS data based on a coupled energy and mass balance model, such as the production log analysis software KAPPA Emeraude (Kotlar et al., 2021), which is widely used in the oil and gas industry.

During the first operation of the monitored well, the installed DTS system provided real-time monitoring in the reservoir and generated flowing temperature data that can be studied inversely to characterize the inflow zones of the reservoir. These results were compared with conventional flow meter interpretations carried out at a time when the ESP was not yet installed to analyze if contributions of the flow zones derived at injection conditions are equivalent to production conditions.

8.2 Geological Setting and Studied Well

One of Europe's most important low-enthalpy geothermal regions is the Bavarian Molasse Basin in Germany, a north alpine foreland basin spreading between the Swabian and Franconian Alb near the river Danube and the northern alpine front (Meyer and Schmidt-Kaler, 1990). Here, the main target for hydrogeothermal exploration are the Upper Jurassic 'Malm' carbonates, which lay in shallow depths in the North and are dipping to the South where they can be found in depths of 4000 – 6000 m near the northern alpine front (Flechtner et al., 2020). These sedimentary layers partly show high porosities with up to 27.5 % (Zosseder et al., 2022) and high permeabilities (Bohnsack et al., 2020b), but also high heterogeneity on small regional scales. The production temperatures range between under 40 °C in the north and over 160 °C in the South (Weber et al., 2019).

The largest geothermal wellsite in the Bavarian Molasse Basin is the 'Schäftlarnstraße' (SLS) site in Munich, where six wells were drilled from 2018 to 2020 to depths of approximately 2400 m TVD to 3100 m TVD. Three producer wells and three injector wells transverse the stratigraphic layers of Purbeck and Upper Jurassic at different depths, separated by two major faults (see Figure 8-1).

Consequently, the highest production temperatures are at the southern and deepest wells with around 105 °C. Our studied well is the well SLS TH4 that explores the reservoir to the west. The well is 3.7 km (MD) deep (around 2.9 km TVD) and completed with a perforated liner in the reservoir section. In summer 2019, a spinner flow meter log was recorded over the reservoir in the well SLS TH4 to observe the hydraulic active zones of the well during injection conditions. In November/December 2019, this production well was equipped with a permanent fiber-optic cable, allowing for gathering distributed acoustic and distributed temperature data, as well as point pressure and temperature (P/T gauge) data at top of the reservoir. The cable was first installed from the wellhead down to a depth of 3690 m MD (2918 m TVD), hanging freely along a sucker-rod construction below a crossover mounted to the liner hanger. Two months after installation, DTS data was collected during two cold-water injection tests in January and February 2020 to verify the flow meter interpretation. The results and further details about the installation were discussed in (Schölderle et al., 2021) and indicated that a small karstified region (25 m thick) directly at the top of the reservoir is the dominant hydraulically active zone of the well. It was supposed that less than 8 % of flow contributes from regions deeper in the well. When the ESP was installed in April 2021, the free-hanging sucker-rod construction was installed below the pump at 760 m depth to a total depth of 3684 m MD (2914 m TVD). Above the pump, the cable was routed outside the production tubing to the wellhead. After further 16 months of shut-in time, the well was set into production for the first time in summer 2021.

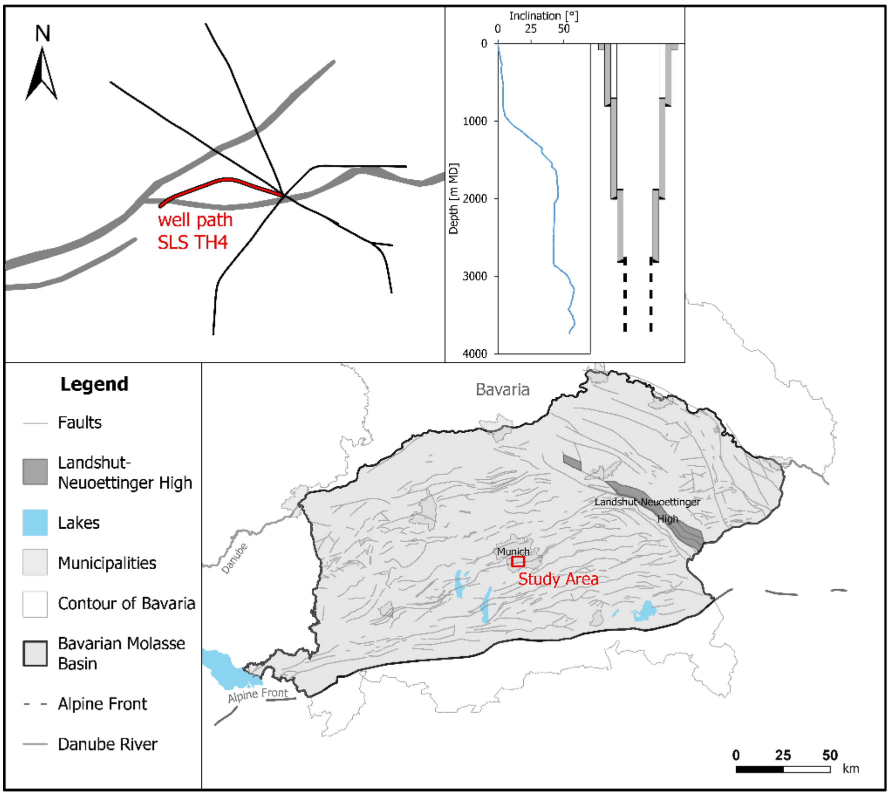

Figure 8-1. Map of the Bavarian Molasse Basin, cropped to Bavaria, and the six well paths at the geothermal study site Schäftlarnstraße with inclination and well scheme of well completion of SLS TH4.

8.3 Methods

We used the fiber-optic monitoring system at the geothermal site 'Schäftlarnstraße' to collect DTS data during the start of production. At this production period, two of the three doublets at the study site were simultaneously producing.

An energy balance model was used to inversely derive a production flow profile from the DTS profiles of the SLS TH4 well using the software KAPPA Emeraude (v5.40). Reservoir pressure and geothermal gradient are two required model inputs, which we estimated from the fiber optic system. The thermal gradient inside the reservoir was evaluated based on a series of DTS profiles measured over one year of the shut-in period. The pressure could be derived from the fiber-optic P/T gauge located at top of the reservoir.

8.3.1 Fiber-Optic Data at the Well SLS TH4

Fiber-optic temperature data has been collected continuously since the installation of the system in November/December 2019, except for two major interruptions in the spring of 2020 when the

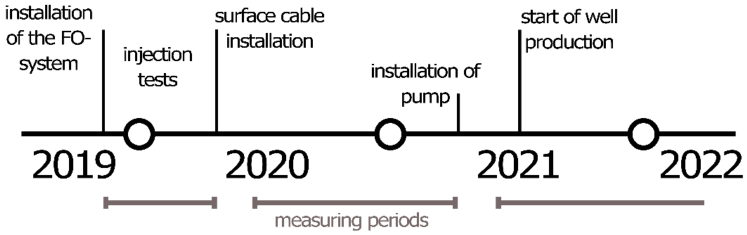

Figure 8-2. Timeline of fiber optic DTS measurements at SLS TH4.

measurements had to be stopped due to surface installation work, and in April 2021, when the monitoring system was modified during ESP installation (see Figure 8-2).

We acquired DTS profiles every 10 minutes at a spatial sampling of 0.25 m and processed the data by averaging over a window of 6 hours and spatial resolution of 1 m. The resulting temperature resolution of the profiles is about 0.13 K.

To derive the geothermal gradient in the reservoir, we studied the profiles collected immediately before the start of production, as in the early stage of geothermal wells, borehole temperature logs reflect the geothermal gradient insufficient because the near surrounding of the well is often still thermally affected by the preceding drilling or testing works (Eppelbaum et al., 2014). Figure 8-3 a shows the heating of the borehole after drilling and testing based on a series of DTS profiles averaged over 6 hours from the period between the cold-water injection tests in winter 2020 and the start of production in summer 2021.

The segment presented in Figure 8-3a shows a part of the cased 12.25-inch section and the upper 250 m of the reservoir section, where we can see a non-linear anomaly in the profiles compared to the remaining more uniform trend. At stable conditions, changes in the slope of temperature profiles can imply groundwater flow in up- or downwards direction e.g., Lim et al. (2020). Since we can still see a dynamic behavior at the thermal anomaly, stable conditions are not met in this region. From Figure 8-3b, it becomes clear that the region between 2800 m MD and 2950 m MD was still warming up, while the sections above and below the anomaly seem to be thermally fully equilibrated. To estimate the geothermal gradient, we therefore extrapolated over the anomaly, starting from the stable DTS profiles deeper in the reservoir.

8.3.2 Inverse Flow Profiling from DTS Data

We used the commercial well interpretation software KAPPA Emeraude (v5.40) to calculate a flow profile from the collected DTS production data. The underlying physical equations are based on the works of Pucknell and Clifford (1991), Chen et al. (1995) and Hasan and Kabir (2002) and their integration into the Emeraude energy model was described by Kotlar, Allain et al. (2021).

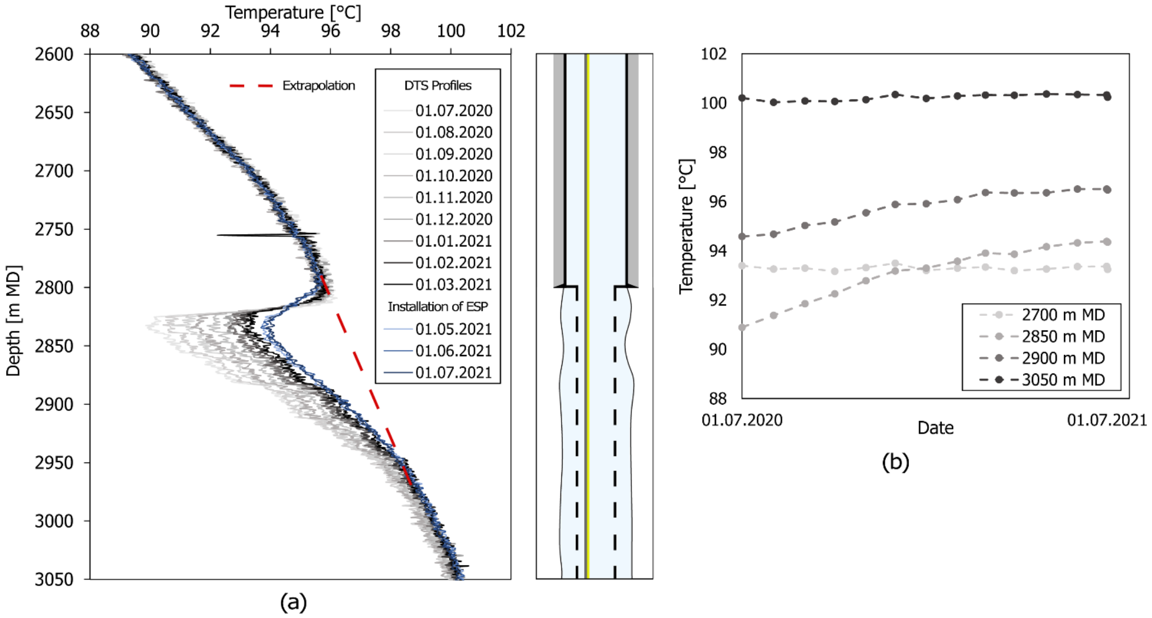

Figure 8-3. (a) DTS profiles between July 2020 and July 2021 and a schematic of the wellbore with sketched fiber-optic cable (yellow line) clamped to sucker rod (grey line) and (b) temperatures at different depths plotted versus time. The grey DTS profiles in (a) are from the shut-in period before the ESP was installed and the blue DTS profiles were measured after installation. The displayed DTS data are averaged over 6 hours at a spatial resolution of 1 m. The temperature anomaly below 2750 m in (a) is a measuring fragment due to the inline splice from the downhole P/T gauge.

The used model builds on a coupling of pressure and temperature into an energy balance model for segments of the wellbore and respective volume for the reservoir.

The energy balance for an infinite segment of a producing well in steady-state condition is given as:

$$\begin{aligned} q_{s,a} \cdot \rho_{s,a} \left(h_{s,a} + \frac{1}{2} \cdot \left(\frac{q_{s,a}}{A \cdot \rho_{s,a}} \right)^2 \right) = \; & q_{s,b} \cdot \rho_{s,b} \left(h_{s,b} + \frac{1}{2} \cdot \left(\frac{q_{s,b}}{A \cdot \rho_{s,b}} \right)^2 + g \cdot dl \right) + \\ & q_{s,s} \cdot \rho_{s,s} \left(h_{s,sf} + \frac{1}{2} \cdot \left(\frac{q_{s,s}}{A \cdot \rho_{s,sf}} \right)^2 + g \cdot dl \right) + D \cdot \Delta T_{sf}, \text{ with } \Delta T_{sf} = T_{sf} - T_s, \end{aligned} \qquad \text{(eq. 7-1)}$$

where q_s $((kg/s)/kg)$ is the specific mass rate (mass rate divided by mass), h_s (J/kg) the specific enthalpy, which is dependent on pressure, A (m^2) the flow area, ρ_s $((kg/m^3)/kg)$ the specific density, $g = 9.81$ (m^2/s) the gravitational acceleration, dl (m) the length of the respective segment and ΔT (K) the temperature change. D is the thermal conductance term as defined by Kotlar et al. (2021) and its unit is given through its definition as (1/(mKs^3)). The subscripts in the equation represent b below the segment, a above the segment, s in the segment and sf the sand face (wellbore/reservoir interface). Eq. 7-1 can be read as follows: The convective heat flux out of the segment (term on the left-hand side) equals the convective heat flux into the segment from below (first term on the right-hand side) plus the convective heat flux from the reservoir into the wellbore (second term on the right-hand side) plus the conductive heat flux from the sand face to the well (third term on the right-hand side). The conductive term D bases on Ramey's (1962) approach of calculating a total heat transfer coefficient for the wellbore system. The convective terms include the transport of internal, kinetic and potential energy, e.g., the expansion work dependent on the respective pressure.

For neglected vertical conductive transport, the energy balance for a small volume inside the reservoir in steady state writes as:

$$0 = q_s \cdot \rho_s \left(h_{sf} + \frac{1}{2} \cdot \left(\frac{q_{sf}}{A \cdot \rho_{sf}} \right)^2 - h_{res} \right) + D \cdot \Delta \mathrm{T}_{sf} + D_{res} \cdot \Delta \mathrm{T}_{res}, \qquad \text{(eq. 7-2)}$$

$$\text{with} \qquad \Delta T_{res} = T_{sf} - T_{geo},$$

where the subscript res represents the reservoir and T_{geo} $(°C)$ is the geothermal temperature far away from the borehole. The exact deduction of eq. 7-1 and eq. 7-2 can be reviewed in Kotlar et al. (2021).

The modeling workflow is as follows: We assume that the reservoir fluid far away from the well is at the temperature of the geothermal gradient T_{geo}. With knowledge of T_{geo}, fluid properties and pressure, eq. 6-1 and eq. 6-2 can be solved iteratively for the temperature at the interface reservoir/well T_{sf} and the temperature at the segment T_s until convergence with the measured temperature profile (DTS production profile). At convergence (minimized error between simulated temperature profile and measured DTS profile), a quantitative production profile over the different segments of the well can be generated. Finally, with the known flow rate from the surface (pump rate during production), the flow profile can be evaluated by checking the deviation of the cumulative sum of the flow profile from the known pump rate.

To estimate the geothermal gradient, we used the extrapolated temperature as shown in Figure 8-3a. The radius of the reservoir section was taken from open-hole caliper measurements. The sand face pressure was estimated from measured data at the fiber-optic P/T gauge. Eq. 7-1 and eq. 7-2 include the flow model (mass rates q). Additional required input parameters for the applied production profiling are shown in Table 8-1. The model of Kotlar et al. (2021) can either calculate the pressure drop due to frictional loss at the flow zones between the reservoir pressure (pressure at large distance to the well) and sand face pressure from Skin, via porosity and permeability inputs (Kotlar et al., 2021), or let the user manually define a pressure loss at each segment.

Table 8-1. Input parameter for the inverse DTS profiling with KAPPA Emeraude

Parameter	**Definition of Parameter**	**Value**
T_{geo}	Geothermal gradient in the reservoir section from DTS measurements	26.93 °C/km
P_{sf}	Pressure at the interface well/reservoir from P/T gauge, extrapolated to bottom end of fiber-optic installation	$2.24 \cdot 10^7$ Pa
Q	Surface flow rate of produced thermal fluid	6600 l/min
λ_{res}	Rock thermal conductivity	3.7 W/(mK)
r	Estimated external radius	1000 m

Due to the injection profiling, we know that the upper part of the reservoir is a highly hydraulically active zone. A higher friction related pressure loss can therefore expected here due to changing flow velocity:

$$\Delta p = f \cdot \frac{l}{d} \cdot \frac{v^2 \cdot \rho}{2}, \tag{eq. 7-3}$$

where $\Delta p\ (Pa)$ is the loss of pressure, $f\ (-)$ is the friction factor, $l\ (m)$ is the length of the segment, $\rho\ (kg/m^3)$ is the density of the fluid, which was calculated according to the IAPWS-IF97 formulation (IAPWS, 2011), $d\ (m)$ is the diameter and $v\ (m/s)$ is the flow velocity. During the modeling process we manually assumed the pressure loss until a good fit (minimized error of modeled with measured temperature and pump rate) was achieved.

8.4 Results

We used the permanent fiber-optic monitoring system of the well SLS TH4 to gather DTS data during start of production and derived a production flow profile with the inverse model of Kotlar, Allain et al. (2021). Figure 8-4a shows the converged modeled temperature compared to the DTS profile during production and the temperature gradient from extrapolating the undisturbed DTS profiles as shown in Figure 8-3a. Figure 8-4b shows the interpreted inflow as a cumulative profile and contribution per flow zone.

A satisfactory fit with both DTS production profile and surface pump rate was achieved. From the interpreted contributions, we can distinguish four different hydraulically active zones. The most prominent zone is between 2820 m MD and 2855 m MD, for which an inflow participation of 78 % was interpreted. About 14 % flow were calculated at 2875 m MD to 2955 m MD. The calculations show two minor flow zones at 3255 m MD to 3400 m MD and 3455 m MD to 3555 m MD with less than 5 %, respectively 3 % flow.

8.5 Discussion

In Schölderle et al. (2021), more than 90 % of flow were interpreted at injection conditions (spinner flow meter measurements) at a karstified zone at the very top of the reservoir in the stratigraphic layer of the Purbeck. Table 8-2 shows a comparison of the updated interpretation at production conditions with the flow meter interpreted zone contributions at injection conditions. In a qualitative manner, both methods show that the upper 25 m thick (from flow

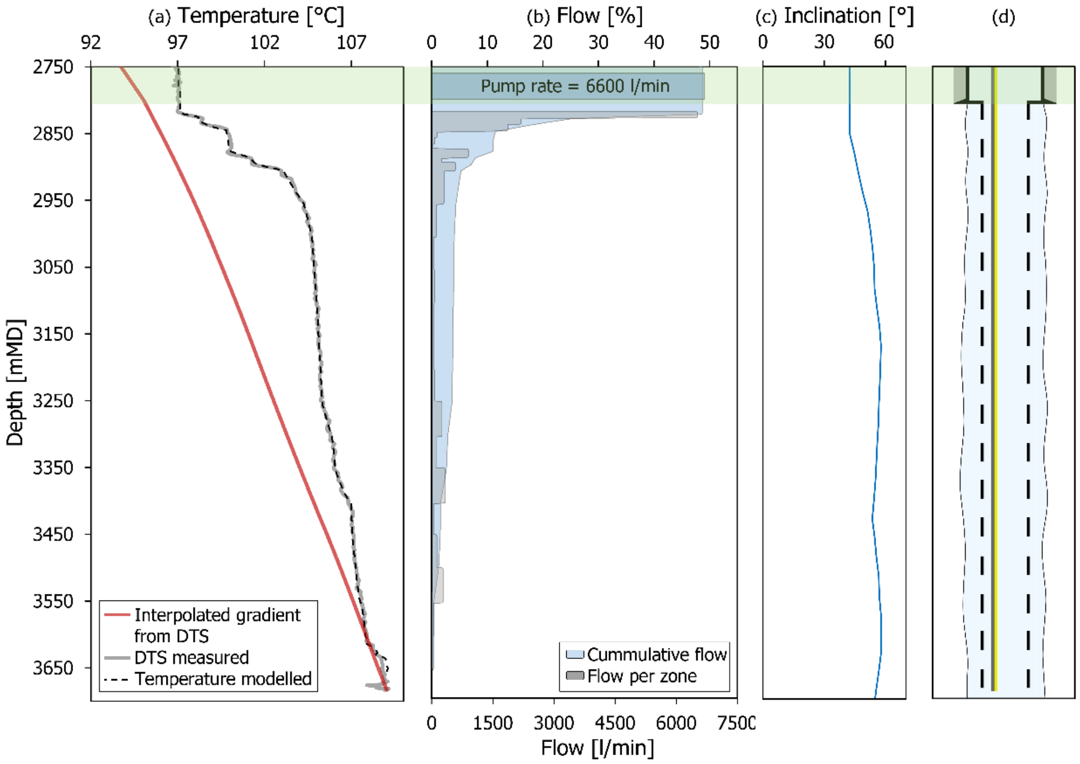

Figure 8-4. Results of DTS production profiling model inside the reservoir of SLS TH4. (a) Measured temperature (DTS, grey line) and modeled temperature (black dashed line) with estimated geothermal gradient (red line) versus depth, (b) modeled contribution of flow (grey) and cumulative flow in the bore (light blue) in comparison to surface pump rate (blue), (c) Inclination of the well, (d) well sketch of reservoir section. The olive band highlights the casing section. The shown results were generated with KAPPA Emeraude (v5.40).

meter interpretation), respectively 35 m thick (from inverse modeling) karstified zone is the dominant hydraulic contributor in the reservoir. However, a higher inflow rate in deeper regions of the reservoir was interpreted from the production DTS data than was previously possible using only flow meter data at injection.

Both methods, flow meter interpretation and inverse DTS production profiling bear some uncertainties. Concerning the spinner flow meter run, we have to consider the high inclination (see Figure 8-4c) in the reservoir section and the completion with the perforated liner, which is likely to provoke complicated flow regimes and turbulences, e.g., due to flow behind the liner (Ben Haoua et al., 2015; Zarrouk and McLean, 2019). Furthermore, the quality of flow meter measurements is dependent on a smooth run of the tool (Schlumberger, 1997). In addition, due to the closeness of the hydraulically active zone to the liner hanger, it is likely that the change of the diameter leads to turbulences that might disturb the spinner velocity.

The uncertainty of the modeling solution on the other hand is dependent on the models limitations and the errors that lie in the assumed input parameters. As shown in Figure 8-3a and b, we had to assume parts of the geothermal gradient as the shut-in DTS profiles were not yet

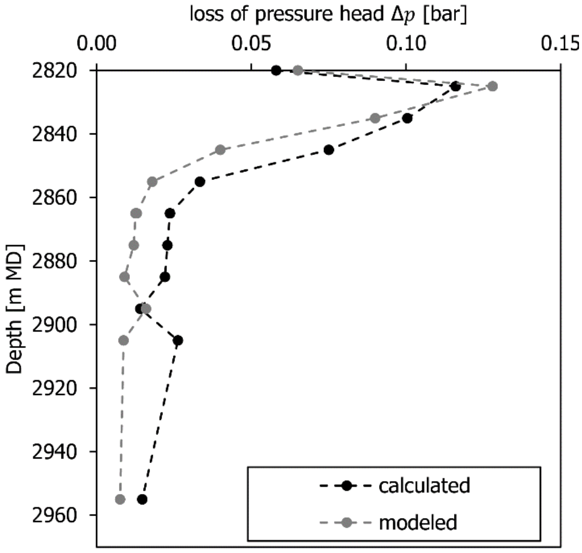

Figure 8-5. Comparison of pressure loss at the main flow zone estimated as input for Emeraude modeling with analytically calculated pressure loss.

completely equilibrated. Concerning the reservoir pressure, we used the data measured at the P/T gauge during shut-in and during production. The production-profiling module (Emeraude, n.d.; Kotlar et al., 2021) allows for calculating the production pressure profile from user input of skin factor at each flow zone and permeability and porosity. As those values were unknown, we iteratively changed the pressure loss at the zones manually until the model converged. A simple friction pressure loss model can show if the assumed pressure loss beforehand can be calculated from the achieved flow profile. To do so, we calculated the flow velocity from the modeled flow profile with a simplified flow cross-section, taking the drill bit size of the reservoir section (8.5 inch) subtracted with the thickness of the perforated liner and neglecting outbreaks in the rock and the narrowing of the cross-section due to the fiber-optic cable. We took the roughness of the pipe (perforated liner) as $2.05 \cdot 10^{-4}$ m (Codo et al., 2012) and calculated the friction factor f with the common equations of Nikuradse, Colebrook and White and Blasius (Lipovka and Lipovka, 2014). Following eq. 7-3, we then determined the pressure loss at different depths.

Table 8-2. Comparison of flow zones interpreted from DTS production data with flow zone interpretation from flow meter data at injection taken from Schölderle et al. (2021).

Interpreted flow zones at production		**Interpreted flow zones at injection (Schölderle et al., 2021)**	
Zone (m MD)	Flow contribution of zone	Zone (m MD)	Flow contribution of zone
2820 - 2855	78 %	2820 - 2845	92 %
2875 - 2955	14 %	2900 - 2950	< 5 %
3255 - 3400	< 5 %	3050 - 3300	< 3 %
3455 - 3555	< 3 %		

As shown in Figure 8-5, the assumed pressure loss used as input for the model and the calculated pressure loss from the obtained flow profile follow the same trend and are in the same magnitude at the different flow zone depths.

8.6 Conclusion

The results presented show that the permanent fiber-optic system can lead to a deeper understanding of the reservoir, which is important to ensure sustainable and secure use of the heat source thermal water. DTS data from production can be used for inverse production profiling as a viable alternative to common injection profiling methods and additionally enable permanent monitoring of any changes and divergences in production. Throughout the acquisition of the presented data, two of the three doublets at the site were running and might have affected each other. Therefore, DTS measurements for inverse production profiling will be continued during the upcoming long-term production tests to evaluate if different configurations (only one active doublet or all three doublets in production) lead to different model solutions.

Author contributions: FS performed the analyses and modeling. FS, DP and KZ shaped the research and wrote the manuscript. KZ helped providing funding and revised the manuscript. All authors read and agreed to the published version of the manuscript.

Code availability: The code for the inverse model is included in the commercial software KAPPA Emeraude. Please contact the corresponding author for information about the additional code used for the pressure loss model.

Data availability: Data is available from the corresponding author on reasonable request.

Special issue statement: This article is part of the special issue 'European Geosciences Union General Assembly 2022, EGU Division Energy, Resources & Environment (ERE)'. It is a result of the EGU General Assembly 2022, Vienna, Austria, 23–27 May 2022.

Acknowledgments: We are grateful for the support of Stadtwerke München SWM, who are the owners of the monitored well and who made the research possible. We would like to especially thank Michael Meinecke for his commitment to the project. We also thank the two anonymous reviewers for their generous time in providing comments and suggestions that helped us to improve the paper.

Financial support: This research has been supported by the Bundesministerium für Wirtschaft und Energie (grant no. 0324332B) and the Bayerisches Staatsministerium für Wissenschaft und Kunst (grant no. Geothermie-Allianz Bayern). This work was supported by the German Research Foundation (DFG) and the Technical University of Munich (TUM) in the framework of the Open Access Publishing Program.

Review statement: This paper was edited by Gregor Giebel and reviewed by two anonymous referees.

9 SYNOPTIC DISCUSSION AND CONCLUSION

9.1 Brief Overview

In Ch. 4 (Schölderle et al. 2023), we developed an alternative approach based on probability theory to the current methods for correcting poor-quality BHT data. We reassessed the raw NAFB temperature data set in Bavaria by estimating the uncertainties of the relevant inputs and correcting them with the common methods using a Monte Carlo approach. This considers the preliminary estimated uncertainty of the input data and provides the corrected values as density distributions. Taking the p10 and p90 values of these distributions as worst-case and best-case scenarios, their spacing was defined as the uncertainty range of each corrected value. These distributions can form the basis for a new static 3D temperature model or for improving the established models in the future.

In Ch. 5 (Schölderle et al. 2021), we discussed the installation of a fiber optic cable in a geothermal production well to continuously monitor the thermal behavior in the reservoir. We performed DTS measurements during shut-in, injection tests, and start of operating the well (Ch. 8, Schölderle et al. 2022) and tested the suspended fiber optic cable in relation to its relative motion along the borehole by combining DTS and DAS dynamic strain rate measurements (Ch. 6, Lipus et al. 2022). With the established measuring system, the undisturbed temperature in the rock could be derived in high quality, and an inflow zone characterization and monitoring could be carried out. This provides insight into the relationship between the estimated static temperature and the production temperature later controlled by the inflow zones for the example well.

9.2 On the Prediction of the NAFB Natural Thermal Field

9.2.1 Uncertainty Assessment of the Developed BHT-Correction Workflow

9.2.1.1 Predicted Uncertainties and Comparison with the Literature

Deming (1989) stated that due to unknown errors in the raw BHT data and the general unavailability of precise data sets, “accurate BHT correction is not difficult; it is, in fact impossible”. When screening the NAFB temperature data set, we rated the quality of the

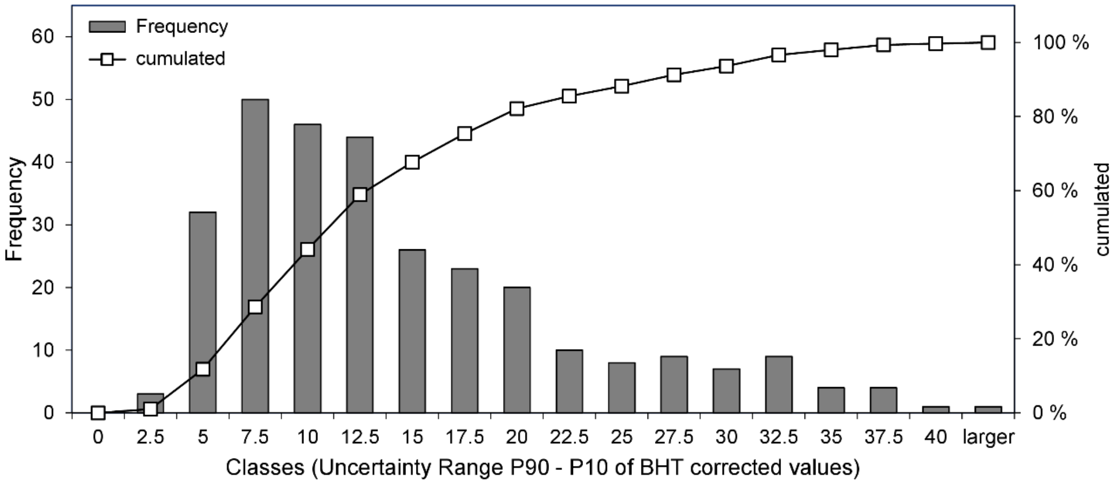

Figure 9-1. Histogram of the uncertainty range of all corrected BHT data sets in the NAFB.

individual BHT data sets in Ch. 4 and found confirmation of Deming's statement. In none of the cases, a perfect data set was available in which the depth of the recorded BHTs, their accuracy, and exact shut-in times did not have to be questioned (e.g., possible rounding, missing information on the accuracy, or calibration of the measuring device). Consequently, errors on these had to be estimated. Even when confidence in the input data set was high, parameters such as bulk thermal diffusivity and mud temperature downhole always had to be estimated. All this leads to generally high uncertainty estimates for the input data and consequently to relatively high p90-p10 ranges. It should be noted that the p90-p10 uncertainty range is in most cases an asymmetric distribution (see Ch. 4), in which the p50 value is shifted to the left side of the distribution. The comparison with other values from the literature, e.g. Förster (2001) and Goutorbe et al. (2007) or the GeotIS temperature model, should be considered against this background, as these assume standard distributions when specifying uncertainties. Figure 9-1 shows the distribution of the uncertainty ranges obtained after applying the developed good-practice workflow (see Figure 4-14 and descriptions in Ch. 4.4) to the whole NAFB data set. In less than 20 %, the estimated uncertainty is lower than 5 K, and in 50 %, the uncertainty is higher than 10 K. Around 5 % of the data are of such low quality that a high error of 30 K or larger was estimated. Goutorbe et al. (2007) stated the uncertainty mostly being ± 10 K. Förster (2001) found that corrected BHT values in the Northeast German Basin do not reflect undisturbed conditions (taken from equilibrated logs) better than with a standard deviation $\sigma = \pm 8$ K (68 % confidence), respectively $2\sigma = \pm 16$ K (96 % confidence). The p90-p10 value of one of our corrected BHT distributions corresponds to the 80 % confidence interval. A comparison of uncertainties of our data set to the findings of Förster (2001) is possible if we calculate the data point X under the assumption of normally distributed values at a confidence of 80 %, for which the z-value z is 1.28 (ztable.io) as (eq. 9-1):

$$X = z \cdot \sigma = 1.28 \cdot \pm 8\,K = \pm 10.24\,K. \qquad \text{(eq. 9-1)}$$

This corresponds to an uncertainty range (similar to the p90-p10 value) of about 20 K. Figure 9-1 shows that the assessed uncertainties are in good agreement with Förster (2001) and Goutorbe et al. (2007), although higher uncertainties were found for about 20 % of the corrected BHT values in the NAFB. Considering how sensitive the temperature parameter is to the subsequent thermal output (see eq. 1-1 and the example calculations in Ch. 4.4.3 showing reductions of heat outputs of over 58 % when the uncertainty range is as high as 30 K), this uncertainty can have a decisive influence on the economic success or failure of a project.

9.2.1.2 Comparison with DTS Data

In contrast, the accuracy of the BHT correction methods themselves can be evaluated (without the influence of the usual uncertainties in the input data) if a theoretically perfect BHT data set is created synthetically. This can be done by correcting temperatures at several depths taken at different time intervals from the high-quality fiber optic temperature profiles that were measured after cold-water injection and the subsequent shut-in of several months (see Figure 4-8). These injection tests should essentially reflect the same thermal conditions that prevail during BHT measurements: Instead of being cooled by the drilling mud, the borehole was cooled by the injected tap water. Instead of geophysical logging and subsequent BHT measurement with a temperature probe, the temperature of the water downhole was measured with the fiber optic monitoring system. However, thanks to the fiber optic measures, the temperatures during injection and in defined shut-in intervals as well as the undisturbed formation temperature are known with significantly higher quality compared to common BHT data sets (see Figure 4-7, Figure 4-8, Figure 5-7, Figure 8-3). In Figure 4-8, we found that BHT correction leads to very high errors when the BHT was measured in the depth of a dominant hydraulically active zone. As the BHT corrections used are based on the assumption of purely conductive heat transport, they fail at those locations.

To examine the susceptibility to errors of the exemplary methods of Horner and Brennand in more detail, four different depths from Figure 4-8 are examined in Figure 9-2. In the NAFB, there are often only a few BHT data sets in a series (see Table 4-1), so the methods were tested for the worst case of only two measurements (at $t_1 = 12$ h and $t_2 = 18$ h shut-in time which are typical shut-in times in the database). The results are shown in Table 9-1. Both methods perform similarly and predict values that deviate at the four exemplary examined depths not better than 1.7 K from the SFT measured by fiber optics before the cold water injection. The highest deviation is about 7.3 K at a depth of 800 m. A strong decline of the deviations can be found when t_2 is substituted by a long shut-in time ($t_4 = 178$ h) in the calculations. Then, Horner method performs better, resulting in deviations less than 0.3 K at all considered depths. The errors given by Brennand's method are not higher than 1.5 K, but systematically higher compared to Horner. A possible explanation for a systematic shift lies in the constant $p = 0.785$ (see Ch. 4.2.2.3 and eq. 4-4) which was originally calibrated by Brennand (1984) on a Philippines data set. What becomes

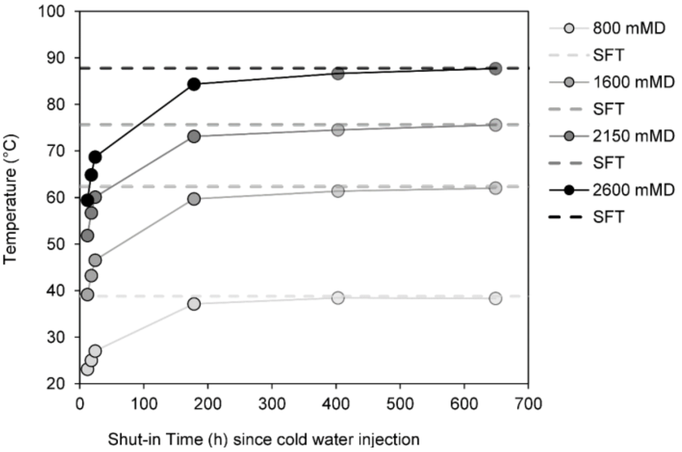

Figure 9-2. Synthetic BHT data sets (points) at four different depths measured with the fiber optic monitoring system in the well SLS TH4 at different time intervals after a cold-water injection test and known static formation temperatures (dashed line) derived from a distributed temperature profile at undisturbed thermal conditions. The transparent points at 400 h and 660 h were not used in Table 9-1 to test the BHT correction methods.

clear from these calculations, however, is that at least with regard to the graphical methods, a correction of BHT values that were recorded at short shut-in times should be treated with caution. This is in agreement with the statements in the literature that the reliability of these methods increases with longer shut-in times (e.g., Goutorbe et al., 2007). Unfortunately, the analytical correction methods Linearization Method (Ch. 4.2.2.4), Forward Modeling FM (Schulz, R. & Werner, 1987) and 1BHTM (Ch. 4.2.2.6) cannot be compared similarly at an ideal BHT data set, as they require the specification of the thermal diffusivity κ for their methodology.

Table 9-1. Synthetic BHT values at different depths from the fiber optic monitored well SLS TH4. The bold values t1, t2, and t4 at 12h, 18h, 178h shut-in time were used for BHT correction with Horner and Brennand method for a typical case (short shut-in times t1, t2) and an optimal case (t1, t4) to compare the results with the static formation temperature known from fiber optic sensing before the thermal disturbance.

Shut-in Time (h)	**Temperature (°C) at**			
	800 m MD	1600 m MD	2150 m MD	2600 m MD
t1 = 12	23.13	39.18	51.84	59.43
t2 = 18	25.02	43.23	56.70	64.87
t3 = 24	27.05	46.54	60.12	68.70
t4 = 178	37.17	59.73	73.15	84.37
t5 = 403	38.44	61.38	74.53	86.63
t6 = 649	38.31	62.00	75.58	87.70
SFT from equilibrated temperature (DTS profile)	38.77	62.34	75.65	87.80
Horner corrected t1,t2	**31.39**	**56.88**	**73.09**	**83.21**
Deviation from SFT	7.38	5.46	2.56	4.59
Brennand corrected t1,t2	**34.73**	**64.05**	**81.68**	**92.83**
Deviation from SFT	4.03	-1.71	-6.03	-5.04
Horner corrected t1,t4	**39.00**	**62.40**	**75.92**	**87.61**
Deviation from SFT	-0.23	-0.06	-0.27	0.19
Brennand corrected t1,t4	**39.78**	**63.55**	**77.11**	**89.00**
Deviation from SFT	-1.01	-1.21	-1.46	-1.21

The literature values for κ are given as bulk values for the system drilling mud and rock. The DTS measurements we consider in Table 9-1 and Figure 9-2, however, were performed in the cased well. For such a system, values of κ are missing.

Overall, it should be emphasized repeatedly that the reference to BHT-corrected values can always be misleading despite all due care, as the documentation of the relevant parameters is likely to be inaccurate. The workflow presented in Ch. 4 with the published BHT_Unct python tool offers the possibility to carry out the corrections with greater care than was previously the practice. However, the correction and the final range of the distributed results depend on how high the uncertainty in the input parameters is estimated to be. This must be done by an expert estimate after reviewing the data. Incorrect values can still be overlooked or misinterpreted here. Comparing the derived SFT values with high-quality temperature measurements, such as undisturbed temperature logs, is therefore highly recommended.

9.2.2 Comparison with Real-World Data and Other BHT-Based Models

9.2.2.1 Depth Projection to Top of the Reservoir

As described in Ch. 2.5.2, there are various models for the static deep temperature in the Bavarian part of the NAFB. The fact that these models can differ greatly in their predictions (see Figure 2-4) underlines how difficult it is to make an accurate forecast. The best-established temperature model in Germany, GeotIS, is based to a large extent on BHT-corrected temperature data (Agemar et al., 2012; Agemar, 2022a). It is a good tool for preliminary temperature assessment, but it does not comprehensively and correctly reflect the large uncertainties in the input data.

The SFT values derived with the new workflow have not yet been converted into a regionalized 2D or 3D temperature model. They are available at a wide range of depths. However, to compare them and the respective deviations of the expected p50 value to p10 and p90 values with the established temperature models GeotIS (Agemar, 2022a) and GeoMol (Team GeoMol, 2015a), they have to be extrapolated to the same depth. As a first simplified approach, this can be done using the geothermal gradients that are known from an analysis of the existing undisturbed temperature logs. With a robust fit regression on the undisturbed temperature logs and the fiber optic temperature log available (Figure 4-2 and Figure 5-7), mean thermal gradients can be calculated for the main stratigraphic layers of the NAFB as shown in Supplementary 9 - 1. Then, similar to (Team GeoMol, 2015c), the BHT corrected temperature SFT_{ref} $(°C)$ can be extrapolated to the depth of top reservoir (Purbeck or Upper Jurassic) as SFT_{Res} $(°C)$ for each stratigraphic layer i and respective depth D_i (m) and geothermal gradient ∇T_i $(°C/m)$ according to Fourier's law of heat conduction as eq. 9-2:

$$SFT_{Res} = SFT_{ref} + \sum_i \left((D_{i+1} - D_i) \cdot \nabla T_i \right) \qquad \text{(eq. 9-2)}$$

9.2.2.2 Comparison to Known Static Formation Temperatures

In Figure 9-3, p50 temperatures corrected with our workflow and simplified extrapolated to the top of the reservoir are shown at six locations of the NAFB together with GeoMol and GeotIS temperatures. The selected sites are wells from Figure 4-2 and Supplementary 4-1, 9-2 for which undisturbed temperature profiles are available. The temperature at the respective depth of the top reservoir was taken from these profiles and is also shown in Figure 9-3. The uncertainty of the p50 values is given as an error bar, calculated as the distance to the respective p10 and p90 value. The GeotIS model specifies the uncertainty as an estimated standard deviation based on Kriging variance (Agemar et al., 2014; Agemar and Tribbensee, 2018). This was also displayed as an error bar, as can be found at every location in the GeotIS online tool. The GeoMol model specifies the uncertainties from indicator Kriging to be within ± 15 K in 81 % of cases (Team GeoMol, 2015a). A site-specific inaccuracy cannot be indicated from the indicator Kriging maps and the error bars in Figure 9-3 are therefore shown as a dashed line and should only be understood as a rough indication. Except for well no. 7, where the calculated p10 value exceeds the measured value by 1.7 K, the known SFT is within the specified p10-p90 uncertainty ranges. The probabilistic calculated and depth projected p50 value provides the best estimate for wells no. 5 and no. 6, the GeoMol model for wells no. 4 and no. 12, and the GeotIS model for wells no. 7 and no. 13. Across all sites, the three methods perform similarly, with the cumulative deviations between the expected and measured values being 31 K for our method, 30 K for the GeoMol model, and 34 K for the GeotIS model. Unfortunately, there are only a few wells that have an undisturbed temperature profile and information on the depth of the uppermost reservoir and where correctable BHT measurements are known. The informative value of Figure 9-3 is therefore limited and other locations should also be compared.

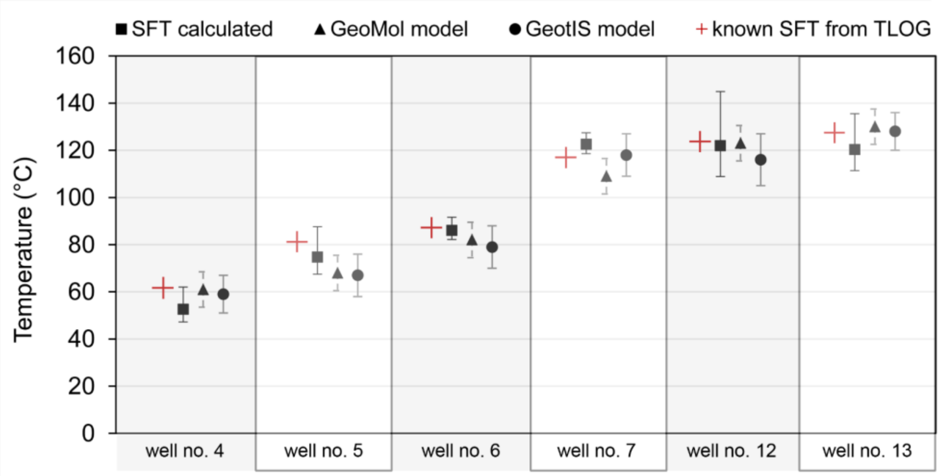

Figure 9-3. Comparison of extrapolated BHT corrected p50 values (probabilistic workflow) and their uncertainties from p90 and p10 values with GeoMol and GeotIS temperatures at six wells from Supplementary 4-1, where SFT values were measured at top of the reservoir (red) with undisturbed temperature logs.

9.2.2.3 Basin-Wide Comparison with Other Models and Outflow Temperatures

In Table 9-2 and Figure 9-4, p50 temperatures corrected with our workflow and simplified extrapolated to the top of the reservoir are shown at some exemplary locations of the NAFB together with GeoMol and GeotIS temperatures. Six of the sites are geothermal wells for which outflow temperatures from operation data were available, representing real-world data.

Comparing the p50 values to GeoMol and GeotIS shows good agreement with the GeotIS model, but higher deviations are observed from the GeoMol model. Note that the quality score in Table 9-2 refers to the quality of the individual BHT data sets and not to the overall correction. For example, for wells with only one, but well-documented BHT value and the corresponding shut-in time and other parameters, the quality may be good, but the correction still results in a large error due to the more erroneous correction method used (1BHTM). In other wells, high uncertainty ranges are simulated although they have a range of BHT values and corresponding other parameters that allow the application of better correction methods (e.g. Brennand Method BM, Linearization Method LM, or Forward Modeling FM).

The p50 values match the actual measured outflow temperatures T_{Out} with deviations of 2.0 to 7.0 K. At three of the wells, the outflow temperatures are better represented as from the GeoMol and GeotIS model. For the other three wells, GeotIS gives the best guess. The significance of this comparison of the measured flow temperatures on the surface with the undisturbed static temperatures on the top Reservoir is difficult to evaluate. First, the heat loss from the reservoir to the surface is unknown and depends primarily on the well design and production parameters. Second, the temperature in the borehole changes during pumping, as a mixed temperature is established that depends on the inflows of different temperatures in the reservoir. Despite these unknowns, the p50 appears to be suitable for an initial estimate of the expected outflow temperature. However, T_{Out} is also 2 K or 1 K outside the uncertainty in two cases (M_{NAFB},M and E_{NAFB},S, see Figure 9-4).

Compared to GeotIS and GeoMol, the uncertainties of our model have a wider range, as higher quality BHT data sets are stored with lower uncertainties in the inputs. This results in smaller uncertainty ranges and vice versa. At four of the exemplary wells in Table 9-2, the estimated uncertainty, which is a result of the erroneous BHT correction inputs, exceeds the uncertainty of the GeotIS model (Wells at location W_{NAFB},S; M_{NAFB},$S_{(2)}$; E_{NAFB},$E_{(1)}$; E_{NAFB},$S_{(1)}$). Considering that the probabilistically calculated values in Table 9-2 do not contain any uncertainty about the regionalization or extrapolation to other depths compared to GeotIS, even higher uncertainties can be assumed. It can thus be concluded that the uncertainties due to the variability in the BHT correction input parameters are in part considerably higher than they are represented by the temperature models.

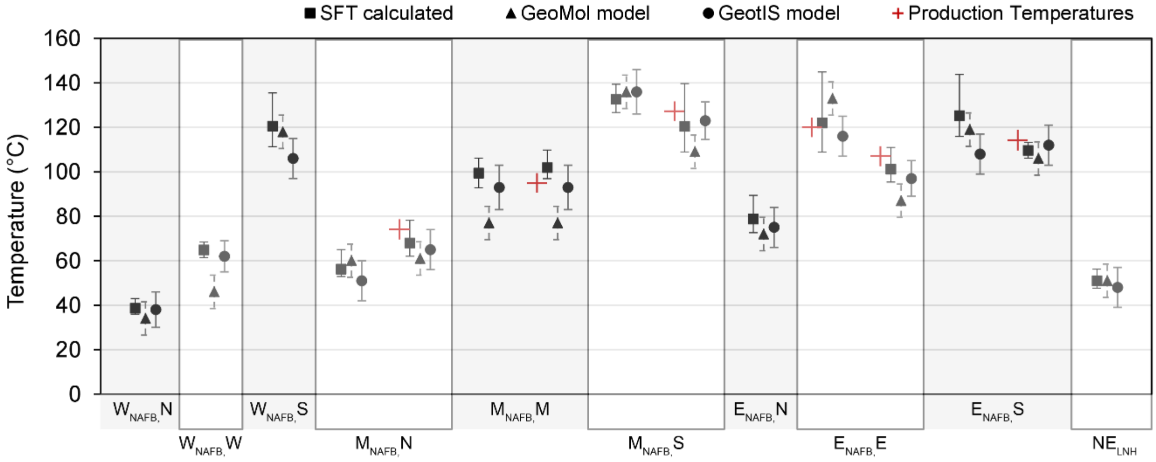

Figure 9-4. Calculated SFT compared to GeotIS and GeoMol temperatures at top of the reservoir of 15 exemplary wells dispersed in cardinal directions North, West, East and South (N, W, E, S) of the western NAFB, the middle (M, Munich area), eastern NAFB and northeast of the Landshut Neuoetting High (LNH) with uncertainties and measured outflow temperatures (red) available at six of the wells.

Table 9-2. Comparison of extrapolated BHT corrected p50 values (probabilistic workflow) and their uncertainties from p90 and p10 values with GeoMol and GeotIS temperatures at 15 exemplary wells in the NAFB dispersed in cardinal directions North, West, East, and South (N, W, E, S) of the western NAFB, the middle (M, Munich area), eastern NAFB and northeast of the Landshut Neuoetting High (LNH), see e.g., Figure 2-4. For six of these wells, wellhead (outflow) temperatures T_{Out} from operating data, provided by the Geothermal-Alliance Bavaria, were available that are listed as well for comparison.

Well location	T_{Out} (°C)(*)	BHT Quality	Proposed BHT correction workflow		GeoMol Model(**)	GeotIS Model(***)		Residual temperature to GeotIS (K)
			SFT_{Res} (°C)	p10 / p90 (K)	SFT_{Res} (°C)	SFT_{Res} (°C)	Uncertainty (K)	
W_{NAFB},N		3	38.6	-2.7 / +4.4	34.0	38.0	± 8.0	+0.6
W_{NAFB},W		1	64.9	-3.5 / +3.5	46.0	62.0	± 7.0	+2.9
W_{NAFB},S		2	109.7	-9.2 / +15.0	119.0	109.0	± 9.0	+0.7
M_{NAFB},$N_{(1)}$		2	56.2	-3.3 / +8.8	60.0	51.0	± 9.0	+5.2
M_{NAFB},$N_{(2)}$	74.0	3	67.9	-5.9 / +10.3	61.0	65.0	± 9.0	+2.9
M_{NAFB},$M_{(1)}$		3	99.4	-6.6 / +6.8	77.0	93.0	± 10.0	+6.4
M_{NAFB},$M_{(2)}$	95.5	3	101.9	-5.0 / +7.9	77.0	93.0	± 10.0	+8.9
M_{NAFB},$S_{(1)}$		2	132.7	-6.0 / +6.7	136.0	136.0	± 10.0	-3.3
M_{NAFB},$S_{(2)}$	127.2	2	120.4	-11.4 / +19.3	109.0	123.0	± 8.5	-2.6
E_{NAFB},N		2	78.8	-6.2 / +6.6	72.0	75.0	± 9.0	+3.8
E_{NAFB},$E_{(1)}$	120.0	3	122.0	-13.1 / +22.9	133.0	116.0	± 9.0	+6.0
E_{NAFB},$E_{(2)}$	107.1	3	101.2	-5.8 / +9.8	87.0	97.0	± 8.0	+4.2
E_{NAFB},$S_{(1)}$		2	125.3	-9.4 / +18.5	119.0	108.0	± 9.0	+17.3
E_{NAFB},$S_{(2)}$	114.2	2	109.6	-3.4 / +3.6	106.0	112.0	± 9.0	-2.4
NE_{LNH}		1	51.0	-3.4 / +5.2	51.0	48.0	± 9.0	+3.0

references: (*)Geothermal-Alliance Bavaria, (**)(Team GeoMol, 2015a), (***)(Agemar et al., 2012; Agemar, 2022a)

9.2.3 Further Use of the Developed Workflow: Prospects and Potential

The uncertainty-based corrected BHT values are only available as point values at their respective measurement depth. Geostatistical methods, which introduce additional uncertainty into the temperature forecast were not yet used at this time. As shown in Figure 9-1 and Table 9-2, uncertainties in the established temperature models are likely to be higher than specified. To build a full-temperature model of the corrected temperatures, sophisticated geostatistical methods are needed that account for the uncertainty ranges from a 3D approach. Albarrán-Ordás et al. (2023) performed such by implementing uncertainties in shallow lithological borehole data into a 3D geomodel using the D_i model approach from a previous study (Albarrán-Ordás and Zosseder, 2021). This method can be a blueprint for the creation of an uncertainty-based depth temperature model from the distributed BHT corrected values in the future.

The workflow and the Python tool introduced in Ch. 4 are also applicable to geothermal settings other than the NAFB. BHT corrections are used globally in a wide variety of geological contexts for temperature forecasting (Andaverde et al., 2005; Goutorbe et al., 2007; Zarrouk and McLean, 2019; Barba et al., 2021). The sole requirement for an adaption of the proposed workflow is that reliable reservoir temperatures or undisturbed temperature profiles are distributed in the respective area to check the accuracy of the respective BHT corrections. In particular, the order of magnitude of the parameters thermal diffusivity, borehole radius, and mud temperature, as implemented in the published Python tool, are specific to the geological conditions in the NAFB and the drilling practices prevalent there. For example, other geological settings like high enthalpy geothermal plays might require different drilling mud temperatures. The thermal diffusivity depends highly on the thermal properties of the present geology. A value of $3.5 \cdot 10^{-7}$ m^2/s, as proposed by Leblanc et al. (1982) for a Canadian well data set of the sedimentary basin of Alberta, and a value of $3.0 \cdot 10^{-7}$ m^2/s tested on wells in the sedimentary Cooper basin in Australia by Middleton (1982) worked out good for the NAFB (see Ch. 4.2.3.2). To find a reasonable value for the thermal diffusivity for the specific geothermal setting, a fitting with model runs with varying values can be carried out, as shown in Ch. 4.3.1 and Figure 4-10. Alternatively, a two-media borehole model as proposed by Middleton (1982) could be used. The Python tool BHT_Unct can then be modified according to the realistic value ranges. The use of other analysis methods than the six correction methods presented is also conceivable and fairly simple.

9.3 On the Integrated FO System and the Reservoir Characterization of the Study Well

9.3.1 Suitability of the System for Reservoir Measurements

With the successful installation in 2019 and the largely permanent DTS and P/T monitoring (Figure 7-1) as well as DAS campaigns, the system has proven its concept. The primary focus of its design was to enable distributed temperature measurements over as much of the reservoir length as possible, which is why the suspended construction along a sucker rod inside the casing was chosen. The technical consequences for the borehole and recommendations for future similar installations and interventions such as pump changes and the operation of the measuring system have already been described in Ch. 7. However, there are also implications with regard to the evaluability of the measurements. Due to the suspension design, the sucker rod/cable system only has one fixed point at the crossover to the production tubing, respective the tubing that was used before the pump was installed. For the rest of the borehole, the cable and sucker rod rest loosely against the wall, allowing dynamic movement along the axis of the well. The DAS measurements evaluated during the cold water injection strongly indicated that thermal stress on the structure in particular triggers such movements (Figure 5-11 and Ch. 6). With an assumed thermal expansion coefficient of 10 – 13 $\mu\varepsilon/\mathrm{K}$ (Hidnert, 1931), we calculated a theoretical strain on the sucker rod that is in good agreement to the actual measured strain by DAS (Figure 5-11, Figure 6-4). Additionally, we calculated a displacement of the bottom end of the sucker rod/cable of 1.5 m from the DTS data (see Figure 5-13). Compared to the spatial resolution of the processed data of approximately 1 m (Ch. 5.2.3), this is not much, however, the movements of the sucker rod/cable appear sudden, which is regarded by the DAS as strain events with a large extension. We found a strong indication that these events that we called ‘sucker rod events’ are explained by stress on the rod due to thermal contraction overcoming the friction of the cable/sucker rod at the borehole wall. With a stick-slip approach, we found regions where the forces are exceeded so that sucker rod events can appear (Ch. 6.4.3). Particularly high are those in around 2800 m MD, which is near the uppermost dominant hydraulically active zone. As a consequence for DAS monitoring in a suspended system, we can conclude that events recorded with DAS should be treated with caution. Strong events might not be associated with microseismic events (as e.g., described in Ghahfarokhi et al., 2018), nor is the tracking of fluid movement within the wellbore possible by DAS analysis if the errors in the data caused by the mechanical movement of the system are not taken into account. A workflow to make this possible must be developed in the future.

To assess the suitability of the DTS measurements of the converted system for reservoir characterization, the accuracy of the measurements must be known. In Ch. 7.4.3, an error propagation calculation was performed considering various uncertainties in the positioning of the cable and uncertainties of the absolute temperature values given by the DTS. From this and the calculated standard deviations of both temperature measurement and the displacement, we expect an error of less than ± 1.6 K. A resolution accurate to the meter is not particularly important in the 900 m MD long monitored borehole, considering the positional inaccuracies that also apply in part to other logs (e.g., time-depth correlation of a tool or thermal expansion). Changes in temperature due to inflows can easily amount to several tens of Kelvin over short distances (see e.g., Zarrouk and McLean, 2019). Integrated over a longer measuring distance, the error of the DTS measurements is relativized and analyses based on the measured DTS temperature are then possible at high quality. This is also supported by the good agreement between the characterization of the hydraulically active zones based on the DTS data (Ch. 5.4.3 and Ch. 8.4) and the conventional PLT evaluation (Ch. 5.2.4).

9.3.2 Insights into the Monitored Borehole and the Reservoir

SFT measurements are usually done with temperature wireline logs. Such covering the entire reservoir section is rare, as is costly, bear a risk to the well, especially when completed open hole, and may not even be possible at high deviated wells. For example, only 5 logs of 13 available supposed undisturbed logs in the NAFB cover the entire reservoir section (see Supplementary 9 - *1*). Furthermore, those wireline logs are run only once during the shut-in time of the well and it is not clear if the duration given for the well to equilibrate to the undisturbed conditions was enough. The reservoir of the studied well was extensively characterized using conventional data (e.g., sonic log and flowmeter, Figure 5-6) and fiber optic DTS and DAS data (Figure 5-9, Figure 5-14, Figure 5-15, Figure 8-4, Figure 8-5). Flowmeter spinner PLT analysis is the standard tool for hydraulically zone characterization of deep geothermal wells (Zarrouk and McLean, 2019), however not always possible or prone to errors (e.g., Haoua et al., 2015). The SLS TH4 study well is a prime example of a well whose reservoir is difficult to characterize with standard PLT. It is heavily deviated and has a slotted liner that is likely to trigger complex flow conditions. As a result, the informative value of the flowmeter evaluation could be questioned. Nevertheless, the DTS measurements during the injection test and under production conditions confirmed the qualitative statement of the inflow determination of the PLT (Figure 5-14, Figure 5-15, and Figure 8-4). It was difficult to evaluate the DAS measurements during the injection test, as the noise was very high due to the sucker rod events described in Ch. 6, especially at top of the reservoir. However, in the very first minutes of the injection tests, before the first sucker rod events were recorded, DAS signals were captured that are in strong agreement with the analyzed inflow profile of PLT (see Figure 5-14). Unfortunately, no DAS record was available at the Schäftlarnstraße site when the well was first put into production and the DTS profiles analyzed in Ch. 8 were measured. An analysis of DAS data in the reservoir, while the well is producing, may be the subject of a future study, as well as the possible derivation of flow velocities from the DAS profile shown in Figure 5-14b, e.g., by analyzing the frequency information as described by Paleja et al. (2015).

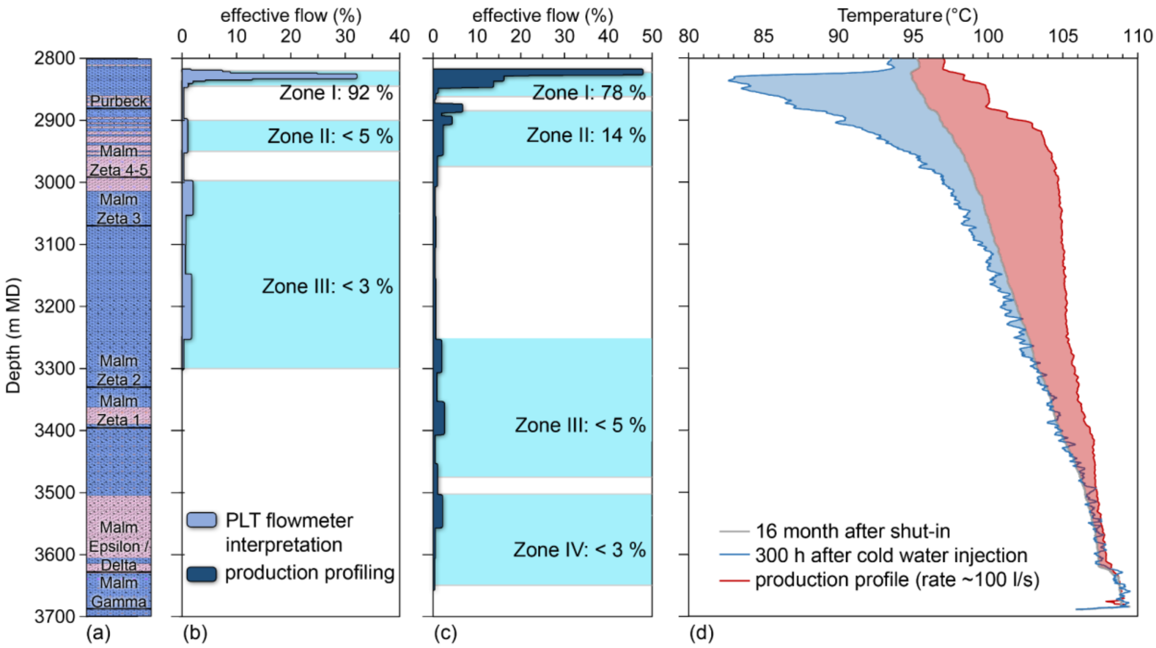

Figure 9-5. Summarizing comparison of the flow zone characterization in reservoir section of well SLS TH4. (a): stratigraphy in the reservoir with schematically drawn Karst in the Purbeck layer, (b): PLT flowmeter interpretation (Ch. 5.2.4) with cumulated flow contribution outlined in light blue zone, (c): DTS production profiling from invers model (Ch. 8.4) and interpreted zones in light blue and (d): exemplary DTS profiles during warm-back of the injection test (blue, see Ch. 5.2.7), during well production (red, see Ch. 8.4) and during shut-in (grey, see Ch. 8.3.1). The deviation of the cold and warm DTS profile from the assumed undisturbed (shut-in profile) is sketched in (d) as a blue and red area respectively.

Not only could we compare the conventional PLT analysis with fiber optic methods qualitatively, but also quantitatively by calculating a flow profile from the DTS production profile with inverse methods following a mass balance approach (Figure 8-4, Table 8-2). Figure 9-5 shows the summarized interpretation of the inflow distribution during injection (flowmeter, PLT) and production (DTS profiling). The corresponding equations of the mass balance (see eq. 8-1 and eq. 8-2 in Ch. 8.3.2) are solved iteratively for two temperature parameters, the temperature inside the borehole of a well segment T_s and the temperature at the interface to the rock T_{sf}, whereby multiple model results are possible. This ambiguity is a well-known problem (e.g., Parker, 1977; Jaynes, 1984) and thus, the flow profile shown in Figure 8-4 and Figure 9-5c should be regarded as only one possible interpretation. However, it gives a further strong indication that the inflow to the borehole and also the production temperature is very strongly controlled by the dominant karstified uppermost hydraulically active zone. It can also be said, that injection profiling (PLT) cannot necessarily be projected one-to-one onto production conditions.

9.3.3 On the Influence of Hydraulically Active Zones

The NAFB reservoir is known to be very heterogeneous (Birner, 2013; Drews et al., 2018; Bohnsack et al., 2020b; Heine et al., 2021; Konrad et al., 2019, 2021), and the hydraulics and production temperatures sometimes change significantly over short distances. The depth and extent of flow zones at a site are therefore uncertain in the planning phase. In Munich, Karst, often located at the top of the reservoir, seems to play a dominant role. The FO-monitored SLS TH4 study well is a role model for this reservoir type. With about 80 - 90 % of the hydraulic contribution of a zone at or near the top reservoir (Table 8-2), the production temperature is near the SFT at this depth. At SLS TH4, the mixing temperature at the entry to the cased section at 2810 m MD measured during production is only around 1.2 K hotter than the undisturbed static formation temperature at the same depth known from DTS measurements at longer shut-in phases (Figure 8-4, Figure 8-3). Disregarding the heat loss along the borehole and the heat gain at the pump, in such a system, the SFT as given by GeotIS, GeoMol, or our BHT correction workflow can serve well as an estimate for the later generated temperature. Moreover, it can be concluded that the SFT taken from these models represents a worst-case temperature in the forecast of production temperatures.

The idea of packing off such a dominant flow zone at the upper end of the reservoir to generate more inflow from further down and promote a higher mixing temperature is obvious. A rough calculation can be used to test the effects of such a measure on the productivity of the SLS TH4 study well. In Table 9-3, the flow contributions and respective flow rates are given at the most prominent hydraulically active zones as known from the inverse model (see Table 8-2) for the well in its original state and for an imaginary scenario where the cold uppermost hydraulically active zone is packed off. The contributions and flow rates of the second state were calculated under the assumption that the inflow is distributed to the other inflow zones to the same extent as in the initial state. The temperature of the produced fluid where taken from the DTS profile for both states at the upper end of the hydraulically active zones and the thermal power was calculated using eq. 1-1 and the same values for the fluid density and thermal capacity as proposed in Ch. 4.4.3. Based on these rough assumptions, the packaging would lead to an increase in the outlet temperature of 3 K, which would result in an increase in heat output of around 6 percent from 21.57 MW to 22.95 MW.

Table 9-3. Theoretical heat output (th. power) for SLS TH4 at an assumed injection temperature of 50 °C and assuming that the production temperature corresponds to the mixing temperature $Temp_{Mix}$. $Temp_{Mix}$ was taken from a production DTS profile (Figure 8-4) for both the original state as in Figure 8-4 and Table 8-2 and the well at a theoretical state where the uppermost flow zone was packed off.

	Well in the original state		**Well with Packer in upper zone**	
Flow zone (m MD)	Contribution	Flow (l/s)	Contribution	Flow (l/s)
2820-2855	0.78	85.8	Packer	
2875-2955	0.14	15.4	0.64	70.4
3255-3400	0.05	5.5	0.23	25.3
3455-3555	0.03	3.3	0.14	14.3
Pump rate (l/s)	110.0		110.0	
$Temp_{Mix}$ from DTS (°C)	97.0		100.0	
Th. power (MW)	21.57		22.95	

Table 9-4. Theoretical heat output for well SLS for different pump rate scenarios due to the removal of the uppermost zone with an imaginary packer at an assumed injection temperature of 50 °C and assuming a mixing temperature of 100.0 °C (see Table 9-3).

Pump rate (l/s)	Th. power (MW)
105	21.91
95	19.82
80	16.69
60	12.52
35	7.3

In reality, however, it is very likely that the original total pumping capacity of 110 l/s cannot be maintained if the highly productive zone is removed. Removing an inflow zone, especially if it is dominant, means that either a significantly lower flow rate is to be expected or the drawdown must be increased. In SLS TH4, the pump is already very low in the first section, so the drawdown cannot be increased much further. The thermal output is therefore also calculated for the packed-off well for decreasing pump rates in Table 9-4. The example calculation shows that lower flow rates quickly lead to a drop in thermal output despite the higher mixing temperature of the thermal water. It can therefore be concluded that the Karst-dominated zone causes reduced temperatures, but is supposedly essential for the hydraulics of the well.

In other wells that show warmer inflow in deeper zones, however, the packing of cold inflow zones may be an effective way to increase productivity. A fiber optic measurement system in a well with such different hydraulic behavior would therefore be welcome for comparison.

9.3.4 Further Use of Integrated Geothermal Fiber Optic Monitoring: Prospects and Potential

Integration of fiber optics into geothermal wells is particularly suitable for measuring the geophysical properties of the borehole and the reservoir, even when the well is produced. For such purpose, the FO system in the SLS TH4 borehole was developed and successfully implemented as a prototype within the Geothermal-Alliance Bavaria for the borehole. As described in Ch. 7, there have already been several interventions due to pump failures and other actions that have not yet (as of early 2024) affected the measurement quality.

The potential of DTS monitoring for reservoir characterization is summarized in Ch.9.3.2 and Ch. 9.3.3. Beyond that, the gathered temperature profiles could be used for calculating heat flow density or inverse calculation of thermal properties of the reservoir rock. This was not done in the course of this thesis but can be part of subsequent studies. The system could be also used for microseismic studies. However, the usefulness for this must be questioned. As shown in Ch. 6 and summarized in Ch. 9.3.1, the suspended sucker rod/cable system is susceptible to axial movement due to thermal stresses (contraction, expansion), which is recorded in the DAS data as a fairly large local event when the friction on the wall is overcome. Systems in which the cable is fixed at any depth and thus better coupled to the formation, for example by being cemented in as described in various studies (Henninges et al., 2005b; Reinsch and Henninges, 2012; Lipus et al., 2021), are therefore more suitable for such monitoring purposes.

9.4 Conclusions

Next to the quality of a thermal fluid (hydrochemical composition) and its quantity (possible extraction rate), its temperature plays a decisive role in utilizing geothermal heat. The extraction temperature in conductive-dominated low-enthalpy hydrothermal systems depends on the undisturbed temperature inside the heterogeneous reservoir and on the location and characteristics of the flow zones. Flow zones define how much water can enter at a certain temperature. The inflows of different temperatures mix until a mixed temperature is finally reached at the top of the uppermost inflow zone, which is transported towards the surface with the pumped water. With that, a geothermal well has its characteristic thermal signature in the reservoir.

At the beginning of this work, it was stated that the available temperature models remain unclear in terms of their actual uncertainty and that there is a general lack of tools and data in deep geothermal energy to distinguish production temperatures from undisturbed rock temperatures and prospective flow zones. It was assumed that the static temperature models which are based on BHT correction are too optimistic. The results of this thesis show that indeed the uncertainties can be much higher when the available data is poor and the error in the inputs to the correction methods have to be estimated high. By the same token, however, if the quality of the input data is sufficiently good, the uncertainties of the estimates can also be lower than those indicated by the usual methods. The methodology developed is therefore suitable for improving existing temperature models in the future. A projection of the corrected temperatures distributed over the depth into the surface is pending and an approach must also be found to project these onto a common depth (e.g., the top of the reservoir). In conductive-dominated hydrothermal systems, which is the standard case for NAFB, a SFT projected to the upper reservoir, i.e. where the fluid enters the cased section of a wellbore, can represent the production temperature as a worst-case temperature. Inflows from below the top reservoir would increase the production temperature. However, this theory is not fully applicable, as in some cases the uncertainty in the BHT corrections is so large that the SFT is estimated to be much higher than the known operating temperature (see Figure 9-4). Estimating the outflow temperature from the static temperature alone is therefore generally not recommended. Nevertheless, static temperature models have a strong justification for preliminary studies, productivity studies, and extrapolation planning. The BHT correction workflow developed can be a new tool for improving existing models or creating new ones, and it enables a valid error assessment that has not previously been considered.

To measure the undisturbed static temperature in place and study the thermal dynamics in the reservoir of a flowing deep well in the study area of the NAFB, a permanent fiber optic monitoring system was developed and successfully integrated into a commercial 3.7 km deep well. This closes the monitoring gap in hydrothermal wells to enable continuous long-term monitoring of the reservoir temperature and to monitor the future stability of the hydraulically active zones during production. The spatially distributed and high-resolution measurements of the fiber optic system proved to be advantageous for reservoir characterization under different well operating conditions. Hence, the hydraulically active zones were evaluated differently and compared to conventional PLT analysis under these different operating phases. The results draw the same picture of a strongly karstified characteristic of the upper reservoir and underline the relevance of the hydraulics in the study well for the temperature of the extracted water.

REFERENCES

Aabø, T. M. and Hermanrud, C.: Toward a global model for correction of bottomhole temperature data: Progress and limitations, AAPG Bulletin, 103, 139–155, https://doi.org/10.1306/0607181612117167, 2019.

Acuña, J. and Palm, B.: Distributed thermal response tests on pipe-in-pipe borehole heat exchangers, Applied Energy, 109, 312–320, https://doi.org/10.1016/j.apenergy.2013.01.024, 2013.

Agemar, T.: 3D Subsurface Temperature Model of Germany and Upper Austria. Compilation of gridded data (25 MB) and documentation, https://www.geotis.de/homepage/references, 2022a.

Agemar, T.: Bottom hole temperature correction based on empirical correlation, Geothermics, 99, 102296, https://doi.org/10.1016/j.geothermics.2021.102296, 2022b.

Agemar, T. and Tribbensee, K.: Geotis composite 3D model of the top of the upper Jurassic (Malm) in the area of the north Alpine Foreland Basin, Zeitschrift der Deutschen Gesellschaft fur Geowissenschaften, 169, 335–341, https://doi.org/10.1127/zdgg/2018/0126, 2018.

Agemar, T., Schellschmidt, R., and Schulz, R.: Subsurface temperature distribution in Germany, Geothermics, 44, 65–77, https://doi.org/10.1016/j.geothermics.2012.07.002, 2012.

Agemar, T., Alten, J.-A., Ganz, B., Kuder, J., Kühne, K., Schumacher, S., and Schulz, R.: The Geothermal Information System for Germany ? GeotIS, Zeitschrift der Deutschen Gesellschaft für Geowissenschaften, 165, 129–144, https://doi.org/10.1127/1860-1804/2014/0060, 2014.

Ahrendts, F., Drechsler, B., Hendricks, J., Küpper, J., Lang, S., Peil, T., Scholz, D., Timofeeva, E., Utri, M., Weidinger, L., Kraus, A., Weiß, U., and Müller, S.: Roll-out von Großwärmepumpen in Deutschland, accessed December 10, 2023, https://www.agora-energiewende.de/publikationen/roll-out-von-grosswaermepumpen-in-deutschland, 2023.

Albarrán-Ordás, A. and Zosseder, K.: The Di models method: geological 3-D modeling of detrital systems consisting of varying grain fractions to predict the relative lithological variability for a multipurpose usability, Bulletin of Engineering Geology and the Environment, 81, 34, https://doi.org/10.1007/s10064-021-02538-2, 2021.

Albarrán-Ordás, A. and Zosseder, K.: Uncertainties in 3-D stochastic geological modeling of fictive grain size distributions in detrital systems, Applied Computing and Geosciences, 19, 100127, https://doi.org/https://doi.org/10.1016/j.acags.2023.100127, 2023.

Ali, L., Bentley, R. E., Gutierrez, A. A., and Gonzalez, Y.: Using distributed temperature sensing (DTS) technology in acid gas injection design, Acta Geotechnica, 9, 135–144, https://doi.org/10.1007/s11440-013-0239-2, 2014.

Allen, R. V: Automatic earthquake recognition and timing from single traces, Bulletin of the Seismological Society of America, 68, 1521–1532, https://doi.org/10.1785/BSSA0680051521, 1978.

Andaverde, J., Verma, S. P., and Santoyo, E.: Uncertainty estimates of static formation temperatures in boreholes and evaluation of regression models, Geophysical Journal International, 160, 1112–1122, https://doi.org/10.1111/j.1365-246X.2005.02543.x, 2005.

Anderson, M. P.: Heat as a ground water tracer, Ground Water, 43, 951–968, https://doi.org/10.1111/j.1745-6584.2005.00052.x, 2005.

Angel, S. M. and Hirschfeld, T. B.: Fiber-optic sensors for use in the geothermal well, in: Conference on Lasers and Electro-Optics, FR4, https://doi.org/10.1364/cleo.1986.fr4, 2020.

ztable.io: accessed March 03, 2024, https://ztable.io/.

Pressure Drop Online-Calculator for Mobile and PDA: accessed February 15, 2024, http://www.pressure-drop.mobi/0103.html.

Arkwright, J. W., Underhill, I. D., Maunder, S. A., Jafari, A., Cartwright, N., and Lemckert, C.: Fiber optic pressure sensing arrays for monitoring horizontal and vertical pressures generated by traveling water waves, IEEE Sensors Journal, 14, 2739–2742, https://doi.org/10.1109/JSEN.2014.2311806, 2014.

Ascencio, F., Garcia, A., Rivera, J., and Arellano, V.: Estimation of Undisturbed Formation Temperatures Under Spherical-Radial Heat Flow Conditions, Geothermics, 23, 317–326, https://doi.org/10.1016/0375-6505(94)90027-2, 1994.

Axelsson, G.: Geothermal well testing, in: Developments in Water Science, https://doi.org/10.1016/S0167-5648(09)70036-X, 2013.

Banks, E. W., Shanafield, M. A., and Cook, P. G.: Induced Temperature Gradients to Examine Groundwater Flowpaths in Open Boreholes, Groundwater, 52, 943–951, https://doi.org/10.1111/gwat.12157, 2014.

Banks, J. and Harris, N. B.: Geothermal potential of Foreland Basins: A case study from the Western Canadian Sedimentary Basin, Geothermics, 76, 74–92, https://doi.org/10.1016/j.geothermics.2018.06.004, 2018.

Barba, D. P., Barragán, R., Gallardo, J., and Salguero, A.: Geothermal Gradients in the Upper Amazon Basin derived from BHT data, International Journal of Terrestrial Heat Flow and Applications, 4, 85–94, https://doi.org/10.31214/ijthfa.v4i1.58, 2021.

Barberan, C., Allanic, C., Avila, D., Hy-Billiot, J., Hartog, A., Frignet, B., and Lees, G.: Multi-offset seismic acquisition using optical fiber behind tubing, in: 74th European Association of Geoscientists and Engineers Conference and Exhibition 2012 Incorporating SPE EUROPEC 2012: Responsibly Securing Natural Resources, 11–16, https://doi.org/10.3997/2214-4609.20148798, 2012.

Bassam, A., Santoyo, E., Andaverde, J., Hernández, J. A., and Espinoza-Ojeda, O. M.: Estimation of static formation temperatures in geothermal wells by using an artificial neural network approach, Computers and Geosciences, 36, 1191–1199, https://doi.org/10.1016/j.cageo.2010.01.006, 2010.

Baticci, F., Genter, A., Huttenloch, P., and Zorn, R.: Corrosion and Scaling Detection in the Soultz EGS Power Plant, Upper Rhine Graben, France, in: Proceedings World Geothermal Congress, 25–29, 2010.

Bauer, M., Freeden, W., Jacobi, H., and Neu, T.: Handbuch Tiefe Geothermie Prospektion, Exploration, Realisierung, Nutzung, Springer-Verlag Berlin Heidelberg, https://doi.org/10.1007/978-3-642-54511-5, 2014.

Becker, M. W., Ciervo, C., Cole, M., Coleman, T., and Mondanos, M.: Fracture hydromechanical response measured by fiber optic distributed acoustic sensing at milliHertz frequencies, Geophysical Research Letters, 44, 7295–7302, https://doi.org/10.1002/2017GL073931, 2017.

Becker, M. W., Coleman, T. I., and Ciervo, C. C.: Distributed Acoustic Sensing as a Distributed Hydraulic Sensor in Fractured Bedrock, Water Resources Research, 56, e2020WR028140, https://doi.org/https://doi.org/10.1029/2020WR028140, 2020.

Bense, V. F., Read, T., Bour, O., Le Borgn, T., Coleman, T., Krause, S., Chalari, A., Mondanos, M., Ciocca, F., and Selker, J. S.: Distributed Temperature Sensing as a downhole tool in hydrogeology, Water Resources Research, 1–433, https://doi.org/10.1002/2016WR018869.Received, 2008.

Berman, A. D., Ducker, W. A., and Israelachvili, J. N.: Origin and Characterization of Different Stick–Slip Friction Mechanisms, Langmuir, 12, 4559–4563, https://doi.org/10.1021/la950896z, 1996.

Beyreuther, M., Barsch, R., Krischer, L., Megies, T., Behr, Y., and Wassermann, J.: ObsPy: A Python

Toolbox for Seismology, Seismological Research Letters, 81, 530–533, https://doi.org/10.1785/gssrl.81.3.530, 2010.

Birner, J.: Hydrogeologisches Modell des Malmaquifers im Süddeutschen Molassebecken, Freie Universität Berlin, 86 pp., accessed August 20, 2021, https://refubium.fu-berlin.de/handle/fub188/1492?show=full, 2013.

Birner, J., Fritzer, T., Jodocy, M., Savvatis, A., Schneider, M., and Stober, I.: Hydraulische Eigenschaften des Malmaquifers im Süddeutschen Molassebecken und ihre Bedeutung für die geothermische Erschließung, Z. Geol. Wiss., 40, 133–156, 2012.

Blöcher, G., Reinsch, T., Henninges, J., Milsch, H., Regenspurg, S., Kummerow, J., Francke, H., Kranz, S., Saadat, A., Zimmermann, G., and Huenges, E.: Hydraulic history and current state of the deep geothermal reservoir Groß Schönebeck, Geothermics, 17, https://doi.org/10.1016/j.geothermics.2015.07.008, 2015.

Bohl, W. and Elmendorf, W.: Technische Strömungslehre: Stoffeigenschaften von Flüssigkeiten und Gasen, Hydrostatik, Aerostatik, inkompressible Strömungen, kompressible Strömungen, Strömungsmesstechnik, 504 pp., ISBN 3834330299, 2005.

Böhm, F., Savvatis, A., Steiner, U., Schneider, M., and Koch, R.: Lithofazielle Reservoircharakterisierung zur geothermischen Nutzung des Malm im Großraum München, Grundwasser - Zeitschrift der Fachsektion Hydrogeologie, 18, 3–13, https://doi.org/10.1007/s00767-012-0202-4, 2013.

Bohnsack, D., Zosseder, K., Potten, M., Käsling, H., and Thuro, K.: Geomechanical investigation of a geothermal aquifer in the south german molasse basin, in: Rock Mechanics for Natural Resources and Infrastructure Development- Proceedings of the 14th International Congress on Rock Mechanics and Rock Engineering, ISRM 2019, 3136–3143, 2020a.

Bohnsack, D., Potten, M., Pfrang, D., Wolpert, P., and Zosseder, K.: Porosity–permeability relationship derived from Upper Jurassic carbonate rock cores to assess the regional hydraulic matrix properties of the Malm reservoir in the South German Molasse Basin, Geothermal Energy, 8, 12, https://doi.org/10.1186/s40517-020-00166-9, 2020b.

Bolotovskiy, I., Schellschmidt, R., and Schulz, R.: Fachinformationssystem Geophysik: Temperaturkorrekturverfahren, Hannover, accessed October 05, 2021, https://www.fis-geophysik.de/fis_gp/help/en/info_material.htm, 2015.

Bourdet, D.: Well Test Analysis: The Use Of Advanced Interpretation Models Handbook of Petreleum Exploration and Production, Elsevier, Paris, 426 pp., https://doi.org/10.1016/S1567-8032(03)80031-9, 2002.

Bremer, K., Lewis, E., Leen, G., Moss, B., Lochmann, S., Mueller, I., Reinsch, T., and Schroetter, J.: Fibre optic pressure and temperature sensor for geothermal wells, in: 2010 IEEE Sensors, 538–541, https://doi.org/10.1109/ICSENS.2010.5690125, 2010.

Bremer, K., Reinsch, T., Leen, G., Roth, B., Lochmann, S., and Lewis, E.: Pressure, temperature and refractive index determination of fluids using a single fibre optic point sensor, Sensors and Actuators A: Physical, 256, 84–88, https://doi.org/https://doi.org/10.1016/j.sna.2017.01.025, 2017.

Brennand, A. W.: A new methodfor the analysis of static formation temperature tests, in: Proceedings 6th NZ Geothermal Workshop, 45–47, 1984.

Brown, G.: Reservoir Surveillance - Distributed Temperature Analysis, Sensa a Schlumberger company, 2003.

Brown, G.: Downhole Temperatures from Optical Fiber, Oilfield Review, 20, 34–39, 2009.

Bruno, M. S., Lao, K., Oliver, N., and Becker, M.: Use of Fiber Optic Distributed Acoustic Sensing for

Measuring Hydraulic Connectivity for Geothermal Applications, United States, https://doi.org/10.2172/1434494, 2018.

Bücker, C. and Grosswig, S.: Distributed temperature sensing in the oil and gas industry - insights and perspectives, Oil Gas European Magazine, 43, 209–215, 2017.

Bukhamsin, A. and Home, R.: Cointerpretation of distributed acoustic and temperature sensing for inflow profiling, JPT, Journal of Petroleum Technology, 69, 64–67, https://doi.org/10.2118/0517-0064-jpt, 2017.

Bullard, E. C.: The Time Necessary for a Bore Hole to Attain Temperature Equilibrium, Geophysical Supplements to the Monthly Notices of the Royal Astronomical Society, 5, 127–130, https://doi.org/10.1111/j.1365-246X.1947.tb00348.x, 1947.

Burhenne, S., Jacob, D., and Henze, G. P.: Sampling based on sobol′ sequences for monte carlo techniques applied to building simulations, Proceedings of Building Simulation 2011: 12th Conference of International Building Performance Simulation Association, 1816–1823, 2011.

Cannon, S.: Petrophysics: A Practical Guide, Wiley, ISBN 9781118746745, 2015.

Capuano, L. E.: Geothermal well drilling, in: Geothermal Power Generation: Developments and Innovation, edited by: DiPippo, R., Woodhead Publishing, 107–139, https://doi.org/10.1016/B978-0-08-100337-4.00005-X, 2016.

Cardarelli, F.: Ferrous Metals and Their Alloys, in: Materials Handbook: A Concise Desktop Reference, Springer International Publishing, Cham, 101–248, https://doi.org/10.1007/978-3-319-38925-7_2, 2018.

Casper, S., Bohnsack, D., and Zosseder, K.: Temperaturverteilung entlang der Malm/Purbeck-Grenze im Bayerischen Molassebecken - Prognose anhand von BHT-Korrekturverfahren, in: In: [Holzheu, St., Kaufmann-Knoke, R. & Thies, B.]: Grundwasser trifft Boden und Energie. Tagungsband FH-DGG 2014, 2014.

Chang, H. and Nakata, N.: Investigation of the time-lapse changes with the DAS borehole data at the Brady geothermal field using deconvolution interferometry, in: SEG Technical Program Expanded Abstracts 2020, 3417–3421, https://doi.org/10.1190/segam2020-3426023.1, 2020.

Chen, G., Tehrani, D. H., and Peden, J. M.: Calculation Of Well Productivity In A Reservoir Simulator (I), SPE-29121-MS, https://doi.org/10.2118/29121-MS, 1995.

Christiansen, R. O., Clavel, F., Gonzalez, M., García, H. P. A., Ortiz, D. A., Ariza, J. P., Martinez, M. P., and Wohnlich, S.: Low-enthalpy geothermal energy resources in the Central Andes of Argentina: A case study of the Pismanta system, Renewable Energy, 177, 1234–1252, https://doi.org/10.1016/j.renene.2021.06.065, 2021.

Clauser, C.: Geothermal Energy, in: Landolt-Börnstein, Group VIII: Advanced Materials and Technologies, Energy Technologies · Renewable Energy, vol. Vol. 3, edited by: Heinloth, K., Springer, Heidelberg, https://doi.org/10.1007/b83039, 2006.

Clauser, C.: Heat Transport Processes in the Earth ' s Crust, Surv Geophys, 30, 163–191, https://doi.org/10.1007/s10712-009-9058-2, 2009.

Codo, F. P., Adomou, A., and Adanhounmè, V.: Analytical Method for Calculation of Temperature of the Produced Water in Geothermal Wells, International Journal of Scientific & Engineering Research, 3, 1–7, 2012.

Correa, J., Van Zaanen, L., Tertyshnikov, K., Dean, T., Pevzner, R., and Bona, A.: DAS versus geophones: A quantitative comparison of a VSP survey at a dedicated field laboratory, 4th EAGE Borehole Geophysics Workshop, 2017-Novem, https://doi.org/10.3997/2214-4609.201702477, 2017.

Cox, B., Wills, P., Kiyashchenko, D., Mestayer, J., Lopez, J., Grandi Karam, S., Mateeva, A., Lopez, J., Bourne, S., Lupton, R., Solano, G., Henderson, N., Hill, D., and Roy, J.: Distributed acoustic sensing for geophysical monitoring, 74th European Association of Geoscientists and Engineers Conference and Exhibition 2012 Incorporating SPE EUROPEC 2012: Responsibly Securing Natural Resources, 22–25, https://doi.org/10.3997/2214-4609.20148800, 2012.

Cressie, N. A. C.: Statistics for spatial data, Wiley, New York, https://doi.org/10.1002/9781119115151, 1993.

Daimler Truck AG: Daimler Truck, EnBW und Stadt Wörth am Rhein gründen Joint Venture für Zukunftsprojekt: Nachhaltige Wärmegewinnung durch Geothermie in Wörth, Press Release, 6th October, 2023, accessed October 20, 2023, https://www.daimlertruck.com/newsroom/pressemitteilung/daimler-truck-enbw-und-stadt-woerth-am-rhein-gruenden-joint-venture-fuer-zukunftsprojekt-nachhaltige-waermegewinnung-durch-geothermie-in-woerth-52424101, 2023.

Dakin, J. P. and Pratt, D. J.: Distributed optical fibre raman temperature sensor using a semiconductor light source and detector, Electronics Letters, 21, 172–174, https://doi.org/10.1016/S1081-1206(10)60430-9, 1985.

Daley, T. M., Berkeley, L., Ajo-franklin, J., Dou, S., Berkeley, L., and Pevzner, R.: Field testing of fiber-optic distributed acoustic sensing (DAS) for subsurface seismic monitoring, The Leading Edge, 36, 936–942, https://doi.org/10.1190/tle32060699.1, 2013.

Daley, T. M., Miller, D. E., Dodds, K., Cook, P., and Freifeld, B. M.: Field testing of modular borehole monitoring with simultaneous distributed acoustic sensing and geophone vertical seismic profiles at Citronelle, Alabama, Geophysical Prospecting, 64, 1318–1334, https://doi.org/https://doi.org/10.1111/1365-2478.12324, 2016.

Delbeke, J., Runge-Metzger, A., Slingenberg, Y., and Werksman, J.: THE PARIS AGREEMENT, https://doi.org/10.4324/9789276082569-2, 2019.

Deming, D.: Application of bottom-hole temperature corrections in geothermal studies, Geothermics, 18, 775–786, https://doi.org/10.1016/0375-6505(89)90106-5, 1989.

Deutsche ErdWärme GmbH: Graben-Neudorf 1 heißeste Bohrung Deutschlands bis 4.000 Meter Tiefe, Press Release, 22nd August, 2023, accessed October 10, 2023, https://www.deutsche-erdwaerme.de/presse/graben-neudorf-1-heisseste-bohrung-deutschlands-bis-4-000-meter-tiefe/, 2023.

DiPippo, R.: Geothermal Power Plants: Principles, Applications, Case Studies and Environmental Impact, Edition, 4., Butterworth-Heinemann, 1–762 pp., https://doi.org/10.1016/B978-0-08-100879-9.00024-0, 2015.

Dowdle, W. L. and Cobb, W. M.: Static Formation Temperature From Well Logs - An Empirical Method, Journal of Petroleum Technology, 27, 1326–1330, https://doi.org/10.2118/5036-PA, 1975.

Drews, M., Bauer, W., and Stollhofen, H.: Porenüberdruck im Bayerischen Molassebecken, Erdoel Erdgas Kohle/EKEP, 134(7/8), 308–310, https://doi.org/10.19225/180703, 2018.

Drews, M. C., Shatyrbayeva, I., Bohnsack, D., Duschl, F., Obermeier, P., Loewer, M., Flechtner, F., and Keim, M.: The role of pore pressure and its prediction in deep geothermal energy drilling – examples from the North Alpine Foreland Basin, SE Germany, Petroleum Geoscience, 28, petgeo2021-060, https://doi.org/10.1144/petgeo2021-060, 2022.

Dussel, M., Moeck, I., Wolfgramm, M., Kahnt, R., Straubinger, R., and Gahr, A.: Geothermal Development of Fracture Dominated Aquifers: the Case Study of the Deep Well Geretsried (Germany), in: Proceedings World Geothermal Congress 2020+1, 2021.

Edenhofer, O., Madruga, R. P., Sokona, Y., Seyboth, K., Matschoss, P., Kadner, S., Zwickel, T., Eickemeier, P., Hansen, G., Schlömer, S., and von Stechow, C.: Renewable energy sources and climate change mitigation: Special report of the intergovernmental panel on climate change, Cambridge University Press, 1–1075 pp., https://doi.org/10.1017/CBO9781139151153, 2011.

Ekechukwu, G. K. and Sharma, J.: Well-scale demonstration of distributed pressure sensing using fiber-optic DAS and DTS, Scientific Reports, 11, 12505, https://doi.org/10.1038/s41598-021-91916-7, 2021.

Emeraude, K.: Emeraude thermal models: a sensitivity study, accessed May 05, 2022, https://www.kappaeng.com/software/emeraude/tutorials, 2011.

Emeraude, K.: KAPPA - Emeraude, https://www.kappaeng.com/software/emeraude/.

Eppelbaum, L., Kutasov, I., and Pilchin, A.: Applied Geothermics, Springer Berlin Heidelberg, https://doi.org/10.1016/0160-9327(87)90297-3, 2014.

Eppelbaum, L. V. and Kutasov, I. M.: Wellbore and Formation Temperatures during Drilling, Shut-in and Cementing of Casing, in: Proceed. of the World Geothermal Congress, Melbourne, Australia, 1–12, 2015.

European Commission: The European Green Deal, Brussels, 1–24 pp., accessed September 20, 2023, https://eur-lex.europa.eu/legal-content/EN/TXT/?uri=COM%3A2019%3A640%3AFIN, 2019.

Eyerer, S., Schifflechner, C., Hofbauer, S., Bauer, W., Wieland, C., and Spliethoff, H.: Combined heat and power from hydrothermal geothermal resources in Germany: An assessment of the potential, Renewable and Sustainable Energy Reviews, 120, 109661, https://doi.org/10.1016/j.rser.2019.109661, 2020.

Federal Ministry for Economic Affairs and Climate Action (BMWK): Eckpunkte für eine Erdwärmekampagne - Geothermie für die Wärmewende, accessed October 10, 2023, https://www.bmwk.de/Redaktion/DE/Downloads/Energie/eckpunkte-geothermie.html, 2022.

Fenta, M. C., Potter, D. K., and Szanyi, J.: Fibre Optic Methods of Prospecting: A Comprehensive and Modern Branch of Geophysics, Surveys in Geophysics, 42, 551–584, https://doi.org/10.1007/s10712-021-09634-8, 2021.

Finfer, D. C., Mahue, V. ., Shatalin, S. V., Parker, T. R., and Farhadiroushan, M. .: Borehole Flow Monitoring using a Non-intrusive Passive Distributed Acoustic Sensing (DAS), in: All Days, https://doi.org/10.2118/170844-MS, 2014.

Fink, J., Heim, E., and Klitzsch, N.: State of the Art in Deep Geothermal Energy in Europe, 1st ed., Springer Cham, 0–92 pp., https://doi.org/10.1007/978-3-030-96870-0, 2022.

Flechtner, F., Loewer, M., and Keim, M.: Updated stock take of the deep geothermal projects in Bavaria, Germany (2019), in: Proceedings World Geothermal Congress 2020 Reykjavik, Iceland, April 26 – May 2, 2020 Updated, 1–10, 2020.

Förster, A.: Analysis of borehole temperature data in the Northeast German Basin: Continuous logs versus bottom-hole temperatures, Petroleum Geoscience, 7, 241–254, https://doi.org/10.1144/petgeo.7.3.241, 2001.

Förster, A., Schrötter, J., Merriam, D. F., and Blackwell, D. D.: Application of optical-fiber temperature logging - An example in a sedimentary environment, Geophysics, 62, 1107–1113, https://doi.org/10.1190/1.1444211, 1997.

Franco, A. and Conti, P.: Clearing a path for ground heat exchange systems: A review on Thermal Response Test (TRT) methods and a geotechnical routine test for estimating soil thermal properties, Energies, 13, 1–21, https://doi.org/10.3390/en13112965, 2020.

Fraunhofer-Gesellschaft and Helmholtz-Gemeinschaft: Roadmap for Deep Geothermal Energy for Germany - Recommended Actions for Policymakers, Industry and Science for a Successful Heat Transition - Strategy paper by six institutes of the Fraunhofer-Gesellschaft and the Helmholtz-Gemeinschaft, https://doi.org/10.24406/publica-248, 2022.

Freifeld, B. M., Finsterle, S., Onstott, T. C., Toole, P., and Pratt, L. M.: Ground surface temperature reconstructions: Using in situ estimates for thermal conductivity acquired with a fiber-optic distributed thermal perturbation sensor, Geophysical Research Letters, 35, https://doi.org/10.1029/2008GL034762, 2008.

Fridleifsson, I. B.: Geothermal energy for the benefit of the people, Renewable and Sustainable Energy Reviews, 5, 299–312, https://doi.org/10.1016/S1364-0321(01)00002-8, 2001.

Frings, J. and Walk, T.: Distributed fiber optic sensing enhances pipeline safety and security, Oil Gas European Magazine, 37, 132–136, 2011.

Fuchs, S., Förster, A., and Norden, B.: Evaluation of the terrestrial heat flow in Germany: A case study for the reassessment of global continental heat-flow data, Earth-Science Reviews, 235, 104231, https://doi.org/10.1016/j.earscirev.2022.104231, 2022.

Fujii, H., Okubo, H., and Itoi, R.: Thermal response tests using optical fiber thermometers, in: Transactions - Geothermal Resources Council, GRC 2006 Annual Meeting: Geothermal Resources-Securing Our Energy Future ; Conference date: 10-09-2006 Through 13-09-2006, 545–551, 2006.

Fujii, H., Okubo, H., Nishi, K., Itoi, R., Ohyama, K., and Shibata, K.: An improved thermal response test for U-tube ground heat exchanger based on optical fiber thermometers, Geothermics, 38, 399–406, https://doi.org/10.1016/j.geothermics.2009.06.002, 2009.

García Gil, A., Garrido Schneider, E. A., Mejías Moreno, M., and Santamarta Cerezal, J. C.: Shallow Geothermal Energy, Springer International Publishing, Cham, https://doi.org/10.1007/978-3-030-92258-0, 2022.

Ghahfarokhi, P. K., Carr, T., Song, L., Shukla, P., and Pankaj, P.: Seismic Attributes Application for the Distributed Acoustic Szensing Data for the Marcellus Shale: New Insights to Cross-Stage Flow Communication, in: Day 2 Wed, January 24, 2018, https://doi.org/10.2118/189888-MS, 2018.

GmbH, I. S.: Best Practices Guide for Geothermal Exploration, 194 pp., accessed October 12, 2023, https://documents.worldbank.org/en/publication/documents-reports/documentdetail/190071480069890732/best-practices-guide-for-geothermal-exploration 2014.

Goetzl, Faber, G., Janda, Schubert, C., and Zekiri, G. &: Coupled Geothermal-Hydraulic 3D Modeling of the Southern Vienna Basin. a State of the Art Decision Planning Tool for Sustainable Hydrothermal Exploitation Inside an Environ-ment of Sensitive Hydraulic Circulation Systems, Proceedings World Geothermal Congress, 25–29, 2010.

Götz, J., Lüth, S., Henninges, J., and Reinsch, T.: Vertical seismic profiling using a daisy-chained deployment of fibre-optic cables in four wells simultaneously – Case study at the Ketzin carbon dioxide storage site, Geophysical Prospecting, 66, 1201–1214, https://doi.org/10.1111/1365-2478.12638, 2018.

Götzl, G., Motschka, K., Janda, C., Bottig, M., Hoyer, S., Brüstle, A. K., Zekiri, F., Faber, R., Gegenhuber, N., Schubert, G., and Berka, R.: Drei-dimensionales geothermisches Modell in Teilen der Ostalpen unter Berücksichtigung der Temperaturleitfähigkeit, der Wärmeproduktion und regionaler Grundwasserkonvektionsströme, Geologische Bundesanstalt Wien, Wien, 1–161 pp., https://doi.org/10.1553/thermalps1, 2013.

Goutorbe, B., Lucazeau, F., and Bonneville, A.: Comparison of several BHT correction methods : a case study on an Australian data set, Geophysical Journal International, 913–922, https://doi.org/10.1111/j.1365-246X.2007.03403.x, 2007.

Grant, M. A. and Bixley, P. F.: Geothermal Reservoir Engineering, 2nd ed., https://doi.org/10.1016/C2010-0-64792-4, 2011.

Group, G. H. F. D. A., Fuchs, S., Neumann, F., Norden, B., Beardsmore, G., Chiozzi, P., Colgan, W., Anguiano Dominguez, A. P., Duque, M. R. A., Ojeda Espinoza, O. M., Forster, F., Förster, A., Fröhder, R., Fuentes, K., Hajto, M., Harris, R., Jõeleht, A., Liebing, H., Liu, S., Lüdtke, G., Madon, M., Negrete-Aranda, R., Poort, J., Reznik, I. J., Riedel, M., Rolandone, F., Stål, T., Verdoya, M., and Wu, J.-N.: The Global Heat Flow Database: Update 2023. V. 1. GFZ Data Service, https://doi.org/10.5880/fidgeo.2023.008, 2023.

Haffen, S., Geraud, Y., Diraison, M., and Dezayes, C.: Determination of fluid-flow zones in a geothermal sandstone reservoir using thermal conductivity and temperature logs, Geothermics, 46, 32–41, https://doi.org/10.1016/j.geothermics.2012.11.001, 2013.

Ben Haoua, T., Abubakr, S., Pazzi, J., Djessas, L., Ali, A. M., Ayyad, H. B., Boumali, A., Boulkaila, Z., and Brahim, M. H.: Combining horizontal production logging and distributed temperature interpretations to diagnose annular flow in slotted-liner completions, SPE Middle East Oil and Gas Show and Conference, MEOS, Proceedings, 2015-Janua, 793–805, https://doi.org/10.2118/172593-ms, 2015.

Harris, K., White, D., Melanson, D., Samson, C., and Daley, T. M.: Feasibility of time-lapse VSP monitoring at the Aquistore CO2 storage site using a distributed acoustic sensing system, International Journal of Greenhouse Gas Control, 50, 248–260, https://doi.org/10.1016/j.ijggc.2016.04.016, 2016.

Hartog, A.: A distributed temperature sensor based on liquid-core optical fibers, Journal of Lightwave Technology, 1, 498–509, https://doi.org/10.1109/JLT.1983.1072146, 1983.

Hartog, A. and Gamble, G.: Photonic distributed sensing, Physics World, 4, 45, https://doi.org/10.1088/2058-7058/4/3/30, 1991.

Hartog, A., Frignet, B., Mackie, D., and Clark, M.: Vertical seismic optical profiling on wireline logging cable, Geophysical Prospecting, 62, 693–701, https://doi.org/10.1111/1365-2478.12141, 2014.

Hartog, A. H.: An introduction to distributed optical fibre sensors, 1st ed., CRC Press., 1–440 pp., https://doi.org/10.1201/9781315119014, 2017.

Hasan, A. R. and Kabir, C. S.: Modeling two-phase fluid and heat flows in geothermal wells, Journal of Petroleum Science and Engineering, 71, 77–86, https://doi.org/10.1016/j.petrol.2010.01.008, 2010.

Hasan, R. and Kabir, S.: Fluid Flow and Heat Transfers in Wellbores, Society of Petroleum Engineers, https://doi.org/10.2118/9781613995457, 2018.

Heine, F., Zosseder, K., and Einsiedl, F.: Hydrochemical zoning and chemical evolution of the deep upper jurassic thermal groundwater reservoir using water chemical and environmental isotope data, Water (Switzerland), 13, https://doi.org/10.3390/w13091162, 2021.

Henninges, J., Huenges, E., and Burkhardt, H.: In situ thermal conductivity of gas-hydrate-bearing sediments of the Mallik 5L-38 well, Journal of Geophysical Research: Solid Earth, 110, 1–11, https://doi.org/10.1029/2005JB003734, 2005a.

Henninges, J., Schrötter, J., Erbas, K., and Huenges, E.: Temperature field of the Mallik gas hydrate occurrence - implications on phase changes and thermal properties, Bulletin-Geological Survey of Canada, 585, 128, https://doi.org/10.4095/220890, 2005b.

Henninges, J., Zimmermann, G., Schrötter, J., Erbas, K., and Huenges, E.: Wireline Distributed Temperature Measurements and Permanent Installations Behind Casing, in: Proceedings World Geothermal Congress, 24–29, 2005c.

Henninges, J., Martuganova, E., Stiller, M., Norden, B., and Krawczyk, C. M.: Wireline distributed acoustic sensing allows 4.2km deep vertical seismicprofiling of the Rotliegend 150C geothermal reservoir in the North German Basin, Solid Earth, 12, 521–537, https://doi.org/10.5194/se-12-521-2021, 2021.

Herman, J. and Usher, W.: SALib: An open-source Python library for Sensitivity Analysis, The Journal of Open Source Software, 2, 97, https://doi.org/10.21105/joss.00097, 2017.

Hermanrud, C., Cao, S., and Lerche, I.: Estimates of virgin rock temperature derived from BHT measurements: Bias and error, GEOPHYSICS, 55, 924–931, https://doi.org/10.1190/1.1442908, 1990.

Hidnert, P.: Thermal expansion of heat resisting alloys: Nickel-Chromium, iron-chromium, and nickel-chromium-iron alloys, Bureau of Standards Journal of Research, 7, 1031, https://doi.org/10.6028/jres.007.062, 1931.

Hohn, M. E.: Indicator kriging, in: Geostatistics and petroleum geology, Springer Netherlands, Dordrecht, 151–179, https://doi.org/10.1007/978-94-011-4425-4_6, 1999.

Hole, H.: Geothermal Well Completion Tests, Petroleum Engineering Summer School, 1–5, 2008.

Homuth, S.: Aufschlussanalogstudie zur Charakterisierung oberjurassischer geothermischer Karbonatreservoire im Molassebecken, Technische Universität Darmstadt, 312 pp., accessed October 17, 2023, https://tuprints.ulb.tu-darmstadt.de/4209/, 2014.

Horne, R. N.: Characterization, evaluation, and interpretation of well data, in: Geothermal Power Generation: Developments and Innovation, edited by: DiPippo, R., Woodhead Publishing, 141–163, https://doi.org/10.1016/B978-0-08-100337-4.00006-1, 2016.

Horner, D. R.: Pressure build-up in wells, in: World Petroleum Congress Proceedings, 503–521, 1951.

Hu, J., Jiang, G., Wang, Y., and Hu, S.: Thermal Conductivity Estimation Based on Well Logging, Mathematics, 9, https://doi.org/10.3390/math9111176, 2021.

Hurtig, E., Großwig, S., Jobmann, M., Kühn, K., and Marschall, P.: Fibre-optic temperature measurements in shallow boreholes: experimental application for fluid logging, Geothermics, 23, 355–364, https://doi.org/10.1016/0375-6505(94)90030-2, 1994.

Hurtig, E., Großwig, S., and Kühn, K.: Fibre optic temperature sensing: Application for subsurface and ground temperature measurements, Tectonophysics, 257, 101–109, https://doi.org/10.1016/0040-1951(95)00124-7, 1996.

IAPWS: The International Association for the Properties of Water and Steam 1 Nomenclature Thermodynamic quantities, 1–7 pp., 2011.

Electricity Information: Overview: acessed October 17, 2023, https://www.iea.org/reports/electricity-information-overview/electricity-consumption.

Inaudi, D. and Glisic, B.: Long-range pipeline monitoring by distributed fiber optic sensing, Journal of Pressure Vessel Technology, Transactions of the ASME, 132, 0117011–0117019, https://doi.org/10.1115/1.3062942, 2010.

Jessell, M. W. and Valenta, R. K.: Structural geophysics: Integrated structural and geophysical modelling, in: Computer Methods in the Geosciences, vol. 15, edited by: De Paor, D. G., Pergamon, 303–324, https://doi.org/10.1016/S1874-561X(96)80027-7, 1996.

Johannessen, K., Drakeley, B., and Farhadiroushan, M.: Distributed Acoustic Sensing - A New Way of Listening to Your Well/Reservoir, in: All Days, https://doi.org/10.2118/149602-MS, 2012.

Johnson, D. O., Sierra, J. R., Kaura, J. D., and Gualtieri, D.: Successful Flow Profiling of Gas Wells Using Distributed Temperature Sensing Data, in: SPE Annual Technical Conference and Exhibition, San Antonio, Texas, USA, September 2006, https://doi.org/10.2118/103097-MS, 2006.

Jousset, P., Reinsch, T., Ryberg, T., Blanck, H., Clarke, A., Aghayev, R., Hersir, G. P., Henninges, J., Weber, M., and Krawczyk, C. M.: Dynamic strain determination using fibre-optic cables allows imaging of seismological and structural features, Nature Communications, 9, 2509, https://doi.org/10.1038/s41467-018-04860-y, 2018.

Kaiser, B. O., Cacace, M., Scheck-Wenderoth, M., and Lewerenz, B.: Characterization of main heat transport processes in the Northeast German Basin: Constraints from 3-D numerical models, Geochemistry, Geophysics, Geosystems, 12, https://doi.org/10.1029/2011GC003535, 2011.

Kämmlein, M.: The Franconian Basin temperature anomaly, SE Germany: Methodically aspects on the determination of rock thermal conductivity and modelling of potential heat sources, Friedrich-Alexander-Universität Erlangen-Nürnberg, accessed October 15, 2023, https://open.fau.de/items/c65d653c-4365-4491-8eb4-2182909ab03e, 2019.

Kanev, K., Ikeuchi, J., Kimura, S., and Okajima, A.: Heat loss to the surrounding rock formation from a geothermal wellbore, Geothermics, 26, 329–349, https://doi.org/10.1016/S0375-6505(96)00046-6, 1997.

Kavvadias, K., Jiménez-Navarro, J. P., and Thomassen, G.: Decarbonising the EU heating sector, Luxembourg, 105 pp., https://doi.org/10.2760/943257, 2019.

Kenkmann, T., Hesse, T., Hülsmann, F., Timpe, C., and Hoppe, K.: Klimaschutzziel und – strategie München 2050 Endbericht, Freiburg, accessed November 20, 2023, https://www.oeko.de/publikation/klimaschutzziel-und-strategie-muenchen-2050-1/, 2017.

Kersey, A. D.: Optical fiber sensors for permanent downwell monitoring applications in the oil and gas industry, IEICE Transactions on Electronics, E83-C, 400–404, 2000.

Khankishiyev, O., Salehi, S., Hasanov, G., and Hu, Z.: Application of Distributed Temperature Sensing (DTS) in Geothermal Wells, in: Proceedings, 2024.

KLIP, T., Zosseder, K., Bohnsack, D., Casper, S., and Beecken, C.: Abschlussbericht zum Forschungsvorhaben „Aktualisierung der flächenverteilten Temperaturangaben im Tiefengrundwasserleiter in zwei Pilotgebieten („MaTemp“) im Rahmen des KLIP-Projekts“, 2012.

Koch, A., Jorand, R., Vogt, C., Arnold, R., Mottaghy, D., Pechnig, R., and Clauser, C.: Erstellung statistisch abgesicherter thermischer und hydraulischer Gesteinseigenschaften für den flachen und tiefen Untergrund in Deutschland Phase 2 – Westliches Nordrhein-Westfalen und bayerisches Molassebecken, 202 pp., 2009.

Köhl, B., Grundy, J., and Baumann, T.: Rippled scales in a geothermal facility in the Bavarian Molasse Basin : a key to understand the calcite scaling process, Geothermal Energy, 8:23, 27, https://doi.org/10.1186/s40517-020-00177-6, 2020.

Konrad, F., Savvatis, A., Wellmann, F., and Zosseder, K.: Hydraulic behavior of fault zones in pump tests of geothermal wells : a parametric analysis using numerical simulations for the Upper Jurassic aquifer of the North Alpine Foreland Basin, Geothermal Energy, https://doi.org/10.1186/s40517-019-0137-4, 2019.

Konrad, F., Savvatis, A., Degen, D., Wellmann, F., Einsiedl, F., and Zosseder, K.: Productivity enhancement of geothermal wells through fault zones: Efficient numerical evaluation of a parameter space for the Upper Jurassic aquifer of the North Alpine Foreland Basin, Geothermics, 95, https://doi.org/10.1016/j.geothermics.2021.102119, 2021.

Kotlar, N., Allain, O., Benano, L., and Artus, V.: Cased Hole Analysis: The theory and practice of cased hole log acquisition and analysis and their application to well integrity, production profiling and reservoir monitoring., 366 pp., 2021.

Kunold, H. and Zurawski, M.: Geothermie im Kreis Karlsruhe: Anlage in Graben-Neudorf fördert erstmals Thermalwasser, Press Release, 15th August, 2023, https://www.swr.de/swraktuell/baden-wuerttemberg/karlsruhe/geothermie-graben-neudorf-karlsruhe-thermalwasser-100.html#:~:text=Die%20Geothermie%2DAnlage%20in%20Graben,W%C3%A4rme%2D%20und%20Stromerzeugung%20verwendet%20werden, 2023.

Kutasov, I. M. and Eppelbaum, L. V.: Prediction of formation temperatures in permafrost regions from temperature logs in deep wells - Field cases, Permafrost and Periglacial Processes, 14, 247–258, https://doi.org/10.1002/ppp.457, 2003.

Kutasov, I. M. and Eppelbaum, L. V.: Determination of formation temperature from bottom-hole temperature logs — a generalized Horner method, Journal of Geophysics and Engineering, 2, 90–96, https://doi.org/10.1088/1742-2132/2/2/002, 2005.

Lachenbruch, A. H. and Brewer, M. C.: Dissipation of the Temperature Effect of Drilling a Well in Arctic Alaska, United States Geological Survey Bulletin, 1083, 73–109, https://doi.org/10.3133/b1083C, 1959.

Latal, J., Koudelka, P., Siska, P., Skapa, J., Hanáeck, F., Vasinek, V., Vitásek, J., Hejduk, S., and Bocheza, J.: Fiber optic DTS system application in the research of accumulation possibilities of thermal energy in the rock mass, Proceedings of SPIE - The International Society for Optical Engineering, https://doi.org/10.1117/12.887082, 2011.

Leblanc, Y., Lam, H. -L, Pascoe, L. J., and Jones, F. W.: A Comparison of Two Methods of Estimating Static Formation Temperature From Well Logs, Geophysical Prospecting, 30, 348–357, https://doi.org/10.1111/j.1365-2478.1982.tb01311.x, 1982.

Lee, C.-H. and Polycarpou, A. A.: Static Friction Experiments and Verification of an Improved Elastic-Plastic Model Including Roughness Effects, Journal of Tribology, 129, 754–760, https://doi.org/10.1115/1.2768074, 2007.

Li, J., Li, Z., Yang, J., Zhang, Y., and Ren, C.: Microfiber Fabry-Perot interferometer used as a temperature sensor and an optical modulator, Optics and Laser Technology, 129, 106296, https://doi.org/10.1016/j.optlastec.2020.106296, 2020.

Liang, M., Fang, X., and Ning, Y.: Temperature Compensation Fiber Bragg Grating Pressure Sensor Based on Plane Diaphragm, Photonic Sensors, 8, 157–167, https://doi.org/10.1007/s13320-018-0417-9, 2018.

Lim, W. R., Hamm, S. Y., Lee, C., Hwang, S., Park, I. H., and Kim, H. C.: Characteristics of deep groundwater flow and temperature in the tertiary Pohang area, South Korea, Applied Sciences (Switzerland), 10, https://doi.org/10.3390/app10155120, 2020.

Lipovka, A. Y. and Lipovka, Y. L.: Determining Hydraulic Friction Factor for Pipeline Systems, Journal of Siberian Federal University. Engineering & Technologies, 1, 62, 2014.

Lipus, M., Reinsch, T., Schmidt-Hattenberger, C., Henninges, J., and Reich, M.: Gravel pack monitoring with a strain sensing fiber optic cable, Oil Gas European Magazine, 44, 179–185, https://doi.org/10.19225/181202, 2018.

Lipus, M. P., Reinsch, T., Weisenberger, T. B., Kragset, S., Stefánsson, A., and Bogason, S. G.: Monitoring of a reverse cement job in a high-temperature geothermal environment, Geothermal Energy, 9, https://doi.org/10.1186/s40517-021-00187-y, 2021.

Lipus, M. P., Schölderle, F., Reinsch, T., Wollin, C., Krawczyk, C., Pfrang, D., and Zosseder, K.: Dynamic motion monitoring of a 3.6\,km long steel rod in a borehole during cold-water injection with distributed fiber-optic sensing, Solid Earth, 13, 161–176, https://doi.org/10.5194/se-13-161-2022, 2022.

Liu, C., Li, K., Chen, Y., Jia, L., and Ma, D.: Static formation temperature prediction based on bottom hole temperature, Energies, 9, 1–14, https://doi.org/10.3390/en9080646, 2016.

Luheshi, M. N.: Estimation of formation temperature from borehole measurements, Geophysical Journal of the Royal Astronomical Society, 74, 747–776, https://doi.org/10.1111/j.1365-246X.1983.tb01902.x, 1983.

Lumens, P. G. E.: Fibre-optic sensing for application in oil and gas wells, 132 pp., https://doi.org/10.6100/IR769555, 2014.

Madsen, K. N., Tøndel, R., and Kvam, Ø.: Data-driven depth calibration for distributed acoustic sensing, Leading Edge, 35, 610–614, https://doi.org/10.1190/tle35070610.1, 2016.

Majorowicz, J. and Minea, V.: Geothermal Energy Potential in Low Enthalpy Areas as a Future Energy Resource: Identifying Feasible Targets, Quebec, Canada, Study Case, Resources, 4, 524–547, https://doi.org/10.3390/resources4030524, 2015.

Majorowicz, J. A. and Smith, S. L.: Review of ground temperatures in the Mallik field area: A constraint to the methane hydrate stability, Bulletin of the Geological Survey of Canada, 45–56, 1999.

Martuganova, E., Stiller, M., Bauer, K., Henninges, J., and Krawczyk, C. M.: Cable reverberations during wireline distributed acoustic sensing measurements: their nature and methods for elimination, Geophysical Prospecting, 69, 1034–1054, https://doi.org/10.1111/1365-2478.13090, 2021.

Masoudi, A. and Newson, T. P.: Contributed Review : Distributed optical fibre dynamic strain sensing, Review of Scientific Instruments, 87, https://doi.org/10.1063/1.4939482, 2016.

Masoudi, A., Belal, M., and Newson, T. P.: A distributed optical fibre dynamic strain sensor based on phase-OTDR, Measurement Science and Technology, 24, https://doi.org/10.1088/0957-0233/24/8/085204, 2013.

Mateeva, A., Lopez, J., Potters, H., Mestayer, J., Cox, B., Kiyashchenko, D., Wills, P., Grandi, S., Hornman, K., Kuvshinov, B., Berlang, W., Yang, Z., and Detomo, R.: Distributed acoustic sensing for reservoir monitoring with vertical seismic profiling, Geophysical Prospecting, 62, 679–692, https://doi.org/10.1111/1365-2478.12116, 2014.

Mayrhofer, C., Niessner, R., and Baumann, T.: Hydrochemistry and hydrogen sulfide generating processes in the Malm aquifer, Bavarian Molasse Basin, Germany, Hydrogeology Journal, 22, 151–162, https://doi.org/10.1007/s10040-013-1064-2, 2014.

Meyer, R. K. F. and Schmidt-Kaler, H.: Paläogeographie und Schwammriffentwicklung des süddeutschen Malm-ein Überblick, Facies, 23, 175–184, https://doi.org/10.1007/BF02536712, 1990.

Middleton, M. F.: A model for bottom-hole temperature stabilization, Geophysics, 44, 1458–1462, https://doi.org/10.1190/1.1441018, 1979.

Middleton, M. F.: Bottom-hole temperature stabilization with continued circulation of drilling mud., Geophysics, 47, 1716–1723, https://doi.org/10.1190/1.1441321, 1982.

Miller, D. E., Coleman, T., Zeng, X., Patterson, J. R., Reinisch, E. C., Cardiff, M. A., Wang, H. F., Fratta, D., Trainor-Guitton, W., Thurber, C. H., Robertson, M., Feigl, K., and The PoroTomo Team: DAS and DTS at Brady Hot Springs: Observations about Coupling and Coupled Interpretations, in: Stanford Geothermal Workshop, 1–13, 2018.

Moeck, I. S.: Catalog of geothermal play types based on geologic controls, Renewable and Sustainable Energy Reviews, 37, 867–882, https://doi.org/10.1016/j.rser.2014.05.032, 2014.

Mraz, E.: Reservoir Characterization to Improve Exploration Concepts of the Upper Jurassic in the Southern Bavarian Molasse Basin, Technische Universität München, 135 pp., https://mediatum.ub.tum.de/?id=1464081, 2019.

Munn, J. D., Coleman, T. I., Parker, B. L., Mondanos, M. J., and Chalari, A.: Novel cable coupling technique for improved shallow distributed acoustic sensor VSPs, Journal of Applied Geophysics, 138, 72–79, https://doi.org/10.1016/j.jappgeo.2017.01.007, 2017.

Muraki, M., Kinbara, E., and Konishi, T.: A laboratory simulation for stick-slip phenomena on the hydraulic cylinder of a construction machine, Tribology International, 36, 739–744, https://doi.org/10.1016/S0301-679X(03)00054-9, 2003.

Naldrett, G., Cerrahoglu, C., and Mahue, V.: Production Monitoring Using Next-Generation Distributed Sensing Systems, Petrophysics - The SPWLA Journal of Formation Evaluation and Reservoir Description, 59, 496–510, https://doi.org/10.30632/PJV59V4-2018a5, 2018.

Nath, D. K., Finley, D. B., and Kaura, J. D.: Real-Time Fiber-Optic Distributed Temperature Sensing (DTS)-New Applications in the Oilfield, in: SPE Annual Technical Conference and Exhibition, San Antonio, Texas, USA, September 2006, https://doi.org/10.2118/103069-MS, 2006.

Nitschke, F., Held, S., Villalon, I., Neumann, T., and Kohl, T.: Assessment of performance and parameter sensitivity of multicomponent geothermometry applied to a medium enthalpy geothermal system, Geothermal Energy, 5, https://doi.org/10.1186/s40517-017-0070-3, 2017.

Oliver, A. M. and Webster, R.: Basic Steps in Geostatistics: The Variogram and Kriging, 100 pp., ISBN 9783319158648, 2015.

Paleja, R., Mustafina, D., In't Panhuis, P., Park, T., Randell, D., Van Der Horst, J., and Crickmore, R.: Velocity tracking for flow monitoring and production profiling using distributed acoustic sensing, Proceedings - SPE Annual Technical Conference and Exhibition, 2015-Janua, 1365–1380, https://doi.org/10.2118/174823-ms, 2015.

Parker, R. L.: Understanding Inverse Theory, Annual Review of Earth and Planetary Sciences, 5, 35–64, https://doi.org/10.1146/annurev.ea.05.050177.000343, 1977.

Patterson, J., Cardiff, M., Coleman, T., Wang, H., Feigl, K., Akerley, J., and Spielman, P.: Geothermal reservoir characterization using distributed temperature sensing at Brady Geothermal Field, Nevada, The Leading Edge, 36, 1024a1-1024a7, https://doi.org/10.1190/tle36121024a1.1, 2017.

Pearce, J. G., Rambow, F. H. K., Shroyer, W., Huckabee, P., de Jongh, H., Dria, D. E., Childers, B. A., Hall, T. S., and Dominique, T.: High Resolution, Real-Time Casing Strain Imaging for Reservoir and Well Integrity Monitoring: Demonstration of Monitoring Capability in a Field Installation, in: All Days, https://doi.org/10.2118/124932-MS, 2009.

Poirier, E. J. and Poirier, D. R.: Conduction of heat in solids, Oxford University, Oxford, UK, 158–188 pp., https://doi.org/10.1007/978-3-319-65130-9_9, 2016.

Pouladiborj, B.: The use of heat for subsurface flow quantification and understanding the subsurface heterogeneity, Université Rennes, 1–129 pp., http://www.theses.fr/2021REN1B008/document, 2021.

Poulsen, S. E., Nielsen, S. B., and Balling, N.: Estimation of the equilibrium formation temperature in the presence of bore fluid invasion, Geophysical Journal International, 1551–1561, https://doi.org/10.1111/j.1365-246X.2012.05571.x, 2012.

Przybycin, A. M., Scheck-Wenderoth, M., and Schneider, M.: The 3D conductive thermal field of the North Alpine Foreland Basin: influence of the deep structure and the adjacent European Alps, Geothermal Energy, 3, 17, https://doi.org/10.1186/s40517-015-0038-0, 2015.

Przybycin, A. M., Scheck-Wenderoth, M., and Schneider, M.: The origin of deep geothermal anomalies in the German Molasse Basin: results from 3D numerical models of coupled fluid flow and heat transport, Geothermal Energy, 5, 1–28, https://doi.org/10.1186/s40517-016-0059-3, 2017.

Pucknell, J. K. and Clifford, P. J.: Calculation of total skin factors, 25–38, https://doi.org/10.2118/23100-ms, 1991.

Qi, B., Pickrell, G., Zhang, P., Duan, Y., Peng, W., Xu, J., Huang, Z., Deng, J., Xiao, H., Wang, Z., Huo, W., May, R. G., and Wang, A.: Fiber Optic Pressure and Temperature Sensors for Oil Down Hole Application, Proceedings of SPIE - The International Society for Optical Engineering, 4578, https://doi.org/10.1117/12.456071, 2002.

Quenstedt, F. A.: Der Jura : Mit 3 Uebersichtstafeln, 42 Holzschnitten und einem Atlas von 100 Tab. , Laupp, Tübingen, 1858.

Raab, T. ., Reinsch, T. ., Aldaz Cifuentes, S. R., and Henninges, J. .: Real-Time Well-Integrity Monitoring Using Fiber-Optic Distributed Acoustic Sensing, SPE Journal, 24, 1997–2009, https://doi.org/10.2118/195678-PA, 2019.

Ramey Jr., H. J.: Wellbore Heat Transmission, Journal of Petroleum Technology, 14, 427–435, https://doi.org/10.2118/96-PA, 1962.

Reinsch, T.: Structural integrity monitoring in a hot geothermal well using fibre optic distributed temperature sensing, Clausthal University of Technology, 243 pp., http://d-nb.info/1028623232/34, 2012.

Reinsch, T. and Henninges, J.: Temperature dependent characterization of optical fibres for distributed temperature sensing in hot geothermal wells, Measurement Science & Technology - MEAS SCI TECHNOL, 21, https://doi.org/10.1088/0957-0233/21/9/094022, 2012.

Reinsch, T., Henninges, J., and Ásmundsson, R.: Thermal, mechanical and chemical influences on the performance of optical fibres for distributed temperature sensing in a hot geothermal well, Environmental Earth Sciences, 70, 3465–3480, https://doi.org/10.1007/s12665-013-2248-8, 2013.

Reinsch, T., Thurley, T., and Jousset, P.: On the mechanical coupling of a fiber optic cable used for distributed acoustic/vibration sensing applications—a theoretical consideration, Measurement Science and Technology, 28, 127003, https://doi.org/10.1088/1361-6501/aa8ba4, 2017.

Sahota, J., Gupta, N., and Dhawan, D.: Fiber Bragg grating sensors for monitoring of physical parameters: A comprehensive review, Optical Engineering, 59, 1, https://doi.org/10.1117/1.OE.59.6.060901, 2020.

Sakaguchi, K. and Matsushima, N.: Temperature Logging By the Distributed Temperature Sensing, in: Proceedings World Geothermal Congress 2000, Kyushu - Tohoku, Japan, May 28 - June 10, 2000, 1657–1661, 2000.

Saltelli, A., Ratto, M., Andres, T., Campolongo, F., Cariboni, J., Gatelli, D., Saisana, M., and Tarantola, S.: Global Sensitivity Analysis, The Primer. John Wiley & Sons, Ltd, 2008.

Saltelli, A., Annoni, P., Azzini, I., Campolongo, F., Ratto, M., and Tarantola, S.: Variance based sensitivity analysis of model output. Design and estimator for the total sensitivity index, Computer Physics Communications, 181, 259–270, https://doi.org/10.1016/j.cpc.2009.09.018, 2010.

Sanders, P. E.: Fiber-Optic Sensors: Playing Both Sides of the Energy Equation, Opt. Photon. News, 22, 36–42, https://doi.org/10.1364/OPN.22.1.000036, 2011.

Sanyal, S. K.: Classification of Geothermal Systems - a Possible Scheme, Thirtieth Workshop on Geothermal Reservoir Engineering, 1–8, 2005.

Sarmiento, Z. F.: Application of Well Testing in Assessing Geothermal Resources, in: “Short Course on Geothermal Drilling, Resource Development and Power Plants“, 2011.

Scales, J. A. and Tenorio, L.: Prior information and uncertainty in inverse problems, Geophysics, 66, 389–397, https://doi.org/10.1190/1.1444930, 2001.

Schlumberger: Cased Hole Log Interpretation Principles/Applications, 4th ed., Schlumberger, Houston, Texas, 1997.

Schlumberger: Log Interpretation Principles/Applications, Schlumberger, 7th ed., Schlumberger, 1998.

Schölderle, F., Lipus, M., Pfrang, D., Reinsch, T., Haberer, S., Einsiedl, F., and Zosseder, K.: Monitoring cold water injections for reservoir characterization using a permanent fiber optic installation in a geothermal production well in the Southern German Molasse Basin, Springer Berlin Heidelberg, https://doi.org/10.1186/s40517-021-00204-0, 2021.

Schulz, R. & Werner, K.-H.: Einfache Korrekturverfahren für Temperaturmessungen - Unveröffentlichter Bericht. – 23 S., Hannover (Niedersächsisches Landesamt für Bodenforschung)., 1987.

Schulz, R., Agemar, T., Alten, J.-A., Brunken, J., Heber, M., Kuder, J., Kühne, K., Maul, A.-A., Pester, S., Schönhofen, K., Fritzer, T., Birner, J., Schneider, M., Rauppach, K., Seibt, P., Wolfgramm, M., Brandes, J., Feldrappe, H., Obst, K., Jodocy, M., and Stober, I.: Aufbau eines geothermischen Informationssystems für Deutschland. – Endbericht (LIAG-Bericht, Archivnummer 0128452), Hannover, 114 pp., 2009.

Schulz, R., Pester, S., Schellschmidt, R., and Thomas, R.: Quantification of Exploration Risks as Basis for Insurance Contracts, Proceedings World Geothermal Congress, 25–29, 2010.

Schumacher, S. and Moeck, I.: A new method for correcting temperature log profiles in low-enthalpy plays, Geothermal Energy, 8, https://doi.org/10.1186/s40517-020-00181-w, 2020.

Sharma, W. S. K., Seki, A., Angel, S. M., and Garvis, D. G.: Field testing of an optical fiber temperature sensor in a geothermal well, Geothermics, 19, 285–294, https://doi.org/10.1016/0375-6505(90)90048-G, 1990.

Shen, P. Y. and Beck, A. E.: Stabilization of Bottom Hole Temperature With Finite Circulation Time and Fluid Flow, Geophysical Journal of the Royal Astronomical Society, 86, 63–90, https://doi.org/10.1111/j.1365-246X.1986.tb01073.x, 1986.

Singh, P. T., Spencer, J. W., Li, G., Jones, G. R., Humphries, J. E., Dancaster, J., Pinnock, R., and Dean, E.: Temperature sensor based on a Fabry-Perot interferometer addressed by low coherent light, in: IEE Colloquium (Digest), 7/1-7/4, https://doi.org/10.1049/ic:19951121, 1995.

Siska, P., Latal, J., Bujok, P., Vanderka, A., Klempa, M., Koudelka, P., Vasinek, V., and Pospisil, P.: Optical fiber based distributed temperature systems deployment for measurement of boreholes temperature profiles in the rock massif, Optical and Quantum Electronics, 48, https://doi.org/10.1007/s11082-016-0379-3, 2016.

Smithpeter, C., Normann, R., Krumhansl, J., Benoit, D., and Thompson, S.: Evaluation of a distributed fiber-optic temperature sensor for logging wellbore temprature at the Beowawe and Dixie Valley geothermal fields, Twenty-Fourth Workshop on Geothermal Reservoir Engineering, 1999.

Smolen, J. J. and Spek, A. Van Der: A DTS Primer for Oil & Gas Production, 2003.

Sobol, I. M.: Global sensitivity indices for nonlinear mathematical models and their Monte Carlo estimates, Mathematics and Computers in Simulation, 55, 271–280, https://doi.org/10.1016/S0378-4754(00)00270-6, 2001.

Steiner, U., Savvatis, A., Böhm, F., and Schubert, A.: Explorationsstrategie tiefer geothermischer Ressourcen am Beispiel des süddeutschen Oberjura, in: Handbuch Tiefe Geothermie, Bauer et al., 421–461, 2014.

Steingrimsson, B.: Geothermal Well Logging: Temperature And Pressure Logs,United Nations University, Geothermal Training Programme, 3, 2013.

Stober, I. and Bucher, K.: Geothermie, 3rd ed., Springer-Verlag GmbH, Freiburg, ISBN

9783662609392, 2020.

Storch, T., Grab, T., Gross, U., and Wagner, S.: Visual Observations Inside a Geothermal Thermosyphon, Heat Pipe Science and Technology, An International Journal, 4, 217–226, https://doi.org/10.1615/heatpipescietech.2014011210, 2013.

Sun, Y., Xue, Z., Park, H., Hashimoto, T., and Zhang, Y.: Optical Sensing of CO2 Geological Storage Using Distributed Fiber-Optic Sensor: From Laboratory to Field-Scale Demonstrations, Energy & Fuels, 35, 659–669, https://doi.org/10.1021/acs.energyfuels.0c03925, 2021.

Team, G.: Abschlussbericht zum Forschungsvorhaben AccordTemp@GeoMol Vergleich der verschiedenen Temperaturprognosen im Molassebecken im Rahmen des GeoMol-Projektes aus dem "Alpine Space"-Förderprogramm, Munich, 2015a.

Team, G.: Abschlussbericht zum Forschungsvorhaben Temp@GeoMol Prognose der flächenverteilten Temperaturen Im Rahmen des Projekts GeoMol des EU „Alpine Space " Förderprogramm, Munich, 2015b.

Team, G.: GeoMol - Assessing subsurface potentials of the Alpine Foreland Basins for sustainable planning and use of natural resources, Augsburg, 2015c.

Tilley, B. S. and Baumann, T.: On temperature attenuation in staged open-loop wells, Renewable Energy, 48, 416–423, https://doi.org/10.1016/j.renene.2012.03.007, 2012.

Toolbox, E.: Engineering Toolbox, Metals and Alloys – Young's Modulus of Elasticity, accessed June 2020, https://www.engineeringtoolbox.com/%0Ayoung-modulus-d_773.html.

Toth, A. and Bobok, E.: Flow and Heat Transfer in Geothermal Systems: Basic Equations for Describing and Modeling Geothermal Phenomena and Technologies, 1–382 pp., ISBN 9780128002773, 2016.

Tregubov, A. V., Svetukhin, V. V., Novikov, S. G., Berintsev, A. V., and Prikhodko, V. V.: A novel fiber optic distributed temperature and strain sensor for building applications, Results in Physics, 6, 131–132, https://doi.org/10.1016/j.rinp.2016.01.008, 2016.

Ukil, A., Braendle, H., and Krippner, P.: Distributed temperature sensing: Review of technology and applications, IEEE Sensors Journal, 12, 885–892, https://doi.org/10.1109/JSEN.2011.2162060, 2012.

Umweltbundesamt: Indicator: Greenhouse gas emissions, 2023, accessed November 10, 2023, https://www.umweltbundesamt.de/en/data/environmental-indicators/indicator-greenhouse-gas-emissions.

Vaezi, Y. and Van der Baan, M.: Comparison of the STA/LTA and power spectral density methods for microseismic event detection, Geophysical Journal International, 203, 1896–1908, https://doi.org/10.1093/gji/ggv419, 2015.

Villinger, E.: Bemerkungen zur Verkarstung des Malms unter dem westlichen süddeutschen Molassebecken, Bulletin der Vereinigung Schweiz. Petroleum-Geologen und -Ingenieure, 54, 1988.

Wang, J., Nitschke, F., Gholami Korzani, M., and Kohl, T.: Temperature log simulations in high-enthalpy boreholes, Geothermal Energy, 7, https://doi.org/10.1186/s40517-019-0149-0, 2019.

Wang, J., Nitschke, F., Gaucher, E., and Kohl, T.: Uncertainty analysis of numerical inversions of temperature logs fromboreholes under injection conditions, Journal of Geophysics and Engineering, 18, 1022–1034, https://doi.org/10.1093/jge/gxab069, 2021.

Weber, J., Born, H., and Moeck, I.: Geothermal energy use_ country update for Germany 2016-2018, in: European Geothermal Congress, 11–14, 2019.

WEMAG AG: Geothermie-Anlage in Neustadt-Glewe erhält Erweiterung, Press Release, 3rd August, 2023, accessed November 10, 2023, https://www.wemag.com/aktuelles-presse/geothermie-anlage-neustadt-glewe-erhaelt-erweiterung.

Williams, T., Lee, E., Chen, J., Wang, X., Lerohl, D., Armstrong, G., and Hilts, Y.: Fluid ingress location determination using distributed temperature and acoustic sensing, Society of Petroleum Engineers - SPE Digital Energy Conference and Exhibition 2015, 554–567, https://doi.org/10.2118/173446-ms, 2015.

Winter, T. and Einsiedl, F.: Combining 14CDOC and 81Kr with hydrochemical data to identify recharge processes in the South German Molasse Basin, Journal of Hydrology, 612, 128020, https://doi.org/10.1016/j.jhydrol.2022.128020, 2022.

Wisian, K. W., Blackwell, D. D., Bellani, S., Henfling, J. A., Normann, R. A., Lysne, P. C., Förster, A., and Schrötter, J.: Field comparison of conventional and new technology temperature logging systems, Geothermics, 27, 131–141, https://doi.org/10.1016/S0375-6505(97)10013-X, 1998.

Wolfgramm, M., Obst, K., Rauppach, K., Thorwart, K., Beichel, K., Brandes, J., and Koch, R.: Produktivitätsprognosen geothermischer Aquifere in Deutschland, in: Der Geothermiekongress 2009, 17–19, 2009.

Wong-Loya, J. A., Andaverde, J., and Santoyo, E.: A new practical method for the determination of static formation temperatures in geothermal and petroleum wells using a numerical method based on rational polynomial functions, Journal of Geophysics and Engineering, 9, 711–728, https://doi.org/10.1088/1742-2132/9/6/711, 2012.

World Development Indicators database: Gross domestic product 2022, accessed January 20, 2024, https://databank.worldbank.org.

Wyllie, M. R. J., Gregory, A. R., and Gardner, L. W.: Elastic Wave Velocities in Heterogeneous and Porous Media, Geophysics, 21, 41–70, https://doi.org/10.1190/1.1438217, 1956.

Ystroem, L. H., Nitschke, F., Held, S., and Kohl, T.: A multicomponent geothermometer for high-temperature basalt settings, Geothermal Energy, 8, https://doi.org/10.1186/s40517-020-0158-z, 2020.

Zarrouk, S. J. and McLean, K.: Geothermal Well Test Analysis: Fundamentals, Applications and Advanced Techniques, Elsevier, 1–349 pp., https://doi.org/10.1016/C2017-0-02723-4, 2019.

Zhang, L., Yang, Z., Szostkiewicz, Ł., Markiewicz, K., Mikhailov, S., Geernaert, T., Rochat, E., and Thévenaz, L.: Long-distance distributed pressure sensing based on frequency-scanned phase-sensitive optical time-domain reflectometry, Opt. Express, 29, 20487–20497, https://doi.org/10.1364/OE.425501, 2021a.

Zhang, Y., Lei, X., Hashimoto, T., and Xue, Z.: Toward Retrieving Distributed Aquifer Hydraulic Parameters From Distributed Strain Sensing, Journal of Geophysical Research: Solid Earth, 126, e2020JB020056, https://doi.org/10.1029/2020JB020056, 2021b.

Zhou, F.: Research on heat transfer in geothermal wellbore and surroundings, Technische Universität Berlin, 1–153 pp., 2013.

Zhou, F., Xiong, Y., and Tian, M.: Predicting initial formation temperature for deep well engineering with a new method, Journal of Earth Science, 26, 108–115, https://doi.org/10.1007/s12583-015-0512-4, 2015.

Zhou, X., Yu, Q., and Peng, W.: Simultaneous measurement of down-hole pressure and distributed temperature with a single fiber, Measurement Science and Technology, 23, https://doi.org/10.1088/0957-0233/23/8/085102, 2012.

Zhu, C., Zheng, H., Ma, L., Yao, Z., Liu, B., Huang, J., and Rao, Y.: Advances in Fiber-Optic Extrinsic Fabry–Perot Interferometric Physical and Mechanical Sensors: A Review, IEEE Sensors Journal, 23, 6406–6426, https://doi.org/10.1109/JSEN.2023.3244820, 2023.

Zosseder, K., Pfrang, D., Schölderle, F., Bohnsack, D., and Konrad, F.: Characterisation of the Upper Jurassic geothermal reservoir in the South German Molasse Basin as basis for a potential assessment to foster the geothermal installation development – Results from the joint research project Geothermal Alliance Bavaria, Geomechanics and Tunnelling, 15, 17–24, https://doi.org/https://doi.org/10.1002/geot.202100087, 2022.

SUPPLEMENTARY

Supplementary 4 - 1. Available continuous temperature logs (wireline and fiber-optic (FO-DTS)) in the North Alpine Foreland Basin in Bavaria. The estimated temperature (T) gradient was derived as an interpolated linear between the annual mean temperature at the surface calculated after (Team, 2015b) and the maximum temperature of the temperature log at the respective depth.

TLog	Type	Description	Shut-in Time	Estimated T gradient
TLog no. 1	Wireline	Log extends only in the cased section	> 3 months	0.03487 °C/m
TLog no. 2	FO-DTS	Log extends into the reservoir section	16 months	0.03431 °C/m
TLog no. 3	Wireline	Log extends down to half of the reservoir section	3 months	0.03216 °C/m
TLog no. 4	Wireline	Log extends only in the cased section	> 2 years	0.02538 °C/m
TLog no. 5	Wireline	Log extends into the reservoir section	2 months	0.05359 °C/m
TLog no. 6	Wireline	Log extends only in the cased section	3.5 months	0.03854 °C/m
TLog no. 7	Wireline	Log extends into the reservoir section	6.5 months	0.03602 °C/m
TLog no. 8	Wireline	Log extends into the reservoir section	13 months	0.03043 °C/m
TLog no. 9	Wireline	Log extends into the reservoir section	3 months	0.03438 °C/m
TLog no. 10	Wireline	Log extends to 200 m above bottom end	N/A	0.03432 °C/m
TLog no. 11	Wireline	Log extends into the reservoir section	N/A	0.03232 °C/m
TLog no. 12	Wireline	Log extends into the reservoir section	> 8 months	0.03256 °C/m
TLog no. 13	Wireline	Log extends into the reservoir section	N/A	0.03604 °C/m
TLog no. 14	Wireline	Log extends into the reservoir section	N/A	0.03646 °C/m
TLog no. 15	Wireline	Log extends into the reservoir section	2 months	0.03662 °C/m

Supplementary 4 - 2. Wells with BHT data and known SFT from DTS or Wireline TLogs used for the uncertainty analysis. Well no. 1 to well no. 7 were used for the uncertainty analysis of the 1BHTM correction scheme. Well no. 9 and the series of two BHT measurements in a row at 2240 m MD depth of well no. 8 were used for the uncertainty analysis of the LBM, HM, FM, and BM correction schemes. The series of four BHTs at 2355 m MD depth of well no. 8 was used for the uncertainty analysis of the LM correction scheme.

Well	BHT available	Depth of BHT	Borehole radius	Shut-in time	Static formation temperature at depth of BHT measurement
well no. 1 (SLS TH4)	105.4 °C	2924 mMD	0.10668 m	24 h	109.4 °C from TLog no. 2
well no. 2 (SLS TH6)	88 °C	2540.8 mMD	0.15558 m	18 h	99.0 °C from TLog no. 2 in 1200 m distance
	88.4 °C	2533.5 mMD	0.15558 m	24 h	99.1 °C from TLog no. 2 in 1200 m distance
well no. 3	82 °C	1959 mMD	0.10795 m	26.3 h	87.4 °C from TLog no. 6
well no. 4	116.68 °C	2958 mMD	0.10795 m	45 h	120.32 °C from TLog no. 7
well no. 5	80 °C	2574.2 mMD	0.10795 m	10 h	93.1 °C from TLog no. 8
well no. 6	81 °C	2660 mMD	0.10795 m	8 h	95.3 °C from well no. 5 in 1700 m distance
well no. 7	111.7 °C	3053.8 mMD	0.10795 m	52.5 h	116.12 °C from TLog no. 9
	58.5 °C	2240 mMD	0.10795 m	6.5 h	66.5 °C TLog no. 4
	59.5 °C			11.2 h	
well no. 8	63 °C	2335 mMD	0.0762 m	8 h	N/A no Wireline TLog at depth
	64 °C			10.5 h	
	65 °C			12.5 h	
	65.5 °C			15 h	
well no. 9	67 °C	1492 mMD	0.10795 m	11.8 h	81.25 °C from TLog no. 5 in 2300 m distance
	69 °C			16.2 h	

Supplementary 5 - 1. Completion of the geothermal wells at Schäftlarnstraße that were used for the FO-monitoring system.

Well 1 (Producer)	Depth (m MD)	Depth (m TVD)	Completion	KOP (m MD)	Inclination
	870	870	20 inch	250	4°
	2010	1812	13 3/8 inch	880	44°
	2819	2408	9 5/8 inch	2220	42°
	3741	2947	7 inch	2850	58°
Well 2 (Injector)	**Depth [m MD]**	**Depth [m TVD]**	**Completion**	**KOP [m MD]**	**Inclination**
	880	880	20 inch	250	4°
	2311	1980	13 3/8 inch	880	44°
	3345	2610	9 5/8 inch	2220	42°
	4443	2723	Open Hole	2850	58°

Supplementary 5 - 2. Optical Time Domain Reflectometry Measurements of the FO-system in the geothermal Schäftlarnstraße site. (a): OTDR of Multi-mode fibers inside production well 1 with B and F being the splice at the wellhead, C and E the y-splice at the P/T gauge and D the minibend at TD. (b): OTDR of Single-mode fibers of the looped whole system with B being the minibend inside the injector well 2, C the splice at the injectors wellhead, D the loss at the connector that connects the fibers of both wells, E the splice at the wellhead of the producer, F the y-splice at the P/T gauge and G being the FO cable termination at TD.

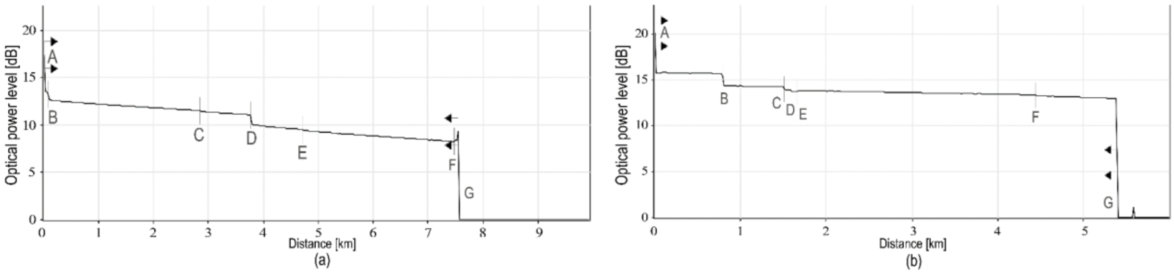

(a)

(b)

Supplementary 5 - 3. Graphical velocity analysis for cold water injection test Inj2.

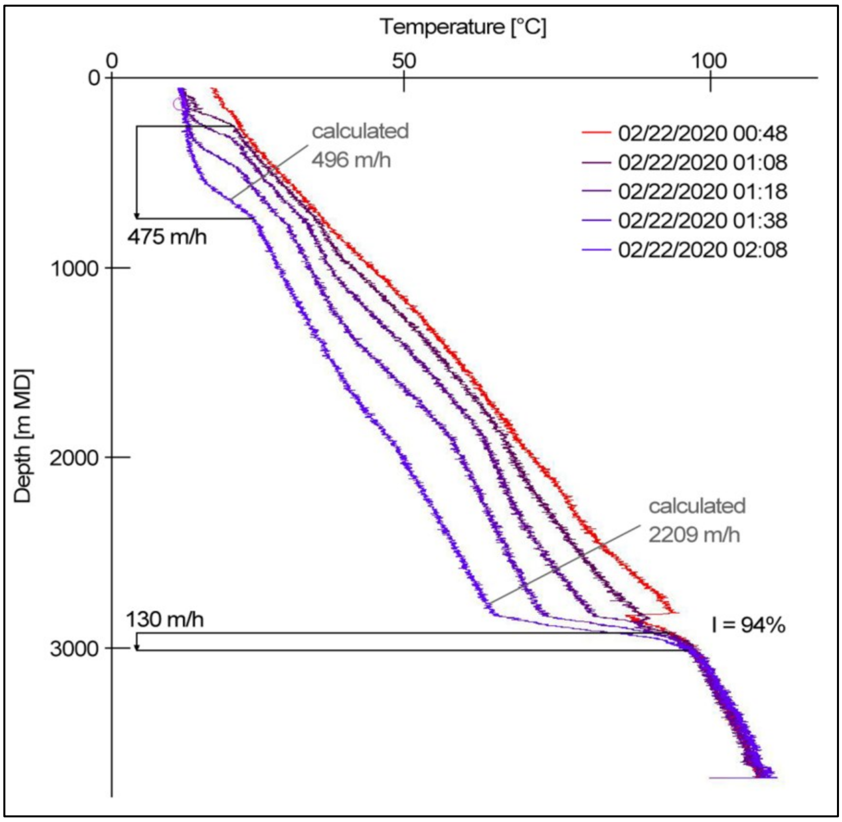

Supplementary 5 - 4. DTS profiles during warm-back of Inj1 in comparison to stratigraphic units and the well completion.

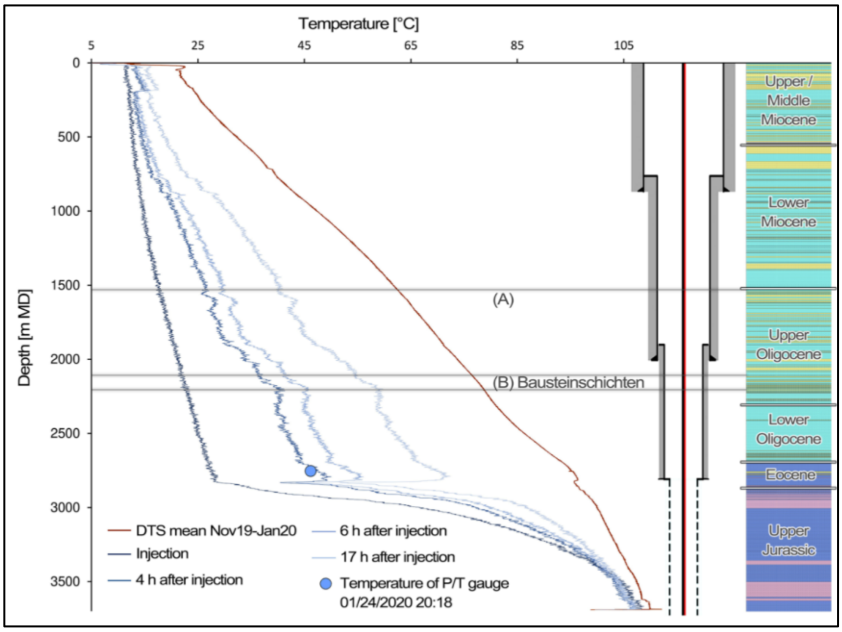

Supplementary 9 - 1. Temperature gradients derived for the North Alpine Foreland Basin in Bavaria over different stratigraphic layers by analyzing undisturbed temperature logs in the region with a robust fit calculation.

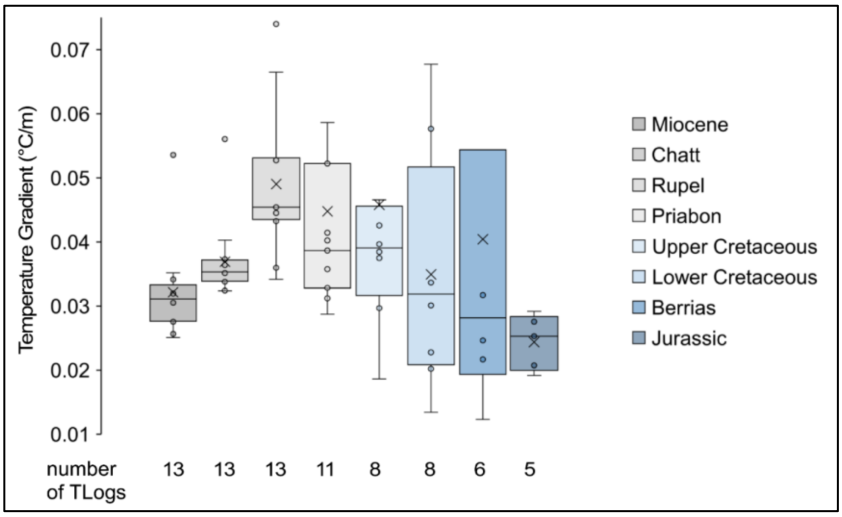

Supplementary 9 – 2. Available undisturbed temperature logs from Supplementary 4 - 3 in the North Alpine Foreland Basin in Bavaria.